Development and Application of Adjoint Sensitivity to Potential Vorticity and Unbalanced Flows in a Numerical Weather Prediction Model

By

Nuo Chen

A dissertation submitted in partial fulfillment of
the requirements for the degree of

Doctor of Philosophy
(Atmospheric and Oceanic Sciences)

at the
UNIVERSITY OF WISCONSIN-MADISON
2023

Date of final oral examination: 07/17/2023

The dissertation is approved by the following members of the Final Oral Committee:
Jonathan Martin, Professor, Atmospheric and Oceanic Sciences
Ángel Adames-Corraliza, Professor, Atmospheric and Oceanic Sciences
Brett T. Hoover, Affiliated Staff, Atmospheric and Oceanic Sciences
Leslie Smith, Professor, Mathematics
Gregory Tripoli, Emeritus Professor, Atmospheric and Oceanic Sciences
Hyun Mee Kim, Professor, Department of Atmospheric Sciences, Yonsei University

Abstract

Development and Application of Adjoint Sensitivity to Potential Vorticity and Unbalanced Flows in a Numerical Weather Prediction Model

by Nuo Chen

The adjoint of a numerical model provides a tool to measure the sensitivity of a chosen forecast aspect to small model state perturbations in the earlier time. For the response function describing the growth or behavior of extratropical and tropical systems, the sensitivity gradient provides dynamical information about certain aspects of storm development.

Previous studies employed Numerical Weather Prediction (NWP) models with either their adjoint or ensemble experiments to investigate dynamical mechanisms contributing to the change in the response function. However, most of them focus on the impact of individual model variable perturbation on the response function. This study is one of the first to derive the sensitivities to three-dimensional Quasi-geostrophic (QG) potential vorticity (PV) and Ertel PV that combine different sensitivity variables and the first to provide a "PV thinking" in the adjoint framework.

Same to the invertibility of PV, provided a balance constraint, a balanced model state sensitivity can be obtained from sensitivity to PV. Using balanced sensitivity fields as the adjoint forcing is shown to alleviate the geostrophic adjustment process often seen in the adjoint integration which emanates an unphysical high-frequency wave that contaminates

the interpretation of the adjoint analysis result. In addition to the balanced adjoint dynamics, the physical meaning of the deviation from the geostrophic balance, imbalance, is explored under the adjoint framework for the first time.

Sensitivities to QGPV, geostrophic imbalance, and Ertel PV all integrate wind and temperature sensitivities. Applying these tools to different cases reveals their individual attributes that help understand the dynamical mechanism of storm intensification. The case study of the March 2020 Atlantic midlatitude cyclone development confirms the general application of sensitivity to QGPV. In the case study of the November 1998 Winter Storm, sensitivity to winds is found to be dominated by the balanced component recovered from sensitivity to QGPV, while the sensitivity to potential temperature is dominated by the unbalanced component recovered from sensitivity to geostrophic imbalance. Further, the collocation between the unbalanced temperature sensitivity and diabatic heating separates the temperature sensitivity into adiabatic and diabatic sources. Balanced and unbalanced initial small perturbations are found to insert a similar amount of impact on the storm development. The ability of sensitivity to Ertel PV to integrate the features of sensitivity to QGPV and sensitivity to geostrophic imbalance suggests the better compatibility of "adjoint nonlinear balance" than the "adjoint geostrophic balance" in the case study of Hurricane Ian (2022).

Acknowledgements

These three and half years haven't been an easy journey, especially with all the other uncontrollable events happening back to back. I would not be able to make it through without my former advisor, Michael, for his guidance, support, and encouragement all along. I shall always remember when new ideas sparkled when we were chatting by the office or scribbling on the whiteboard. He has become my role model for being a mentor, a scientist, and a person.

To my committee members: Jon, thank you for stepping in as my advisor at the last minute, I always appreciate your feedback and your passion at our group meetings. Brett, your responses are always timely, thoughtful, and precise. Greg, thank you for leading me into the world of tropical cyclones with your unconventional insights. Leslie, you provided me with an opportunity to dive deep into modeling. Ángle, thank you for advocating modern tropical meteorology in the department. And finally, Dr. Kim, you have set a great example for me as an Asian woman in atmospheric science.

How fortunate I am that I chose to be a visiting student in this exact department in my junior year, where I was surrounded by the warmth of my peer undergraduate students, graduate students, and professors. I would not be truly interested in dynamical meteorology if weren't for this experience. To Pete Pokrandt, you fix all computer problems like a magician. Like everyone in the department, I always come to you for help, for you are such a kind and caring person. Dee and Christi, thank you for sorting out all the logistics problems, which are particularly hard for foreign students. To Zoë and Ian, having discussions with peers like you two always inspires me. Patrick, Poush, Libby, Kari, and other people in the high-impact weather group, sharing our progress and ideas makes my research journey less lonely. Witnessing the growth of undergraduate students like Kaylan and Issac has made me feel so proud.

My high school teachers, Xiao Fei and Yan Jie, one made me realize I am curious about the principle of everything, and the other one taught me life lessons beyond math. My friends, Wang Mengling and Xue Wenbo, ranting about our individual struggles with graduate school and life made me feel less alone. Finally, thank you, Dad, for single-handedly holding the family together when I am away. To my mom, for all the unconditional support you used to provide. And my grandma, who brought me up and made everything I achieve today possible.

Contents

List of Figures

List of Tables

Abbreviations

WRF	**W**eather **R**easerch and **F**orecast
PV	**P**ontential **V**orticity
QGPV	**Q**uasi-**G**eostrophic **P**ontential **V**orticity

Physical Constants

Speed of Light	c	=	$2.997\ 924\ 58 \times 10^8$ $\mathrm{ms}^{-\mathrm{S}}$ (exact)
Gravity Acceleration	g	=	$9.8\ m \cdot s^{-2}$
Specific Heat at Constant Pressure for Dry Air	C_p	=	$1005\ J \cdot kg^{-1} \cdot K^{-1}$
Gas Constant for Dry Air	R_d	=	$718\ J \cdot kg^{-1} \cdot K^{-1}$

Symbols

a	geostrophic imbalance	$m^2 \cdot s^{-1}$
q_g	quasi-geostrophic potential vorticity	s^{-1}
q_E	Ertel's potential vorticity	$K \cdot m^2 \cdot kg^{-1} \cdot s^{-1}$
R	response function	
θ	potential temperature	K
μ	perturbation dry air mass in column	Pa
Ψ	streamfunction	$m^2 \cdot s^{-1}$
Φ	geopotential	m^2
κ	exponent in Poisson's equation	dimensionless
π	Exner coordinate	$J \cdot kg^{-1} \cdot K^{-1}$
$\hat{a}$	sensitivity to geostrophic imbalance	$R \cdot s \cdot m^{-2}$
$\hat{q}_g$	sensitivity to quasi-geostrophic potential vorticity	$R \cdot s$
$\hat{q}_E$	sensitivity to Ertel's potential vorticity	$R \cdot kg \cdot s \cdot K^{-1} \cdot m^{-2}$

Chapter 1

Introduction

1.1 Potential Vorticity

Due to its unique characteristics of conservation and invertibility, potential vorticity (PV) has been used as both a forecasting and pedagogical tool to understand large-scale dynamical processes in meteorology. PV was first developed in the 1940s by Ertel and Rossby and studied in the 1950s by Kleinschmidt. In 1985, Hoskins, McIntyre, and Robertson reviewed its utility by plotting the Ertel PV on isentropic surfaces and combining the surface temperature to identify dynamical processes for the development of midlatitude cyclones, Rossby wave propagation, and blocking events. The conservation property of PV states that for inviscid flows, without any diabatic source, PV is conserved following the fluid motion.

Ertel's potential vorticity can also be simplified into several forms based on the applicability of simplifying assumptions for the atmospheric flow. Shallow water PV is often used in theoretical development and understanding due to its simplifying the flow as effectively 2D barotropic Quasi-geostrophic (QG) PV is extensively used in the midlatitudes given the midlatitude cyclone is subject to QG assumptions of small Rossby number and small Froude number.

The invertibility principle of PV states that the three-dimensional distribution of PV inside the domain and on the domain boundary uniquely determines the balanced velocity and temperature field (or the streamfunction and geopotential). One of the first successful numerical models, described as the barotropic model by Charney et al. (1950), used the geostrophic wind that is inverted from QGPV to advect QGPV.

The erosion of otherwise conserved PV is a crucial indicator for weather forecasting, usually caused by latent heating redistributing the upper-level PV to the low level. Adiabatic heating creates the low-level positive PV anomaly and, at the same time, erodes upper tropospheric PV (e.g., Stoelinga 1996). This erosion of the upper tropospheric PV serves to steepen the slope of the PV isopleth downstream of the upper-level positive PV anomaly. Such steepening is the PV equivalent of shortening the wavelength between the upper-level trough and the downstream ridge which was emphasized in the description of self-development (e.g., Sutcliffe and Forsdyke (1950)).

1.2 Balance Constraint

The PV invertibility is defined by which balance is chosen. The most general balance constraint is the nonlinear balance (e.g., Charney 1955; Allen 1991; Raymond 1992), which is obtained by omitting the divergence-related term in the divergence equation. Other balances more commonly known are dependent on stricter assumptions about the atmospheric flow. The geostrophic balance between the pressure gradient force and the Coriolis force is a good approximation in mid- and high-latitude flow; the gradient wind balance among the pressure gradient force, the Coriolis force, and the centrifugal force is often used in tropical cyclone studies; the cyclostrophic balance is used in mesoscale meteorology studies. Averaging over a time period long enough, the atmosphere's basic state is always in balance, and any perturbation will be adjusted towards the balanced state such as geostrophic balance in mid- and high-latitude (e.g., Holton and Hakim 2019 Section 5.6) and weak temperature gradient in the tropics. Beyond the real world, the balance constraint is also important in the numerical model simulation, where an unbalanced initial condition will cause the generation of unphysical inertio-gravity waves (e.g., Charney 1955).

However, it is the deviation from these balanced states that leads to various kinds of weather phenomena. Besides forcings from external sources such as surface friction, diabatic heating, etc., the violation of balance can happen inside the atmospheric process. The most famous example is the geostrophic paradox which states near the jet core, the geostrophic momentum advection destroys the geostrophic balance. Other violations of

balance constraint can be found in the tropical cyclone's outflow (e.g., Cohen et al. 2017; Wang et al. 2020), and in jet exit region (e.g., Charney and Stern 1962; Zhang et al. 2000; Thompson and Schultz 2021). Zhang et al. (2000) found the violation of nonlinear balance in the jet exit region leads to the generation of high-frequency gravity waves using the Mesoscale Model (MM5).

1.3 Adjoint Sensitivity

A numerical weather prediction (NWP) model integrates a system of partial differential equations that describes fundamental principles of fluid dynamics, thermodynamics, and conservation of mass to compute the time tendencies of the atmospheric model state. At the most abstract level, the nonlinear NWP model repeatedly calculates the prognostic variables (state variable) at the future time step as a function of the current and/or previous time steps. The NWP model has become more and more complicated in recent years, including different microphysics schemes for calculating precipitation types and amounts, parameterization schemes for describing boundary layer turbulent processes, and land/ocean-air mass/momentum flux exchanges, radiation schemes for calculating the longwave and shortwave radiation that also takes aerosols into account. Thus the state-of-art numerical weather model is an integration of knowledge across several research fields in geoscience and the model itself is highly nonlinear. The nonlinearity of the natural system and the numerical model is widely known as the butterfly effect, recognized by (Lorenz, 1963), a term frequently misused by the general public. In his 1963 paper, he demonstrated even with a simple system with just three variables and three equations,

the long-term integration results can be very different due to a small perturbation in the initial condition. Although the finding dims the light on long-range weather forecasts, it addresses the importance of obtaining precise initial conditions and the necessity of ensemble weather prediction.

The dependence of any given aspect of the model forecast state (defined as the response function, R, later) on the perturbation of any collection of model variables at the initial or any previous time step is generalized as the term "sensitivity". For high-impact weather, the forecast output aspects can be some measure of the model forecast error, intensity of a weather system by either pressure, wind speed, total rainfall, or other dynamical or thermodynamical aspects — essentially anything of interest that one would like to research if the response function can be well represented (Errico, 1997). The model variable could be some variable at the interior points of the model domain, at the model boundary, or even the model parameters defined either on a map grid or as spectral coefficients.

Two popular ways to evaluate sensitivity are direct methods (e.g. Dickinson and Gelinas 1976) and adjoint methods (e.g. Hall and Cacuci 1983). The direct method compares the results among an ensemble of perturbation experiments to determine which combination of perturbations could lead to the largest change in the response function. Thus the direct method is called ensemble sensitivity as well. The ensemble sensitivity analysis utilizes a collection of model forecasts to sample the probability density function of the model state (e.g., Ancell and Mass 2006; Hakim and Torn 2008; Torn and Hakim 2008).

A relationship between the response function and the initial condition can be established by calculating the variance in the ensemble state vector. Ancell and Mass (2006) revealed that the ensemble sensitivities exhibit syntopic-scale, tropospheric-deep structures near the major synoptic feature of interest.

In this study, the adjoint method views the sensitivity as the first-order derivative of the response function to the state vector or some diagnostics variable by performing the first-order Taylor series expansion,

$$R(\mathbf{x}+\mathbf{x}') = R(\mathbf{x}) + \frac{\partial R(\mathbf{x})}{\partial \mathbf{x}}\mathbf{x}' + \mathcal{O}(\mathbf{x}'^2) \tag{1.1}$$

which infers that the sensitivity gradient of the response function $\partial R(\mathbf{x})/\partial \mathbf{x}$ could describe the impact of a small perturbation on the response function to the first order. The ability to indicate the most sensitive region of a model forecast error made the adjoint and other sensitivity analysis techniques useful tools for targeted observation field campaigns. These techniques include the ensemble sensitivity method (e.g., Aberson 2003; Ancell and Mass 2006; Brown and Hakim 2015) and singular vector method (e.g., Pu et al. 1997; Wu et al. 2007; Jung et al. 2010). Having knowledge of the most sensitive regions allows an effective observation platform deployment, such as truck-mounted radar and aircraft reconnaissance, to observe specific regions of the atmosphere that demands the smallest initial condition error for the most accurate forecast.

In addition to being an indication of the region and variable that the final forecast state

is most sensitive to, sensitivity is also an essential part of data assimilation. The introduction of data assimilation improves the quality and accuracy of numerical weather prediction. In three-dimensional variational data assimilation, the adjoint sensitivity or the error covariance matrix propagates the information (innovation) on the observation point to the surrounding grid point. In the four-dimensional variational data assimilation (4D-Var), observations (from satellite, sounding, etc.) taken at different times in the assimilation time window are assimilated into the prior model output at the beginning of the assimilation time window (analysis time) carried by the adjoint backward integration (e.g., Lewis and Derber 1985; Dimet and Talagrand 1986; Thacker and Long 1988; Zhang et al. 2013). Using the ensemble method, the background covariance matrix (e.g. GSI, DART; Hu et al. 2018; Anderson et al. 2009) can also propagate the forecast error from the next analysis time back to the previous analysis time. The analysis that gained new information from the observation will serve as a more accurate initial condition for the next forecast cycle. By performing a singular value decomposition on the adjoint sensitivity matrix, one can get singular vectors. These singular vectors provide a set of orthogonal vectors that represent the dominant patterns in the initial condition and the leading vectors added to the initial condition will grow fastest. Thus in ensemble forecasting, the ensemble initial condition seeded by singular vectors could capture the widest range of possible forecast direction and uncertainty (e.g. 500 hPa geopotential spaghetti plot or tropical cyclone ensemble track forecast).

The development of an adjoint model includes first linearizing the nonlinear expression M (1.2) about the nonlinear NWP model trajectory to obtain the tangent linear model $\mathbf{M}$

operates on the small perturbation $\mathbf{x}$ (1.3). Then the adjoint model $\mathbf{M}^T$ can be obtained by transposing the TLM model in most cases under the Euclidean norm (1.4).

$$\mathbf{x}_{t+1} = M(\mathbf{x}_t) \tag{1.2}$$

$$\mathbf{x}'_{t+1} = \mathbf{M}\mathbf{x}'_t \tag{1.3}$$

$$\frac{\partial R}{\partial \mathbf{x}_t} = \mathbf{M}^T \frac{\partial R}{\partial \mathbf{x}_{t+1}} \tag{1.4}$$

If we denote $\langle f, g \rangle$ as the norm or the inner product of f and g, the adjoint of an operator L, L^* should satisfy $\langle f, Lg \rangle = \langle L^* f, g \rangle$ under the Euclidean norm (or other norms if specified). In many cases, with a homogeneous boundary condition, the adjoint of an operator is the same as the transpose of this operator, $L^* = L^T$. Two simple rules of adjoint are followed in this work: 1) the adjoint of a constant is itself; 2) the adjoint of a derivative operator, such as d/dx, is its additive inverse, $-d/dx$.

Practically, the adjoint of a numerical model is developed by adjointing the model line-by-line and reserving the order of each code line. However, as NWP becomes increasingly complicated and coupled with other models, the adjoint model becomes difficult to develop. The ensemble method like Ensemble Kalman Filter (EnKF), though it requires more computation resources, is compatible with most models (e.g. DART; Anderson et al. 2009).

The adjoint technique has other limitations. The biggest limitation is that the adjoint is **linear**. If the response function or the model is nonlinear, there will likely be a perturbation size for which the linearization becomes inadequate since both using a tangent linear model and using an adjoint suggest the wrong response to the perturbation is the nonlinear model (Errico, 1997). That is why the moisture adjoint sensitivity should be taken with caution because the parameterization of microphysics procures contains too many "if-else" statements, which are presented by nonlinear Heaviside function, along the phase change of water vapor or species change of hydrometeors.

The adjoint sensitivity analysis is also constrained by the validity of the first-order Taylor series approximation, meaning the second-order term should be small enough to neglect. This requires the perturbations to be relatively small compared to the basic state through the integration period. Once the perturbations become too large either due to being initially prescribed so or due to the dynamical nonlinearity or computational or dynamical instability, the usefulness of the adjoint sensitivity should be scrutinized. Many aspects contribute to the constraints on the accuracy and utility of adjoint models, such as turbulent, diabatic heating related to phase change of water, topographical effect, etc. These assumptions restrict the quantitative accuracy of the adjoint-derived sensitivity to 72 hours if only dry physics is considered or less than 24 hours if the weather system is highly nonlinear and associated with deep convections and topographical effect (e.g., Park and Droegemeier 1997; Errico and Raeder 1999). Of course, the second-order adjoint model can alleviate the time limitation (Godinez and Daescu, 2009) but this is beyond the scope of this proposed work. Finally, noted by Ancell and Mass (2006), adjoint sensitivity from

the weather forecast and research has its predominance in the lower troposphere, as we will see in this study.

1.4 Research Questions

This work seeks to explore the derivation of the sensitivity to PV, present the physical interpretation of the sensitivity to PV and to imbalance, along with various implementations of the sensitivity to PV in different case studies. Through the case studies, the ability of the sensitivity to PV shall be examined, as either a diagnostic tool to understand the dynamic process that leads to the weather system's development or an auxiliary procedure that has the potential to improve the result of adjoint sensitivity analysis and data assimilation. The research questions (RQs) to be considered include:

RQ1: How to derive the sensitivity to PV, to geostrophic imbalance, and other related variables? How does one interpret the sensitivity to PV, and to the geostrophic imbalance?

RQ2: For real case studies, we can use sensitivity to QGPV to generate a geostrophically balanced adjoint forcing in the adjoint model. The following shall be tested: 1) can this balanced adjoint forcing filter out the gravity wave pattern in the adjoint sensitivity field? 2) How do balanced perturbations and unbalanced perturbations, when added to the model initial condition, contribute to the evolution of an intensifying mid-latitude cyclone and an intensifying tropical cyclone? 3) Can the sensitivity to PV be approximated by the PV perturbation? 4) Is sensitivity to the geostrophic imbalance important?

RQ3: Derivation of the sensitivity to Ertel PV. What is the difference between the sensitivity to Ertel PV and to QGPV when applied to the same tropical cyclone case? Is sensitivity to Ertel PV a better measurement than sensitivity to QGPV?

Chapter 2 shows two different approaches to the derivation of the different forms of sensitivity to PV with a focus on QGPV. Some basic applications of sensitivity to QGPV is demonstrated with a mid-latitude winter storm case study. Chapter 3 focuses on the notion of geostrophic imbalance and the understanding of sensitivity to the geostrophic imbalance in the context of a mid-latitude winter storm. The sensitivity to Ertel PV is fully derived in Chapter 4 and is compared with sensitivity to QGPV and sensitivity to the geostrophic imbalance in a tropical cyclone case study. Chapter 5 summarizes the results of these studies and points out future research directions related to current work.

Chapter 2

Sensitivity to QGPV

2.1 Overview

Adjoint-derived sensitivity analysis is an efficient means to diagnose the sensitivity of a numerical weather prediction (NWP) model forecast state to changes in the model state at earlier times. Adjoint sensitivity analysis has been used in numerous case studies of weather systems (e.g., Rabier and Courtier 1992; Langland et al. 1995; Kleist and Morgan 2005; Hoover and Morgan 2011; Doyle et al. 2014; Goldstein 2018). For a forecast trajectory defined on the time (t) interval from $0 \leq t < t_f$, an adjoint-derived sensitivity at time $t = \tau$ is defined as the gradient of a response function (R), representing a function of interest of the forecast state at final forecast time $t = t_f$, with respect to the model state, ($\mathbf{x}_\tau$), $\partial R/\partial \mathbf{x}_\tau$. The sensitivity is a complete and succinct representation

of how changes to the model state at time $t = \tau$ change the response function at time $t = t_f$.

Sensitivities are most efficiently calculated using an adjoint model (Errico, 1997). The adjoint of an NWP model is defined as the transpose of the tangent linear model (TLM) linearized about the forecast trajectory of a nonlinear NWP model. The adjoint model is initialized with the gradient of R with respect to the final time model state, $\mathbf{x}_{t_f}$ ($\partial R/\partial \mathbf{x}_{t_f}$) and is integrated backward along a forecast trajectory defined by the nonlinear NWP model to arrive at the sensitivity of R with respect to the model state at an earlier time. The response function can be any function of the model final state that is differentiable with respect to the model state variables. The impact of any perturbation at forecast time, τ, ($\mathbf{x}'_\tau, 0 \leq \tau < t_f$) on R is easily estimated quantitatively as the inner product of the perturbation and the sensitivity gradient with respect to the model state at time τ:

$$\Delta R \cong \delta R = \langle \frac{\partial R}{\partial x_\tau}, x'_\tau \rangle \tag{2.1}$$

where ΔR represents the difference between R calculated from a perturbed nonlinear forecast state and R calculated from a control (i.e., unperturbed) nonlinear forecast state. The inner product of the sensitivity with the perturbation is an estimate (δR) of the impact of the perturbation on the response function subject to the limitations of the TLM's linearity and any physical processes omitted or simplified in the TLM for the sake of linearization.

Most modern NWP models have included a tangent linear approximation to microphysics and the adjoint of moist variables in their adjoint component. However due to the complexity of the nonlinear procedure – a Heaviside function that switches between sensitivity to different hydrometeors along the forward forecast trajectory, it is difficult to learn the underlying dynamical process that leads to the change in the response function. Even in a dry-dynamics-only model, it is challenging to provide the physical interpretation of these gradients with respect to model forecast fields like horizontal wind and temperature due to the adjustment process during the geostrophic adjustment time for the backward integration. It is desirable to distill the substantive implications that each model state sensitivity reveals into a single sensitivity field (e.g., Arbogast 1998; Kleist and Morgan 2005; Romero et al. 2005; Kim and Beare 2011). Arbogast (1998) argues that for quasi-balanced flows, that desired sensitivity field is the sensitivity to potential vorticity (PV).

In their review, Hoskins et al. (1985) discussed the principles of conservation and invertibility of PV. The invertibility principle states that the three-dimensional distribution of PV within some domain and boundary conditions on that domain uniquely determine the velocity and temperature distribution consistent with a particular balance constraint. The conservation principle states that for inviscid flows in which the gradient of diabatic heating does not project onto the local absolute vorticity vector, PV is conserved following the fluid motion. Together, conservation and invertibility imply that *the dynamics of quasi-balanced ("nearly" balanced) flows may be expressed simply and* **entirely** *in terms of the distribution of PV and the boundary conditions necessary in the inversion* of the

PV (Morgan and Nielsen-Gammon, 1998). There are many "flavors" of PV ranging from the absolute vorticity, the linearized shallow water PV, the quasi-geostrophic (pseudo-) potential vorticity (QGPV; Charney and Stern 1962), to the Ertel PV (Ertel, 1942).

Adjoint-derived sensitivity gradients have been used to objectively define optimal perturbations to NWP model initial conditions that produce a desired forecast impact (e.g., Vukićević and Raeder 1995; Errico 1997; Doyle et al. 2014; Hoover 2015). Such perturbations produce a prescribed change to the response function, ΔR, while keeping the change added to the model initial state,$\mathbf{x}_0'$, to a minimum. The adjoint-derived optimal perturbation technique has been used to study physical mechanisms and predictability of tropical cyclogenesis (e.g., Doyle et al. 2011; Doyle et al. 2012; Hoover 2015), Kelvin wave interactions with tropical cyclones (Reynolds et al., 2016), extratropical cyclone intensity (e.g., Reynolds et al. 2001; Romero et al. 2005; Argence et al. 2009; Doyle et al. 2014; Doyle et al. 2019), mesoscale convective systems (e.g., Xu et al. 2001), and atmospheric rivers (e.g., Reynolds et al. 2019; Demirdjian et al. 2020).

Some of these studies used the optimal perturbation technique to investigate the impact of a PV perturbation on the forecast (e.g., Vukićević and Raeder 1995; Fehlmann and Davies 1997; McTaggart-Cowan et al. 2004; Doyle et al. 2019). In these studies, the physical mechanisms responsible for the sensitivity of the response function to changes to the model initial state are investigated through a perturbation-response technique in which optimal perturbations for a given response function and optimization norm are

computed, inserted into the initial conditions, and evolved in the nonlinear model to observe the result.

It is important to note that vorticity (or PV) perturbations computed from optimal horizontal wind (and temperature) perturbations however, are not optimized in the same sense as being proportional to the sensitivity gradient with respect to vorticity or PV. A QGPV perturbation derived from optimal perturbations to the constituent wind and temperature fields is presumed to project onto the sensitivity of QGPV but doesn't necessarily conform to the spatial scale of the QGPV sensitivity itself (Doyle et al., 2019). In order to compute a truly optimized QGPV perturbation, a sensitivity with respect to QGPV is required as is an appropriate energy weighting norm operator.

The goals of the present study are to first demonstrate two means for computing the sensitivity with respect to QGPV, given sensitivities with respect to the state variables of the model (horizontal wind and potential temperature) in section 2.2. The interpretation of the sensitivity to QGPV is provided in section 2.3. Followed by the derivation of sensitivity to other forms of PV in section 2.4. Then in section 2.5 we apply this technique to a simulation of an explosive Atlantic cyclogenesis event to demonstrate how the sensitivity to QGPV can be used to interpret the sensitivity of the forecast intensity of the cyclone to small QGPV perturbations to the model initial state. Additionally, we derive expressions for "balanced" adjoint sensitivities to horizontal wind and hydrostatic temperature and demonstrate in the case study how adjoint integration of these balanced sensitivities

removes large oscillations of the sensitivity representing sensitivity to unbalanced perturbations undergoing adjustment from the adjoint integration while preserving the balanced information contained in the sensitivity to QGPV for certain response function. Finally, a comparison between the spatial distribution of the sensitivity to QGPV and the QGPV perturbation created by inserting the initial optimal wind and temperature perturbations is presented to answer the validity of treating the PV perturbation as an approximation for sensitivity to PV used in many previous studies[1]. Section 2.6 concludes this chapter.

2.2 Derivation of Sensitivity to QGPV Using Energy Norm

2.2.1 QGPV

In the quasigeostrophic (QG) system, the quasigeostrophic potential vorticity (also known as the pseudo-PV) is conserved following the geostrophic flow (Charney and Stern, 1962). In isobaric coordinates, the QGPV is given by:

$$q_p = f + \frac{1}{f_0}\nabla^2\varphi' + \frac{\partial}{\partial p}(\frac{f_0}{S}\frac{\partial \varphi'}{\partial p}) = f + \wp(\varphi') \tag{2.2}$$

where f is the planetary vorticity, f_0 is the planetary vorticity averaged over the domain within which the QGPV is calculated, $S = S(p)$ is a reference state static stability parameter (defined below), and p is pressure. This definition of QGPV is also a statement

[1]Most of this chapter is from a revised version of a paper submitted to Monthly Weather Review following the reviewers' comments.

of the invertibility principle: through a three-dimensional, elliptic operator, $\wp$, the QGPV is related to perturbation geopotential, $\varphi'(x,y,p,t) = \Phi - \bar{\Phi}(p)$, defined as the deviation of the full geopotential from a horizontally-averaged hydrostatic reference state geopotential, $\bar{\Phi}(p)$ where $\frac{\partial \bar{\Phi}}{\partial p} = -\frac{R_d}{p}\left(\frac{p}{p_0}\right)^{\frac{R_d}{c_p}} \bar{\theta}$, θ is the potential temperature, and the overbars indicate horizontal averaging. In the example to follow, the reference state used is the U.S. Standard Atmosphere with the associated reference state stratification, $S(p) = -\frac{\bar{\alpha}}{\bar{\theta}}\frac{\partial \bar{\theta}}{\partial p}$ where $\bar{\alpha}$ is the reference state specific volume. The deviations of the geopotential from its reference state, φ', are associated with geostrophic flow, $\mathbf{V}_g = \frac{\mathbf{k}}{f_0} \times \nabla\varphi' = u_g\mathbf{i} + v_g\mathbf{j}$. The potential temperature perturbation is defined as $\theta' = -\frac{p}{R_d}\left(\frac{p_0}{p}\right)^{\frac{R_d}{c_p}} \frac{\partial \varphi'}{\partial p}$, where R_d is the dry gas constant. With these definitions, the perturbation QGPV, defined as the difference between the full QGPV and the planetary vorticity, may be written also in terms of the geostrophic wind components and potential temperature deviations:

$$q_p' = q_p - f = \frac{\partial v_g}{\partial x} - \frac{\partial u_g}{\partial y} - \frac{\partial}{\partial p}\left(\frac{f_0}{S}\frac{RT'}{p}\right)$$

$$q_p' = \frac{\partial v_g}{\partial x} - \frac{\partial u_g}{\partial y} - \frac{\partial}{\partial p}\left(\frac{f_0}{S}\gamma\theta'\right) \tag{2.3}$$

where $\gamma = \frac{R_d}{p}\left(\frac{p}{p_0}\right)^{\frac{R_d}{c_p}}$.

2.2.2 Optimal Perturbations and an Energy Norm

To answer the question "What is the smallest change to the model initial state, $\mathbf{x}'_0$, that produces a prescribed change to the response function", it is intuitive to put perturbations in the most sensitive region. Specifically, we wish to minimize the $\mathbf{W}$ weighted initial perturbation energy norm, $\mathscr{E} = \langle \mathbf{x}'_0, \mathbf{W}\mathbf{x}'_\mathbf{0} \rangle$, subject to the constraint that the specified change in R satisfies: $\delta R = \langle \frac{\partial R}{\partial \mathbf{x}_0}, \mathbf{x}'_0 \rangle$. The prescribed change in the response function, δR, represents the first-order Taylor series expansion of the change in the response function due to changes in the initial state. The weighting matrix $\mathbf{W}$ (which can also be viewed as a linear operator) defines the coefficients of an energy norm (e.g., Ehrendorfer et al. 1999) and allows for a scalar quantity with dimensions of energy per unit mass to be defined from the model state variables with different dimensional attributes. In this way, the smallest perturbation to the model initial state that produces the prescribed change in the response function is the perturbation that minimizes the energy norm.

This constrained minimization problem may be formulated as a Lagrangian $\mathscr{L}$:

$$\mathscr{L} = \mathscr{E} + \lambda \left(\delta R - \left\langle \frac{\partial R}{\partial \mathbf{x}_0}, \mathbf{x}'_0 \right\rangle \right)$$

where the initial energy $\mathscr{E} = \langle \mathbf{x}'_0, \mathbf{W}\mathbf{x}'_\mathbf{0} \rangle$ and λ is the Lagrange multiplier. The minimum is found where $\nabla_{\mathbf{x}_0}\mathscr{L} = \nabla_\lambda \mathscr{L} = 0$. $\nabla_{\mathbf{x}_0}\mathscr{L} = \mathbf{W}\mathbf{x}'_0 + \lambda \frac{\partial R}{\partial \mathbf{x}_0} = 0$ gives formulation for the optimal initial condition $\mathbf{x}'_0 = \mathbf{W}^{-1}\lambda \frac{\partial R}{\partial \mathbf{x}_0}$. Substitute λ back into $\delta R = \left\langle \frac{\partial R}{\partial \mathbf{x}_0}, \mathbf{x}'_0 \right\rangle$ gives

the expression for λ

$$\lambda = \frac{\delta R}{\left(\frac{\partial R}{\partial \mathbf{x}_0}\mathbf{W}^{-1}\frac{\partial R}{\partial \mathbf{x}_0}\right)} \tag{2.4}$$

Note that the optimal initial condition perturbation ($\mathbf{x}_0'$) is proportional to the adjoint-derived sensitivity gradient ($\frac{\partial R}{\partial \mathbf{x}_0}$). Each component of the sensitivity to the initial condition state vector is multiplied by the inverse of the weighting operator used to define an energy norm for the variables under consideration. In addition, the initial perturbations are scaled by the *same* Lagrange multiplier, λ. This suggests that any other optimal perturbation that is a function of the model state, i.e., $\mathbf{a}' = f(\mathbf{x}_0)$, may be written:

$$\mathbf{a}' = \lambda \mathbf{W}_a^{-1}\frac{\partial R}{\partial \mathbf{a}} = \lambda \mathbf{W}_a^{-1}\hat{\mathbf{a}} \tag{2.5}$$

where $\mathbf{W}_a$ is the energy-norm defining operator for that variable. Provided a linearized relationship (e.g. (2.3)), an appropriate $\mathbf{W}_a$, and other prognostic sensitivities, we can solve for the unknown sensitivity, $\hat{\mathbf{a}} = \frac{\partial R}{\partial \mathbf{a}}$[2].

2.2.3 QGPV Energy Norm

The technique to calculate the sensitivity to QGPV ($\hat{q}$) is motivated by the observation in (2.5) that while *each* of the model state variables comprising the optimal adjoint-informed initial condition state vector have unique weights to calculate an energy norm, all of the variables are scaled by a common factor, the Lagrange multiplier, λ. In this derivation,

[2]In the sequel, for convenience, we adopt the "hat" notation so that the sensitivity to a variable $\mathbf{a}$, $\hat{\mathbf{a}} = \partial R/\partial \mathbf{a}$

we wish to express all the perturbation terms in (2.3) with the sensitivity using (2.5). Therefore we need to first find the energy norm weighting suitable for QGPV, $\mathbf{W}_{q_p}^{-1}$.

The choice of the energy norm follows the conservation of energy criteria, meaning the kinetic energy and thermal energy can be converted into each other while keeping the total energy conserved. The energy norm should also be constructed by variables whose sensitivity is available from the WRF adjoint model. Thus we define an energy norm that is consistent with QG dynamics in terms of the model state variables (here u, v, θ) that can also be computed from the QGPV. This is the quasi-geostrophic pseudo-energy, $\mathscr{E}_{PE}$, which may be written as:

$$\begin{aligned}\mathscr{E}_{PE} &= \frac{1}{2}\iiint \left(u_g'^2 + v_g'^2 + \frac{\left(\frac{\partial \varphi'}{\partial p}\right)^2}{S} \right) dxdydp \\ &= \frac{1}{2}\langle (\mathbf{u}', \mathbf{v}', \theta') \, , \mathbf{W}_{u,v,\theta} \, (\mathbf{u}', \mathbf{v}', \theta')^T \rangle\end{aligned}$$

The weighting matrix

$$\mathbf{W} = \mathbf{W}_{u,v,\theta} = \begin{pmatrix} \mathbf{I} & 0 & 0 \\ 0 & \mathbf{I} & 0 \\ 0 & 0 & \frac{\gamma^2}{S}\mathbf{I} \end{pmatrix}$$

is block diagonal with the identity matrix along the diagonal for the wind components and γ^2/S for the elements multiplying the potential temperature components of the state

vector.

2.2.4 Sensitivity to QGPV

We seek the sensitivity to QGPV, a variable not in the state vector of the NWP model, with $\mathbf{q}_p(\mathbf{x}) = \mathbf{q}_p(\mathbf{u}, \mathbf{v}, \theta)$. Consider the optimal initial condition with the state vector that inserts minimal QG pseudo-energy:

$$\mathbf{x}' = (\mathbf{u}', \mathbf{v}', \theta') = \lambda \left(\hat{\mathbf{u}}, \hat{\mathbf{v}}, \frac{S}{\gamma^2}\hat{\theta} \right)$$

The weighting matrix, $\mathbf{W}_{q_p}$, is determined by that matrix defining the perturbation pseudo-energy per unit mass, $\mathscr{E}_{PE}$ that can be written in terms of the perturbation geopotential (assuming that the perturbation geopotential, perturbation geostrophic wind, and perturbation potential temperature field vanish along the domain boundaries) as:

$$\begin{aligned}
\mathscr{E}_{PE} &= \frac{1}{2} \iiint \left(u_g'^2 + v_g'^2 + \frac{\left(\frac{\partial \varphi'}{\partial p}\right)^2}{S} \right) dxdydp \\
&= \frac{1}{2} \iiint (u_g'^2 + v_g'^2 + \frac{\gamma^2}{S}\theta'^2) dxdydp
\end{aligned}$$

We can also express $\mathscr{E}_{PE}$ in the form of the inner product of potential vorticity and geopotential:

$$\mathscr{E}_{PE} = -\frac{1}{2f_0} \iint q_p' \varphi' dxdydp = -\frac{1}{2f_0} \langle \mathbf{q}_p', \varphi' \rangle$$

or using the inverse of the QGPV calculation operator $\wp^{-1}$ defined in (2.2)

$$\mathscr{E}_{PE} = -\frac{1}{2}\langle \mathbf{q}'_p, \frac{1}{f_0}\wp^{-1}\mathbf{q}'_p\rangle = \frac{1}{2}\langle \mathbf{q}'_p, \mathbf{W}_{q_p}\mathbf{q}'_p\rangle$$

where we find the weighting matrix to be $\mathbf{W}_{q_p} = -\frac{1}{f_0}\wp^{-1}$.

Given (2.5) that $\mathbf{u} = \lambda\mathbf{W}_{\mathbf{u}}^{-\mathbf{1}}\hat{\mathbf{u}} = \lambda\hat{\mathbf{u}}$, $\mathbf{v} = \lambda\mathbf{W}_{\mathbf{v}}^{-\mathbf{1}}\hat{\mathbf{v}} = \lambda\hat{\mathbf{v}}$, and $\theta = \lambda\mathbf{W}_{\theta}^{-\mathbf{1}}\hat{\theta} = \lambda\frac{\mathbf{S}}{\boldsymbol{\gamma}^{\mathbf{2}}}\hat{\theta}$, the optimal initial condition for QGPV is then:

$$\mathbf{q}'_{\mathbf{p}} = \lambda\mathbf{W}_{\mathbf{q_p}}^{-\mathbf{1}}\hat{\mathbf{q}}_{\mathbf{p}} = \frac{\partial}{\partial\mathbf{x}}(\lambda\hat{\mathbf{v}}) - \frac{\partial}{\partial\mathbf{y}}(\lambda\hat{\mathbf{u}}) - \frac{\partial}{\partial\mathbf{p}}\left(\mathbf{f_0}\frac{\gamma}{\mathbf{S}}\left(\lambda\frac{\mathbf{S}}{\boldsymbol{\gamma}^{\mathbf{2}}}\hat{\theta}\right)\right)$$

$$-f_0\wp\hat{\mathbf{q}}_p = \frac{\partial\hat{\mathbf{v}}}{\partial x} - \frac{\partial\hat{\mathbf{u}}}{\partial y} - \frac{\partial}{\partial p}\left(\frac{f_0}{\gamma}\hat{\theta}\right)$$

$$\hat{\mathbf{q}}_p = -\frac{1}{f_0}\wp^{-1}\left[\frac{\partial\hat{\mathbf{v}}}{\partial x} - \frac{\partial\hat{\mathbf{u}}}{\partial y} - \frac{\partial}{\partial p}(\frac{f_0}{\gamma}\hat{\theta})\right] \tag{2.6}$$

or,

$$\hat{\mathbf{q}}_p = \wp^{-1}\left(\frac{1}{f_0}\hat{\psi} + \hat{\varphi}\right)$$

The sensitivity to QGPV may also be writ ten in terms of the sensitivity to the *three-dimensional* geostrophic streamfunction, $\psi_g = \psi_g(x, y, p, t) = \frac{\varphi'}{f_0}$: that satisfies:

$$q'_p = \nabla^2\psi_g + \frac{\partial}{\partial p}\left(\frac{f_0^2}{S}\frac{\partial\psi_g}{\partial p}\right) = \widetilde{\wp}(\psi_g)$$

where $\widetilde{\wp} = f_0 \wp$ is a self-adjoint operator[3]. As a consequence, the sensitivity to geostrophic streamfunction is:

$$\hat{\psi}_g = \widetilde{\wp}\hat{\mathbf{q}}_p, \quad \hat{\psi}_g = \frac{1}{f_0}\hat{\psi} + \hat{\varphi} \tag{2.7}$$

so that the sensitivity to QGPV is given by:

$$\hat{\mathbf{q}}_p = \widetilde{\wp}^{-1}\hat{\psi}_g$$

The sensitivity to the geostrophic streamfunction[4] is therefore:

$$\hat{\psi}_g = -\left[\frac{\partial \hat{\mathbf{v}}}{\partial x} - \frac{\partial \hat{\mathbf{u}}}{\partial y} - \frac{\partial}{\partial p}\left(\frac{f_0}{\gamma}\hat{\theta}\right)\right] \tag{2.8}$$

This derivation largely depends on whether one is able to find the appropriate energy norm and weighting for the streamfunction and PV, in the next section, a general and more straightforward formulation of sensitivity to PV will be shown following Arbogast (1998).

2.2.5 Derivation of Sensitivity to QGPV using Arbogast 1998

A second and more general method to derive the sensitivity to any kind of PV would be to follow the derivation proposed in Arbogast (1998). This method does not require any specification of the energy norm which is consistent with the fact that although we

[3] A self-adjoint operator, $\wp$, is one for which $\langle \mathbf{f}, \wp\mathbf{g}\rangle = \langle \wp\mathbf{f}, \mathbf{g}\rangle$.

[4] (Romero et al., 2005) presented an expression (their equation 8) for the sensitivity to QGPV that uses the sensitivity to the two-dimensional, non-divergent streamfunction (as the forcing on the right-hand side of their elliptic equation.

invoked the energy norm in the previous section, the final expression for the sensitivity to QGPV does not explicitly include the energy norm. The method also lays the foundation for the following chapters in this dissertation.

Here we restate the derivation in Arbogast (1998), first by denoting L as the linear operator that calculates a general form of PV and B as the balance operator acting on the streamfunction Ψ and geopotential Φ, with the deviation from the balance constraint defined as the imbalance $a = \bar{a} + a'$. [5] Since the mean state of the atmosphere is under the balance constraint, we assume $\bar{a} = 0 = B(\bar{\Psi}, \bar{\Phi})$ and $a = a'$. The potential vorticity perturbation (q') and balance constraint can be expressed in the following linearized form as:

$$\begin{cases} q' = L(\Psi', \Phi') \\ \\ a' = B(\Psi', \Phi') \end{cases}$$

or in the matrix form, since both operators are linear,

$$\begin{pmatrix} L_\Psi & L_\Phi \\ \\ B_\Psi & B_\Phi \end{pmatrix} \begin{pmatrix} \Psi' \\ \\ \Phi' \end{pmatrix} = \begin{pmatrix} q' \\ \\ a' \end{pmatrix} \tag{2.9}$$

[5] a in this section is different from $\mathbf{a}$ in section 2.2.4 which refers to a general variable, and a in the remaining part of this dissertation represent the imbalance or geostrophic imbalance unless otherwise specified.

By performing the adjoint of (2.9), the adjoint sensitivity to streamfunction ($\hat{\Psi}$), to geopotential ($\hat{\Phi}$), to PV ($\hat{q}$), and to the imbalance ($\hat{a}$) can be obtained as following:

$$\begin{pmatrix} L_\Psi^* & B_\Psi^* \\ L_\Phi^* & B_\Phi^* \end{pmatrix} \begin{pmatrix} \hat{q} \\ \hat{a} \end{pmatrix} = \begin{pmatrix} \hat{\Psi} \\ \hat{\Phi} \end{pmatrix} \tag{2.10}$$

We call L^* the adjoint of L if $\langle f, Lg \rangle = \langle L^* f, g \rangle$ and use the superscript * to denote the adjoint of an operator. In many cases, with a homogeneous boundary condition, the adjoint of an operator is the same as the transpose of this operator, $L^* = L^T$. If both B_Ψ^*, B_Φ^* and L_Ψ^*, L_Φ^* are commutable, (2.10) can be simplified into:

$$\begin{pmatrix} B_\Phi^* L_\Psi^* - B_\Psi^* L_\Phi^* & 0 \\ 0 & L_\Phi^* B_\Psi^* - L_\Psi^* B_\Phi^* \end{pmatrix} \begin{pmatrix} \hat{q} \\ \hat{a} \end{pmatrix} = \begin{pmatrix} B_\Phi^* \hat{\Psi} - B_\Psi^* \hat{\Phi} \\ L_\Phi^* \hat{\Psi} - L_\Psi^* \hat{\Phi} \end{pmatrix}$$

or,

$$\begin{cases} (B_\Phi^* L_\Psi^* - B_\Psi^* L_\Phi^*)\hat{q} = B_\Phi^* \hat{\Psi} - B_\Psi^* \hat{\Phi} \\ (L_\Phi^* B_\Psi^* - L_\Psi^* B_\Phi^*)\hat{a} = L_\Phi^* \hat{\Psi} - L_\Psi^* \hat{\Phi} \end{cases} \tag{2.11}$$

In the case of QGPV, we use the geostrophic balance constraint between the streamfunction and the perturbation streamfunction $\Psi = \frac{\Phi'}{f_0}$. The geostrophic balance is obtained by omitting the Jacobian term in the nonlinear balance (Charney, 1955) $\nabla^2 \Phi = \nabla \cdot (f \nabla \Psi) + 2 \frac{\partial(\partial\Psi/\partial x, \partial\Psi/\partial y)}{\partial(x,y)}$, and that is $\nabla^2 \Phi = \nabla \cdot (f \nabla \Psi)$. The form used here is a further simplified version if we invoke the f-plane assumption, $f = f_0$, and cancel out the Laplace operator on both sides. Therefore the linearized geostrophic balance constraint

gives the equation set to solve for sensitivity to QGPV:

$$\begin{cases} q' = \nabla^2\Psi' + \dfrac{\partial}{\partial p}(\dfrac{f_0}{S}\dfrac{\partial}{\partial p})\Phi' & \text{(2.12a)} \\ a' = \Psi' - \dfrac{\Phi'}{f_0} & \text{(2.12b)} \end{cases}$$

Where the definition for f_0, S, $\bar{\alpha}$, and $\bar{\theta}$ are the same as in section 2.2.4. Comparing (2.12a), (2.12b) and (2.9), we can easily find

$$L_\Psi = \nabla^2; \qquad L_\Phi = \frac{\partial}{\partial p}(\frac{f_0}{S}\frac{\partial}{\partial p}) \qquad B_\Psi = 1 \qquad B_\Phi = -\frac{1}{f_0}$$

Note these operators are all self-adjoint, meaning for an operator L and its adjoint L^* under any norm $\langle f, Lg\rangle = \langle L^*f, g\rangle = \langle Lf, g\rangle$, or simply put as $L = L^*$ if we denote $\langle f, g\rangle$ as the inner product of f and g. Therefore

$$L^*_\Psi = \nabla^2; \qquad L^*_\Phi = \frac{\partial}{\partial p}(\frac{f_0}{S}\frac{\partial}{\partial p}); \qquad B^*_\Psi = 1; \qquad B^*_\Phi = -\frac{1}{f_0} \tag{2.13}$$

Substitute the above expressions into (2.11) gives the formulation of sensitivity to QGPV and to the geostrophic imbalance

$$\begin{aligned} \left(-\frac{1}{f_0}\nabla^2 - \frac{\partial}{\partial p}\left(\frac{f_0}{S}\frac{\partial}{\partial p}\right)\right)\hat{q} &= -\frac{1}{f_0}\hat{\Psi} - \hat{\Phi} \\ \left(\frac{\partial}{\partial p}\left(\frac{f_0}{S}\frac{\partial}{\partial p}\right) + \frac{1}{f_0}\nabla^2\right)\hat{a} &= \frac{\partial}{\partial p}\left(\frac{f_0}{S}\frac{\partial}{\partial p}\right)\hat{\Psi} - \nabla^2\hat{\Phi} \end{aligned} \tag{2.14}$$

Remember the perturbation QGPV can be written as a function of perturbation geopotential alone (e.g. (2.2)), where we denoted the QGPV operator as $\wp = \frac{1}{f_0}\nabla^2 - \frac{\partial}{\partial p}(\frac{f_0}{S}\frac{\partial}{\partial p})$.

We can simplify (2.14) into

$$\hat{q} = \wp^{-1}\left(\frac{1}{f_0}\hat{\Psi} + \hat{\Phi}\right) \tag{2.15}$$

This is exactly the same expression for the sensitivity to QGPV as found in section 2.2.4. In addition, the sensitivity to geostrophic imbalance (shortened to imbalance thereafter) is given by:

$$\hat{a} = \wp^{-1}\left(\frac{\partial}{\partial p}\left(\frac{f_0}{S}\frac{\partial}{\partial p}\right)\hat{\Psi} - \nabla^2\hat{\Phi}\right) \tag{2.16}$$

To find the sensitivity to QGPV, we need to know $\hat{\Psi}$ and $\hat{\Phi}$. Luckily both are easy to calculate with the sensitivity of state variables in many standard NWP adjoint models. Kleist and Morgan (2005) derived the expression of sensitivity to streamfunction with sensitivity to horizontal winds. The sensitivity to the geopotential can be obtained by taking the adjoint of the expression for perturbation potential temperature $\frac{\partial \Phi'}{\partial p} = -\gamma\theta'$, where γ is defined on each pressure level p following Eliassen (1962) as $\gamma = \frac{R_d}{p}(\frac{p}{p_0})^{R_d/C_p}$, p_0 is the reference pressure, C_p is the heat capacity under constant pressure, and R_d is the dry gas constant:

$$\hat{\Psi} = -\left(\frac{\partial \hat{v}}{\partial x} - \frac{\partial \hat{u}}{\partial y}\right) = \nabla^2\hat{\zeta} \tag{2.17}$$

$$\hat{\Phi} = \frac{1}{\gamma}\frac{\partial \hat{\theta}}{\partial p} \tag{2.18}$$

2.3 Interpretation of Balanced Sensitivities

2.3.1 Sensitivities to Geostrophic Wind and Hydrostatic Potential Temperature

Similar to the invertibility of PV, the sensitivity to QGPV is also invertible in the sense that we can recover the "balanced" sensitivities to the geostrophic wind components and hydrostatic potential temperature. These sensitivities, which follow from the adjoint of (2.3) are expressed as gradients of the sensitivities to QGPV:

$$\begin{cases} \hat{\mathbf{u}}_g = \dfrac{\partial \hat{q}}{\partial y} & \text{(2.19a)} \\ \hat{\mathbf{v}}_g = -\dfrac{\partial \hat{q}}{\partial x} & \text{(2.19b)} \\ \hat{\theta} = \dfrac{f_0 \gamma}{S} \dfrac{\partial \hat{q}}{\partial p} & \text{(2.19c)} \end{cases}$$

These sensitivities may be used to initialize the adjoint model with a (thermal wind-like) balanced initial state that should reduce (but not necessarily remove) the amplitude of the high-frequency waves seen in adjoint integrations (Morgan, 2018).

2.3.2 Interpretation of Sensitivity to QGPV

Equation 2.15 describes an elliptic partial differential equation relating the sensitivity to QGPV to the curl of the sensitivity to the (geostrophic) wind and the weighted vertical gradient of sensitivity to potential temperature. Figure 2.1 is a schematic depicting the relationships between sensitivities to wind and temperature with sensitivities to QGPV. A

positive vertical component of the curl of the sensitivity to the horizontal wind (Fig. 2.1a) is associated with a local maximum in the sensitivity to QGPV. Because homogeneous boundary conditions are applied, that local maximum is associated with a positive sensitivity to QGPV. Similarly, a positive vertical gradient to potential temperature (Fig. 1b) is associated with positive sensitivity to QGPV. That is, a positive sensitivity to QGPV is surrounded by cyclonic sensitivity to horizontal winds, with warm sensitivity above and cold sensitivity below. These results are fully consistent with the concepts of PV invertibility (Hoskins et al., 1985), equation set (2.19), and the sensitivity to Ertel PV demonstrated in Arbogast (1998). Practically, in adjoint case studies, one can point to the single variable – sensitivity to QGPV, to determine the dry dynamical aspect of cyclone development using the "PV thinking" instead of examining the sensitivity to horizontal winds and to potential temperature individually. One can take a step further to extrapolate towards the sensitivity to vertical motion using "PV thinking" since the advection of PV leads to upward vertical motion.

2.3.3 Thermal Wind Balance between Sensitivity Fields

The adjoint model is similar to the nonlinear forward model on the computational coding level when we view the adjoint variable as the state variable. Thus physical laws such as thermal wind balance should have a complementing adjoint counterpart. For example, if we consider the thermal wind balance between the geostrophic wind u_g and temperature, $\frac{\partial u_g}{\partial p} = \frac{R}{fp}\frac{\partial T}{\partial y}$, and substitute T with θ using $\theta = T\left(\frac{p_0}{p}\right)^{R/C_p}$ and $\gamma = \frac{R_d}{p}\left(\frac{p}{p_0}\right)^{R/C_p}$. $\frac{\partial u_g}{\partial p} = \frac{1}{f}\frac{R}{p}\left(\frac{p}{p_0}\right)^{R/C_p}\left(\frac{p_0}{p}\right)^{R/C_p}\frac{\partial T}{\partial y} = \frac{\gamma}{f}\frac{\partial \theta}{\partial y}$. Take the adjoint of the thermal wind equation

and apply the same procedure to the meridional component:

$$\frac{\partial \hat{\theta}}{\partial p} = \frac{\gamma}{f}\frac{\partial \hat{u}_g}{\partial y}$$
$$\frac{\partial \hat{\theta}}{\partial p} = -\frac{\gamma}{f}\frac{\partial \hat{v}_g}{\partial x}$$

Combining the "thermal wind balance" between geostrophic wind and potential temperature sensitivity with (2.18) gives

$$\gamma\hat{\phi} = \frac{\gamma}{f}\left(\frac{\partial \hat{u}_g}{\partial y} - \frac{\partial \hat{v}_g}{\partial x}\right) = \frac{\gamma}{f}\hat{\psi}$$
$$\hat{\phi} = \frac{1}{f}\hat{\psi}$$

The above result circles back to the adjoint form of our simplified geostrophic balance $\Psi = \Phi'/f_0$. Morgan (2018) also pointed out that in a shallow water system, the sensitivity to perturbation height and winds will eventually achieve a balanced state given enough integration time. If a thermal wind/geostrophic balance exists for the adjoint model, we should hypothesize the existence of "geostrophic adjustment" in the adjoint model and that these adjustment processes will generate high-frequency waves (e.g. inertio-gravity waves) just like in the NWP model (Charney, 1955). After achieving the geostrophic balance among sensitivity states, small amplitude inertio-gravity waves will continue to be produced if forcings from the nonlinear model are continuously added to the adjoint integration and knock the sensitivity states out of balance.

2.4 Derivation of Sensitivity to Other Forms of PV

2.4.1 Sensitivity to Vorticity Using Energy Norm

In this section, we demonstrate the extensibility of the technique for diagnosing the sensitivity to potential vorticity for the two-dimensional non-divergent barotropic flow and for "two-dimensional" divergent barotropic flow (i.e., shallow water flow).

The vorticity is conserved in two-dimensional, non-divergent barotropic flow, thus we can treat it as a form of PV. The areal-integrated kinetic energy per unit mass over a given domain may be written as:

$$\mathscr{E}_{KE} = \frac{1}{2}\iint (u'^2 + v'^2)dxdy = \frac{1}{2}\langle \mathbf{x}'_0, \mathbf{W}\mathbf{x}'_0 \rangle$$

where the state vector, $\mathbf{x}' = (\mathbf{u}', \mathbf{v}')^T$ has only the horizontal wind components u and v at the initial time. For this system, the weighting matrix, $\mathbf{W} = \mathbf{I}$ is the identity matrix.

We seek the sensitivity to vorticity, a variable not being used in the state vector of the NWP model; however, we note: $\mathbf{a} = \zeta(\mathbf{x}) = \zeta(\mathbf{u}, \mathbf{v})$. Consider the calculation of the sensitivity to barotropic vorticity, ζ, calculated from the sensitivities to the zonal (u) and meridional (v) wind components.

$$\mathbf{x}'_0 = \lambda \mathbf{W}^{-1}\frac{\partial R}{\partial \mathbf{x}_0} = (\mathbf{u}'_0, \mathbf{v}'_0) = \lambda \mathbf{I}\left(\frac{\partial R}{\partial \mathbf{u}_0}, \frac{\partial R}{\partial \mathbf{v}_0}\right) = \lambda\left(\frac{\partial R}{\partial \mathbf{u}_0}, \frac{\partial R}{\partial \mathbf{v}_0}\right)$$

because, as noted above, $\mathbf{W}_u = \mathbf{W}_v = \mathbf{I}$.

The state vector for the (vertical component of) vorticity may be calculated from the state vector components of the zonal and meridional winds as:

$$\zeta' = \frac{\partial \mathbf{v}'}{\partial x} - \frac{\partial \mathbf{u}'}{\partial y}$$

Use (2.5) to express optimal initial condition for vorticity, $\mathbf{u}$, and $\mathbf{v}$:

$$\begin{aligned}\zeta' &= \frac{\partial}{\partial x}(\lambda \hat{\mathbf{v}}) - \frac{\partial}{\partial y}(\lambda \hat{\mathbf{u}}) = \lambda \left(\frac{\partial \hat{\mathbf{v}}}{\partial x} - \frac{\partial \hat{\mathbf{u}}}{\partial y} \right) \\ &= \lambda \mathbf{W}_\zeta^{-1} \hat{\zeta}\end{aligned}$$

or

$$\mathbf{W}_\zeta^{-1} \hat{\zeta} = \frac{\partial \hat{\mathbf{v}}}{\partial x} - \frac{\partial \hat{\mathbf{u}}}{\partial y} \tag{2.20}$$

The weighting matrix, $\mathbf{W}_\zeta$, is determined by the matrix (operator) defining the kinetic energy. We recognize first that the kinetic energy per unit mass may be written in terms of streamfunction (assuming that the streamfunction or wind field vanishes at the domain boundaries) as:

$$\begin{aligned}\mathscr{E}_{KE} &= -\frac{1}{2} \iint \zeta' \psi' dx dy \\ &= -\frac{1}{2} \iint \zeta' \nabla^{-2} \zeta' dx dy = -\frac{1}{2} \langle \zeta', \nabla^{-2} \zeta' \rangle \\ &= \frac{1}{2} \langle \zeta', \mathbf{W}_\zeta \zeta' \rangle\end{aligned}$$

where the integral is written as an inner product of the discretized vorticity state vector (ζ). It is obvious that $\mathbf{W}_\zeta = -\nabla^{-2}$ and therefore, $\mathbf{W}_\zeta^{-1} = -\nabla^2$. Thus (2.20) may be rewritten as:

$$-\nabla^2\hat{\zeta} = \frac{\partial\hat{\mathbf{v}}}{\partial x} - \frac{\partial\hat{\mathbf{u}}}{\partial y}$$
$$\text{or } \hat{\zeta} = -\nabla^{-2}\left(\frac{\partial\hat{\mathbf{v}}}{\partial x} - \frac{\partial\hat{\mathbf{u}}}{\partial y}\right)$$

which is the same as shown by Kleist and Morgan (2005). Note that the result is independent of the Lagrange multiplier and therefore the size of the prescribed energy norm or the size of the response function change, δR. We further note that for *two-dimensional* non-divergent flow, a streamfunction, ψ, may be defined such that, $\nabla^2\psi = \zeta$, so that $\frac{\partial R}{\partial\zeta} = \nabla^2\left(\frac{\partial R}{\partial\psi}\right)$. This gives us the sensitivity to streamfunction (e.g. (2.17)) $\hat{\psi} = -\left(\frac{\partial\hat{\mathbf{v}}}{\partial x} - \frac{\partial\hat{\mathbf{u}}}{\partial y}\right)$.

2.4.2 Sensitivity to Shallow Water PV Using Energy Norm

For two-dimensional, divergent, barotropic flow (i.e., shallow water flow), the energy per unit area for the linearized system may be written as:

$$\mathscr{E}_{SW} = \frac{1}{2}\iint\left(u'^2 + v'^2 + \frac{g\eta^2}{H}\right)dxdy$$
$$= \frac{1}{2}\langle(\mathbf{u}', \mathbf{v}', \eta)\,, \mathbf{W}_{u,v,\eta}\,(\mathbf{u}', \mathbf{v}', \eta)^T\rangle$$

The weighting matrix

$$\mathbf{W} = \mathbf{W}_{u,v,\eta} = \begin{pmatrix} \mathbf{I} & 0 & 0 \\ 0 & \mathbf{I} & 0 \\ 0 & 0 & \frac{g}{H}\mathbf{I} \end{pmatrix}$$

is block diagonal with the identity matrix along the diagonal for the wind components and g/H for the elements multiplying the perturbation fluid depth (η) component of the state vector.

We seek the sensitivity to shallow water potential vorticity (SWPV) with $q_{SW}(\mathbf{x}) = q_{SW}(\mathbf{u}, \mathbf{v}, \eta)$. Consider the optimal initial condition with the state vector:

$$\mathbf{x}' = (\mathbf{u}', \mathbf{v}', \eta') = \lambda \left(\mathbf{I}\frac{\partial R}{\partial \mathbf{u}}, \mathbf{I}\frac{\partial R}{\partial \mathbf{v}}, \frac{H}{g}\mathbf{I}\frac{\partial \mathrm{R}}{\partial \eta} \right) = \lambda \left(\frac{\partial R}{\partial \mathbf{u}}, \frac{\partial R}{\partial \mathbf{v}}, \frac{H}{g}\frac{\partial R}{\partial \eta} \right)$$

with minimum SW energy. The weighting matrix, $\mathbf{W}_{q_p}$, is determined by that matrix defining the SW energy per unit mass, $\mathscr{E}_{SW}$ may be written in terms of the geopotential (assuming that the geopotential, geostrophic wind, or potential temperature field vanishes along the domain boundaries) as:

$$\begin{aligned} \mathscr{E}_{SW} &= \frac{1}{2} \iint (u'^2 + v'^2 + \frac{g\eta^2}{H}) dxdy \\ &= -\frac{gH}{2f_0} \iint q'_{SW} \eta'_b dxdy = \frac{1}{2} \langle \mathbf{q}'_{SW}, -\frac{gH}{f_0} \eta'_b \rangle \end{aligned}$$

where η_b is the balanced height perturbation. The geostrophic balance states $\Psi' = \frac{\Phi'}{f} = \frac{g\eta}{f}$. Substitute into the SWPV definition $q' = \frac{1}{H}\nabla^2\Psi' - \frac{f\eta}{H^2} = \frac{1}{H}\nabla^2\frac{g\eta}{f} - \frac{f\eta}{H^2} = \frac{1}{H^2}(\nabla^2 -$

$\frac{f^2}{gH})\frac{gH}{f}\eta$. Denote the SWPV inversion operator as $\wp_{SW} = \nabla^2 - \frac{f_0^2}{gH}$, we can equate $H^2 q'_{SW} = \wp_{SW}\frac{gH}{f}\eta$ and rewrite the above equation:

$$\mathscr{E}_{SW} = \frac{1}{2}\langle \mathbf{q}'_{SW}, -H^2\wp_{SW}^{-1}\mathbf{q}'_{SW}\rangle = \frac{1}{2}\langle \mathbf{q}'_{SW}, \mathbf{W}_{q_{SW}}\mathbf{q}'_{SW}\rangle$$

which reveals the weighting matrix $\mathbf{W}_{q_{SW}} = -H^2\wp_{SW}^{-1}$.

Use (2.5) to express optimal initial condition for η, $\mathbf{u}$, and $\mathbf{v}$:

$$\begin{aligned}\mathbf{q}'_{SW} &= \frac{1}{H}\left[\frac{\partial}{\partial x}(\lambda\hat{\mathbf{v}}) - \frac{\partial}{\partial y}(\lambda\hat{\mathbf{u}})\right] - \left(\lambda\frac{f_0}{H^2}\frac{H}{g}\hat{\eta}\right) \\ &= \lambda\mathbf{W}_{q_{SW}}^{-1}\hat{\mathbf{q}}_{SW} = -\frac{\lambda}{H^2}\wp_{SW}\hat{\mathbf{q}}_{SW}\end{aligned}$$

$$\hat{\mathbf{q}}_{SW} = -H^2\wp_{SW}^{-1}\left[\frac{1}{H}\left(\frac{\partial\hat{\mathbf{v}}}{\partial x} - \frac{\partial\hat{\mathbf{u}}}{\partial y}\right) - \frac{f_0}{gH}\hat{\eta}\right] = \wp_{SW}^{-1}\left[H\hat{\psi} + \frac{f_0 H}{g}\hat{\eta}\right] \tag{2.21}$$

The final expression (2.21) is exactly the expression derived in Morgan (2018) relating the sensitivity to linearized SWPV and the sensitivity to "balanced" height, η_b. We can define a sensitivity to the balanced "height" similar to (2.8): $\hat{\eta}_b = H\hat{\psi} + \frac{f_0 H}{g}\hat{\eta}$.

2.4.3 Sensitivity to Shallow Water PV Using Arbogast method

First, define the shallow water PV and use the geostrophic balance.

$$q' = \frac{1}{H}\nabla^2\Psi' - \frac{f\eta}{H^2}$$
$$a' = \Psi' - \frac{g}{f_0}\eta$$

H is the basic state height, η is the perturbation height. Substituting the operators on Φ as the operators on η find the operators in (2.11), we find

$$L_\Psi = \frac{1}{H}\nabla^2; \qquad L_\eta = -\frac{f}{H^2}; \qquad B_\Psi = 1; \qquad B_\eta = -\frac{g}{f_0}$$

All the operators are self-adjoint. Substitute the above expressions into Eq. (2.11),

$$(\nabla^2 - \frac{f_0^2}{gH})\hat{q} = H\hat{\Psi} + \frac{f_0 H}{g}\hat{\eta}$$
$$-(\nabla^2 - \frac{f_0^2}{gH})\hat{a} = \frac{f_0^2}{gH}\hat{\Psi} + \frac{f_0}{g}\nabla^2\hat{\eta}$$

Using the SWPV operator $\wp_{SW}$ to simplify the above equation yields the same expression as (2.21):

$$\hat{q} = \wp_{SW}^{-1}(H\hat{\Psi} + \frac{f_0 H}{g}\hat{\eta})$$
$$\hat{a} = \wp_{SW}^{-1}(-\frac{f_0^2}{gH}\hat{\Psi} - \frac{f_0}{g}\nabla^2\hat{\eta})$$

2.5 Case study of an Atlantic Cyclogenesis in March 2020

2.5.1 Case and Methodology

We demonstrate the calculation and interpretation of the sensitivity to QGPV by solving (2.15) using output from the Weather Research and Forecasting (WRF) model V3.8.1 (Skamarock and Klemp 2008) and the WRF adjoint model V3.8.1 (Zhang et al., 2013) on a centered finite difference with the successive over-relaxation (SOR) algorithm. The discussion that follows is not intended to be a complete case study, but rather a demonstration of the insights that may be drawn from this calculation. The case under consideration is that of an explosive, western Atlantic cyclogenesis event that occurred over the 24-h period beginning 1200 UTC 6 March 2020 (e.g., Fig. 2.2a). The simulation was initialized using the ERA5 reanalyses (Hersbach et al., 2020) at 1200 UTC 6 March 2020. The simulation was conducted on a 30 km grid with 41 equally spaced layers from the surface to 50 hPa. The response function chosen for this example is minus the column dry air mass perturbation (WRF model variable, μ): $R = -\bar{\mu}'$ within the simulated 988 hPa sea level pressure isobar at forecast hour 24 (Fig. 2.2b). The negative sign in the response function is chosen so that a positive (negative) perturbation in regions of positive (negative) sensitivity corresponds to perturbations that would intensify the cyclone (more specifically, lowering the surface pressure within the region enclosed by that isobar). The

forward and adjoint model outputs were interpolated vertically to equally spaced isobaric surfaces from 1000 hPa to the 50 hPa model top using wrf-python (Ladwig, 2017). Adjoint sensitivities for all variables below ground were set to zero.

The nascent cyclone was located within a broad sea level pressure minimum over the western Atlantic to the east of Cape Hatteras, NC at the beginning of the simulation. Two minima appeared in the analysis with mean sea level pressures below 1004 hPa. The deepening of the cyclone commenced upon the arrival of a vigorous upper-tropospheric shortwave trough from the Midwest. By 6 hours into the simulation a vigorous cyclonic 500 hPa geostrophic vorticity maximum (Fig. 2.3) was located upshear of the developing surface cyclone, suggestive of the potential for strong baroclinic growth for the remaining 18 hours of the simulation.

2.5.2 Distributions of Sensitivities to QGPV

The cyclonic geostrophic vorticity maximum (Fig. 2.3) was associated with a local QGPV maximum (Fig. 2.4a) located inland over coastal North Carolina within the base of the 500 hPa geopotential trough. Upstream of the trough axis, a strip of cyclonic QGPV extended west and northwest along the cyclonic shear region of the flow. Sensitivity to QGPV, calculated following (2.15) is shown in Fig. 2.4b. Two conspicuous dipoles in sensitivity to QGPV are noted at this time - one located over the southeastern US with the maximum positive sensitivity over North Carolina, while the second was located over southeastern Canada and New York state (Fig. 2.4b). As anticipated from (2.19), the sensitivity to the geostrophic wind is characterized by a cyclonic (anticyclonic) sensitivity

to horizontal wind distribution about the positive (negative) sensitivity to QGPV in accord with Fig. 2.1.

The co-location of the 500 hPa QGPV maximum with the maximum sensitivity to 500 hPa QGPV indicates that increasing the QGPV in the region of already cyclonic QGPV (Fig. 2.4) would subsequently intensify the surface cyclone relative the control simulation 18 hours later (forecast time F24). A vertical cross-section of sensitivities to both QGPV and potential temperature, taken nearly parallel to the baroclinic shear, reveals strongly upshear-tilted sensitivities to both fields (Fig. 2.4c). The relationship between the sensitivity to QGPV and to potential temperature again is as depicted in the schematic (Fig. 2.1b) with $\hat{\theta} < 0$ ($\hat{\theta} > 0$) below (above) a $\hat{q} > 0$. Figure 2.4d provides a vertical cross-section dissecting the jet upstream of the trough axis at 300 hPa. The maximum sensitivity to QGPV sits along the edge of the jet core, where high PV is anticipated from the tropopause overfold. Also shown is the sensitivity to geostrophic wind normal to the cross-section with positive values (red). It indicates that the F24 cyclone intensity is associated with stronger geostrophic wind normal to the cross-section. The distribution of sensitivity to the geostrophic wind normal to the cross-section suggests that a more anticyclonically sheared flow southwest of the jet at forecast hour 6 (F06) would result in a lower surface pressure at the final time, F24.

2.5.3 Creation of "QG Balanced" Sensitivity Fields

Interpretation of adjoint sensitivity output from short-term, backward adjoint model integration is complicated by the emergence of strongly divergent high-frequency wave-like structure emanating from the location of specified adjoint forcing (e.g., Vukićević and Raeder 1995; Morgan 2018) and possibly reflecting back into the domain if not absorbed at the boundaries (e.g. Fig. 2.5a). The sensitivity to QGPV and the associated sensitivities to geostrophic winds (2.19a, 2.19b) and potential temperature (2.19c) offer another way to dynamically balance the adjoint integration by effectively filtering the high-frequency structure, other than the widely used normal mode initialization (e.g., Machenhauer 1977; Daley 1978) and averaging over time (Doyle, personal communication). This "balanced" adjoint would be similar to an initialization step in a forward model. Comparing Figs. 2.5a and 2.5b, we notice during the backward integration, the sensitivities for the balanced state show lower amplitude high-frequency wave structures than for the full ("unbalanced") integration. As discussed in section 2.3.3 and suggested in Morgan (2018), no matter with a forward model or with an adjoint model integration, any perturbation or sensitivity gradients need to first adjust to a dynamically balanced state. If a balanced field is initially provided, little to no adjustment will be expected and the adjoint sensitivity gradients from the backward adjoint integration may be easier to interpret during the "spin-up" period.

As a demonstration of this concept, the adjoint model is initialized with the gradient of

a response function measuring the circulation about a box enclosing a middle-to-upper-tropospheric cyclonic vorticity maximum defined on the model's native "eta" coordinate levels 13, 14, and 15. We will call this "exp 1". Because the response function is only a function of u and v, the only non-zero adjoint forcings are $\hat{\mathbf{u}}$ and $\hat{\mathbf{v}}$. The balanced adjoint forcing is calculated as described in the preceding paragraph and necessarily includes not only $\hat{\mathbf{u}}$ and $\hat{\mathbf{v}}$, but also $\hat{\theta}$. The detailed procedure is shown in Fig. 2.9 and we will call it "exp 2". Another experiment which we will call "exp 3" lets the adjoint from "exp 1" integrate backward for 1 hour and invert the balanced forcing at F23, restate the adjoint forcing then integrate backward from F23 to F00, as described in Fig. 2.8.

Figure 2.6 shows that at F00, the sensitivities to QGPV initialized by the balanced and unbalanced adjoint forcing either from F24 or from F23 are similar - suggesting that the salient aspects of the forcing (as defined by the sensitivity to QGPV) were preserved during the balancing process.

However, this conservation of sensitivity to QGPV should be taken with a grain of salt when we choose the response function to be μ as in section 2.5.1. Figure 2.7a shows the equivalent of "exp 1" and Figure 2.7b is the equivalent of "exp 3". When comparing these two experiments, they exhibited a phase shift of the sensitivity pattern. "Exp 1" prefers more QGPV over the midwest while "exp 3" which is initialized with balanced adjoint forcing inserted at F23 prefers less QGPV at the same location. The inability to conserve the sensitivity to QGPV might be contributed to not having a balanced moisture sensitivity at F23. When the response function is $R = -\mu$ (close to the surface) more

moisture processes are involved, while when the circulation at mid-troposphere is chosen as the response function, it might not involve too much moisture sensitivity.

During the backward adjoint integration, the adjoint states associated with the balanced adjoint forcing exhibited smaller amplitude high-frequency wave structures compared with the integration of the unbalanced forcing. As an example, a simple comparison of the 500 hPa $\hat{\mathbf{u}}$ sensitivities at F20 from the experiments initialized by unbalanced forcing at F24 and balanced forcing at F23 both using $R = -\mu$ is shown in Fig. 2.5. The unphysical high-frequency wave that bounces back from the model domain is clear with the unbalanced forcing experiment. In comparison, the sensitivity initialized with the balanced forcing removes the unphysical wave while retaining the main dipole feature of the wind sensitivity offshore of the Carolinas.

2.5.4 Does the QGPV Perturbation Project onto the Sensitivity to QGPV

In section 2.2.2, we demonstrated that given a prescribed amount of perturbation energy measured by $\mathscr{E}$ we can find the optimal distribution of state variable perturbation (2.5) proportional to the adjoint sensitivity by a factor of λ (2.4). This is called adjoint-informed optimal perturbation and has been used in many studies to investigate the role of PV in developing storms as an approximation of sensitivity to PV. To test its validity, an optimal perturbation is created from balanced adjoint sensitivity at F00 and added to the initial condition and the comparison of 500 hPa QGPV between the perturbed and control

run is shown in the first column in Fig. 2.10 from F00 to F18. The second column shows the distribution of the sensitivity to QGPV at the corresponding time step. QGPV dipole strips due to feature shifts and sparse dots associated with convections are common in the perturbations. In contrast, sensitivity to QGPV has a much broader spatial appearance than QGPV perturbation since an inverse-laplacian-like inversion was applied during its calculation (2.15). Up until F12, the main feature of QGPV perturbation is nascent to the QGPV sensitivity. At F18 QGPV perturbation at F18 lags behind the sensitivity to QGPV. For a fair comparison, sensitivity to balanced winds and temperature recovered from sensitivity to QGPV in the second column are added to WRF output at each time step. Again differences in QGPV between unperturbed and additional balanced perturbation is calculated and shown in column 3, with positive values in column 1 overlaid in magenta contour. At F00, two QGPV perturbations are the same since the state vector perturbation added is the same. As time evolves, only some parts of two sets of QGPV perturbation overlap. It cannot be concluded whether QGPV perturbation can represent the sensitivity to QGPV and future research should use this approximation with caution.

2.6 Conclusion

In this chapter, an expression for sensitivity to QGPV and SWPV is derived with two methods: one based on the well-established relationships for adjoint optimal initial condition perturbations; another based on the previous work from Arbogast (1998). Additionally, given sensitivities to QGPV, sensitivities to geostrophic wind and hydrostatically

balanced potential temperature perturbations are also derived. The calculation of the sensitivity to QGPV opens up a number of new avenues for case study applications involving the interpretation of adjoint-derived forecast sensitivities and for "surgically" identifying where and how modifications to QGPV along a simulation forecast trajectory would influence a given response function.

A case study of an explosive Atlantic cyclogenesis event was conducted to demonstrate some applications of this new tool. Firstly, in addition to interpreting each individual sensitivity like the wind or the temperature, one can now examine the location of sensitivity to QGPV relative to ridges and troughs, which provides an easier dynamical understanding of the storm development. Then we showed the ability of a balanced sensitivity field to eliminate the high-frequency waves generated by the adjustment process in the adjoint backward integration, along with the questionable conservation of sensitivity to QGPV. Finally, using this cyclogenesis event we provided the relationship between QGPV perturbation and sensitivity to QGPV and questioned the validity of using QGPV perturbation to approximate sensitivity to QGPV that was assumed in many previous studies (e.g., Vukićević and Raeder 1995; Fehlmann and Davies 1997; McTaggart-Cowan et al. 2004; Doyle et al. 2019).

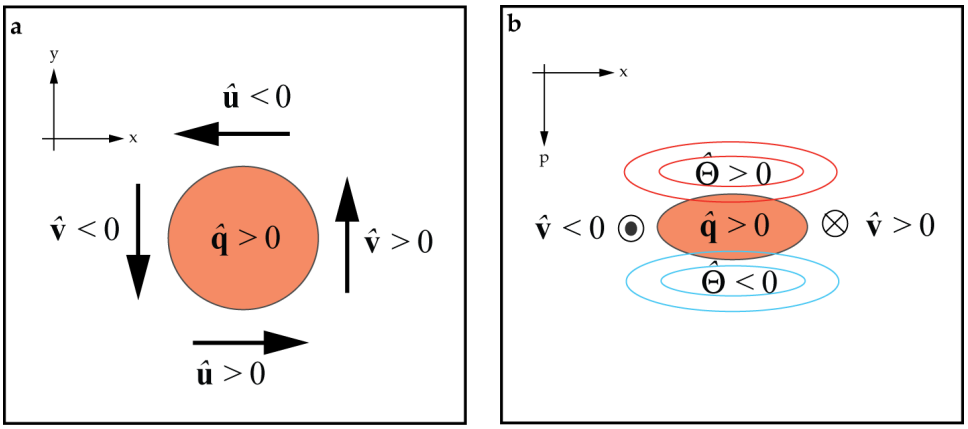

FIGURE 2.1: Schematic depicting the sensitivity to PV (q_p) diagnosed from sensitivities to zonal (u) and meridional (v) wind and sensitivities to potential temperature (θ). Variables with "hats" denote the sensitivity to that variable. Panel (a) depicts a horizontal, isobaric cross-section with sensitivities to horizontal winds (shown as sensitivity vectors, Kleist and Morgan 1995a) associated with a positive sensitivity to QGPV (orange). Note that the sign of the vertical component of the curl of the sensitivity to winds is positive. Panel (b) depicts a vertical cross-section with sensitivities to potential temperature (positive red, negative blue) and the sensitivities to the meridional wind (X positive, dot negative) associated with a positive sensitivity to QGPV. In this scenario, the vertical gradient of sensitivity to potential temperature is positive (i.e., $-\partial\hat{\theta}/\partial p > 0$).

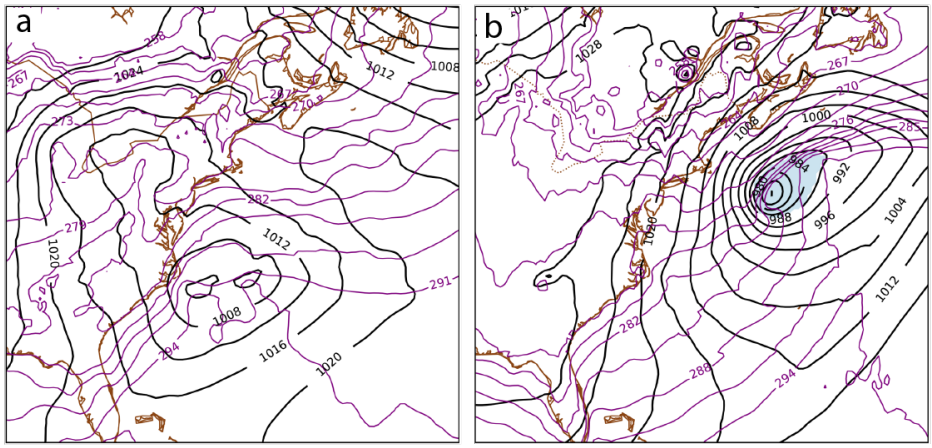

FIGURE 2.2: Mean sea level pressure (black, contoured every 4hPa) and surface potential temperature (purple, contoured every 3K) for (a) forecast time $t = t_0$ =00h valid 1200 UTC 6 March 2020 and (b) forecast time $t = t_f$ =24h valid 1200 UTC 7 March. Light blue region indicates adjoint forcing, *i.e.*, the gradient of response function at $t = t_f$, $\partial R/\partial\mu' = -1$.

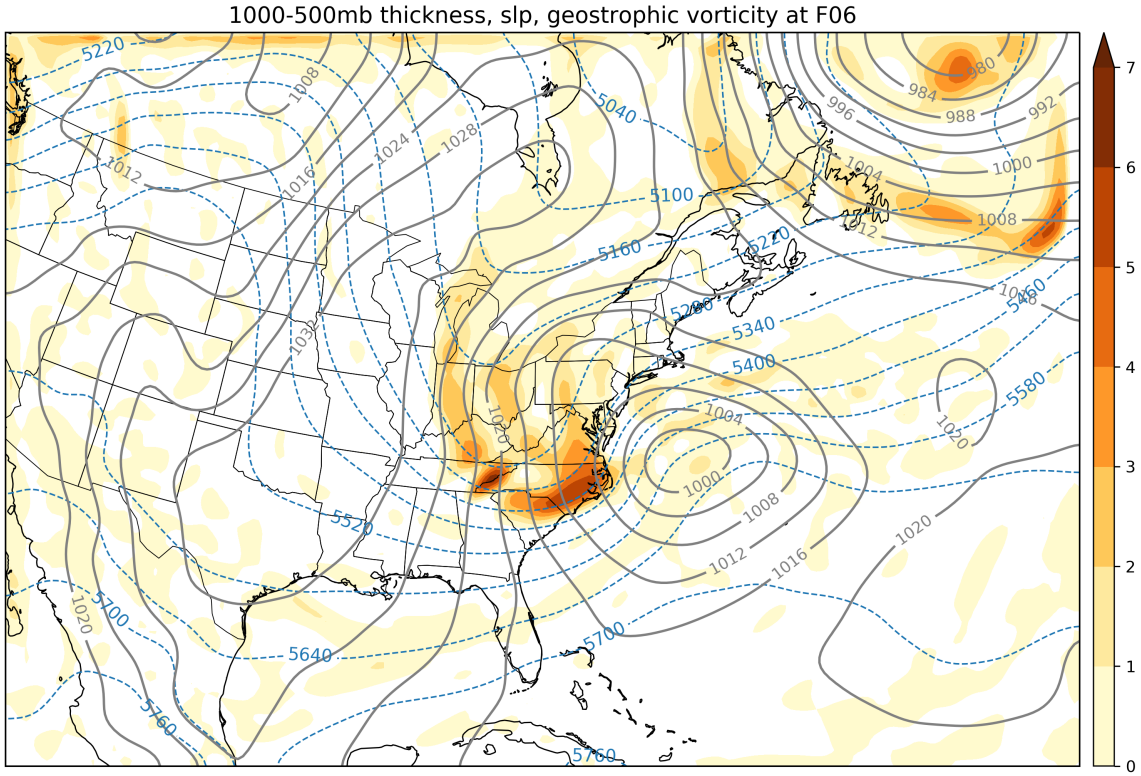

FIGURE 2.3: Mean sea level pressure isobars (interval 4 hPa, grey); 1000-to-500 hPa thickness (interval 60 m, blue); and 500 hPa geostrophic vorticity (fill interval, 1 x 10^{-4} s^{-1}) forecast time 06h valid 1800 UTC 6 March 2020.

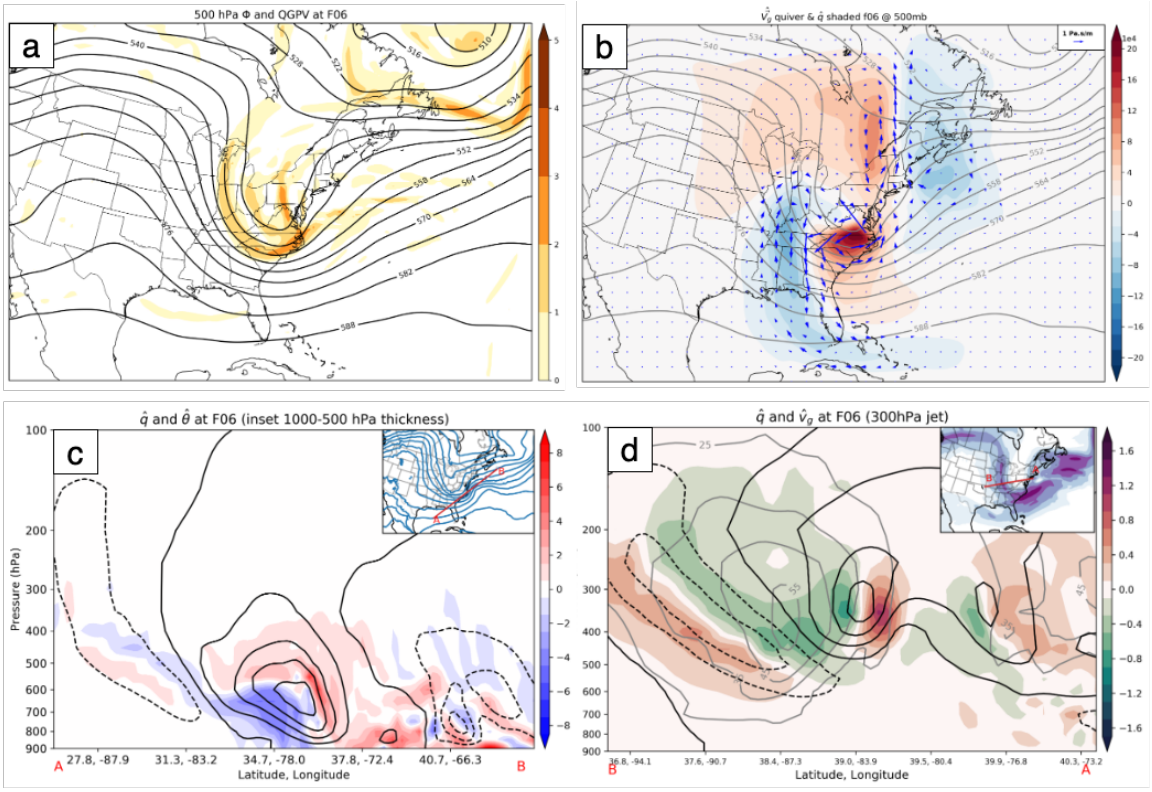

FIGURE 2.4: (a) 500 hPa QGPV (fill interval, 1 x 10^{-4} s^{-1}, and geopotential height isohypses (interval 60 m, black); (b) 500 hPa geopotential height (interval 60 m, gray) with sensitivity to QGPV (fill, interval 1 x 10^{3} hPa s) and sensitivity to geostrophic wind (vector, reference vector shown in lower right); (c) cross-section of sensitivity to QGPV (contoured), the along-jet component of the sensitivity to the geostrophic wind (shaded), and isotach (interval 10 ms^{-1}, gray) for forecast time 06h valid 1800 UTC 6 March 2020. Inset shows the 300hPa wind speed (shaded) and the cross-section (red line across the jet above the Midwest); and (d) cross-section of sensitivity to QGPV (interval 40000 hPa s, black), cross-section normal component of the sensitivity to the geostrophic wind (shaded), and isotach (interval, 10 ms^{-1} gray). Insets show cross-section orientation (red line) along (c) mean 1000-to-500 hPa shear, and (d) normal to 300hPa wind speed (shaded). All fields are for forecast time F06 valid 1800 UTC 6 March 2020.

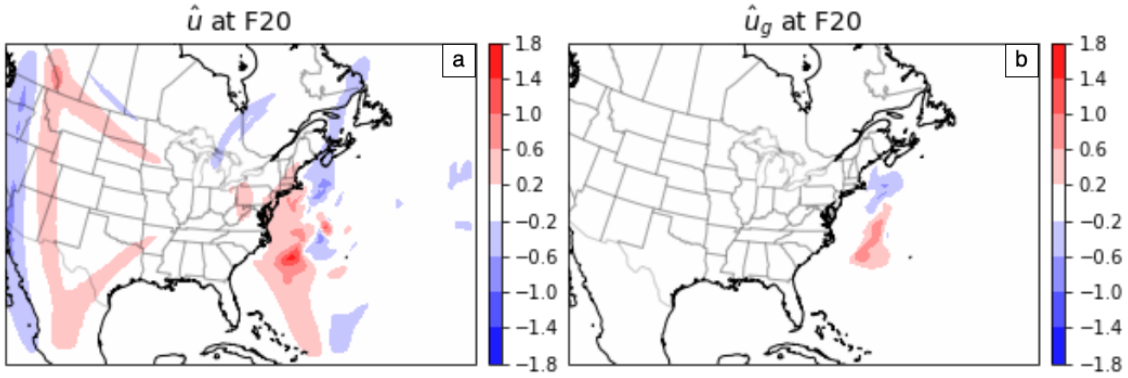

FIGURE 2.5: 500 hPa sensitivity to zonal wind at F20, integrated backward from a) traditional adjoint forcing at F24 and from b) balanced adjoint forcing at F23.

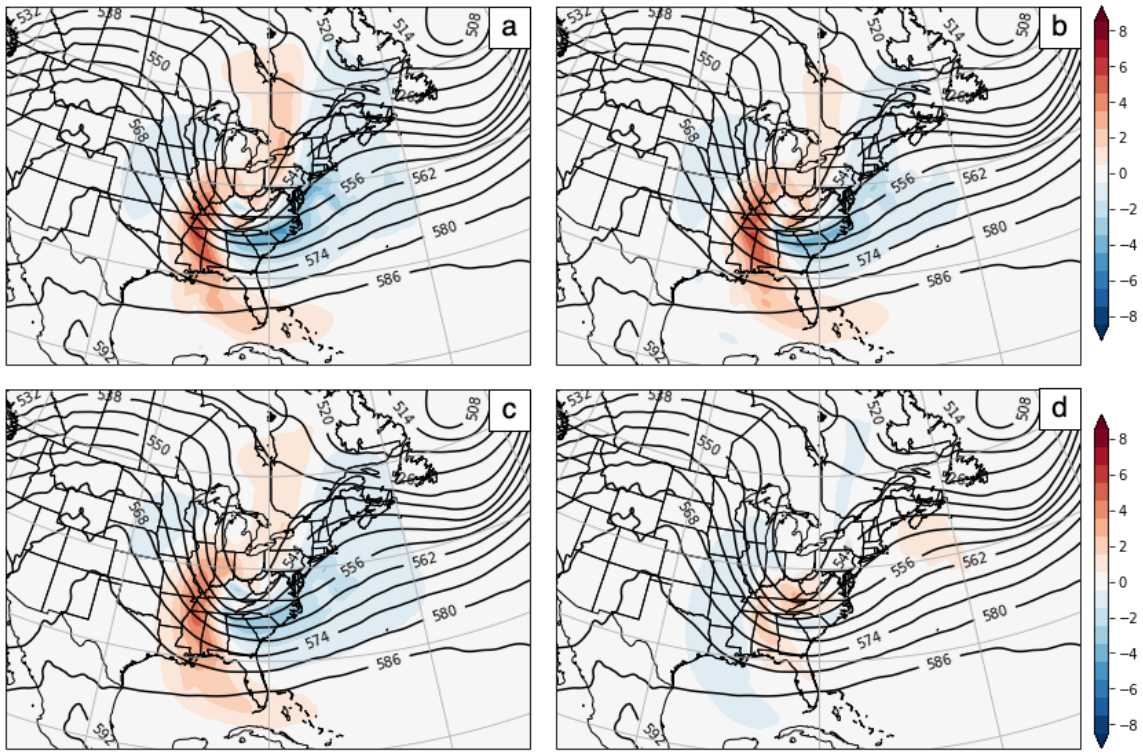

FIGURE 2.6: Sensitivity to QGPV at F00 when using the circulation at eta level 13, 14, 15 as the response function for a) unbalanced adjoint forcing integrated from F24, b) for balanced adjoint forcing integrated from F24, and balanced adjoint forcing integrated from F23. Panel (d) shows the difference between panels (b) and (c). Colorbar scaling is the same for all panels.

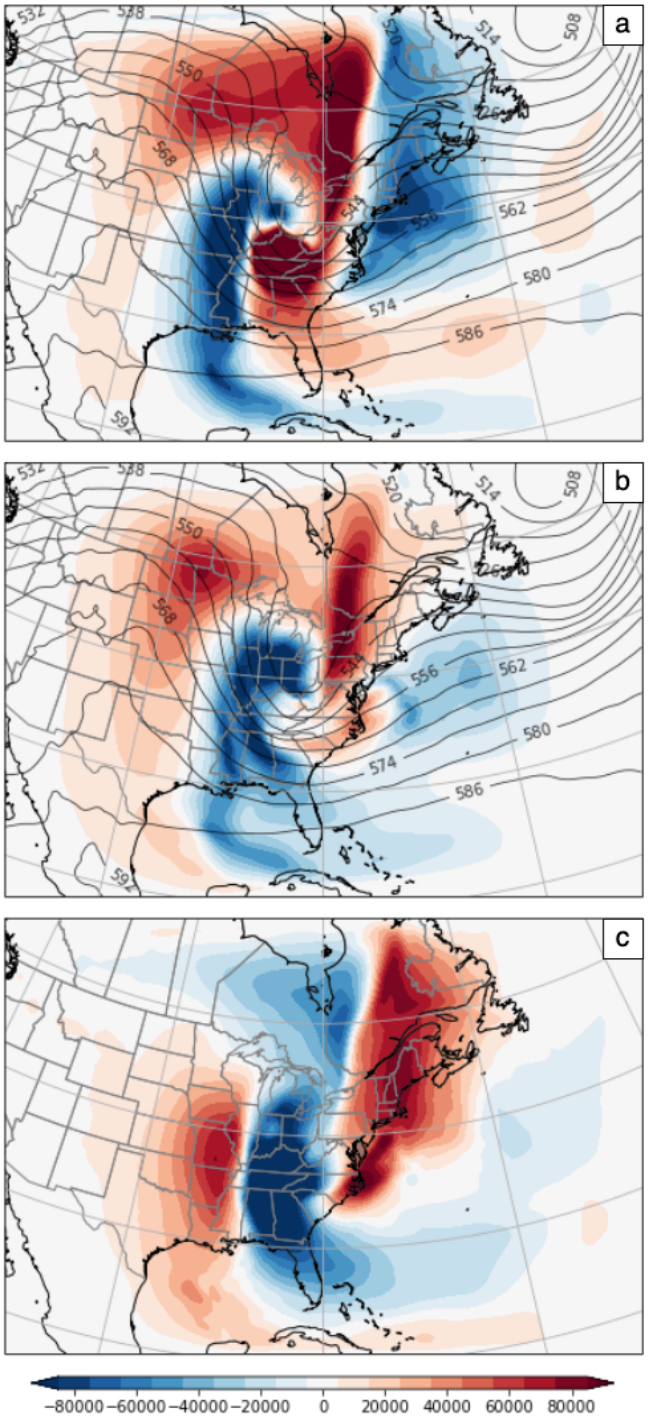

FIGURE 2.7: Sensitivity to QGPV at F00 for (a) unbalanced adjoint forcing and (b) for balanced adjoint forcing. Panel (c) shows the difference between panels (b) and (a). Colorbar is the same for all three panels.

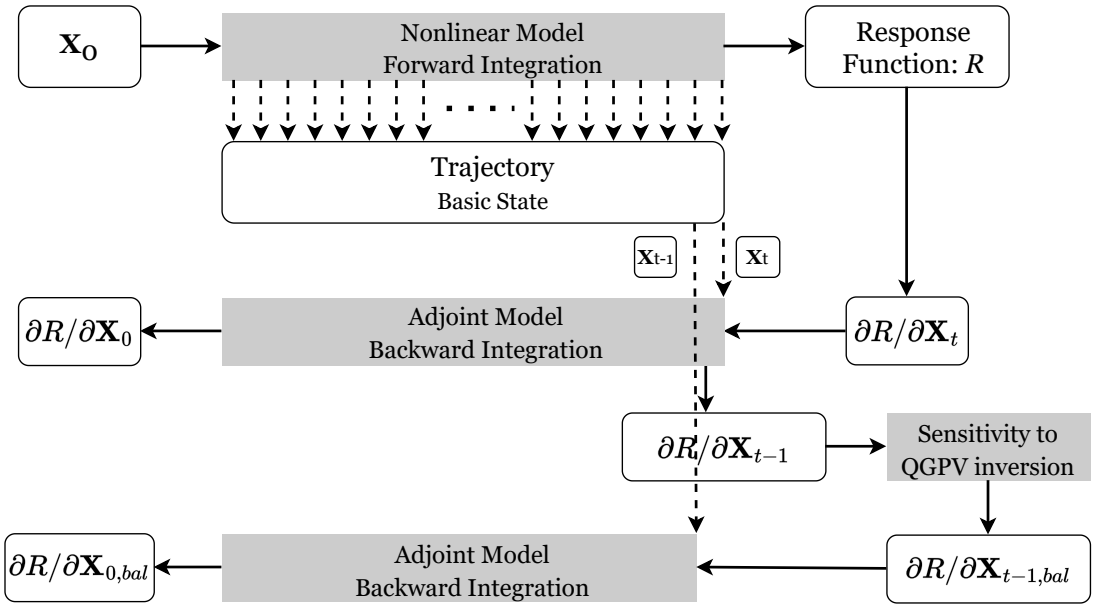

FIGURE 2.8: Adjoint backward integration flowchart for traditional adjoint forcing in Fig. 2.5a and Fig. 2.5b starting at F23.

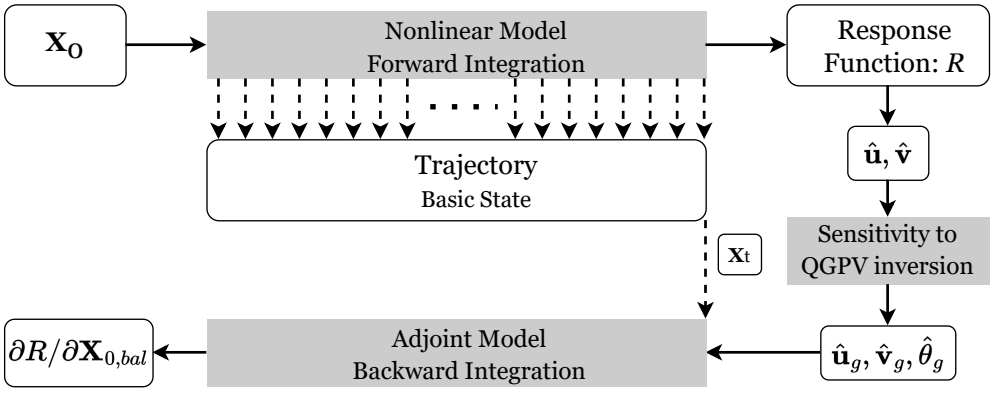

FIGURE 2.9: Adjoint backward integration with balanced adjoint forcing starting at F24.

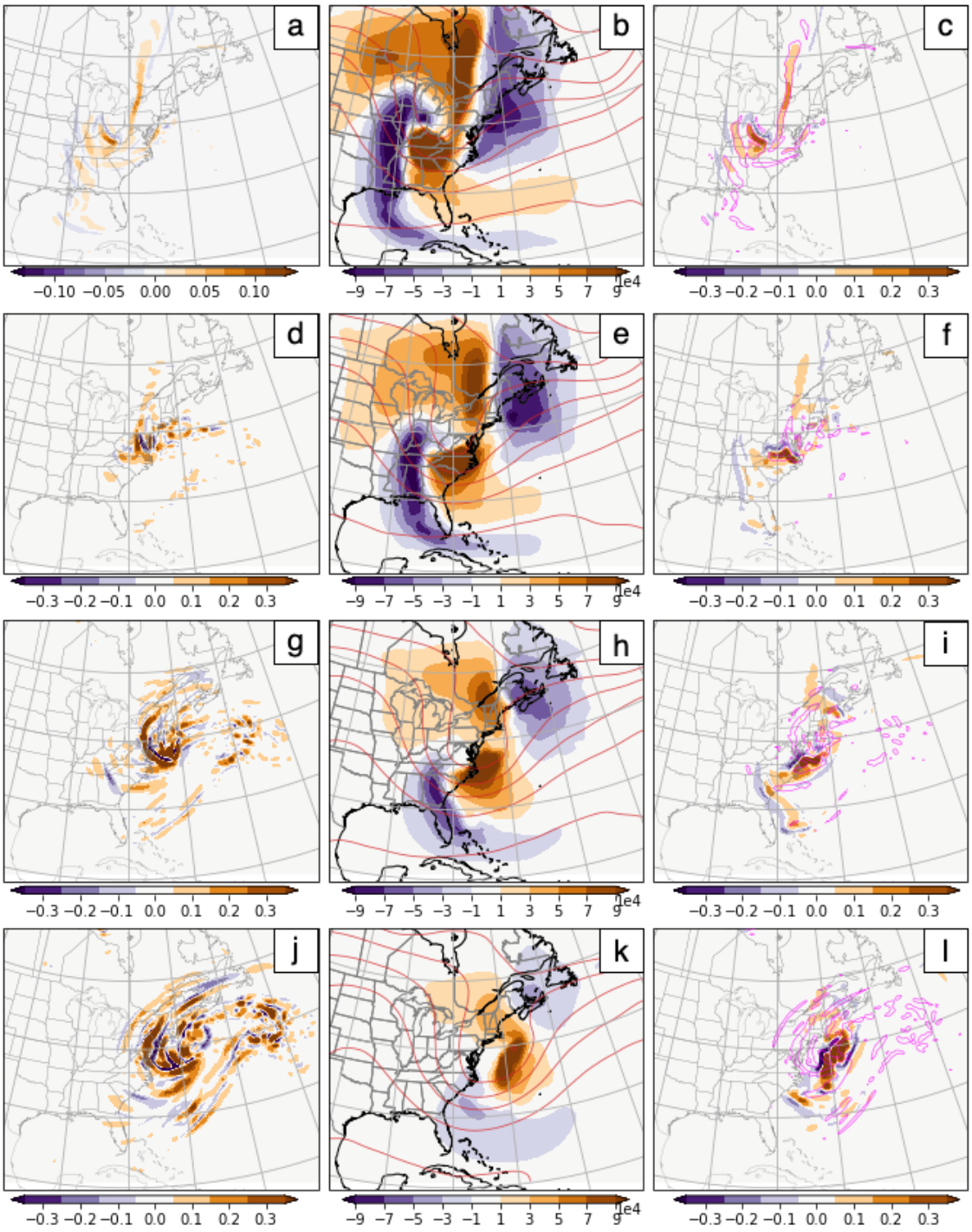

FIGURE 2.10: 500 hPa PV perturbation (shaded, in PVU) as the difference between the unbalanced optimal perturbation run and the unperturbed run (column 1). 500 hPa Sensitivity to PV (shaded, column 2). 500 hPa Perturbation QGPV (shaded) when the balanced perturbation is introduced at each time step (column 3) with a positive value from column 1 contoured in magenta. Time step F00, F06, F12, F18 are shown in rows in ascending order.

Chapter 3

Sensitivity to Imbalance

3.1 Overview

In Arbogast (1998) a general form of sensitivity to PV was derived as shown in Chapter 2 section 2.2.5 (2.15). The sensitivity to imbalance (3.5) comes as a by-product and was noted by Arbogast that it may be computed if, and only if, an invertibility principle for PV exists. However, the notion of imbalance and the interpretation of sensitivity to imbalance was largely undiscussed in Arbogast's original paper.

The imbalance is defined as the deviation from a "balanced" state, as described by a chosen balance constraint. The commonly-used balance constraints are geostrophic balance in midlatitude cyclone studies, gradient wind balance in tropical cyclone studies. For example, the mismatch between the streamfunction and the geopotential or between

the wind and temperature is then often discussed in the context of ageostrophic wind and its contribution to the secondary circulation in surface front development and jet dynamics (e.g., Keyser and Shapiro 1986; Cunningham and Keyser 2004; Kaplan et al. 2011; Thompson and Schultz 2021) or in the context of agradient wind (sub- or super-gradient wind) in tropical cyclone boundary layer processes (e.g., Kepert and Wang 2001; Montgomery and Smith 2017) and outflow dynamics (e.g., Wang et al. 2022; Cohen et al. 2017). Taken from "ageostrophic" and "agradient", we denote imbalance (or unbalance) as a.

The nonlinear balance (e.g., Charney 1955; Allen 1991; Raymond 1992) is less used in the conceptual understanding of atmospheric phenomena due to its complexity. But it is often used in numerical computation like Ertel PV inversion (e.g., Davis and Emanuel 1991; Wu 1993; Ziemiański and Thorpe 2003) and numerical simulation such as constructing the TC bogus in high-resolution models (Rappin et al. 2013). Zhang (2004) found the nonlinear imbalance exists in the region left of the jet exit and is responsible for the generation of gravity waves. Cohen et al. (2017) discussed the importance of imbalance at the upper troposphere of the tropical cyclone outflow level using the Rossby Number, though they emphasized the misalignment of vortices on different levels.

In the other parts of the tropics, where the geopotential field is smooth and divergence is dominant over rotational motions, part of the mismatch between streamfunction and the geopotential is rephrased into the weak temperature balance.

In this chapter, we will try to build an understanding of the geostrophic imbalance a in section 3.2, then extend the interpretation of the sensitivity to the geostrophic imbalance $\hat{a}$ which is left unexplained in Arbogast (1998) in section 3.3. Section 3.4 derives sensitivities to other diagnostic variables and section 3.5 shows the optimal perturbation method. All these tools will be applied to a mid-latitude cyclogenesis event in November 1998 in section 3.6. We conclude this chapter with section 3.7.

3.2 Notion of Geostrophic Imbalance

The geostrophic balance $\Psi' = \Phi'/f_0$ is obtained by omitting the Jacobian term in the nonlinear balance (e.g., Charney 1955), $\nabla \cdot \nabla\Phi = \nabla \cdot (f\nabla\Psi) + 2\frac{\partial(\partial\Psi/\partial x, \partial\Psi/\partial y)}{\partial(x,y)}$, assuming an f-plane, and finally cancelling out the Laplace operator on both sides. The geostrophic imbalance $a = \Psi' - \frac{1}{f_0}\Phi'$,

$$a = \Psi' - \frac{\Phi'}{f_0} \tag{3.1}$$

is the deviation of the geostrophically balanced streamfunction (Φ'/f_0) from the full streamfunction. We can decompose the imbalance into the basic state and the perturbation $a = \bar{a} + a'$. Because the basic state is in balance, $\bar{a} = \bar{\Psi} - \bar{\Phi}'/f_0 = 0$, the imbalance is therefore fully represented by its perturbation, $a = a'$.

To understand the physical meaning of a, we can separate it into the streamfunction/wind part and the geopotential/temperature part. Figure 3.1 shows the situations where the perturbation streamfunction, Ψ', exceeds the $1/f_0$-scaled perturbation geopotential height ($a > 0$) and where Ψ' has a deficit ($a < 0$). The total positive streamfunction would result

in an anticyclonic wind anomaly and a deficit of streamfunction results in a cyclonic wind anomaly. In the North Hemisphere, if we allow sufficient time for the Coriolis effect to influence the winds, this configuration of $a > 0$ above and $a < 0$ below will result in convergence above and divergence below, leading to a downward vertical motion to fulfill the fluid continuity.

When considering the imbalance in terms of perturbation geopotential or temperature, we should take into account its vertical arrangement (Fig. 3.2) and its vertical gradient as suggested by the definition of potential temperature, $\theta = -\frac{\partial \Phi}{\partial p}$. A configuration of $a > 0$ above and $a < 0$ below implies a downward bending geopotential height on an upper-level isobaric surface and an upward bending geopotential height on a lower-level isobaric surface. This configuration compresses the column thickness, which is equivalent to a cold temperature anomaly. Furthermore, if we use the geostrophic adjustment argument, the cold temperature anomaly will induce a downward vertical motion which creates adiabatic warming to balance the cold temperature anomaly. Similarly, when $a < 0$ is above and $a < 0$ is below, this imbalance setup corresponds to a warm temperature anomaly in between, resulting in an upward vertical motion.

This interpretation of a positive imbalance as a more anticyclonic wind anomaly or as stretching between two isobaric surfaces (decrease in static stability) is similar to that a positive PV anomaly can be modified either by changing the vertical vorticity or by changing the static stability.

It would be intuitive to compare the unbalanced winds with the ageostrophic wind since both their definitions are related to the deviation from the geostrophy. If we denote all unbalanced components by the subscript i hereafter, the differences between imbalance/unbalanced wind, u_i, and ageostrophic winds can be found by taking the curl of (3.1)

$$\begin{cases} v_i = \dfrac{\partial a}{\partial x} = \dfrac{\partial \Psi}{\partial x} - \dfrac{1}{f}\dfrac{\partial \Phi'}{\partial x} = v_r - v_g = v_{ag} - v_d & \text{(3.2a)} \\ u_i = -\dfrac{\partial a}{\partial y} = -\dfrac{\partial \Psi}{\partial y} + \dfrac{1}{f}\dfrac{\partial \Phi'}{\partial y} = u_r - u_g = u_{ag} - u_d & \text{(3.2b)} \end{cases}$$

where u_r and v_r are the rotational components of the wind, u_d and v_d are the divergent components, u_g and v_g are the geostrophic components, u_{ag} and v_{ag} are the ageostrophic components of the wind defined as the difference between the geostrophic wind and the full wind $\mathbf{v}_{ag} = \mathbf{v} - \mathbf{v}_g$. Since the geostrophic wind is non-divergent by definition, it is clear that the unbalanced component of the wind is the ageostrophic wind excluding the divergent part. Davis et al. (1996) partitioned the ageostrophic wind into three components: balanced irrotational, balanced nondivergent, and the remainder (e.g. their Fig. 7) and showed the balanced nondivergent ageostrophic wind is dominant, especially in a strongly curved flow like in a mid-latitude cyclone.

Although there is no divergent component in the unbalanced wind or in the imbalance definition, it is possible to relate them to the concept of divergence by observing the

divergence equation. Using the two-dimensional shallow water system as an example

$$\begin{cases} \dfrac{\partial u}{\partial t} = -\dfrac{\partial \Phi'}{\partial x} + fv & \text{(3.3a)} \\ \dfrac{\partial v}{\partial t} = -\dfrac{\partial \Phi'}{\partial y} - fu & \text{(3.3b)} \end{cases}$$

If we take $\frac{\partial}{\partial x}$ of (3.3a) and add it onto $\frac{\partial}{\partial y}$ of (3.3b), we get the divergence equation:

$$\frac{\partial \delta}{\partial t} = f\zeta - \nabla^2 \Phi'$$
$$\frac{\partial \chi}{\partial t} = f_0(\Psi' - \frac{1}{f}\Phi')$$

$$\frac{\partial \chi}{\partial t} = fa \tag{3.4}$$

This suggests that the local tendency of velocity potential and divergence has a component coming from the Coriolis force acting on the imbalance, similar to the divergent isallobaric wind term in the geopotential tendency equation. If we take the gradient of (3.4), we will notice the Coriolis force torques the non-divergent unbalanced wind into the divergent component of the wind.

$$\frac{\partial}{\partial t}\frac{\partial \chi}{\partial x} = f\frac{\partial a}{\partial x} \;\rightarrow\; \frac{\partial u_d}{\partial t} = f\frac{\partial (v_r - v_g)}{\partial t}$$
$$\frac{\partial}{\partial t}\frac{\partial \chi}{\partial y} = f\frac{\partial a}{\partial y} \;\rightarrow\; \frac{\partial v_d}{\partial t} = -f\frac{\partial (u_r - u_g)}{\partial t}$$

3.3 Sensitivity to Geostrophic Imbalance and its Interpretation

The derivation of sensitivity to geostrophic imbalance has already been presented in Chapter 2 section 2.2.5 following Arbogast (1998):

$$\hat{a} = \wp^{-1}\left(\frac{\partial}{\partial p}\left(\frac{f_0}{S}\frac{\partial}{\partial p}\right)\hat{\Psi} - \nabla^2\hat{\Phi}\right) \tag{3.5}$$

where $\wp = \frac{1}{f_0}\nabla^2 - \frac{\partial}{\partial p}(\frac{f_0}{S}\frac{\partial}{\partial p})$ is the QGPV operator. In our explanation of sensitivity to QGPV in Chapter 2 section 2.3, we treated the sensitivity to any variable as putting a small perturbation into the balanced state at the instantaneous time. Following this line of thought, the interpretation of the sensitivity to the imbalance is similar to that of the imbalance itself (Fig. 3.3). Ignoring the contribution from $\hat{\Phi}$, (3.5) is simplified into $\wp\hat{a} = \frac{\partial}{\partial p}(\frac{f_0}{S}\frac{\partial}{\partial p})\hat{\Psi}$. Because both $\wp$ and ∇^2 are second-order derivative operators, $\hat{a}$ and $\hat{\Psi}$ must share the same sign, just as a' and Ψ' share the same sign. Therefore, a positive $\hat{a}$ would be surrounded by an anticyclonic wind sensitivity, while a negative $\hat{a}$ would be accompanied by a cyclonic wind sensitivity. The anticyclonic wind sensitivity will later turn into convergence sensitivity while the cyclonic wind sensitivity turns into divergence sensitivity when torqued by the Coriolis force. To obey the continuity equation, a sensitivity to downward vertical motion ($\hat{\omega} > 0$) will be induced to fulfill the "mass" vacancy between the sensitivity to convergence above and sensitivity to divergence below.

Similarly, (3.5) simplifies to $\wp\hat{a} = -\nabla^2\hat{\Phi}$) by ignoring the contribution from $\hat{\Psi}$. The

simplified equation indicates that $\hat{a}$ and $\hat{\Phi}$ should have opposite signs. If we treat the sensitivity as an approximation to an instantaneous perturbation and refer to Fig. 3.2, then a cold temperature sensitivity should exist between a positive $\hat{a}$ above and a negative $\hat{a}$ below. The geostrophic adjustment argument infers a sensitivity to downward vertical motion which is accompanied by a sensitivity to warm temperature (adiabatic heating), shall be induced to adjust to the geostrophic equilibrium. The diagnostic sensitivities to vertical motion are consistent when viewing from both streamfunction and geopotential perspectives under the same vertical configuration of sensitivity to imbalance.

3.4 Sensitivity to Other Diagnostic Variables

3.4.1 Sensitivity to Geostrophically Unbalanced States

The sensitivity to geostrophically balanced states (2.19) was derived in Chapter 2 section 2.3.1 by simply taking the adjoint of the QGPV definition equation. However, since the notion of imbalance was not well explored by previous studies, there is no clear relation that can be used for a simple adjoint procedure like in the case of QGPV.

Whether the adjoint field is balanced or unbalanced, the general relationship between $\hat{\theta}$ and $\hat{\Phi}$ is given by (2.18). The general relationship between $\hat{\mathbf{v}}$ and $\hat{\Psi}$ can be found by taking the adjoint of the horizontal vorticity definition $\zeta = \frac{\partial v}{\partial x} - \frac{\partial u}{\partial y}$, which gives

$\hat{v} = -\frac{\partial \hat{\zeta}}{\partial x},\ \hat{u} = \frac{\partial \hat{\zeta}}{\partial y}$. Substituting $\nabla^2 \hat{\zeta} = \hat{\Psi}$ in (2.17) yields:

$$\begin{cases} \hat{v} = -\dfrac{\partial \hat{\zeta}}{\partial x} = -\dfrac{\partial \nabla^{-2} \hat{\psi}}{\partial x} & \text{(3.6a)} \\ \hat{u} = \dfrac{\partial \hat{\zeta}}{\partial y} = \dfrac{\partial \nabla^{-2} \hat{\psi}}{\partial y} & \text{(3.6b)} \end{cases}$$

From the adjoint form of the imbalance perturbation definition $a' = \Psi' - \frac{\Phi'}{f_0}$, the unbalanced sensitivity to streamfunction and to geopotential are consequently $\hat{\Psi}_i = \hat{a}$ and $\hat{\Phi}_i = -\frac{1}{f_0}\hat{a}$. We can substitute them into the equation set above (3.6a) and get:

$$\begin{cases} \hat{v}_i = -\dfrac{\partial \nabla^{-2} \hat{a}}{\partial x} & \text{(3.7a)} \\ \hat{u}_i = \dfrac{\partial \nabla^{-2} \hat{a}}{\partial y} & \text{(3.7b)} \\ \hat{\theta}_i = \dfrac{\partial}{\partial p}^{-1} \left(-\dfrac{\gamma}{f_0} \hat{a} \right) & \text{(3.7c)} \end{cases}$$

3.4.2 Sensitivity to Ageostrophic Winds

The ageostrophic wind is defined as the departure of the full wind from the geostrophic wind. Inspired by the derivation of sensitivity to the ageostrophic wind in a two-dimensional shallow water system in Morgan (2018):

$$\begin{aligned} u_{ag} &= u - u_g = -\frac{\partial \Psi}{\partial y} + \frac{\partial \chi}{\partial x} + \frac{1}{f}\frac{\partial \Phi}{\partial y} \\ v_{ag} &= v - v_g = \frac{\partial \Psi}{\partial x} + \frac{\partial \chi}{\partial y} - \frac{1}{f}\frac{\partial \Phi}{\partial x} \\ q' &= \nabla^2 \Psi + \frac{\partial}{\partial p}\left(\frac{f}{S}\frac{\partial \Phi}{\partial p}\right) \end{aligned}$$

which can be written in the matrix form:

$$\begin{pmatrix} u_{ag} \\ v_{ag} \\ q' \end{pmatrix} \begin{pmatrix} -\frac{\partial}{\partial y} & \frac{\partial}{\partial x} & \frac{1}{f}\frac{\partial}{\partial y} \\ \frac{\partial}{\partial x} & \frac{\partial}{\partial y} & -\frac{1}{f}\frac{\partial}{\partial x} \\ \nabla^2 & 0 & \frac{\partial}{\partial p}(\frac{f}{S}\frac{\partial}{\partial p}) \end{pmatrix} = \begin{pmatrix} \Psi \\ \chi \\ \Phi \end{pmatrix}$$

and taking the adjoint of it:

$$\begin{pmatrix} \hat{\Psi} \\ \hat{\chi} \\ \hat{\Phi} \end{pmatrix} \begin{pmatrix} \frac{\partial}{\partial y} & -\frac{\partial}{\partial x} & \nabla^2 \\ -\frac{\partial}{\partial x} & -\frac{\partial}{\partial y} & 0 \\ -\frac{1}{f}\frac{\partial}{\partial y} & \frac{1}{f}\frac{\partial}{\partial x} & \frac{\partial}{\partial p}(\frac{f}{S}\frac{\partial}{\partial p}) \end{pmatrix} = \begin{pmatrix} \hat{u}_{ag} \\ \hat{v}_{ag} \\ \hat{q} \end{pmatrix}$$

where we can express the sensitivity to streamfunction $\hat{\Psi}$, to velocity potential $\hat{\chi}$, and to geopotential $\hat{\Phi}$ as:

$$\begin{cases} \hat{\Psi} = \dfrac{\partial \hat{u}_{ag}}{\partial y} - \dfrac{\partial \hat{v}_{ag}}{\partial x} + \nabla^2 \hat{q} & \text{(3.8a)} \\ \hat{\chi} = -\dfrac{\partial \hat{u}_{ag}}{\partial x} - \dfrac{\partial \hat{v}_{ag}}{\partial y} & \text{(3.8b)} \\ \hat{\Phi} = -\dfrac{1}{f}\dfrac{\partial \hat{u}_{ag}}{\partial y} + \dfrac{1}{f}\dfrac{\partial \hat{v}_{ag}}{\partial x} + \dfrac{\partial}{\partial p}(\dfrac{f_0}{S}\dfrac{\partial \hat{q}}{\partial p}) & \text{(3.8c)} \end{cases}$$

Combine (3.8a) and (3.8b), the sensitivity to ageostrophic wind can be expressed as:

$$\begin{cases} \nabla^2 \hat{u}_{ag} = \dfrac{\partial}{\partial y}(\hat{\Psi} - \nabla^2 \hat{q}) - \dfrac{\partial \hat{\chi}}{\partial x} & \text{(3.9a)} \\ \nabla^2 \hat{v}_{ag} = -\dfrac{\partial}{\partial x}(\hat{\Psi} - \nabla^2 \hat{q}) - \dfrac{\partial \hat{\chi}}{\partial y} & \text{(3.9b)} \end{cases}$$

Note that, combining (3.8a) and (3.8c) brings us back to the expression for sensitivity to QGPV (2.15).

Remember the sensitivity to streamfunction and to velocity potential can also be expressed in terms of the sensitivities to full winds $\hat{\Psi} = -(\frac{\partial \hat{v}}{\partial x} - \frac{\partial \hat{u}}{\partial y}) = \nabla^2 \hat{\zeta}$ and $\hat{\chi} = -(\frac{\partial \hat{u}}{\partial x} + \frac{\partial \hat{v}}{\partial y}) = \nabla^2 \hat{\delta}$ (e.g., (2.17); Kleist and Morgan 2005). If we expand $\nabla^2 \hat{q} = \partial/\partial x(\partial \hat{q}/\partial x) + \partial/\partial y(\partial \hat{q}/\partial y)$ and substitute (2.19a) and (2.19b) in (3.8a), the equation becomes $\hat{\Psi} = (\frac{\partial \hat{u}_{ag}}{\partial y} + \frac{\partial \hat{u}_g}{\partial y}) - (\frac{\partial \hat{v}_{ag}}{\partial x} + \frac{\partial \hat{v}_g}{\partial x})$. This suggests that the sensitivity to the full wind can be decomposed into sensitivity to geostrophic wind and sensitivity to ageostrophic wind, just like the full wind can be decomposed into the geostrophic wind and the ageostrophic wind. Likewise, the adjoint sensitivity $\hat{\chi}$ is solely constructed through $\hat{\mathbf{v}}_{ag}$, resembling how divergence can be entirely attributed to the ageostrophic wind in the forward model. Morgan (2018) pointed out that in a 2D shallow water system, the sensitivities to the ageostrophic components of the flow will eventually become the sensitivities to the irrotational flow when the system achieves the geostrophic equilibrium.

3.4.3 Sensitivity to Vertical Velocity

Equation 3.4 reveals the connection between the local time tendency of velocity potential and the geostrophic imbalance. Considering that velocity potential is linked to divergence and, consequently, linked to the vertical velocity following the continuity equation, it is possible to derive a diagnostic relationship for sensitivity to vertical velocity in the

pressure coordinate, ω. To achieve this, we can take the adjoint of (3.4):

$$-\frac{\partial \hat{a}}{\partial t} = f\hat{\chi} \tag{3.10}$$

From the continuity equation: $-\frac{\partial \omega}{\partial p} = \delta = \nabla^2\chi$, we can get its adjoint form: $\frac{\partial \hat{\chi}}{\partial p} = \nabla^2\omega$. Plug $\hat{\chi}$ from (3.10) into the adjoint continuity equation gives the sensitivity to vertical velocity $\hat{\omega}$:

$$\hat{\omega} = \nabla^{-2}\frac{\partial \hat{\chi}}{\partial p} = \nabla^{-2}\frac{\partial}{\partial p}\left(-\frac{1}{f}\frac{\partial \hat{a}}{\partial t}\right) \tag{3.11}$$

3.5 Optimal Perturbation

The optimal perturbation experiment is used to study the impact of balanced and unbalanced initial perturbation on the development of an explosive winter storm conducted in section 3.6. The methodology follows section 3c in Hoover (2015) and is briefly described in Chapter 2 section 2.2.2.

Given sensitivity gradients, one can construct perturbations to achieve the prescribed amount of change in the response function. The perturbation is optimal in the sense that it inserts minimal energy $\mathscr{E}$ into the system. Here the energy is represented by a norm which is the sum of kinetic energy and thermal energy.

$$\mathscr{E} = \frac{1}{2}\left(u_0'^2 + v_0'^2 + \frac{c_p}{T_{ref}}T_0'^2\right) = \frac{1}{2}\langle \mathbf{x}_0', \mathbf{W}\mathbf{x}_0'\rangle \tag{3.12}$$

The weighting matrix

$$\mathbf{W} = \mathbf{W}_{u,v,T} = \begin{pmatrix} \mathbf{I} & 0 & 0 \\ 0 & \mathbf{I} & 0 \\ 0 & 0 & \frac{c_p}{T_{ref}}\mathbf{I} \end{pmatrix}$$

is block diagonal with the identity matrices for weighting the kinetic energy and $\frac{c_p}{T_{ref}}$ for weighting the thermal energy norm, where $T_{ref} = 300K$ is the reference state temperature. Various norms can produce optimal perturbations that evolve differently and have different growth rates (Snyder and Joly, 1998). In this study, to obtain the optimal initial perturbation, we minimize the energy norm subject to the first-order differentiation constraint, $\delta R = \langle \frac{\partial R}{\partial \mathbf{x}}, \mathbf{x}' \rangle$

$$\min \mathscr{E}$$
$$s.t. \;\; \delta R = \langle \frac{\partial R}{\partial \mathbf{x}}, \mathbf{x}' \rangle$$

The minimization can be solved by minimizing the Lagrangian, with the Lagrange multiplier λ

$$\min \; \mathscr{L} = \mathscr{E} + \lambda \left(\delta R - \left\langle \frac{\partial R}{\partial \mathbf{x}}, \mathbf{x}' \right\rangle \right)$$

From the first order necessary condition for minimization, $\partial \mathscr{L} / \partial \mathbf{x}_0 = 0$, we get the expression for $\mathbf{x}_0'$ which is proportional to the initial sensitivity gradient, $\frac{\partial R}{\partial \mathbf{x}_0}$:

$$\mathbf{x}_0' = \lambda \mathbf{W}^{-1} \frac{\partial R}{\partial \mathbf{x}_0} \tag{3.13}$$

We can plug $\mathbf{x}_0'$ into the first order differentiation, $\delta R = \langle \frac{\partial R}{\partial \mathbf{x}}, \lambda \mathbf{W}^{-1} \frac{\partial R}{\partial \mathbf{x}_0} \rangle$, which gives the expression for the optimal Lagrange multiplier: $\lambda = \frac{\delta R}{\langle \frac{\partial R}{\partial \mathbf{x}}, \mathbf{W}^{-1} \frac{\partial R}{\partial \mathbf{x}_0} \rangle}$. Finally, insert λ back into (3.13)

$$\mathbf{x}_0' = \frac{\delta R \mathbf{W}^{-1} \frac{\partial R}{\partial \mathbf{x}_0}}{\langle \frac{\partial R}{\partial \mathbf{x}}, \mathbf{W}^{-1} \frac{\partial R}{\partial \mathbf{x}_0} \rangle} \tag{3.14}$$

3.6 Case Study of November 1998 Winter Storm

The November 1998 winter storm, known as the November Witch, brought intense convective precipitation to the Midwest and southern plains and produced widespread damaging winds exceeding 20 $m \cdot s^{-1}$ and gust frequently over 35 $m \cdot s^{-1}$ across the upper Great Lakes region in Wisconsin and Minnesota. We wish to use this case as an example to illustrate the application of adjoint sensitivity to QGPV and imbalance in understanding the development of a typical midlatitude cyclone.

3.6.1 Synoptic Overview

The ERA5 reanalysis (Hersbach et al., 2020) shows that a low-pressure system was organizing over eastern Colorado at 1200 UTC 9 November (e.g. Fig. 3.4a). At this time, the 500 hPa trough is located west of the Rockies and is characterized by a linear PV maximum and intense baroclinicity. Over the next 12 hours, the trough tracks east of the Rockies and acquires a negative tilt (e.g. Fig. 3.4b). The thermal wind advection of PV forces the upward vertical motion over the region of minimum sea level pressure in central Kansas. Starting from Kansas, the storm rapidly develops in the next 24 hours,

with the sea level pressure dropping from 996 hPa at 0000 UTC 10 November to 967 hPa around 0000 UTC 11 November just east of Duluth, MN. At 1200 UTC 10 November, the 500 hPa cut-off low stacks directly on the surface low, with the PV strip wrapping the trough like a comma shape (e.g. Fig. 3.4c). The negatively tilted trough is accompanied by a pronounced ridge downstream. At 0000 UTC 11 November, the PV strip detaches from the center of the 500 hPa cut-off low possibly due to the erosion by the latent heat release (e.g. Fig. 3.4d). By the morning of November 11th, the low was located in north central Ontario.

Examining the upper-level forcing, a polar jet core is over California at 1200 UTC 9 November (e.g. Fig. 3.5a). Over the midwest and the southern plains, the polar jet is parallel to the subtropical jet. At 0000 UTC 10 November, the polar jet starts to curve as the upper-level ridge starts to build up. Over the Central Plains, the storm starts to develop with the minimum sea level pressure located beneath the polar jet core (e.g. Fig. 3.5b). The subtropical jet and polar jet start to merge together at 1200 UTC 10 November which creates a starker meridional temperature gradient and stronger baroclinicity that feeds energy into the surface cyclone development beneath the jet's exit region (e.g. Fig. 3.5c).

3.6.2 Numerical Simulation

A numerical simulation of this extreme cyclogenesis event is carried out by the Weather Research and Forecasting (WRF) model (Skamarock et al., 2008) and the WRF adjoint model (V3.8.1, Zhang et al. 2013). We simulate the case from 1800 UTC November

9 (forecast hour 00, F00) to 1800 UTC November 10 (F24), initialized with 0.25 degree NCEP's FNL reanalysis (National Centers for Environmental Prediction, National Weather Service, NOAA, U.S. Department of Commerce, 2015), with 24 km grid spacing and 41 vertical levels from the surface to 50 hPa. In the simulation, the storm reaches an intensity of 961 hPa at 1800 UTC 10 November, which exceeds the real-world intensity within an even shorter development time. We chose the response function to be negative perturbation average surface dry air mass in the column: $R = -\bar{\mu}'$ within the 980 hPa sea level pressure contour at F24 (e.g. Fig. 3.6). The negative sign in the response function infers that a positive perturbation of positive sensitivity corresponds to perturbations that would lower the surface pressure, which is equivalent to deepening the storm intensity within the response function area. The forward and adjoint model outputs are interpolated vertically to equally spaced isobaric surfaces from 1000 hPa to 50 hPa model top using WRF-python (Ladwig, 2017). Adjoint sensitivities for all variables below ground are set to zero.

Adjoint sensitivity to QGPV ($\hat{q}$) and sensitivity to geostrophic imbalance ($\hat{a}$) are calculated using successive over-relaxation on a centered finite-difference grid following (2.15)

$$\hat{q} = \wp^{-1}\left(\frac{1}{f_0}\hat{\Psi} + \hat{\Phi}\right)$$

$$\hat{q} = \wp^{-1}\left(\frac{1}{f_0}\left(\frac{\partial \hat{u}}{\partial y} - \frac{\partial \hat{v}}{\partial x}\right) + \frac{1}{\gamma}\frac{\partial \hat{\theta}}{\partial p}\right) \tag{3.15}$$

where sensitivities to winds ($\hat{u}$, $\hat{v}$) and to potential temperature ($\hat{\theta}$) are obtained from

WRFPLUS adjoint output and interpolated from sigma levels to isobaric levels for the convenience of calculation.

Figure 2.8 describes the simulation procedure: The initial condition is provided for the WRF nonlinear forward integration that generates the forecast trajectory. Given the chosen response function, the adjoint forcing $\frac{\partial R}{\partial \mathbf{x}_t}$ is specified, which in this case, is just $\frac{\partial R}{\partial \mu'} = -1$ inside the 980 hPa contour. Integrating the adjoint model backward along the stored trajectory from F24 for one hour gives the sensitivity output at F23, $\frac{\partial R}{\partial \mathbf{x}_{t-1}}$. We apply the sensitivity to QGPV to filter out gravity waves in the wind and temperature sensitivity fields, which are then used as the adjoint forcing $\frac{\partial R}{\partial \mathbf{x}_{t-1,bal}}$ for a new adjoint backward integration starting at F23 with all other sensitivity variables set to 0, including $\frac{\partial R}{\partial \mu'}$. Figure 3.7 shows the comparison between the 500 hPa $\hat{\theta}$ at F22 from the original adjoint simulation initialized at F24 and from the experiment initialized at F23 with the balanced adjoint forcing. In addition to showing no large-scale gravity wave sensitivity pattern, the balanced adjoint initialization experiment also presents a preference for colder upper-level temperatures for the storm to develop in the next two hours, which fits the cold-core nature of a midlatitude cyclone. Therefore, in this study, we use the adjoint sensitivity from the balanced adjoint initialization experiment and refer to its outputs as "WRF-adjoint".

JRA reanalysis[1] at 1200 UTC 10 November 1998 is used to validate the schematic of

[1]JRA reanalysis provides the streamfunction field while ERA5 or GDAS FNL reanalysis does not.

geostrophic imbalance in Fig. 3.1. At 900 hPa, a positive imbalance overlaps the surface cyclone. As deduced in section 3.2, the unbalance component of the wind and the ageostrophic wind are similar. Both winds are anticyclonic around a maximum, except the ageostrophic wind has a convergent component pointing toward the low-pressure center. At 300 hPa, the strongest ageostrophic wind locates at the jet core and between the largest horizontal gradient of the imbalance. The ageostrophic wind shows a clear divergent pattern in the upper Midwest.

3.6.3 Horizontal Analysis

Figure 3.9 displays the adjoint sensitivity from WRF-adjoint at F14. The physical meaning of sensitivity is that if one perturbs the model state at this time step proportional to the sensitivity, these perturbations will lead to the deepening of the storm (in the case of $R = -\bar{\mu}$) 10 hours later at F24. A cyclonic pattern of sensitivity to winds is evident near the 500 hPa trough in the Central Plains, indicating a demand for increased positive vorticity. Moreover, the sensitivity to southeasterly wind over Saskatchewan implies that a more negatively tilted trough to the north would benefit the storm development. The sensitivity to temperature is broadly negative behind the upper front and positive ahead, aligning with the frontal precipitation area (not shown). This configuration, with more cold air upstream and warm air downstream naturally intensifies the frontal system. A pronounced warm sensitivity area at the Nebraska-Kansas border contrasts with the broad cold sensitivity pattern behind the front and will be elaborated on in section 3.6.5.

Sensitivity to QGPV $\hat{q}$ and geostrophically balanced winds $\hat{\mathbf{v}}_g$ calculated following (2.15),

(2.19a) and (2.19b) are shown in Fig. 3.10 for time step F14. The $\hat{q}$ maximum overlays the 500 hPa trough in southern Kansas, with the 500 hPa Ertel PV strip on its southeastern edge. It suggests adding a positive PV perturbation within the cut-off low could potentially deepen the storm. Notably, $\hat{q}$ extends northwest to the Dakotas and $\hat{\mathbf{v}}_g$ inverted from it is almost identical to that from the WRF-adjoint output (e.g. Fig. 3.9). At the same time, a dipole of sensitivity to imbalance $\hat{a}$ straddles the Ertel PV strip. Referring back to Fig. 3.1 where a dipole of imbalance constructs an easterly unbalanced wind in the westerly jet core, the dipole of $\hat{a}$ suggests adding a more southwesterly wind that is perpendicular to the cyclonic $\hat{\mathbf{v}}_g$ recovered from $\hat{q}$ will help the storm intensify 10 hours later.

3.6.4 Surface Front Vertical Cross Section

Figure 3.11 shows cross-section locations, one across the surface front (red line) and the other across the upper-level jet (black line). The cross-sections are used to investigate the vertical distributions of $\hat{q}$ and $\hat{a}$ in the surface front and the upper-level jet at forecast hour F14.

Figure 3.12 depicts the cross-section of the surface front. In Figure 3.12a, $\hat{q}$ is shown to tilt westward with height, in alignment with the frontal structure. Notably, the $\hat{q}$ maximum coincides with intense low-level frontal baroclinicity. Cyclonic geostrophically balanced sensitivity to wind $\hat{\mathbf{v}}_g$ suggests that reinforcing the southerly wind ahead of the front and the northerly wind behind it would lead to a stronger surface cyclone after 10 hours. The hydrostatically balanced sensitivity to temperature, $\hat{\theta}_g$, is positive above $\hat{q}$

maximum and negative below it. Since $\hat{q}$ is negatively tilted, $\hat{\theta}_g$ also displays this slanting pattern, emulating the condition for storm intensification that rely on a robust zonal temperature gradient. This upshear negative tilted structure has been documented in previous sensitivity studies (e.g., Ancell and Mass 2006; Doyle et al. 2014) and can be attributed to the vortex unshielding based on the Orr Mechanism (e.g., Orr 1907; Nolan and Farrell 1999).

Figure 3.12b shows the relative position of $\hat{q}$ and $\hat{a}$ in the same northwest-southeast cross-section. In the lower level, negative $\hat{a}$ is downstream of the $\hat{q}$ axis and is positive upstream. While there is not much upper-level structure of $\hat{q}$ in this cross-section, there is a clear 500hPa vertical dipole of $\hat{a}$ near 99°W. Unlike the balanced component which calls for colder air near the surface for the storm to intensify, the unbalanced sensitivity to potential temperature, $\hat{\theta}_i$, is consistently positive along the surface front, extending to the 500 hPa (e.g. Fig. 3.12c). This warm sensitivity feature is likely associated with the latent heating released by the frontal precipitation in the forward trajectory (e.g. Fig. 3.12d). Maximum convective accumulated precipitation aligns with the lower level $\hat{\theta}_i$ maximum, while maximum stratiform accumulated precipitation matches the 500 hPa $\hat{\theta}_i$ maximum (e.g. Fig. 3.11). Following the physical interpretation in section 3.2, this warm sensitivity could prompt sensitivity to adiabatic upward vertical motion to "cool down" the warm temperature sensitivity later on. This argument is consistent with the characteristic frontal upward vertical motion.

Focus on the unbalanced wind sensitivity around $\hat{a}$ minimum near 94°W in Fig. 3.12c, we

can observe unbalanced component of sensitivity to horizontal wind $\hat{\mathbf{v}}_i$ inverted from $\hat{a}$ is cyclonic around negative $\hat{a}$. Although the magnitude of the unbalanced component of the wind sensitivity is much smaller than the balanced component, $\hat{\mathbf{v}}_i$ still favors northerly behind and southerly ahead of the front.

3.6.5 Upper Front Vertical Cross Section

Figure 3.13 shows a cross-section of the 400 hPa jet, with the tropopause overfold marked by high Ertel PV wrapping on the poleward flank of the jet core. The maximum positive sensitivity to QGPV is located on the lower poleward edge of the 2 PV unit (PVU) tropopause. This suggests that shifting the existing PV intrusion downward, effectively bringing the tropopause further into the troposphere, can lead to surface storm intensification at the final time.

The sensitivity to geostrophically balanced wind shifts sharply on the northern edge of the Ertel PV. Furthermore, $\hat{\theta}_g$ inverted from $\hat{q}$ suggests that a warmer air layer above and a colder air layer beneath the tropopause would be favorable for storm development. This configuration enhances the static stability, which in turn strengthens both PV and the upper front.

At 500 hPa, a positive sensitivity to imbalance $\hat{a}$ emerges at the same location as the maximum $\hat{q}$ beneath the poleward flank of the jet. A negative counterpart appears at 650 hPa with cold unbalanced temperature sensitivity ($\hat{\theta}_i < 0$) positioned between the dipole. To achieve a positive $\hat{a}$ according to (2.14), the sensitivity to geopotential $\hat{\Phi}$

has to be either negative or much smaller than the sensitivity to the streamfunction $\hat{\Psi}$. Consequently, deepening the 500 hPa geopotential height on the poleward flank of the polar jet could lead to further development. The negative $\hat{\theta}_i$ supplements the balanced component $\hat{\theta}_g$ to tighten the temperature gradient across the upper-level front. Using the geostrophic adjustment argument, sensitivity to downward vertical motion will prompt an unbalanced cold temperature sensitivity. This descent would help bring tropopause PV further down, potentially resulting in a deeper storm 10 hours later.

The same unbalanced warm temperature sensitivity ($\hat{\theta}_i > 0$) at 500 hPa near 40°N, 99°W on the Nebraska-Kansas border, as shown in Fig. 3.12c, is also apparent in Fig. 3.13b. This feature is accompanied by a negative $\hat{a}$ above and a positive $\hat{a}$ below and is not closely related to the circulation around the jet. Interestingly, $\hat{\theta}_g > 0$ inverted from $\hat{q}$ is only slightly positive at this location, indicating that sensitivity to QGPV is unable to capture this feature. This warm temperature sensitivity may imply a reduction in stratification and an increase in baroclinicity in the mid-troposphere (700 hPa - 400 hPa). As discussed in the surface front cross-section, there exhibits a collocation of accumulated precipitation and a positive sensitivity to temperature. This observation suggests that the unbalanced component of temperature sensitivity is closely related to latent heat release.

In a previous case study of this winter storm, Posselt (2001) demonstrated the significant impact of latent heat release in the development of a trough of warm air aloft (TROWAL, Martin 1999) during the occlusion phase of this storm by comparing simulation with and without diabatic processes. The presence of warm sensitivity supports this finding and

further emphasizes the importance of stratiform precipitation-induced latent heating in the development of mid-latitude cyclones.

Figure 3.14 is presented to better illustrate the relative contribution of the balanced and unbalanced components to the total sensitivity fields at 500 hPa. Figure 3.14 a,c,e show both balanced and unbalanced $\hat{u}$ favors a stronger westerly jet, but it is clear that the zonal wind sensitivity is dominated by the geostrophically balanced component. With sensitivity features tilting into the background horizontal shear created by the lower edge of the jet (e.g. Fig. 3.13 inset cross-section), the sensitivity over New Mexico and northern Texas implies exploitation of barotropic growth potential on either side of the jet. A similar pattern is observed in east Pacific tropical cyclogenesis cases along the east Pacific low-level jet (Hoover, 2015) and in an idealized mid-latitude cyclogenesis case along the westerly jet (Langland et al., 1995). Hoover (2015) decomposed $\hat{u}$ into non-divergent component, $\hat{u}_{nd}$, and irrotational component, $\hat{u}_{ir}$, and found $\hat{u} \approx \hat{u}_{nd} + \hat{u}_{ir}$. The summation of geostrophic balanced and unbalanced sensitivities to wind, $\hat{u}_g + \hat{u}_i$, however, does not recover the dipole sensitivity pattern over the eastern CONUS. It suggests that, since both $\hat{u}_g$ and $\hat{u}_i$ are non-divergent, this wind sensitivity pattern is purely driven by the sensitivity to divergence which is generated by the gravity wave adjustment process.

Figure 3.14b,d,f suggest that at 500 hPa the temperature sensitivity is dominated by the unbalanced component $\hat{\theta}_i$ inverted from $\hat{a}$. The addition of balanced and unbalanced components in both wind and temperature sensitivity matches the total sensitivity from the WRF-adjoint output. We might conclude that the sensitivity associated with QG

balance mainly considers the dry dynamical process while the sensitivity associated with the imbalance covers the remaining diabatic process.

3.6.6 Sensitivities to Vertical Motion and to Ageostrophic Winds

The section serves as an illustration of the derivation discussed in section 3.4. Figure 3.15 shows the comparison between the **normalized** $\hat{w}$ directly from the WRFPLUS adjoint output and the **normalized** $-\hat{\omega}$ calculated from $\hat{a}$ using (3.11) in the same cross-section taken across the jet. $\hat{\omega}$ is negated so that the positive value would suggest that positive vertical motion will help the storm development. Both metrics exhibit an upward-downward vertical motion dipole beneath the jet core. The magnitude of $\hat{\omega}$ computed here is on the order of $1 \sim 10$, while the magnitude of $\hat{w}$ is on the order of $0.1 \sim 1$, therefore $\hat{\omega} \approx 10\hat{w}$. If we adjoint the expression $\omega = -\rho g w$ which gives

$$\hat{w} = -\rho g \hat{\omega} \approx 10\hat{\omega}$$

where $\rho \sim 1kg/m^3$ and $g \sim 10m/s^2$. This shows that in theory, $\hat{\omega} \approx 0.1\hat{w}$ which conflicts with the observed ratio ($\hat{\omega} \approx 10\hat{w}$) obtained from the adjoint model. Instead of delving into the WRFPLUS model code, consider focusing on the straightforward relationship: $\Delta R = \langle \frac{\partial R}{\partial \mathbf{x}}, \delta \mathbf{x} \rangle$. If we assume that perturbing each variable contributes a similar amount of change in the response function $\frac{\partial R}{\partial x_i} \delta x_i = \Delta R_i$ to the total ΔR, where x_i is the ith variable in the state vector $\mathbf{x}$, then the corresponding sensitivity of a variable that has a smaller magnitude should be larger. For example, the typical value

for $\hat{u}$ is on the scale of $1 \sim 10$ and its perturbation should have a magnitude of 10^0 such that the small perturbation approximation is not violated. This makes the product $\langle \frac{\partial R}{\partial u}, \delta u \rangle$ to be on the scale of 10^1. The typical value for sensitivity to water vapor mixing ratio ($\hat{q}_{vapor}$) is $10^2 \sim 10^3$ and its perturbation is usually on the scale of 10^{-3} kg/kg, so $\langle \frac{\partial R}{\partial q_{vapor}}, \delta q_{vapor} \rangle \sim 10^0$. Therefore, if the contribution to the change in response function from u and w are on the same magnitude, it would be mind-boggling to have the scale of $\hat{w}$ to be smaller than $\hat{u}$ ($0.1 \ll 1$) when the vertical velocity perturbation is also smaller than the horizontal wind perturbation ($0.1 \ll 1$).

Figure 3.16 shows the qualitative sensitivity to ageostrophic winds at 900 hPa and at 500 hPa at F14. At 900 hPa, the sensitivity to ageostrophic wind exhibits an anticyclonic pattern around the surface trough from Iowa to Arkansas. A noticeable shift in the direction of sensitivity to ageostrophic wind is observed between the 1010 and 1020 hPa contours, extending from Quebec to Tennessee. At 500 hPa, the sensitivity to ageostrophic wind is less rotational compared to 900 hPa, with convergence centered on Oklahoma and the Great Lakes, and divergence centered on Dakotas.

3.6.7 Optimal Perturbation

Three optimal perturbation experiments were conducted (e.g. Fig. 3.17) to investigate the validity of balanced and unbalanced adjoint sensitivities. The first experiment, labeled "exp WRF-adj", is informed by the WRF-adjoint sensitivity output at the initial time ($\hat{u}_0,\ \hat{v}_0,\ \hat{\theta}_0$). The second experiment, "exp bal", is informed by the balanced adjoint sensitivity ($\hat{u}_{g,0},\ \hat{v}_{g,0},\ \hat{\theta}_{g,0}$), and the last one, "exp imb", is informed by the unbalanced

adjoint sensitivity ($\hat{u}_{i,0},\ \hat{v}_{i,0},\ \hat{\theta}_{i,0}$). The original WRF simulation is labeled by "ctrl". The value of ΔR signifies the total perturbation energy introduced into the system. The optimal initial perturbations are created following section 3.5, with an aim of lowering the sea level pressure (SLP) inside the 980 hPa contour by an average of 5 hPa ($\Delta R = 394500$).

The first column of Fig. 3.17 displays the initial optimal zonal wind and temperature perturbation at 500 hPa for three experiments. Three sets of perturbations share a similar temperature perturbation pattern. "Exp imb" generates the strongest temperature perturbation at 500 hPa and "exp bal" produces the largest zonal wind perturbation. On the other hand, "exp WRF-adj" focus most perturbation energy near the surface and deploys less perturbation at 500 hPa. The second column of Fig. 3.17 shows the storm center pressure after 24 hours of integration for these three optimal perturbation experiments. Both "exp bal" (960.5 hPa) and "exp imb" (960.7 hPa) create a deeper cyclone than "exp WRF-adj"'s perturbation (961.0 hPa), but none achieves the targeted 5 hPa average change in SLP. Differences in mean sea level pressure between the perturbed and the control experiments are also shown in the second column in color shading. The balanced perturbation creates a concentric deepening, lowering central pressure while raising surrounding pressure. In all three cases, the dry column air perturbation (μ') difference exhibits a dipole-like shape north of the storm pressure center. This shape is created by the rise (lowering) in SLP caused by the contraction (expansion) of the SLP contour (Fig.3.17 b,e,h zooms in c,f,i near the storm center). The shape of the perturbed SLP contour is similar to the unperturbed control experiment. Both balanced and unbalanced

perturbations raise the pressure along the cold front from Michigan to Tennessee and deepen the pressure on the warm frontal section in Ontario. Additionally, the unbalanced perturbation continues to wrap the deepening effect to the southwest of the storm in Minnesota and Iowa.

Fig. 3.18 shows the SLP difference between the three perturbation experiments and the control simulation at F00 in the first column and at F02 in the second column. At the initiating time (F00), inserting the optimal perturbations results in distinct changes in three scenarios. The unbalanced perturbation has the most widespread impact on SLP over the Rockies and Southern US (Fig. 3.18e). The SLP difference caused by the balanced perturbation is most evident in New Mexico and coastal Texas (Fig. 3.18c), likely due to the deep convection on the Gulf and the topographical effect, respectively. The impact of WRF-adjoint perturbation is minimal southwest of the minimum SLP (Fig. 3.18a). Most of the SLP differences created by perturbations diminished within an hour of integration (not shown, but similar to SLP perturbation evolution at F02) as indicated by a drastic decrease in SLP perturbation magnitude. At F02, all three SLP differences exhibit a gravity wave pattern, especially in the case of the unbalanced perturbation (Fig. 3.18f). A notable commonality is the presence of a dipole pattern in SLP differences, with a decrease in SLP to the east and a rising in SLP to the west. However, the SLP difference in "exp WRF-adj" is 10 times smaller than in "exp bal" and "exp imb".

Figure 3.19 displays the vertical energy distribution of these three perturbations. "Exp

WRF-adj" has most of its energy concentrated at the surface level, with a small portion at 800 hPa and almost no energy above 700 hPa. In contrast, the initial energy perturbations from "exp bal" and "exp imb" are designated to enhance energy in the lower free atmosphere levels below 700 hPa with a gradual transition up to the tropopause. The balanced energy norm perturbation surpasses the unbalanced energy norm at all levels, particularly near the surface level and at 750 hPa, similar to the "exp WRF-adj".

After an hour of integration, the perturbation energy experiences significant growth above 900 hPa in "exp bal" and "exp imb" (dashed line in Fig. 3.19), including levels above 200 hPa where less energy was initially added into the system. In contrast, the energy norm in "exp WRF-adj" near 750 hPa only increases slightly. "exp imb" exhibits larger energy norm growth compared to the balanced perturbation at nearly all levels, except near 700 hPa. In both "exp WRF-adj" and "exp bal", the perturbation energy norm decreases significantly below 900 hPa, where a substantial amount of energy was initially introduced to the system. Conversely, the surface perturbation energy in "exp imb" increases significantly, making it difficult to conclude whether the energy dissipation in "exp bal" and "exp WRF-adj" is due to the boundary layer mixing.

Figure 3.20 shows the evolution of the vertical perturbation energy norm in each optimal perturbation experiment. "Exp imb" generates the largest final-time perturbation energy norm, which is 5 times larger than the perturbation energy norm generated in "exp WRF-adj". The largest growth in the perturbation energy norm occurs near the jet level,

followed by another peak near 750 hPa. The growth pattern of the perturbation energy norm is similar between the balanced and unbalanced cases.

In "exp WRF-adj", the energy norm is capped at 150 hPa and 50 hPa. All perturbations exhibit minimal changes in the first 12 hours, except below 800 hPa. Starting from F13, perturbation starts to grow between 500 hPa and 200 hPa as its influence on the jet or the upper front takes effect. By F18, perturbation in the stratosphere (near 100 hPa) begins to increase, and by F20 perturbation energy shows growth between 800 and 500 hPa.

The perturbation energy norm grows faster in "exp imb" than "exp bal", especially in the free troposphere between 800 hPa and 300 hPa during the first 16 hours, indicated by the more rapid expansion of magenta and lime lines. But overall, the perturbation energy norm growth patterns are similar between these two cases. The jet level energy (between 500 hPa and 300 hPa) increases rapidly before F06 but is capped from F07 to F12 before increasing again towards the final forecast hour. Although the factors suspending the jet-level perturbation energy growth are intriguing, they are beyond the scope of this research. About half of the energy norm growth in the lower troposphere (below 800 hPa) occurs in the first 9-hour integration, with the remaining half of the norm increase occurring in the next 15 hours. Notably, at F23 and F24, a retreat of perturbation energy norm is observed at lower levels. An interesting distinction between balanced and unbalanced perturbation experiments emerges in the last 4 hours of simulation between

600 hPa and 400 hPa. Energy gain continues to change in this layer in "exp bal", while perturbation energy norm growth halts near the end of the simulation in "exp imb".

Hoover (2015) employed an ad hoc method to assess linearity, which relies on the assumption that a purely linear system should exhibit a constant change in response function $\Delta R \approx \delta R = \langle \partial R/\partial \mathbf{x}_\tau, \mathbf{x}'_\tau \rangle$ for any time step $\tau = 0$ ... 24. Figure 3.21 depicts the sum of the product of sensitivity and perturbation over variables (u, v, θ). In a linear model, such as the tangent linear model, $\delta R/\Delta R_0$ should equal 1 at all time steps. However, in all three cases, $\delta R/\Delta R_0$ decreases as the model integrates, indicating the presence of nonlinear processes. Compared to the perturbations informed by WRF-adjoint which only preserves 30% of the initial response function change, both balanced and unbalanced perturbation cases show gentler declines from F00 to F01, retaining nearly 80% of the initial prescribed change in the response function. The ongoing decrease in δR implies the introduction of nonlinearity to the system at each time step. Notice that the change in δR becomes smoother after F12, implying either the system becomes less chaotic, or F12 marks the end of the spin-up of the geostrophic adjustment process caused by the injected perturbations.

3.7 Discussion and Conclusion

In this chapter, we discuss the notion of geostrophic imbalance and explore the interpretation of sensitivity to geostrophic imbalance. As illustrated in Figure 3.3, a positive $\hat{a}$ is associated with an anticyclonic sensitivity to wind pattern and a negative $\hat{a}$ is associated

with a cyclonic sensitivity to wind pattern. Furthermore, sensitivity to cold temperature is accompanied by $\hat{a} > 0$ above and $\hat{a} < 0$ below, potentially leading to sensitivity to downward vertical motion to fulfill the geostrophic adjustment process.

We apply these diagnostic sensitivities to investigate the dynamic aspects of the rapid development of the November 1998 Midwest winter storm from 1800 UTC 9 November to 1800 UTC 10 November with the WRF model. The examination of the surface front cross-section shows a preference for having warmer air ahead and colder air behind the front. This temperature gradient preference is captured by a positive sensitivity to QGPV at a low level tilted along the surface front. The unbalanced component of the sensitivity to potential temperature ($\hat{\theta}_i$) inverted from $\hat{a}$ however suggests overall warming along the front helps the storm to deepen at the final time. The positive sensitivity to QGPV overlaps the upper-level PV partially explains the reason why a cold temperature is preferred below the jet – inserting colder air can increase the static stability and subsequently increase the PV. From an imbalance point of view, a cold temperature sensitivity can trigger a sensitivity to downward vertical motion, which might influence the downward extension of the background tropopause, thereby creating a stronger PV in the mid-troposphere.

The collocation of the unbalanced temperature sensitivity, $\hat{\theta}_i$, and accumulated precipitation from the WRF trajectory output in both surface front and jet cross-section (e.g., Fig. 3.12 and Fig. 3.13) suggests that the $\hat{\theta}_i$ is likely the manifestation of the latent heating. The linkage between latent heat release in the forward trajectory and the presence of unbalanced temperature sensitivity points to the importance of including moist

processes in the adjoint sensitivity study like with WRF version 4 (Skamarock et al. 2019) or COAMPS (Doyle et al., 2012) model. Langland et al. (1995) demonstrated that sensitivity overlapping with certain features of the basic state does not necessarily imply that those basic-state features are important to the response function. Instead, sensitivity is often associated with some basic-state features that are driving the time-tendency of the sensitivity variable. In this study, the time-tendency forcing for potential temperature could arise from either latent heat release or the existing vertical motion in the basic state. Future work could include running the forward trajectory without the option of latent heating. Comparing unbalanced sensitivity to temperature between the control case and the no latent heating case should shed light on whether the connection between the precipitation and the unbalanced temperature sensitivity is physically grounded.

Interestingly, comparing balanced and unbalanced components with the full wind and temperature sensitivity, we find the geostrophically balanced component dominates the wind sensitivity, while the unbalanced component dominates the temperature sensitivity field (e.g. Fig. 3.14). This suggests that although both sensitivities to QGPV and imbalance combine the wind and temperature sensitivity fields, we should treat the sensitivity to QGPV ($\hat{q}$) as an entity that recovers the dynamical aspect and treat the sensitivity to imbalance ($\hat{a}$) as the one that recovers the thermal aspect.

The calculation of sensitivity to QGPV involves the inversion of the QGPV operator, $\wp$. This inversion computes $\hat{q}_g$ with a spatial scale larger than or similar to the Rossby radius of deformation, $L_R = NH/f$, where N is the Brunt–Väisälä frequency, H is the

vertical scale. In the mid-latitudes, the ratio N/f is typically around 100, so L_R is roughly 100 times the vertical scale height, H. If we approximate the vertical scale of both upper-level and lower-level troughs to be 5 km, or half the tropopause height, then L_R is approximately 500 km. This makes the $\hat{q}_g$ pattern to be on the scale of L_R (e.g., Fig. 3.10). We know when the scale of the initial PV perturbation is larger than L_R, the wind field adjusts to the mass field. This might also be true for the adjoint variables. In this case, when the scale of $\hat{q}_g$ is larger than L_R, the sensitivity to wind adjusts to $\hat{q}_g$ in the final balanced state, making the balanced component, $\hat{u}_g$, dominates over the unbalanced component, $\hat{u}_i$. Similarly, when the perturbation scale is smaller than L_R, the mass/temperature field adjusts to the wind field. In Fig. 3.10, as the remnant of the balanced sensitivity field, the sensitivity to imbalance, $\hat{a}$, has a scale much smaller than the L_R. This possibly explains why $\hat{\theta}$ is dominated by $\hat{\theta}_i$, while $\hat{a}$ merely recovers any sensitivity to wind.

Three sets of optimal perturbation informed by the WRF-adjoint, balanced, and unbalanced components of the WRF-adjoint output respectively are added to the initial condition. Both balanced and unbalanced initial perturbations enhance storm intensity at the final forecast time. We anticipate the balanced initial perturbation to create a deeper storm since it filters out the perturbations projected onto the gravity wave in the WRF-adjoint informed perturbation. Surprisingly, the unbalanced initial perturbation also significantly impacts the final storm intensity. From our understanding, an unbalanced wind perturbation contributes very little to the storm development because it will rotate and travel away from the frontal zone as a gravity wave, while a balanced

perturbation is capable of having a sustained impact on the basic state where the cyclone is developing. Defined as the residual of the wind-temperature field inverted from QGPV, the unbalanced component should not contain QGPV perturbation if the inversion converges. One possible explanation is that the wind field with adjust to the strong unbalanced temperature perturbation, creating new QGPV perturbation post-geostrophic adjustment. It should be noted that the balanced initial perturbation does not guarantee the geostrophic adjustment can be avoided (e.g., Fig. 3.18) since it is the full initial state that should be in balance (Arbogast et al., 2008) if one wishes to minimize the spin-up time.

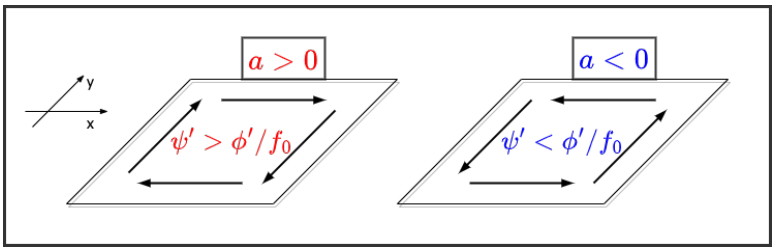

FIGURE 3.1: Anticyclonic wind around ψ' surplus and $a > 0$ indicated in red and cyclonic wind around ψ' deficit and $a < 0$ indicated in blue.

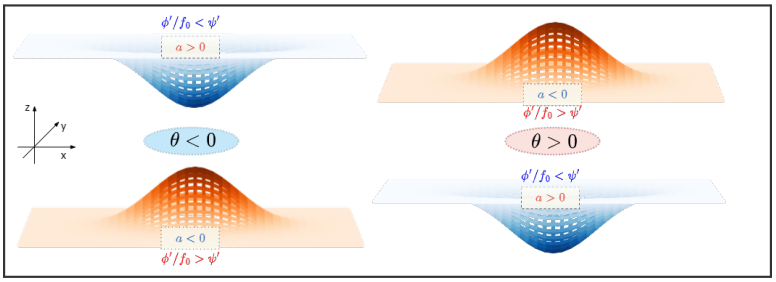

FIGURE 3.2: Blue membrane suggests a ϕ' deficit and $a > 0$ on an isobaric surface, red membrane suggests a ϕ' surplus and $a < 0$ on an isobaric surface. Shaded ovals indicate the perturbation potential temperature anomaly, with cold in blue and warm in red.

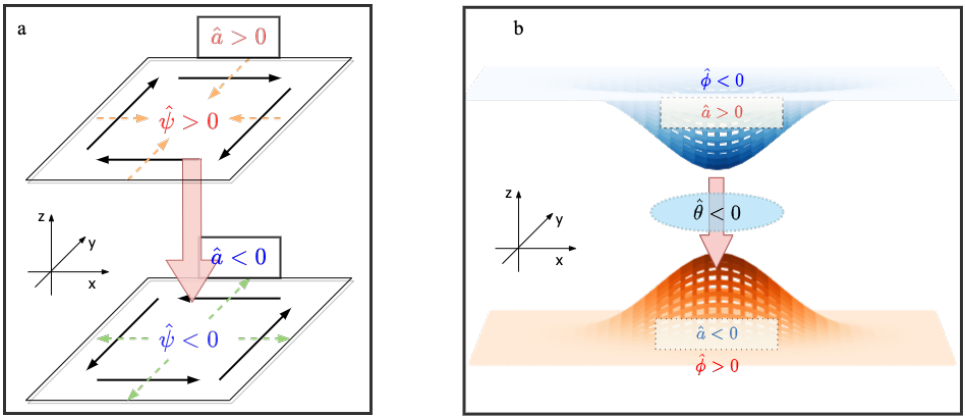

FIGURE 3.3: Schematics depiction of the sensitivity to geostrophic imbalance $\hat{a}$. Panel (a) depicts the streamfunction/wind sensitivity component associated with the sensitivity to geostrophic imbalance. Solid arrows show the instantaneous horizontal wind sensitivity vectors and dash arrows depict the horizontal wind sensitivity vectors after geostrophic adjustment. Panel (b) depicts the geopotential/temperature sensitivity component associated with the sensitivity to geostrophic imbalance. The red and blue membranes are isobaric surfaces. The red convex shows a preference for higher geopotential, while the blue concave shows a preference for lower geopotential. The thick red arrows in both panels show a tendency of sensitivity to downward vertical motion when a positive sensitivity to imbalance ($\hat{a} > 0$) is above and a negative sensitivity to imbalance ($\hat{a} < 0$) is below.

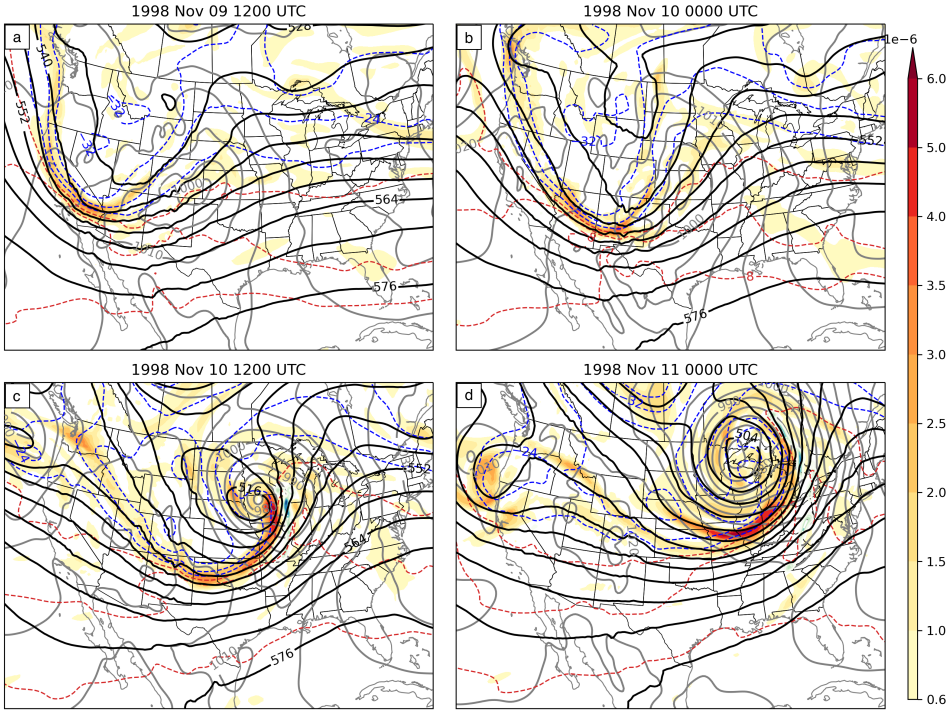

FIGURE 3.4: ERA5 reanalysis of 500 hPa geopotential height (interval 6 dam; black contours), temperature (interval 4 $^{\circ}C$; dashed contours), Ertel PV (shaded, negative value in green), and mean sea level pressure (interval 5 hPa; gray contours) at a) 1200 UTC 9 November, b) 0000 UTC 10 November, c) 1200 UTC 10 November, d) 0000 UTC 11 November.

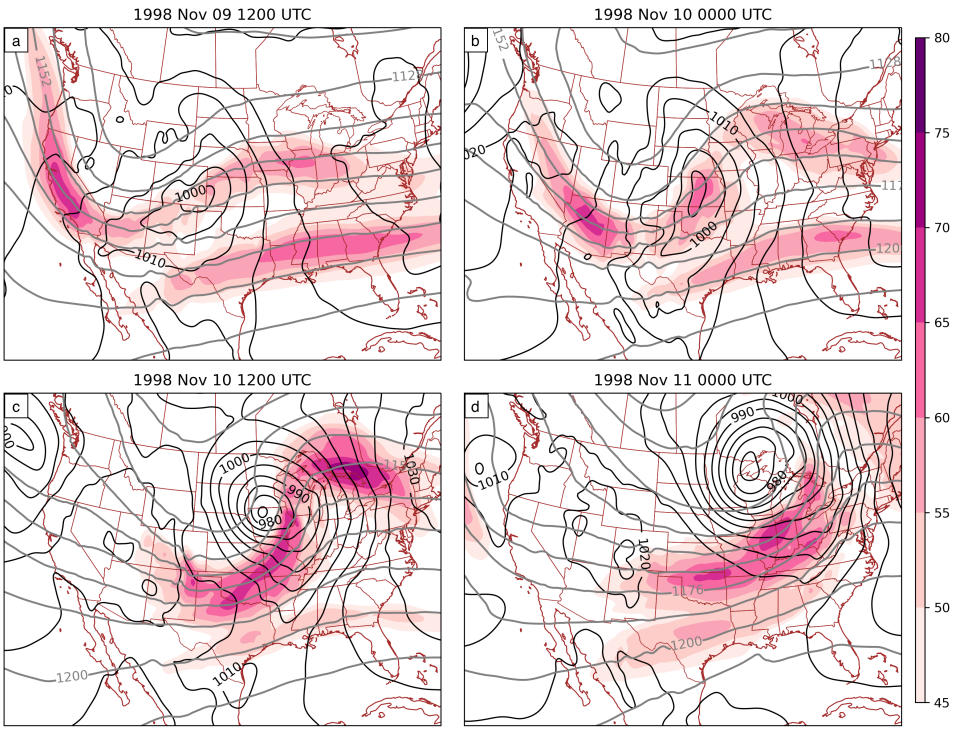

FIGURE 3.5: ERA5 reanalysis of 200 hPa geopotential height (interval 12 dam; gray contours), wind speed in $m \cdot s^{-1}$ (shaded), and mean sea level pressure (interval 5 hPa; black contours) at a) 1200 UTC 9 November, b) 0000 UTC 10 November, c) 1200 UTC 10 November, d) 0000 UTC 11 November.

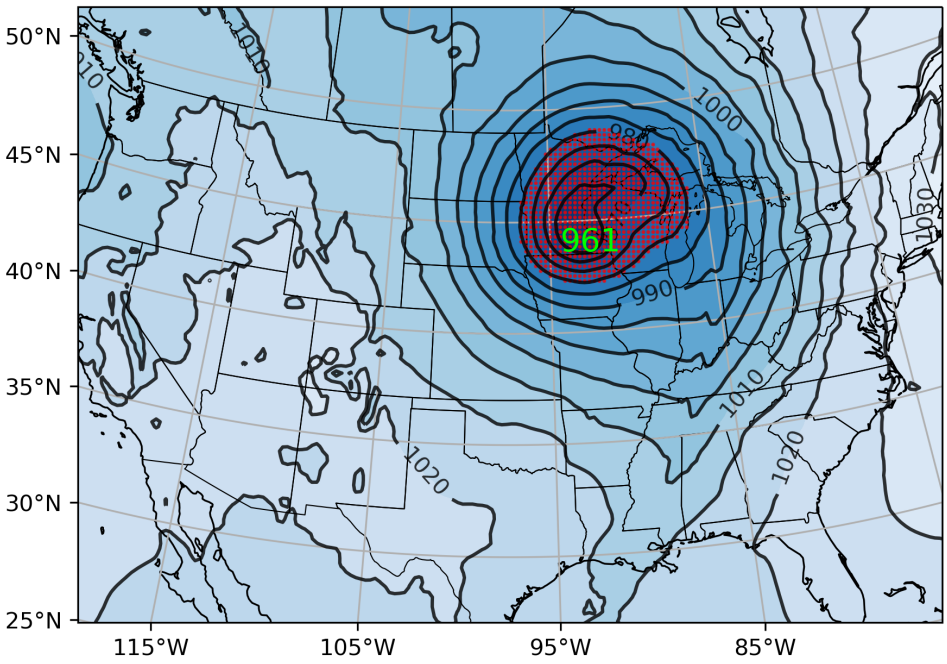

FIGURE 3.6: WRF mean sea level pressure (interval 5 hPa; black contour) at 1800 UTC 10 November. Red meshes cover the region of adjoint forcing i.e. the gradient of response function at F24, $\partial R/\partial \mu' = -1$ inside 980 hPa contour.

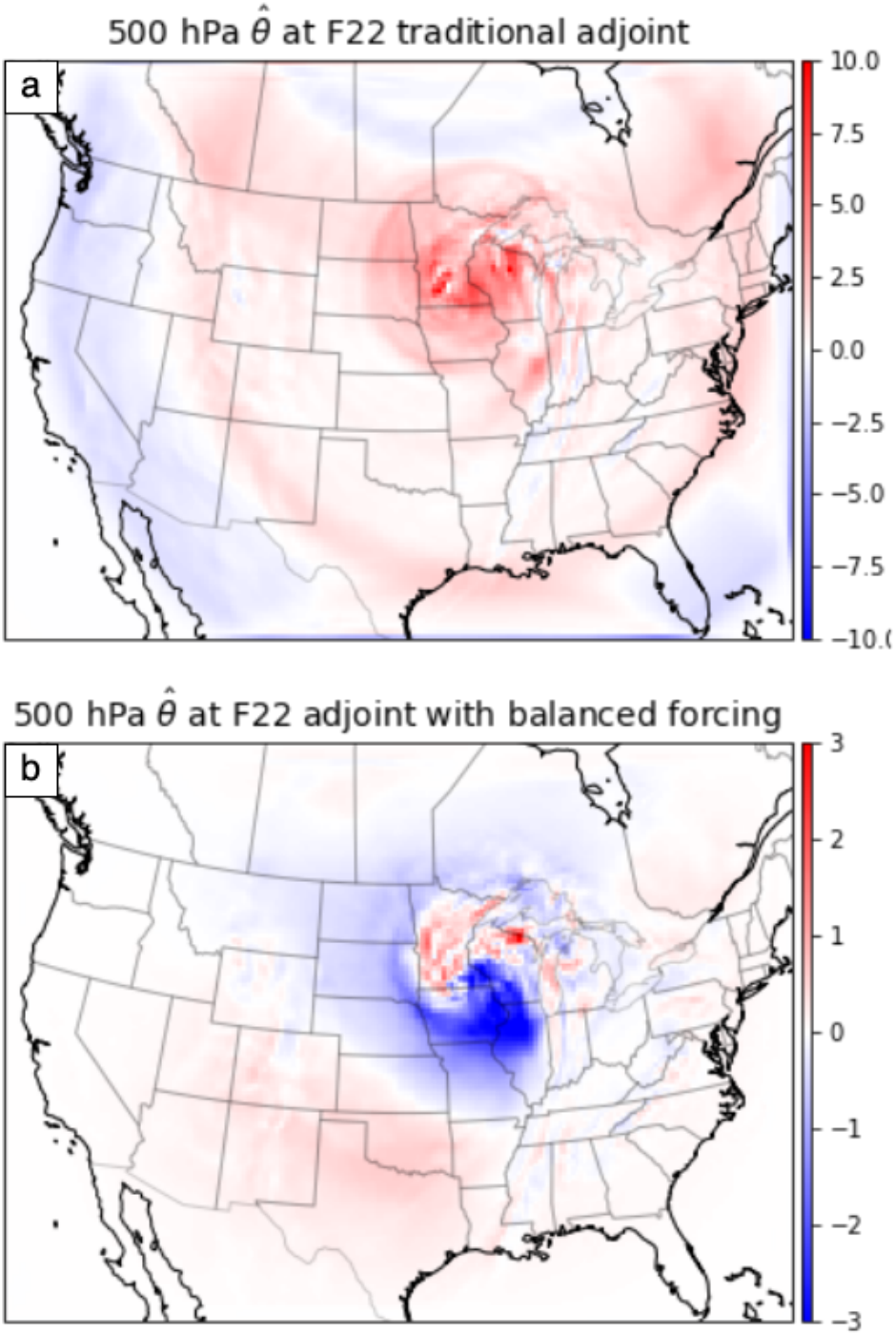

FIGURE 3.7: 500 hPa sensitivity to the potential temperature at 1600 UTC 10 November (F22) from a) adjoint model initialized with just $dR/d\mu = -1$ at F24 (Figure 2.8 row 2) and b) adjoint model initialized with balanced adjoint forcing at F23 (Figure 2.8 row 3)

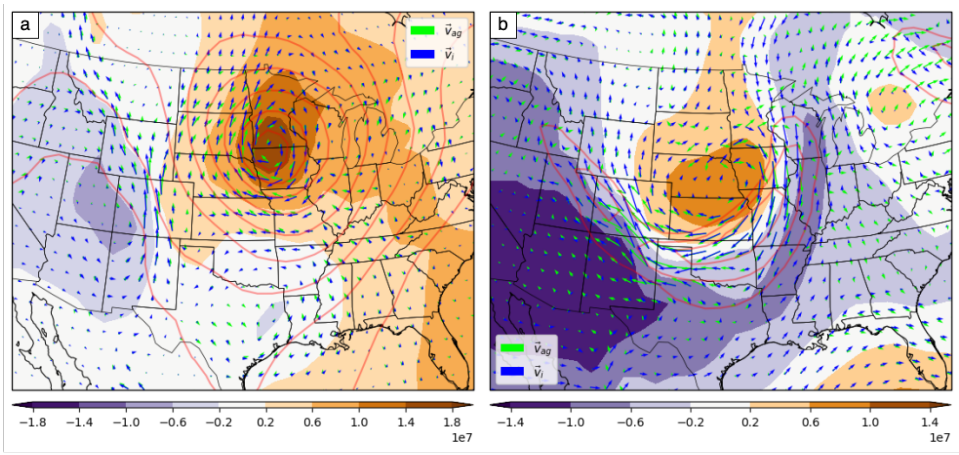

FIGURE 3.8: a) JRA reanalysis of 900 hPa imbalance (shaded), geopotential height (red contour), unbalanced winds (blue vectors), and ageostrophic winds (green vectors); b) 300 hPa imbalance (shaded), wind speed (red contour; interval 10 m/s), unbalanced winds (blue vectors), and ageostrophic winds (green vectors). Both panels are valid at 1200 UTC 10 November 1998.

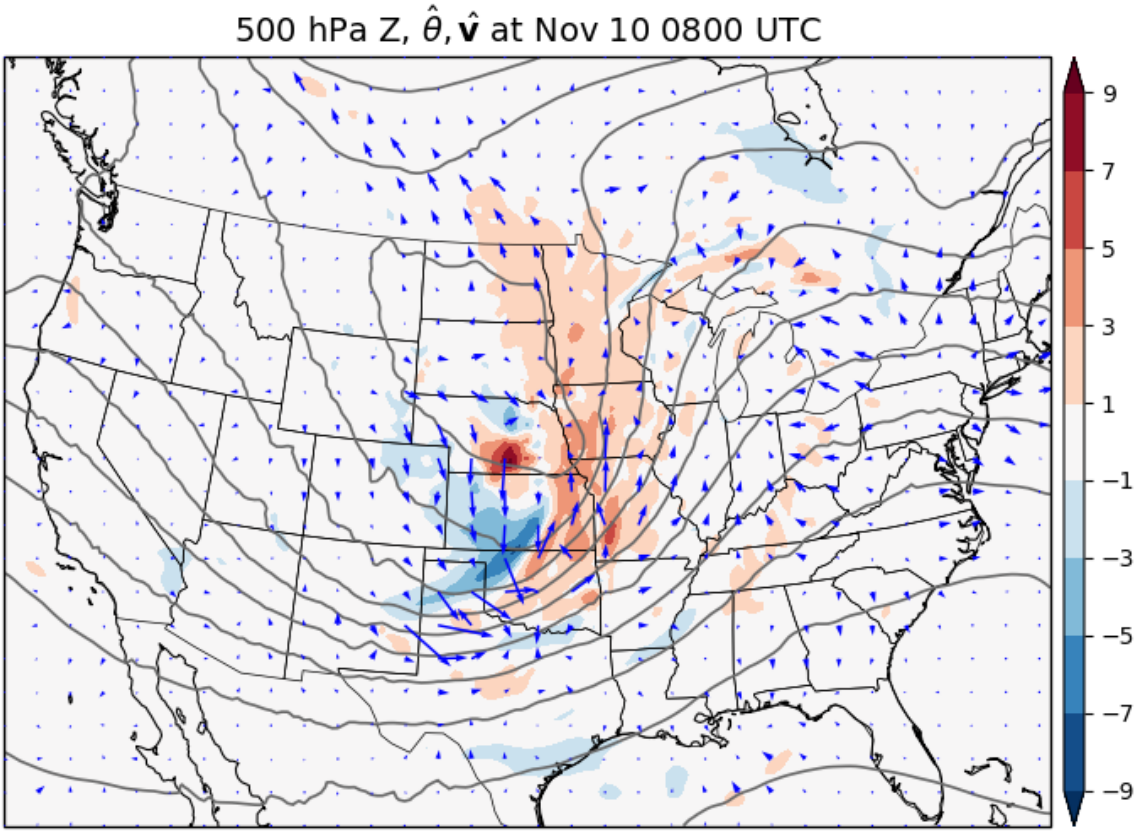

FIGURE 3.9: WRF simulated 500 hPa geopotential height (interval 6 dam; black contour) at 0800 UTC 10 November (F14), with 500 hPa sensitivity to horizontal wind vector $\hat{\mathbf{v}}_g$ from WRFPLUS depicted in blue arrows and sensitivity to potential temperature $\hat{\theta}$ shaded (warm sensitivity in red and cold sensitivity in blue).

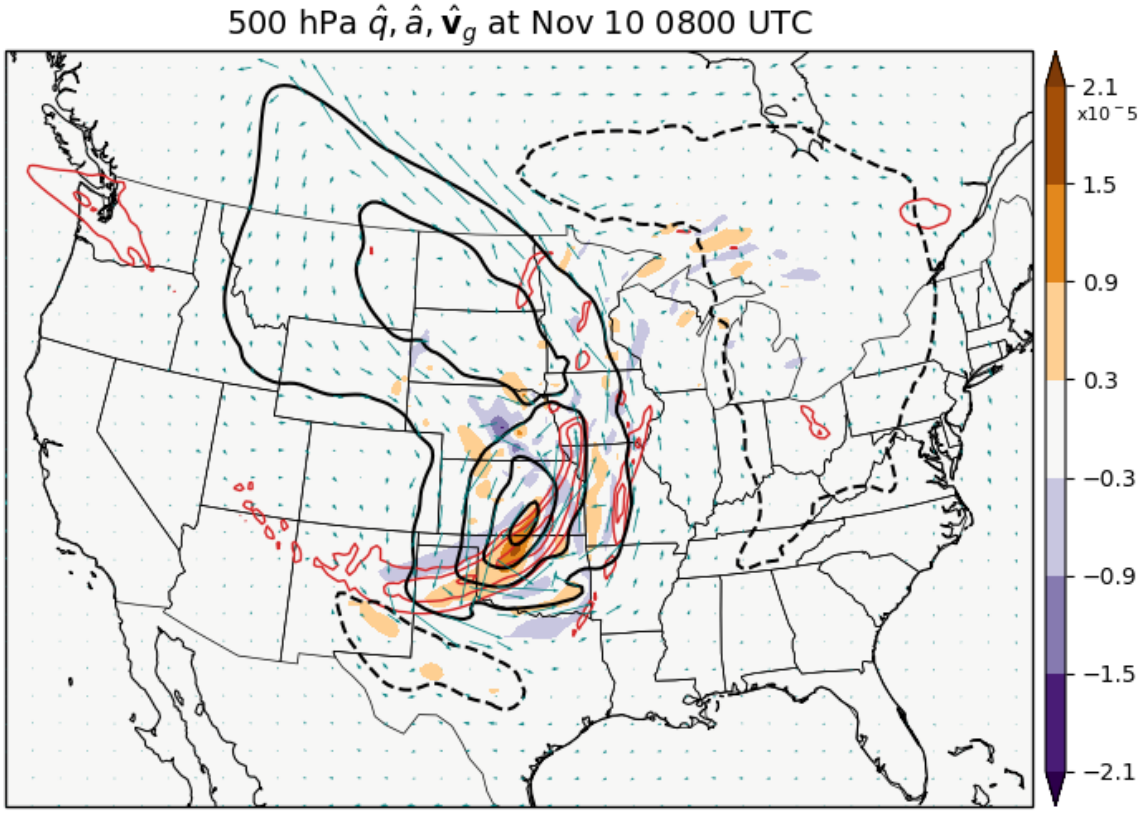

FIGURE 3.10: WRF 500 hPa Ertel PV (interval 1 PVU; thin red contour) at 0800 UTC 10 November (F14), 500 hPa sensitivity to QGPV (interval 10^5 $Pa \cdot s$; thick black contour, solid positive, dashed negative), sensitivity to imbalance $\hat{a}$ (interval 6×10^{-6} $Pa \cdot s \cdot m^{-2}$; shaded, positive in orange and negative in purple) and geostrophically balanced sensitivity to horizontal wind vectors $\hat{\mathbf{v}}_g$ are depicted in teal arrows.

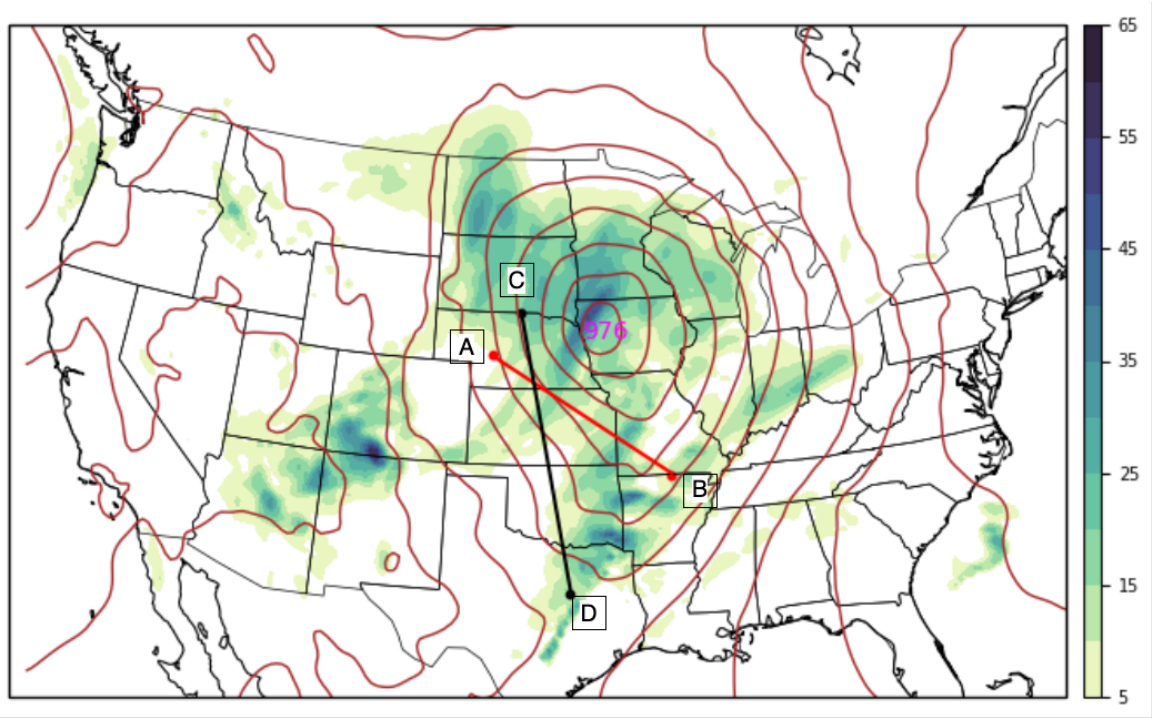

FIGURE 3.11: Accumulated precipitation (interval 5 mm; shaded) in WRF simulation from forecast hour F00 till F14. WRF simulated mean sea level pressure (interval 5 hPa; brown contour) at 0800 UTC 10 November (F14). Two cross sections orientation in Figure 3.12 and Figure 3.13 are plotted in red and black lines respectively.

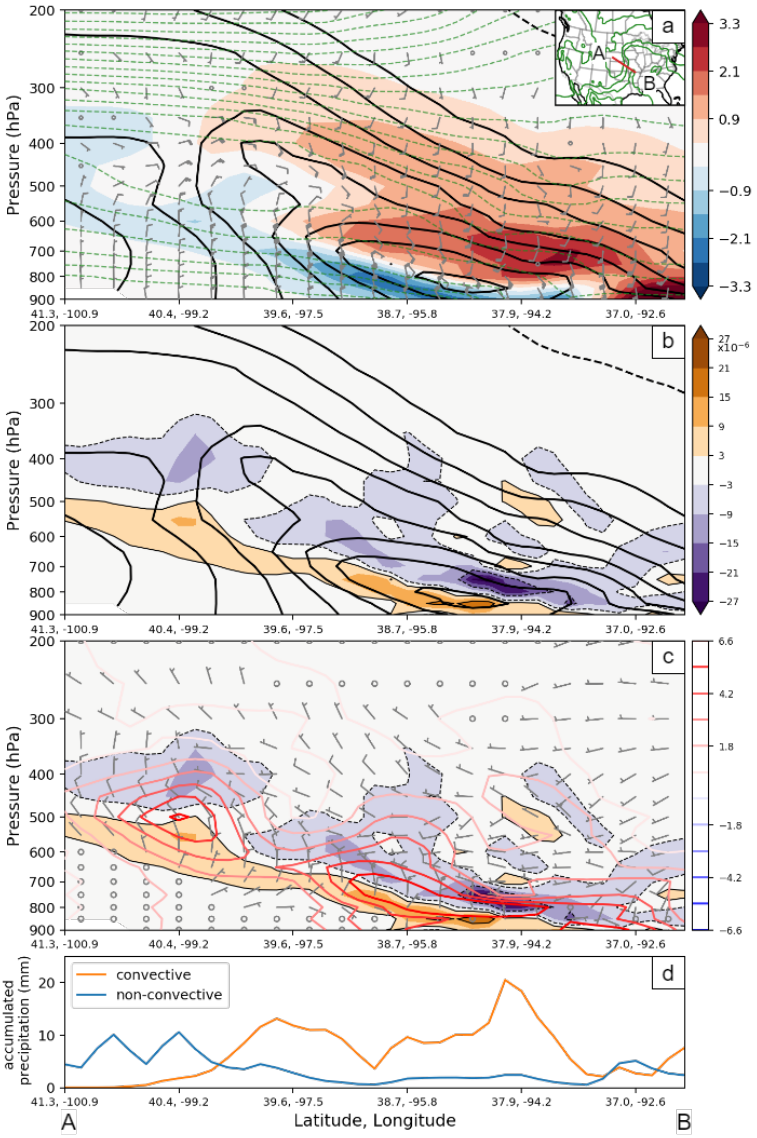

FIGURE 3.12: Cross section across the surface cold front at forecast time F14 valid 0800 UTC 10 November 1998. a) background potential temperature (interval $4K$; green dashed contour), sensitivity to QGPV (interval $6 \times 10^4\ Pa \cdot s$; black contour), geostrophically balanced sensitivity to horizontal winds $\hat{\mathbf{v}}_g$ (gray barbs) and hydrostatically balanced sensitivity to temperature $\hat{\theta}_g$ (interval 0.6 $Pa \cdot K^{-1}$; shaded). The inset plot shows the 850 hPa potential temperature in green contours and cross-section orientation (red line). b) Cross section of sensitivity to QGPV $\hat{q}$ (contour, same as in a)) and the sensitivity to imbalance $\hat{a}$ (interval $6 \times 10^{-6}\ Pa \cdot s \cdot m^{-2}$; shaded, $\hat{a} > 0$ in orange and negative in purple $\hat{a} > 0$). c) sensitivity to imbalance (shaded, same as in b)), the unbalanced component of sensitivity to horizontal winds $\hat{\mathbf{v}}_i$ (gray barbs), and an unbalanced component of sensitivity to potential temperature $\hat{\theta}_i$ (interval 0.6 $Pa \cdot K^{-1}$; color contours, warm sensitivity in red and cold sensitivity in blue). d) Accumulated convective precipitation (orange) and non-convective precipitation (blue) along the cold frontal cross-section.

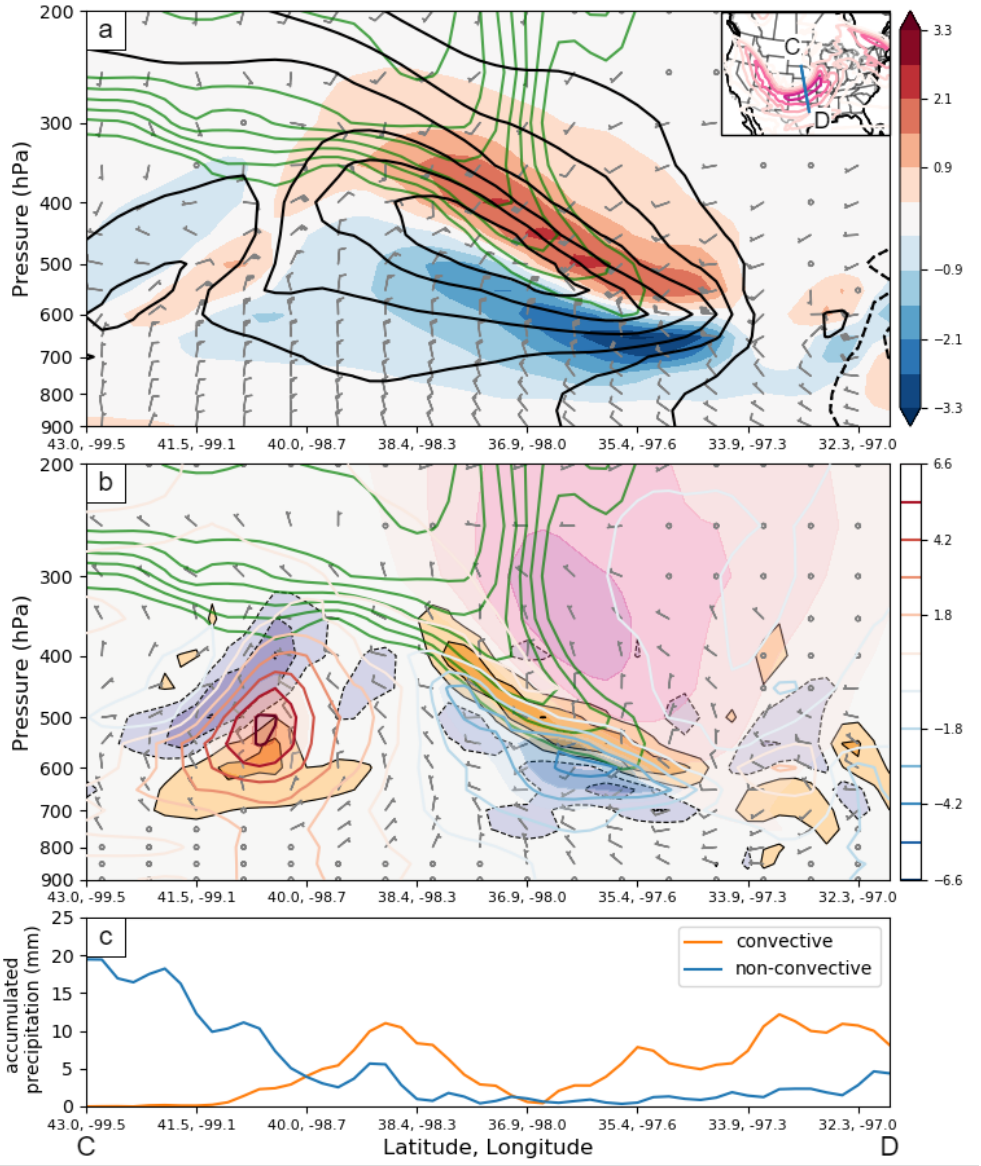

FIGURE 3.13: Cross section across the 400 hPa jet at forecast time F14 valid 0800 UTC 10 November 1998. a) background Ertel PV (interval 1 PVU; green contour), sensitivity to QGPV (interval 6×10^4 $Pa \cdot s$; black contour), geostrophically balanced sensitivity to horizontal winds $\hat{\mathbf{v}}_g$ (gray barbs) and hydrostatically balanced sensitivity to temperature $\hat{\theta}_g$ (interval 0.6 $Pa \cdot K^{-1}$; shaded). The inset plot shows the 400 hPa jet (interval 10 $m \cdot s^{-1}$; pink contour) and cross-section orientation (blue line). b) background Ertel PV in green contour and jet core location indicated by the pink shading, sensitivity to imbalance (interval 6×10^{-6} $Pa \cdot s \cdot m^{-2}$; shaded, $\hat{a} > 0$ in orange and negative in purple $\hat{a} > 0$), the unbalanced component of sensitivity to horizontal winds $\hat{\mathbf{v}}_i$ (gray barbs) and unbalanced component of sensitivity to potential temperature $\hat{\theta}_i$ (interval 0.6 $Pa \cdot K^{-1}$; color contours, warm sensitivity in red and cold sensitivity in blue). c) Accumulated convective precipitation (orange) and non-convective precipitation (blue) along the cross-jet cross-section.

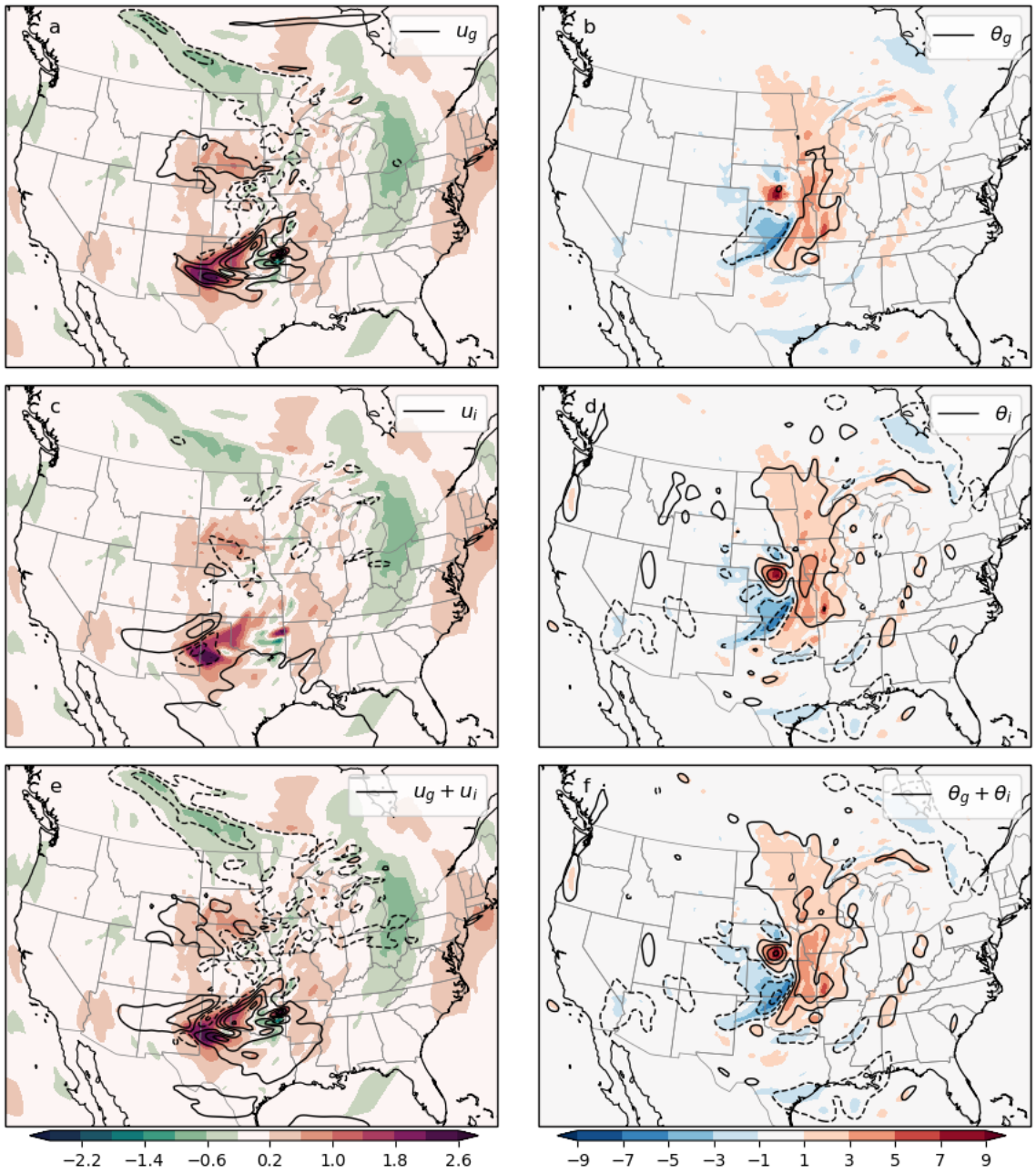

FIGURE 3.14: 500 hPa sensitivity to zonal wind from WRF-adjoint (interval 0.4 $Pa \cdot s \cdot m^{-1}$, shaded) at 0800 UTC 10 November (F14) in all panels, black contours show a) the geostrophically balanced sensitivity to zonal wind $\hat{u}_g$, b) the unbalanced component of sensitivity to zonal wind $\hat{u}_i$, and c) the addition of balanced and unbalanced components, all with an interval of 0.4 $Pa \cdot s \cdot m^{-1}$. 500 hPa sensitivity to potential temperature from WRF-adjoint (interval 2 $Pa \cdot K^{-1}$, shaded) at 0800 UTC 10 November (F14) in all panels, black contours show a) the geostrophically balanced sensitivity to potential temperature $\hat{\theta}_g$, b) the unbalanced component of sensitivity to potential temperature $\hat{\theta}_i$, and c) the addition of balanced and unbalanced components, all with an interval of 2 $Pa \cdot K^{-1}$.

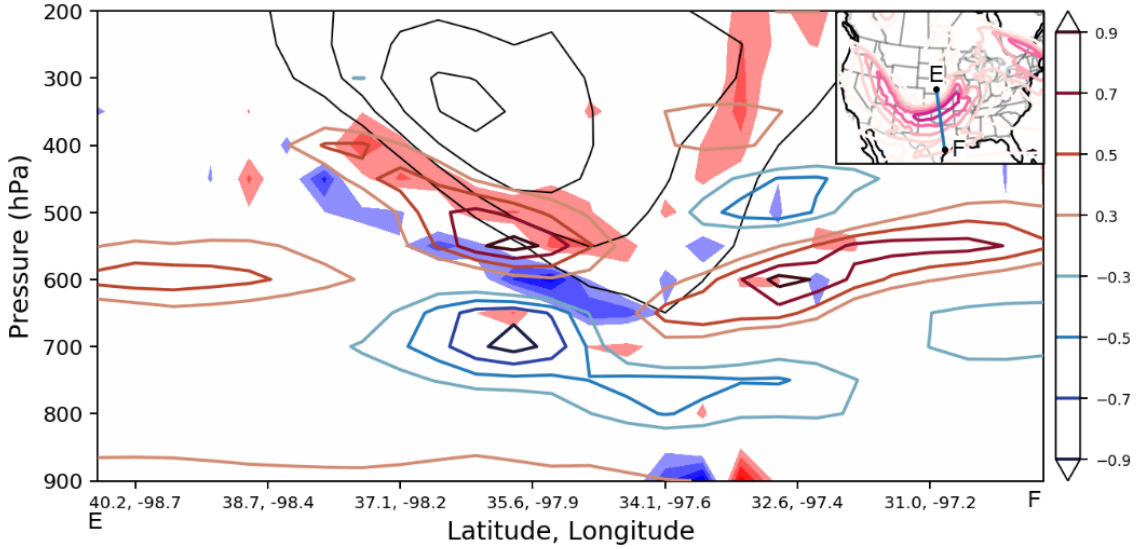

FIGURE 3.15: Cross section of jet core (black contour; 10 m/s interval), normalized $\hat{w}$ (shaded) from WRF-adjoint output and normalized $\hat{\omega}$ (contour) recovered from time tendency of $\hat{a}$ across the 400 hPa jet at forecast time F14 valid 0800 UTC 10 November 1998. Inset plot depicts the cross-section location.

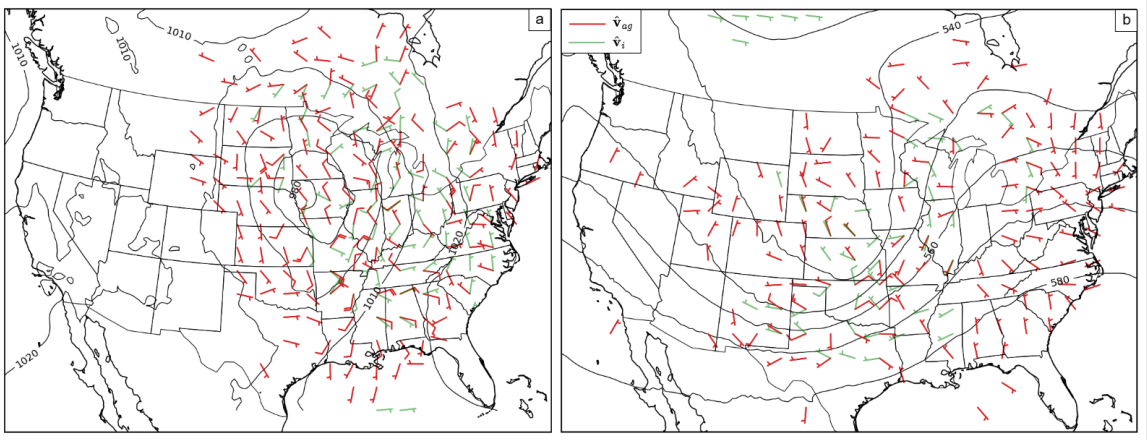

FIGURE 3.16: Qualitative sensitivity to ageostrophic wind (red barbs) and sensitivity to unbalanced wind (green barbs) valid at F14 valid 0800 UTC 10 November 1998 at a) 900 hPa with sea level pressure (contour; 5 hPa interval) and b) 500 hPa with geopotential height (contour; 4 dam interval).

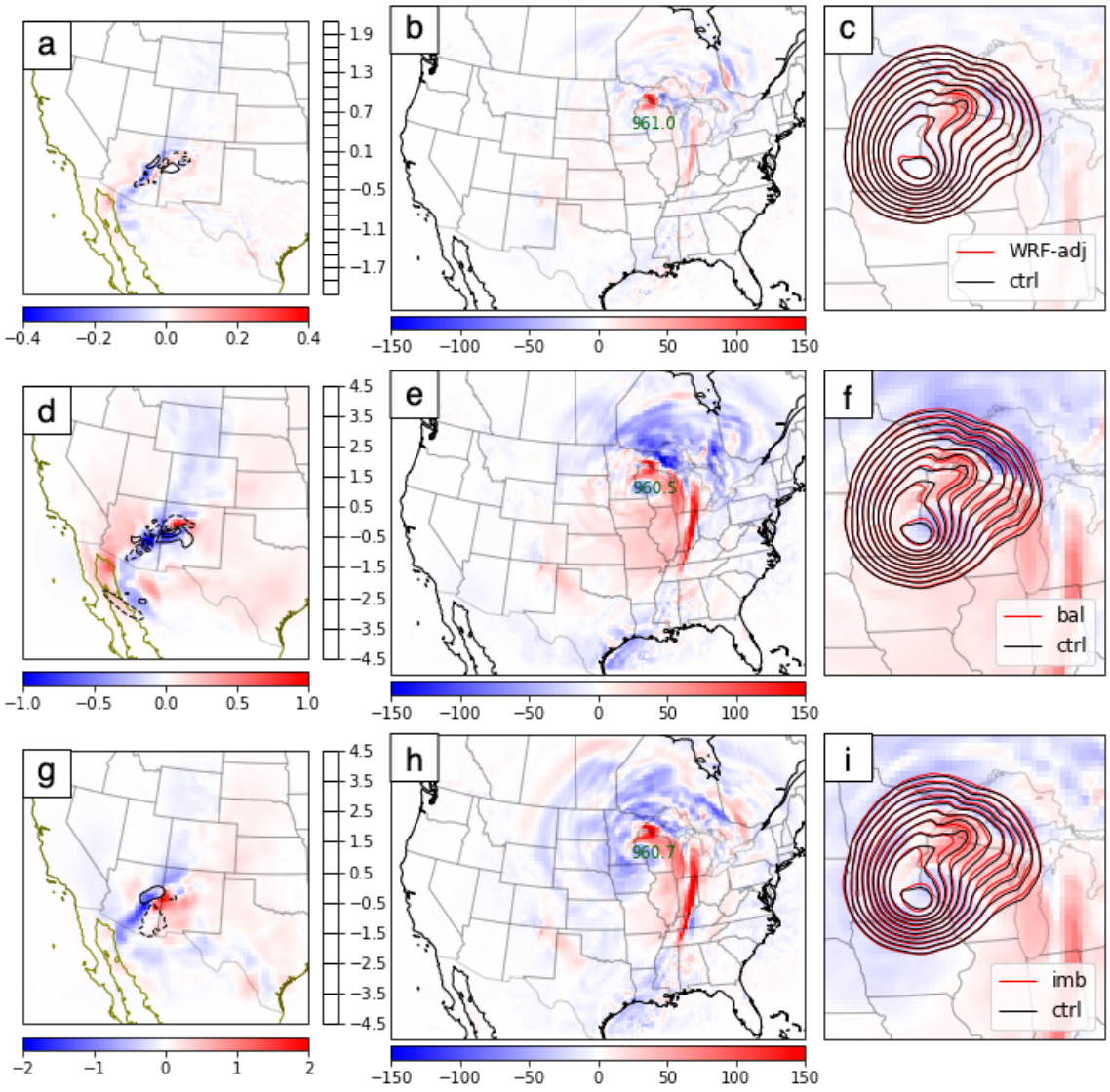

FIGURE 3.17: First column shows the adjoint informed initial optimal perturbation structure of zonal wind (black contour) and temperature (color shading, warm in red and cold in blue, magnitude relative to each color bar) at 500 hPa for the experiment a) "exp WRF-adj", d) "exp bal", g) "exp imb" at forecast hour F00 1800 UTC 09 November. The second column shows the difference in mean sea level pressure between the perturbed experiments and the unperturbed control experiment in color shading for b) "exp WRF-adj", e) "exp bal", h) "exp imb". The minimum sea level pressure for each case is labeled on the plot. The third column zooms in on the second column near the storm center and adds sea level pressure contours from the control experiment in black and from each perturbed case in red.

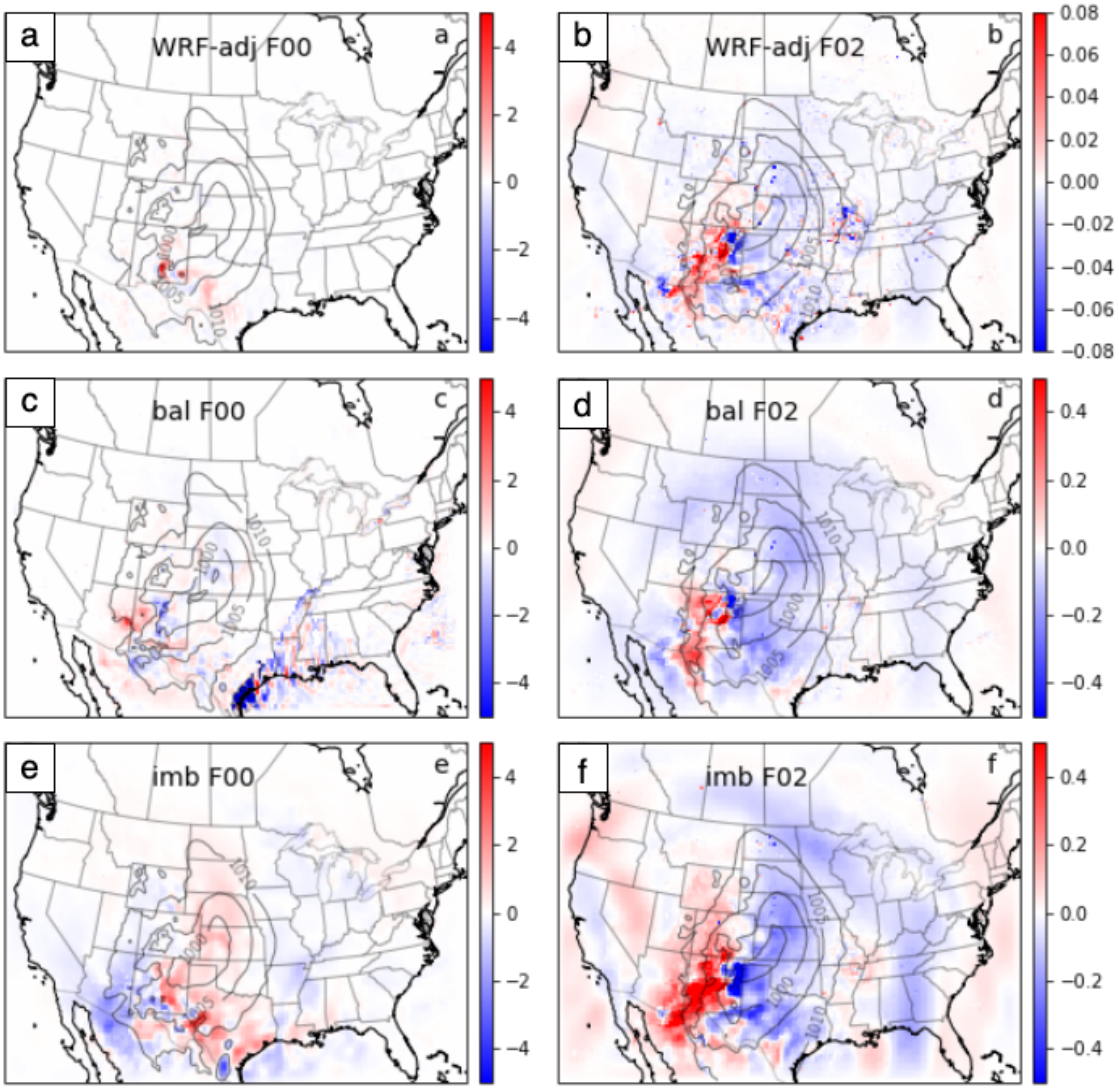

FIGURE 3.18: mean sea level pressure difference (shaded, red if pert>ctrl, blue if pert<ctrl) between the unperturbed control experiment and the optimal perturbed experiment informed by "exp WRF-adj" (a,b), "exp bal" (c,d), and "exp imb" (e,f) at the initial time F00 (left column) and forecast hour F02 (right column). mean sea level pressure contour (interval 5hPa; gray contour) to indicate the low-pressure location at both time steps.

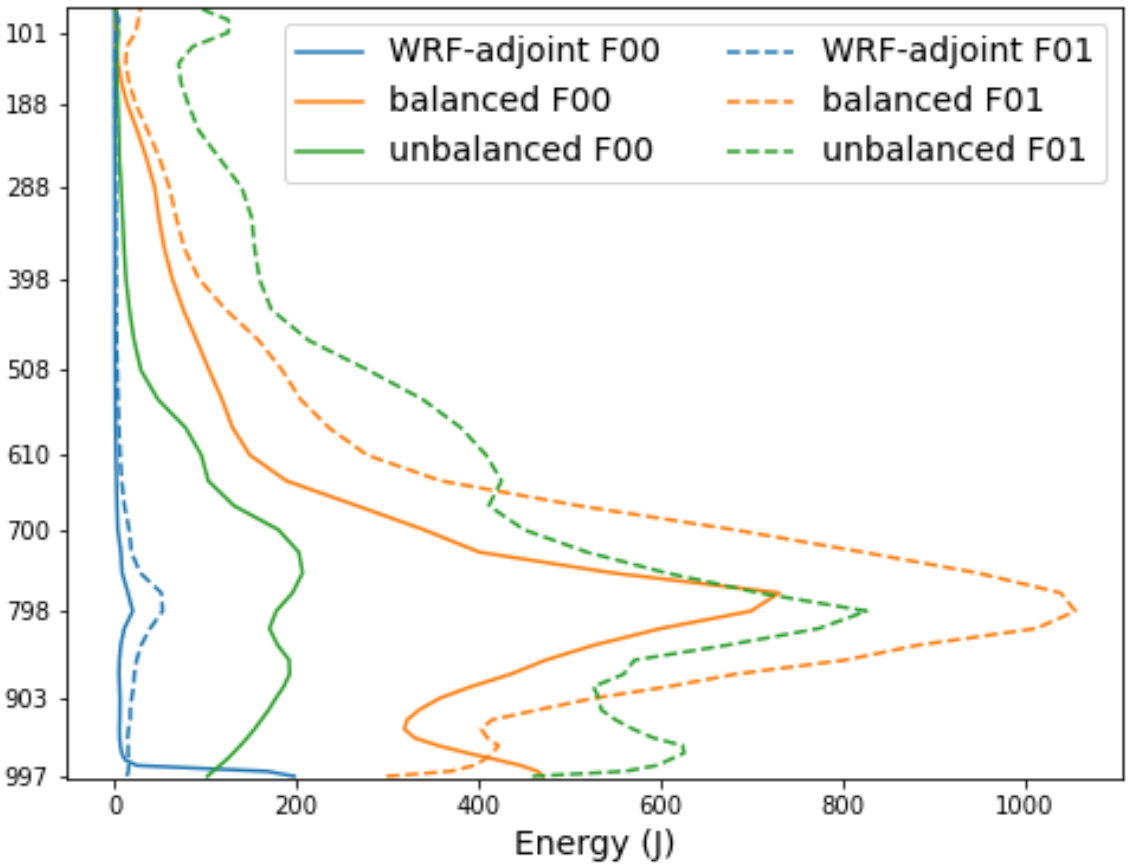

FIGURE 3.19: Perturbation energy norm $\frac{1}{2}\left(u'^2 + v'^2 + \frac{c_p}{T_{ref}}T'^2\right)$ summed over each model level for optimal perturbation informed by WRF-adjoint sensitivity (blue), geostrophically balanced adjoint sensitivity (orange) and unbalanced adjoint sensitivity (green) at initial time F00 (solid line, 1800 UTC 09 November) and forecast hour F01 (dashed line, 1900 UTC 09 November).

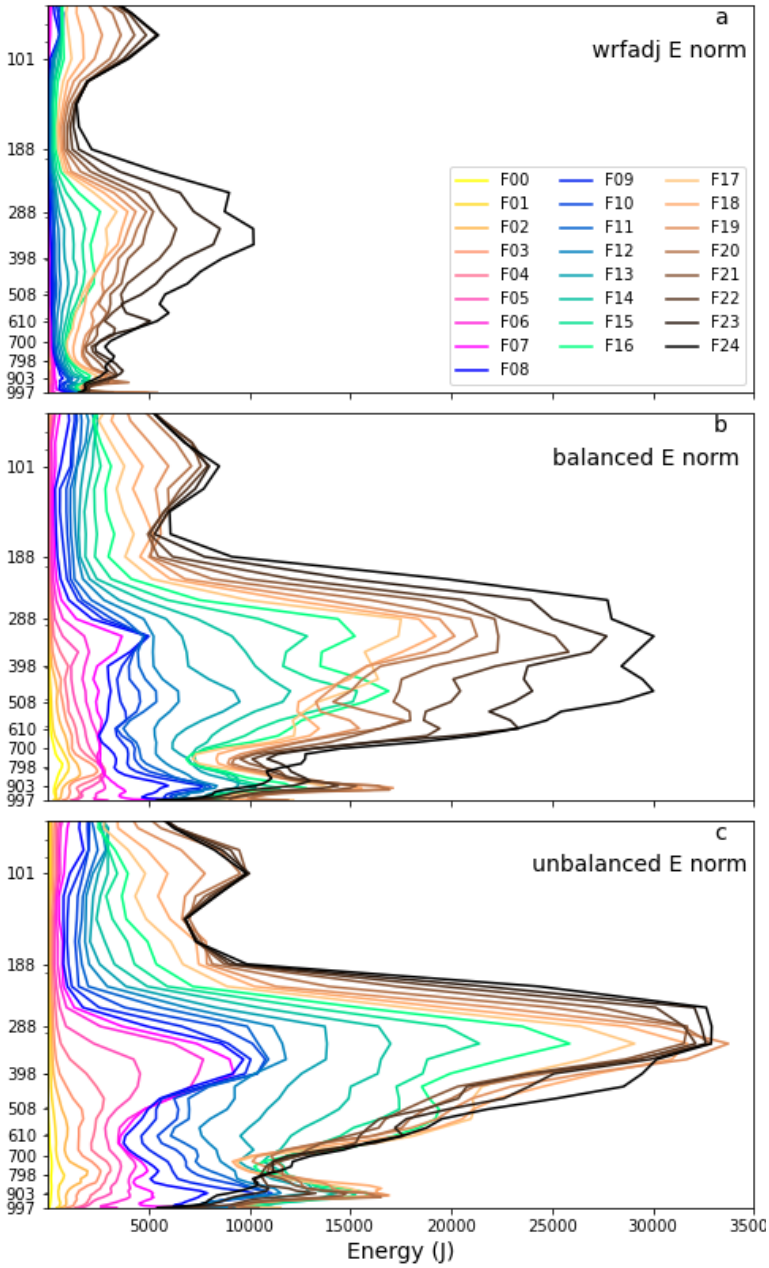

FIGURE 3.20: Same as 3.19 but for all output time steps from forecast hour F00 to F24 for each optimal perturbation experiment a) "WRF-adj", b) "bal", c) "imb". color legends for each time step are shown in panel a.

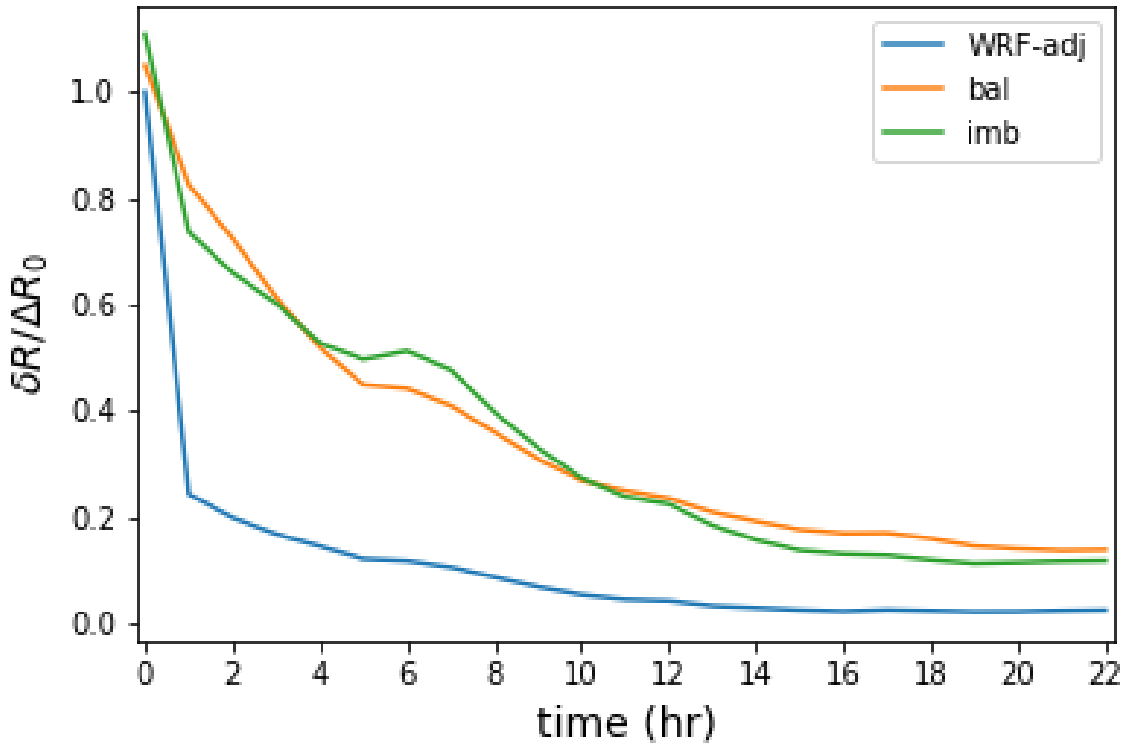

FIGURE 3.21: Time evolution of the ratio of the change in response function ($\delta R = \langle \partial R/\partial \mathbf{x}, \mathbf{x}' \rangle$) to the prescribed change in response function for optimal perturbation informed by WRF-adjoint sensitivity (blue), geostrophically balanced adjoint sensitivity (orange) and unbalanced adjoint sensitivity (green).

Chapter 4

Sensitivity to Ertel PV

4.1 Overview

In the previous chapters, we derived the sensitivity to QGPV and its application with two midlatitude cases and illustrated the values of integrating "PV thinking" in the adjoint sensitivity analysis. However, the Quasi-geostrophic assumption is only valid when the Rossby and Froude numbers are comparable and small. If we wish to apply the "adjoint PV thinking" to the study of tropical cyclones (TCs), where 1) the QG assumption is violated due to larger Rossby numbers at lower latitudes and 2) horizontal wind is no longer balanced by Coriolis force and pressure gradient force, sensitivity to Ertel PV needs to be developed.

Ertel PV, introduced by Hans Ertel in 1942, plays a crucial role in weather forecasting and understanding the dynamics of atmospheric circulation. For a three-dimensional baroclinic compressible flow, Ertel's potential vorticity is defined as $q = \frac{1}{\rho}\eta \cdot \nabla\theta$, where ρ is the flow density, η is the three-dimensional absolute vorticity and θ is the potential temperature and is naturally conserved on the isentropic surfaces if no diabatic heating or friction is introduced. With a specification of independent relation between the wind and temperature field, one could define a boundary value problem from which a "balanced" flow can be recovered given the distribution of Ertel PV (e.g. Hoskins et al. 1985; Davis and Emanuel 1991; Wu 1993).

Based on the definition of PV and the balance constraint, Arbogast (1998) derived a general formulation of adjoint sensitivity to PV. He further demonstrated the method by deriving the sensitivity to Ertel PV under thermal wind balance (geostrophic balance) for two-dimensional steady flow. To extend the utility of this method, so far, we have applied it to obtain adjoint sensitivity to QGPV under the geostrophic balance for three-dimensional flow in Chapter 2. In this chapter, we will choose the combination of Ertel PV and the nonlinear balance constraint and try to calculate adjoint sensitivity to Ertel PV using WRF-adjoint model output.

4.2 Derivation of Sensitivity to Ertel Potential Vorticity

4.2.1 Arbogast 1998 Review

The core concept underlying the general adjoint sensitivity to Ertel PV derivation in Arbogast (1998) has already been presented in Chapter 2 section 2.2.5. It is stated again for clarity.

We start with the general expression for potential vorticity perturbation and any balance equation as functions of perturbation streamfunction Ψ' and perturbation geopotential Φ'.

$$\begin{cases} q' = L(\Psi', \Phi') \\ a' = B(\Psi', \Phi') \end{cases}$$

where we denote L as the linear operator that calculates PV and B as the balance operator. This relationship can be expressed in matrix form:

$$\begin{pmatrix} L_\Psi & L_\Phi \\ B_\Psi & B_\Phi \end{pmatrix} \begin{pmatrix} \Psi' \\ \Phi' \end{pmatrix} = \begin{pmatrix} q' \\ a' \end{pmatrix} \tag{4.1}$$

where q' stands for the PV perturbation, and a' stands for the imbalance. If we denote $\left(\frac{\partial R}{\partial q}, \frac{\partial R}{\partial a}\right) = (\hat{q}, \hat{a})$ and take the adjoint of (4.1), we will get:

$$\begin{pmatrix} L_\Psi^* & B_\Psi^* \\ L_\Phi^* & B_\Phi^* \end{pmatrix} \begin{pmatrix} \hat{q} \\ \hat{a} \end{pmatrix} = \begin{pmatrix} \hat{\Psi} \\ \hat{\Phi} \end{pmatrix} \tag{4.2}$$

As stated in Chapter 2, the superscript $*$ denotes the adjoint of an operator. When a homogeneous boundary condition is applied, the adjoint of an operator is the same as the transpose of this operator, $L^* = L^T$.

We can left multiply both sides of the above matrix equation by $\begin{pmatrix} B_\Phi^* & -B_\Psi^* \\ L_\Phi^* & -L_\Psi^* \end{pmatrix}$ to eliminate one operator in each equation:

$$\begin{pmatrix} B_\Phi^* L_\Psi^* - B_\Psi^* L_\Phi^* & B_\Phi^* B_\Psi^* - B_\Psi^* B_\Phi^* \\ L_\Phi^* L_\Psi^* - L_\Psi^* L_\Phi^* & L_\Phi^* B_\Psi^* - L_\Psi^* B_\Phi^* \end{pmatrix} \begin{pmatrix} \hat{q} \\ \hat{a} \end{pmatrix} = \begin{pmatrix} B_\Phi^* \hat{\Psi} - B_\Psi^* \hat{\Phi} \\ L_\Phi^* \hat{\Psi} - L_\Psi^* \hat{\Phi} \end{pmatrix} \tag{4.3}$$

If $B_\Phi^* B_\Psi^*$ and $B_\Psi^* B_\Phi^*$ are commutable and $L_\Phi^* L_\Psi^*$ and $L_\Psi^* L_\Phi^*$ are commutable, then (4.3) reduces to

$$\begin{pmatrix} B_\Phi^* L_\Psi^* - B_\Psi^* L_\Phi^* & 0 \\ 0 & L_\Phi^* B_\Psi^* - L_\Psi^* B_\Phi^* \end{pmatrix} \begin{pmatrix} \hat{q} \\ \hat{a} \end{pmatrix} = \begin{pmatrix} B_\Phi^* \hat{\Psi} - B_\Psi^* \hat{\Phi} \\ L_\Phi^* \hat{\Psi} - L_\Psi^* \hat{\Phi} \end{pmatrix} \tag{4.4}$$

Alternatively, presented as a set of equations:

$$\begin{cases} (B^*_\Phi L^*_\Psi - B^*_\Psi L^*_\Phi)\hat{q} = B^*_\Phi \hat{\Psi} - B^*_\Psi \hat{\Phi} & \text{(4.5a)} \\ (L^*_\Phi B^*_\Psi - L^*_\Psi B^*_\Phi)\hat{a} = L^*_\Phi \hat{\Psi} - L^*_\Psi \hat{\Phi} & \text{(4.5b)} \end{cases}$$

These are the general form of the expressions that need to be solved to either obtain the sensitivity to PV or the sensitivity to imbalance. If we use subscripts P for PV and B for balance, and denote the operators in (4.4) as:

$$\begin{cases} \varphi_P = B^*_\Phi L^*_\Psi - B^*_\Psi L^*_\Phi & \text{(4.6a)} \\ \varphi_B = L^*_\Phi B^*_\Psi - L^*_\Psi B^*_\Phi & \text{(4.6b)} \\ U_P = B^*_\Phi \hat{\Psi} - B^*_\Psi \hat{\Phi} & \text{(4.6c)} \\ U_B = L^*_\Phi \hat{\Psi} - L^*_\Psi \hat{\Phi} & \text{(4.6d)} \end{cases}$$

(4.5) can be shorthanded into:

$$\begin{cases} \varphi_P \hat{q} = U_P & \text{(4.7a)} \\ \varphi_B \hat{a} = U_B & \text{(4.7b)} \end{cases}$$

To solve (4.7a) and get the sensitivity to PV, we could use the successive over-relaxation method. One could also find the sensitivity to PV by minimizing the L2 norm of the formulated cost function, $J = \frac{1}{2}\langle \varphi_P \hat{q} - U_P, \varphi_P \hat{q} - U_P \rangle$.

4.2.2 Derivation of Sensitivity to Ertel PV Operators

In this section, we will specify the definition of Ertel PV and nonlinear balance as functions of streamfunction and geopotential to find the expression for operators $L_\Phi, L_\Psi, B_\Phi, B_\Psi$.

In Davis and Emanuel (1991), their nonlinear balance equation in spherical coordinates is formulated as follows:

$$\nabla^2\Phi = \nabla\cdot(f\nabla\Psi) + \frac{2}{a^4\cos^2\phi}\frac{\partial\left(\frac{\partial\Psi}{\partial\lambda},\frac{\partial\Psi}{\partial\phi}\right)}{\partial(\lambda,\phi)} \tag{4.8}$$

where λ is longitude, ϕ is latitude, and a is the earth radius. We can convert (4.8) into Cartesian coordinate by noting the relations: $\frac{\partial}{\partial\lambda} = \frac{1}{a\cos\phi}\frac{\partial}{\partial x}$ and $\frac{\partial}{\partial\phi} = \frac{1}{a}\frac{\partial}{\partial y}$[1]

$$\nabla\cdot(f\nabla\Psi) + 2\frac{\partial(\Psi_x,\Psi_y)}{\partial(x,y)} - \nabla^2\Phi = 0 \tag{4.9}$$

$$\nabla\cdot(f\nabla\Psi) + 2\left[\Psi_{xx}\Psi_{yy} - \Psi_{xy}^2\right] - \nabla^2\Phi = 0 \tag{4.10}$$

Before linearizing the whole nonlinear balance equation, we first linearize the Jacobian:

$$J(\Psi_x,\Psi_y)' = \bar{\Psi}_{xx}\Psi'_{yy} + \Psi'_{xx}\bar{\Psi}_{yy} - 2\bar{\Psi}_{xy}\Psi'_{xy}$$

Thus the linearized nonlinear balance equation and the operators B_Φ and B_Ψ are found:

$$\nabla\cdot(f\nabla)\Psi' + 2\left(\bar{\Psi}_{xx}\partial_{yy} + \bar{\Psi}_{yy}\partial_{xx} - 2\bar{\Psi}_{xy}\partial_{xy}\right)\Psi' - \nabla^2\Phi' = 0 \tag{4.11}$$

[1]Subscripts x, y, π denote taking the partial derivative of the variable to x, y, or π and are used interchangeably with $\partial/\partial x$, $\partial/\partial y$, $\partial/\partial\pi$

$$B_\Phi = -\nabla^2$$

$$B_\Psi = \nabla \cdot (f\nabla) + 2\bar{\Psi}_{xx}\partial_{yy} + 2\bar{\Psi}_{yy}\partial_{xx} - 4\bar{\Psi}_{xy}\partial_{xy}$$

We should note that the basic states $\bar{\Psi}$ and $\bar{\Phi}$ in (4.11) should be a set of solutions that satisfy the nonlinear balance equation (4.10) for the purpose of derivation. Practically, it is unclear whether using the time-averaged streamfunction and geopotential directly from the model output leads to failure in Ertel PV inversion or calculating sensitivity to Ertel PV.

Davis and Emanuel (1991) expressed Ertel PV, q, as a function of Ψ and Φ in spherical coordinates:

$$q = \frac{g\kappa\pi}{p}\left[(f + \nabla^2\Psi)\frac{\partial^2\Phi}{\partial\pi^2} - \frac{1}{a^2\cos^2\phi}\frac{\partial^2\Psi}{\partial\lambda\partial\pi}\frac{\partial^2\Phi}{\partial\lambda\partial\pi} - \frac{1}{a^2}\frac{\partial^2\Psi}{\partial\phi\partial\pi}\frac{\partial^2\Phi}{\partial\phi\partial\pi}\right] \tag{4.12}$$

where g is the gravity acceleration, $\kappa = R_d/C_p$ is the ratio of dry air gas constant to the dry air specific heat at constant pressure, p_0 is the surface pressure, and p is the pressure at each vertical level, $\pi = C_p(\frac{p}{p_0})^\kappa$ is the Exner coordinate in the vertical direction. Let $A = \frac{g\kappa\pi}{p}$ and convert (4.12) into the Cartesian coordinate:

$$\frac{q}{A} = \left[(f + \nabla^2\Psi)\frac{\partial^2\Phi}{\partial\pi^2} - \frac{\partial^2\Psi}{\partial x\partial\pi}\frac{\partial^2\Phi}{\partial x\partial\pi} - \frac{\partial^2\Psi}{\partial y\partial\pi}\frac{\partial^2\Phi}{\partial y\partial\pi}\right] \tag{4.13}$$

By linearizing the equation above, we can identify the operators L_Φ and L_Ψ:

$$\frac{q'}{A} = (f + \nabla^2\bar{\Psi})\frac{\partial^2}{\partial\pi^2}\Phi' + \frac{\partial^2\bar{\Phi}}{\partial\pi^2}\nabla^2\Psi' - [\bar{\Psi}_{x\pi}\Phi'_{x\pi} + \bar{\Phi}_{x\pi}\Psi'_{x\pi}] - [\bar{\Psi}_{y\pi}\Phi'_{y\pi} + \bar{\Phi}_{y\pi}\Psi'_{y\pi}] \quad (4.14)$$

$$L_\Phi = A[(f + \nabla^2\bar{\Psi})\frac{\partial^2}{\partial\pi^2} - \bar{\Psi}_{x\pi}\partial_{x\pi} - \bar{\Psi}_{y\pi}\partial_{y\pi}]$$
$$L_\Psi = A[\frac{\partial^2\bar{\Phi}}{\partial\pi^2}\nabla^2 - \bar{\Phi}_{x\pi}\partial_{x\pi} - \bar{\Phi}_{y\pi}\partial_{y\pi}]$$

Notice all terms within L_Φ, L_Ψ, B_Φ, and B_Ψ are second-order derivatives. As a result, these operators are all self-adjoint:

$$\begin{cases} L_\Phi = L_\Phi^* = A[(f + \nabla^2\bar{\Psi})\dfrac{\partial^2}{\partial\pi^2} - \bar{\Psi}_{x\pi}\partial_{x\pi} - \bar{\Psi}_{y\pi}\partial_{y\pi}] & (4.15a) \\ L_\Psi = L_\Psi^* = A[\dfrac{\partial^2\bar{\Phi}}{\partial\pi^2}\nabla^2 - \bar{\Phi}_{x\pi}\partial_{x\pi} - \bar{\Phi}_{y\pi}\partial_{y\pi}] & (4.15b) \\ B_\Phi = B_\Phi^* = -\nabla^2 & (4.15c) \\ B_\Psi = B_\Psi^* = \nabla\cdot(f\nabla) + 2\bar{\Psi}_{xx}\partial_{yy} + 2\bar{\Psi}_{yy}\partial_{xx} - 4\bar{\Psi}_{xy}\partial_{xy} & (4.15d) \end{cases}$$

Now we can plug (4.15) back into (4.6) to obtain all the operators required for the derivation of sensitivity to Ertel PV and to nonlinear imbalance:

$$\begin{aligned} \varphi_P = &- \nabla^2\left(A[\frac{\partial^2\bar{\Phi}}{\partial\pi^2}\nabla^2 - \bar{\Phi}_{x\pi}\partial_{x\pi} - \bar{\Phi}_{y\pi}\partial_{y\pi}]\right) \quad (4.16) \\ &- \left(\nabla\cdot(f\nabla) + 2\bar{\Psi}_{xx}\partial_{yy} + 2\bar{\Psi}_{yy}\partial_{xx} - 4\bar{\Psi}_{xy}\partial_{xy}\right)\left(A[(f + \nabla^2\bar{\Psi})\frac{\partial^2}{\partial\pi^2} - \bar{\Psi}_{x\pi}\partial_{x\pi} - \bar{\Psi}_{y\pi}\partial_{y\pi}]\right) \end{aligned}$$

$$\varphi_B = \left(A[(f + \nabla^2\bar{\Psi})\frac{\partial^2}{\partial\pi^2} - \bar{\Psi}_{x\pi}\partial_{x\pi} - \bar{\Psi}_{y\pi}\partial_{y\pi}] \right) \left(\nabla\cdot(f\nabla) + 2\bar{\Psi}_{xx}\partial_{yy} + 2\bar{\Psi}_{yy}\partial_{xx} - 4\bar{\Psi}_{xy}\partial_{xy} \right) \tag{4.17}$$

$$- \left(A[\frac{\partial^2\bar{\Phi}}{\partial\pi^2}\nabla^2 - \bar{\Phi}_{x\pi}\partial_{x\pi} - \bar{\Phi}_{y\pi}\partial_{y\pi}] \right) \left(-\nabla^2 \right)$$

$$U_P = -\nabla^2\hat{\Psi} - \left(\nabla\cdot(f\nabla) + 2\bar{\Psi}_{xx}\partial_{yy} + 2\bar{\Psi}_{yy}\partial_{xx} - 4\bar{\Psi}_{xy}\partial_{xy} \right) \hat{\Phi} \tag{4.18}$$

$$U_B = \left(A[(f + \nabla^2\bar{\Psi})\frac{\partial^2}{\partial\pi^2} - \bar{\Psi}_{x\pi}\partial_{x\pi} - \bar{\Psi}_{y\pi}\partial_{y\pi}] \right) \hat{\Psi} - \left(A[\frac{\partial^2\bar{\Phi}}{\partial\pi^2}\nabla^2 - \bar{\Phi}_{x\pi}\partial_{x\pi} - \bar{\Phi}_{y\pi}\partial_{y\pi}] \right) \hat{\Phi} \tag{4.19}$$

The sensitivity to Ertel PV can be obtained by substituting (4.16) and (4.18) into (4.7a). Since both (4.16) and (4.18) contain the coefficient A, we can divide both sides of (4.7a) by A:

$$\frac{1}{A}\varphi_P\hat{q} = \frac{1}{A}U_P \tag{4.20}$$

We expand $\frac{1}{A}U_P$ and $\frac{1}{A}\varphi_P$ to show each term used in the code[2] explicitly:

$$U_P/A = \frac{1}{A}\left(-\nabla^2\hat{\Psi} - \nabla\cdot(f\nabla)\hat{\Phi} - 2\bar{\Psi}_{xx}\partial_{yy}\hat{\Phi} - 2\bar{\Psi}_{yy}\partial_{xx}\hat{\Phi} + 4\bar{\Psi}_{xy}\partial_{xy}\hat{\Phi} \right) \tag{4.21}$$

[2]Code available at https://github.com/Nuo-Chen/sensitivity-to-ertel-PV

$$\varphi_P/A = -\nabla^2\bar{\Phi}_{\pi^2}\nabla^2 - \bar{\Phi}_{\pi^2}\nabla^4 + \nabla^2\bar{\Phi}_{x\pi}\partial_{x\pi} + \bar{\Phi}_{x\pi}\nabla^2\partial_{x\pi} + \nabla^2\bar{\Phi}_{y\pi}\partial_{y\pi} + \bar{\Phi}_{y\pi}\nabla^2\partial_{y\pi}$$

(4.22)

$$\begin{aligned}
&- \Big\{ f_x\bar{\zeta}_x\partial_{\pi^2} + f_x\bar{\zeta}\partial_{x\pi^2} + f_y\bar{\zeta}_y\partial_{\pi^2} + f_y\bar{\zeta}\partial_{y\pi^2} + f\nabla^2\bar{\zeta}\partial_{\pi^2} + f\bar{\zeta}\nabla^2\partial_{\pi^2} \\
&- f_x\partial_x\bar{\Psi}_{x\pi}\partial_{x\pi} - f_x\bar{\Psi}_{x\pi}\partial_{x^2\pi} - f_y\partial_y\bar{\Psi}_{x\pi}\partial_{x\pi} - f_y\bar{\Psi}_{x\pi}\partial_{xy\pi} - f\nabla^2\bar{\Psi}_{x\pi}\partial_{x\pi} - f\bar{\Psi}_{x\pi}\nabla^2\partial_{x\pi} \\
&- f_x\partial_x\bar{\Psi}_{y\pi}\partial_{y\pi} - f_x\bar{\Psi}_{y\pi}\partial_{xy\pi} - f_y\partial_y\bar{\Psi}_{y\pi}\partial_{y\pi} - f_y\bar{\Psi}_{y\pi}\partial_{y^2\pi} - f\nabla^2\bar{\Psi}_{y\pi}\partial_{y\pi} - f\bar{\Psi}_{y\pi}\nabla^2\partial_{y\pi} \\
&+ 2\bar{\Psi}_{xx}\left[\bar{\zeta}_{yy}\partial_{\pi^2} + \bar{\zeta}\partial_{y^2\pi^2} - \partial_{yy}\bar{\Psi}_{x\pi}\partial_{x\pi} - \bar{\Psi}_{x\pi}\partial_{xy^2\pi} - \partial_{yy}\bar{\Psi}_{y\pi}\partial_{y\pi} - \bar{\Psi}_{y\pi}\partial_{y^3\pi}\right] \\
&+ 2\bar{\Psi}_{yy}\left[\bar{\zeta}_{xx}\partial_{\pi^2} + \bar{\zeta}\partial_{x^2\pi^2} - \partial_{xx}\bar{\Psi}_{x\pi}\partial_{x\pi} - \bar{\Psi}_{x\pi}\partial_{x^3\pi} - \partial_{xx}\bar{\Psi}_{y\pi}\partial_{y\pi} - \bar{\Psi}_{y\pi}\partial_{x^2y\pi}\right] \\
&- 4\bar{\Psi}_{xy}\left[\bar{\zeta}_{xy}\partial_{\pi^2} + \bar{\zeta}\partial_{xy\pi^2} - \partial_{xy}\bar{\Psi}_{x\pi}\partial_{x\pi} - \bar{\Psi}_{x\pi}\partial_{x^2y\pi} - \partial_{xy}\bar{\Psi}_{y\pi}\partial_{y\pi} - \bar{\Psi}_{y\pi}\partial_{xy^2\pi}\right] \Big\}
\end{aligned}$$

where $\bar{\zeta}$ denotes the trajectory absolute vorticity $f + \nabla^2\bar{\Psi}$. Since the WRF model is configured to use the Lambert Conformal Conic projection which introduces a map factor to each grid point, the gradient of the Coriolis parameter in the x-axis, f_x, becomes nonzero and can not be ignored like under the latitude-longitude coordinate system.

Each term in (4.22) is a product of a constant and an operator that apply on sensitivity to PV, $\hat{q}$. $\hat{\Psi}$ in (4.21) can be obtained from the WRF adjoint model output following (2.17). $\hat{\Phi}$ in (4.21) is in Exner coordinate and can be calculated by taking the adjoint of

the definition of perturbation potential temperature θ' in the Exner coordinate:

$$\theta' = -\frac{\partial \Phi'}{\partial \pi} \tag{4.23}$$

$$\hat{\Phi} = \frac{\partial \hat{\theta}}{\partial \pi} \tag{4.24}$$

4.2.3 Recover Sensitivity to Nonlinear-Balanced Wind and Temperature from Sensitivity to Ertel PV

Once the formulation for sensitivity to Ertel PV is attained, the next step is to recover the sensitivities to winds and to potential temperature. This inversion process opens up two possible applications for the nonlinear-balanced adjoint state 1) to remove of high-frequency wave structure in the adjoint fields and 2) to serve as the "final" adjoint forcing that drives the adjoint model to integrate backward. These two applications have been partially achieved with sensitivity to QGPV and the geostrophically balanced adjoint state shown in Chapter 2 and Chapter 3.

In Chapter 3, we derived a general approach to compute sensitivities to horizontal wind and to temperature. In section 3.4.1 it is shown that $\hat{\mathbf{v}}$ can be recovered from a known $\hat{\Psi}$ field (3.6a) and $\hat{\theta}$ can be recovered from a known $\hat{\Phi}$. Therefore, to recover the nonlinear-balanced sensitivity to wind $\hat{\mathbf{v}}_E$ and to potential temperature $\hat{\theta}_E$ from sensitivity to Ertel PV, $\hat{q}_E$, our first step is to determine the nonlinear-balanced sensitivity to streamfunction

$\hat{\Psi}_E$ and to geopotential $\hat{\Phi}_E$[3]. Note (4.13) can be expressed as:

$$q' = L_\Psi \Psi' + L_\Phi \Phi' \tag{4.25}$$

Taking the adjoint of (4.25) and substituting in (4.15b) and (4.15a), we can get the sensitivity to streamfunction and to geopotential that follows the nonlinear balance constraint:

$$\hat{\Psi}_E = L_\Psi^* \hat{q}_E = A\left(\bar{\Phi}_{\pi\pi}\nabla^2 - \bar{\Phi}_{x\pi}\partial_{x\pi} - \bar{\Phi}_{y\pi}\partial_{y\pi}\right)\hat{q}_E \tag{4.26}$$

$$\hat{\Phi}_E = L_\Phi^* \hat{q}_E = A\left(\bar{\zeta}\frac{\partial^2}{\partial\pi^2} - \bar{\Psi}_{x\pi}\partial_{x\pi} - \bar{\Psi}_{y\pi}\partial_{y\pi}\right)\hat{q}_E \tag{4.27}$$

Substitute (4.26) into $\hat{u} = \frac{\partial\nabla^{-2}\hat{\psi}}{\partial y}$ and $\hat{v} = -\frac{\partial\nabla^{-2}\hat{\psi}}{\partial x}$ (e.g. (3.6a)), the sensitivity to nonlinear-balanced horizontal winds are:

$$\hat{u}_E = \frac{\partial\nabla^{-2}(A[\bar{\Phi}_{\pi\pi}\nabla^2 - \bar{\Phi}_{x\pi}\partial_{x\pi} - \bar{\Phi}_{y\pi}\partial_{y\pi}]\hat{q}_E)}{\partial y}$$
$$\hat{v}_E = -\frac{\partial\nabla^{-2}(A[\bar{\Phi}_{\pi\pi}\nabla^2 - \bar{\Phi}_{x\pi}\partial_{x\pi} - \bar{\Phi}_{y\pi}\partial_{y\pi}]\hat{q}_E)}{\partial x}$$

To find the sensitivity to nonlinear-balanced temperature $\hat{\theta}_E$, we can substitute Φ' with θ' in the geopotential contribution to Ertel PV perturbation in (4.25) using (4.23):

$$q' = A\left((f+\nabla^2\bar{\Psi})\frac{\partial^2}{\partial\pi^2} - \bar{\Psi}_{x\pi}\partial_{x\pi} - \bar{\Psi}_{y\pi}\partial_{y\pi}\right)\Phi'$$
$$= -A\left((f+\nabla^2\bar{\Psi})\frac{\partial}{\partial\pi} - \bar{\Psi}_{x\pi}\partial_x - \bar{\Psi}_{y\pi}\partial_y\right)\theta'$$

[3]From now on, the subscript E denotes sensitivity variables that are related to Ertel PV or nonlinear balance.

Taking the adjoint of the above equation yields the nonlinear-balanced potential temperature $\hat{\theta}_E$:

$$\hat{\theta}_E = A\left(\bar{\zeta}\frac{\partial}{\partial\pi} - \bar{\Psi}_{x\pi}\partial_x - \bar{\Psi}_{y\pi}\partial_y\right)\hat{q}_E$$

To summarize, nonlinear-balanced sensitivities to wind and to potential temperature can be recovered from the sensitivity to Ertel PV as follows:

$$\begin{cases} \hat{u}_E = \dfrac{\partial\nabla^{-2}(A[\bar{\Phi}_{\pi\pi}\nabla^2 - \bar{\Phi}_{x\pi}\partial_{x\pi} - \bar{\Phi}_{y\pi}\partial_{y\pi}]\hat{q}_E)}{\partial y} & \text{(4.28a)} \\ \hat{v}_E = -\dfrac{\partial\nabla^{-2}(A[\bar{\Phi}_{\pi\pi}\nabla^2 - \bar{\Phi}_{x\pi}\partial_{x\pi} - \bar{\Phi}_{y\pi}\partial_{y\pi}]\hat{q}_E)}{\partial x} & \text{(4.28b)} \\ \hat{\theta}_E = A\left(\bar{\zeta}\dfrac{\partial}{\partial\pi} - \bar{\Psi}_{x\pi}\partial_x - \bar{\Psi}_{y\pi}\partial_y\right)\hat{q}_E & \text{(4.28c)} \end{cases}$$

4.2.4 Derivation of Sensitivities to Nonlinear-Imbalance Operators

Unlike the comprehensive discussion regarding the sensitivity to the geostrophic imbalance in Chapter 3, this dissertation refrains from delving into applications or interpretations of the sensitivity to the nonlinear imbalance in this dissertation. The implementation of the derivation below is deferred to future research.

To solve $\varphi_B \hat{a} = U_B$ (e.g. (4.7b)), we notice both (4.17) and (4.19) contain the coefficient A. We expand all the terms in (4.17):

$$\varphi_B/A = \left((f+\nabla^2\bar{\Psi})\frac{\partial^2}{\partial\pi^2} - \bar{\Psi}_{x\pi}\partial_{x\pi} - \bar{\Psi}_{y\pi}\partial_{y\pi}\right)\left(\nabla\cdot(f\nabla) + 2\bar{\Psi}_{xx}\partial_{yy} + 2\bar{\Psi}_{yy}\partial_{xx} - 4\bar{\Psi}_{xy}\partial_{xy}\right)$$
$$- \left(\frac{\partial^2\bar{\Phi}}{\partial\pi^2}\nabla^2 - \bar{\Phi}_{x\pi}\partial_{x\pi} - \bar{\Phi}_{y\pi}\partial_{y\pi}\right)\left(-\nabla^2\right)$$

$$= (\bar{\zeta}f\partial_{\pi\pi}\nabla^2 - \bar{\zeta}f_x\partial_{\pi\pi}\partial_x - \bar{\zeta}f_y\partial_{\pi\pi}\partial_y + 2\bar{\zeta}\bar{\Psi}_{xx\pi\pi}\partial_{yy} + 2\bar{\zeta}\bar{\Psi}_{xx}\partial_{\pi\pi}\partial_{yy}$$
$$+ 2\bar{\zeta}\bar{\Psi}_{yy\pi\pi}\partial_{xx} + 2\bar{\zeta}\bar{\Psi}_{yy}\partial_{\pi\pi}\partial_{xx} - 4\bar{\zeta}\bar{\Psi}_{xy\pi\pi}\partial_{xy} - 4\bar{\zeta}\bar{\Psi}_{xy}\partial_{\pi\pi}\partial_{xy})$$
$$- (\bar{\Psi}_{x\pi}f_{x\pi}\nabla^2 + \bar{\Psi}_{x\pi}f\partial_{x\pi}\nabla^2 - \bar{\Psi}_{x\pi}f_{x^2\pi}\partial_x - \bar{\Psi}_{x\pi}f_x\partial_{x^2\pi} - \bar{\Psi}_{x\pi}f_{xy\pi}\partial_y - \bar{\Psi}_{x\pi}f_y\partial_{xy\pi}$$
$$+ 2\bar{\Psi}_{x\pi}\bar{\Psi}_{x^3\pi}\partial_{yy} + 2\bar{\Psi}_{x\pi}\bar{\Psi}_{xx}\partial_{xy^2\pi} + 2\bar{\Psi}_{x\pi}\bar{\Psi}_{xy^2\pi}\partial_{xx} + 2\bar{\Psi}_{x\pi}\bar{\Psi}_{yy}\partial_{x^3\pi}$$
$$- 4\bar{\Psi}_{x\pi}\bar{\Psi}_{x^2y\pi}\partial_{x\pi} - 4\bar{\Psi}_{xx}\bar{\Psi}_{xy}\partial_{x^2y\pi})$$
$$- (\bar{\Psi}_{y\pi}f_{y\pi}\nabla^2 + \bar{\Psi}_{y\pi}f\partial_{y\pi}\nabla^2 - \bar{\Psi}_{y\pi}f_{xy\pi}\partial_x - \bar{\Psi}_{y\pi}f_x\partial_{xy\pi} - \bar{\Psi}_{y\pi}f_{y^2\pi}\partial y - \bar{\Psi}_{y\pi}f_y\partial_{y^2\pi}$$
$$+ 2\bar{\Psi}_{y\pi}\bar{\Psi}_{x^2y\pi}\partial_{yy} + 2\bar{\Psi}_{y\pi}\bar{\Psi}_{xx}\partial_{y^3\pi} + 2\bar{\Psi}_{y\pi}\bar{\Psi}_{y^3\pi}\partial_{xx} + 2\bar{\Psi}_{y\pi}\bar{\Psi}_{yy}\partial_{x^2y\pi}$$
$$- 4\bar{\Psi}_{y\pi}\bar{\Psi}_{xy^2\pi}\partial_{xy} - 4\bar{\Psi}_{y\pi}\bar{\Psi}_{xy}\partial_{xy^2\pi}) + \left(\bar{\Phi}_{\pi\pi}\nabla^4 - \bar{\phi}_{x\pi}\nabla^2\partial_{x\pi} - \bar{\phi}_{y\pi}\nabla^2\partial_{y\pi}\right)$$

$$U_B/A = \left((f+\nabla^2\bar{\Psi})\frac{\partial^2}{\partial\pi^2} - \bar{\Psi}_{x\pi}\partial_{x\pi} - \bar{\Psi}_{y\pi}\partial_{y\pi}\right)\hat{\Psi} - \left(\frac{\partial^2\bar{\Phi}}{\partial\pi^2}\nabla^2 - \bar{\Phi}_{x\pi}\partial_{x\pi} - \bar{\Phi}_{y\pi}\partial_{y\pi}\right)\hat{\Phi}$$

Like $\hat{q}_E$, $\hat{a}$ can be found by solving $\varphi_B\hat{a} = U_B$ using SOR method or minimizing the L2 norm of the formulated cost function, $J = \frac{1}{2}\langle\varphi_B\hat{a} - U_B, \varphi_B\hat{a} - U_B\rangle$.

4.2.5 Successive Over-Relaxation

Because operator φ_P is linear, it is possible to sort and combine the coefficients in front of each operator, which is summarized in Table 4.1. For 2nd, 3rd, and 4th-order operators listed in column 1 of Table 4.1, we calculate coefficients using second-order finite differencing on neighboring grid points. The vertical finite differencing is carried out on the Exner coordinate following (Sundqvist and Veronis, 1970). At the current stage, operators are not adjusted at the boundaries (e.g. i=1,2,nx-1,nx; j=1,2,ny-1,ny; k=1,nz, where nx, ny, nz are the sizes of the domain) due to their complexity. For example, calculating the three-dimensional operators like $\partial^3/\partial x\partial y\partial\pi$ requires 8 points in the interior, while it requires 18 points in total to get an accurate value on the edges. In addition, accounting for the lower boundary condition in the operators can introduce erroneous lower-level basic state geopotential values (masked by topography) upwards, potentially causing convergence failure even in the domain interior.

The successive over-relaxation (SOR) algorithm is an iterative method commonly used for solving the Poisson equation like vorticity and QGPV inversion. It is also effective for solving the general linear system $\mathbf{Ax} = \mathbf{b}$ when $\mathbf{A}$ is sparse. The SOR algorithm starts with an initial guess for the solution and a relaxation parameter ω ($0 < \omega < 2$) which determines the over-relaxation factor. Then the following step will be repeated until convergence is achieved:

1. Start from grid point (2, 2, 2) and iterate over each grid point (i, j, k) within the computational domain.

2. Update the solution value at the current grid point using the SOR formula:

$$x_{i,j,k}^{new} = x_{i,j,k}^{old} - \omega / A_{i,j,k} \left(b_{i,j,k} - \sum_{m \neq i, n \neq j, l \neq k} A_{m,n,l} x_{m,n,l}^{old} \right)$$

   where $x_{i,j,k}^{new}$ is the updated solution value for $x_{i,j,k}$, $x_{i,j,k}^{old}$ is the previous solution value. $A_{i,j,k}$ represents the coefficient at position (i, j, k) in matrix $\mathbf{A}$, and $b_{i,j,k}$ is the corresponding element in the right-hand side vector $\mathbf{b}$.

3. After updating the solution value at each grid point, check the convergence criterion. If the convergence criterion is not met, repeat the iteration process.

The relaxation parameter ω determines the rate of convergence if the algorithm converges. The SOR algorithm typically converges if the source term $\mathbf{b}$ is well-behaved and $\mathbf{A}$ is positive definite. In the case of solving $\varphi_P \hat{q}_E = U_p$, coefficients in φ depend highly on the basic state (e.g. $\bar{\Phi}$ and $\bar{\Psi}$ from the forward trajectory), therefore φ_P is manually adjusted to achieve reasonable convergence. $\varphi_{P;i,j,k}$ is formulated as follows:

$$\begin{aligned}\varphi_{P;i,j,k} =& \frac{2C\partial^2_{\pi^2;i,j,k}}{d\pi_{k-1} d\pi_k} - 4\frac{C\nabla^2_{i,j,k}}{x^2} - 2\frac{C\partial^3_{x^2\pi;i,j,k}}{x^2}\left(\frac{1}{d\pi_{k-1}} - \frac{1}{d\pi_k}\right) - 2\frac{C\partial^3_{y^2\pi;i,j,k}}{y^2}\left(\frac{1}{d\pi_{k-1}} - \frac{1}{d\pi_k}\right) \\ &+ 20\frac{C\nabla^4_{i,j,k}}{x^4} - 2\frac{C\partial^4_{x^2\pi^2;i,j,k}}{x^2}\frac{2}{d\pi_{k-1} d\pi_k} - 2\frac{C\partial^4_{y^2\pi^2;;i,j,k}}{y^2} - 4\frac{C\nabla^2\partial^2_{x\pi;i,j,k}}{xy}\frac{2}{d\pi_{k-1} d\pi_k}\end{aligned}$$

where $C\partial^2_{\pi^2}$, $C\nabla^2$, $C\partial^3_{x^2\pi}$, $C\partial^3_{y^2\pi}$, $C\nabla^4$, $C\partial^4_{x^2\pi^2}$, $C\partial^4_{y^2\pi^2}$, $C\nabla^2\partial^2_{x\pi}$ are the coefficients on each operator summarized in the second column of Table 4.1 and their typical magnitude at 500 hPa in a mature tropical cyclone are listed in the third column.

4.2.6 The Magnitude of Sensitivity to Ertel PV

A sanity check for the above derivation would be to use the sensitivity to QGPV ($\hat{q}_g$) as an approximation for the sensitivity to Ertel PV ($\hat{q}_E$) then evaluate both the left-hand side (LHS) and the right-hand side (RHS) of (4.20). QGPV serves as a good estimate of Ertel PV in the midlatitudes where the Rossby number $R_o \ll 1$. Even for tropical cyclones, QGPV's location and structure closely resemble that of Ertel PV (e.g., Henderson et al. 1999).

The sensitivity to QGPV for Hurricane Ian (2022) is calculated using the method described in Chapter 2 (2.15), where the response function is minus perturbation surface dry column air, $R = -\mu$. Further details about the WRF model simulation will be described in section 4.3.2.1. Throughout all levels, LHS and RHS share a similar pattern, differing by a factor of 10 to 20. As an example, Fig. 4.1 shows $\frac{1}{A}\varphi\hat{q}_g$ and $\frac{1}{A}U_p$ at 250 hPa. This suggests two key points: first, the structure of $\hat{q}_E$ and $\hat{q}_g$ should be similar and that $\hat{q}_g$ would be a suitable approximation for $\hat{q}_E$ in the case of Hurricane Ian. Secondly, the absolute value of $\hat{q}_E$ is expected to be 1 to 2 orders of magnitude larger than $\hat{q}_g$.

The second point can be validated by performing the scale analysis of (4.20). Suppose the sensitivity to wind and to temperature inverted from $\hat{q}_E$ are of the same magnitude

as that inverted from $\hat{q}_g$. Let's evaluate (4.28a) and (4.28b) and assume the sensitivity to winds is on the order of magnitude of 1, $\hat{u}_E \sim 10^0$, a typical value from the WRF adjoint output when $-\mu$ is selected as the response function. At 500 hPa, when dp =50 hPa, $d\pi \sim 10^1$ and $A \sim 10^{-2}$. Choosing $dx = dy \sim 10^4$, as set in the WRF simulation for Hurricane Ian, we find $\bar{\Phi}_{\pi\pi} \sim 10^{-1}$, $\bar{\Phi}_{x\pi} \sim 10^{-5}$, and $\bar{\Phi}_{y\pi} \sim 10^{-5}$. Further, ∇^2 and $\partial_{x\pi}$ can be approxiated as scales of 10^{-8} and 10^{-5} respectively. Thus making $\bar{\Phi}_{\pi\pi}\nabla^2$ ($\sim 10^{-7}$) is the dominant term compared to $\bar{\Phi}_{x\pi}\partial_{x\pi}$ ($\sim 10^{-10}$) and $\bar{\Phi}_{y\pi}\partial_{y\pi}$ ($\sim 10^{-10}$) in $\hat{u}_E = \frac{\partial \nabla^{-2}(A[\bar{\Phi}_{\pi\pi}\nabla^2 - \bar{\Phi}_{x\pi}\partial_{x\pi} - \bar{\Phi}_{y\pi}\partial_{y\pi}]\hat{q}_E)}{\partial y}$. This implies that at 500 hPa, the magnitude of $\hat{q}_E$ should be on the order of 10^7.

In a similar fashion, examining (4.28c), $\bar{\zeta}$ scales approximately from 10^{-5} to 10^{-4}, and $\bar{\Psi}_{x\pi}$ and $\bar{\Psi}_{y\pi}$ scale around 10^{-2}, which makes the three terms on the right-hand side of $\hat{\theta} = A\left(\bar{\zeta}\frac{\partial}{\partial\pi} - \bar{\Psi}_{x\pi}\partial_x - \bar{\Psi}_{y\pi}\partial_y\right)\hat{q}_E$ to be on the same magnitude (10^{-6}). Taking the typical $\hat{\theta}_E$ value from the WRF adjoint output, which scales between 10^{-1} and 10^0 at 500 hPa and plugging it into the relation (4.28c), we find again $\hat{q}_E$ shall have a magnitude of $10^7 \sim 10^8$, consistent with the above scale analysis.

Finally, remember the typical value for QGPV has a scale of 10^{-4} s^{-1}, while for Ertel PV, the PV unit (PVU) is defined as 10^{-6} $K \cdot m^2 \cdot kg^{-1} \cdot s^{-1}$. Having $\hat{q}_g \sim 10^5$ and $\hat{q}_E \sim 10^6$ at 500 hPa (e.g. Fig. 4.9) makes $\delta R = \langle q'_g, \frac{\partial R}{\partial q_g}\rangle$ and $\delta R = \langle q'_E, \frac{\partial R}{\partial q_E}\rangle$ to be on the approximately same magnitude of $10^0 \sim 10^1$.

4.3 Case Study of Hurricane Ian 2022

4.3.1 Synoptic Overview

Hurricane Ian (2022) hit the west coasts of Cuba and Florida in late September of 2022, causing huge damages including violent winds, flooding, and power outages. Ian originated from a strong tropical wave that emerged from the west coast of Africa around 14-15 September. Over the following six days, the wave slowly traveled across the Atlantic, embedded within the Inter-tropical Convergence Zone (ITCZ) until it reached the Windward Islands in the southeastern Caribbean on 21 September. Ian became a tropical storm 18 hours after its genesis at 0000 UTC 24 September. The intensification of Ian was hindered by moderate-to-strong vertical wind shear which prevented alignment of the low- and mid-level center when Ian was south of Jamaica. While being steered by the subtropical ridge, Ian rapidly intensified at 1800 UTC 25 September and reached hurricane force by 0600 UTC 26 September. The storm continued to intensify over warm sea surface temperature in a lower vertical shear before it made landfall on the west coast of Cuba as a category 3 hurricane.

Steered by the subtropical ridge and a broad trough over the eastern US, Hurricane Ian entered the Gulf, where an eyewall replacement cycle began. Ian became a category 5 hurricane with a peak intensity of 72 $m \cdot s^{-1}$ (140 kt) sustained winds and 937 hPa central pressure at 1200 UTC 28 September after completing the eyewall replacement cycle and

eventually made landfall in mainland southwestern Florida at 1905 UTC 28 September. It caused 161 fatalities and the total losses are estimated to be around $113 billion.

Despite a mature TC being characterized by a deep PV tower in the troposphere, recent studies on TC intensification have predominantly examined the relative vorticity rather than PV. Wang and Zhang (2003) and Smith et al. (2018) investigated the PV structure in tropical cyclones with the MM5 model and an idealized simulation. Wu and Emanuel (1995) explored the contribution of environmental PV to steer the track of Hurricane Bob (1995) on the East Coast of the US. Molinari et al. (1998) studied the intensification and weakening of Tropical Storm Danny (1985) using the superposition principle of PV. Kieu and Zhang (2010) inverted PV anomalies in the TC eyewall and found that lower-level PV contributes more to the TC intensification than the upper-level PV. Doyle et al. (2012) examined the difference in the structure of adjoint sensitivity to relative vorticity between a developing and a non-developing TC genesis event. PV can also be used as a measurement of inertial stability, not just in the boundary layer to examine the primary circulation or in the mid-troposphere to exclude the impact of dry air intrusion, but also in the outflow layer near the tropopause, where small or negative PV indicates low inertial stability (e.g., Mecikalski and Tripoli 1998; Rowe and Hitchman 2016). Komaromi and Doyle (2017) examined the inertial instability structure in intensifying and non-intensifying TC using dropsonde composite. Brooke-Zibton (2022) used adjoint sensitivity analysis to show that the intensification of Irma (2017) is sensitive to the inertial stability at the outflow layer, and upper-tropospheric optimal perturbation is most effective in deepening Irma's minimum pressure.

The rapid intensification (RI) of a tropical cyclone is defined as an increase in the maximum sustained winds of a TC of at least 30 knots in a 24-hour period (Kaplan and DeMaria, 2003) or a deepening in pressure of 42 hPa or greater in a 24-hour period (Holliday and Thompson, 1979). In this case study we will focus on the RI period (green shading in Fig. 4.3a) of Hurricane Ian, with the primary goal to explore the utility of sensitivity to Ertel PV and other diagnostic tools we developed in the previous chapters.

Figure 4.2 shows the synoptic set-up for Ian's rapid intensification period at 1800 UTC 25 September 2022 using ERA5 reanalysis. At that time, Hurricane Ian located south of Jamaica, amid warm sea surface temperature (SST) exceeding 30°C. Conducive atmospheric condition for Ian's RI includes consistent relative humidity above 80% near the storm between 850-700 hPa and no immediate intrusion of dry air at lower levels. Additionally, the vertical wind shear between 200-850 hPa is relatively low, contributing to the intensification. The hurricane track is guided by the subtropical high pressure to its northeast at 500 hPa. Other notable synoptic features that might contribute to the intensification are the broad Rossby wave PV over the northern CONUS and the strong jet near the PV gradient at 200 hPa.

4.3.2 Data and Model

4.3.2.1 WRF Simulation

Model initial condition and boundary conditions are configured using the WRF Preprocessing System (WPS). The WRF-ARW simulation is initialized using the National

Center for Environmental Prediction (NCEP) Final (FNL) operational global analysis on $0.25°\times0.25°$ latitude-longitude grid available from the National Center for Atmospheric Research (NCAR) Research Data Archive (RDA) every 6 hours (0000, 0600, 1200, 1800 UTC daily). The 24-hour simulation focuses on Hurricane Ian's RI period from 1800 UTC 25 September 2022 to 1800 UTC 26 September 2022. WRF model V4.4 (Skamarock et al., 2019) is employed to get a precise forward trajectory which is saved every two minutes. WSM 5-class scheme is chosen for the microphysics scheme, Kain-Fritsch scheme for cumulus parameterization, RRTMG scheme for longwave and shortwave radiation, and YSU scheme for boundary layer parameterization. A 24-hour integration is generally considered valid for the adjoint model to maintain its linearity properties in highly nonlinear simulation (e.g. involves more moist dynamics) in the tropical region (e.g. Park and Droegemeier 1997; Errico and Raeder 1999; Xu et al. 1998). The simulation was conducted on a 24 km grid with 41 equally spaced layers from the surface to 50 hPa, with the lateral boundary condition updated every 6 hours.

The WRF-simulated hurricane achieves a central pressure of 980 hPa and a maximum 10-m wind of 62 kt at the final timestep. The simulated result is weaker than the reality indicated by the Best Track (e.g. Fig. 4.3) measured either by maximum wind speed or by pressure. The initial intensification lags behind the reality by 7 hours, but the intensification rate measured by the central pressure is similar to the Best Track for the rest of the simulation. Therefore the simulation is qualified to serve as a good approximation of Hurricane Ian and can be used to demonstrate the utility of sensitivity to Ertel PV.

WRF adjoint model V3.8.1 (Zhang et al., 2013) is used for the adjoint sensitivity computation. The chosen response function is the minus perturbation surface dry air mass in the column ($R = -\mu$) within simulated 1004 hPa sea level pressure isobar (Fig. 4.3b) at forecast hour 24 (F24). A balanced adjoint forcing is obtained by inverting the adjoint sensitivity to QGPV informed by the adjoint sensitivity output at F23 as illustrated in Fig. 2.8. This process eliminates the high-frequency waves generated by the adjoint model due to the geostrophic adjustment.

4.3.2.2 Basic State in Sensitivity to Ertel PV Calculation

When applying the adjoint technique, we treat the perturbation as a small deviation from the trajectory (basic state). Thus unlike in the Ertel PV inversion in Davis and Emanuel (1991), where they used the average geopotential from the midlatitude cyclone development period as the basic state, we can employ the instantaneous geopotential and streamfunction fields from the model trajectory. However, interpolating geopotential onto the isobaric/Exner levels lead to masking issue over the topographical features like the Rockies. In addition, the WRF model does not directly provide a streamfunction (typically resolved globally in spectral models). To address this issue, streamfunction fields from the $1.25° \times 1.25°$ Japanese 55-year Reanalysis (JRA-55, Kobayashi et al. 2015) at F00, F06, F12, F18 are interpolated on the WRF domain for simplicity and used as $\bar{\Psi}$ in related computations. With $\bar{\Psi}$ known, we can use the nonlinear balance equation (4.10) to calcualte the perturbation geopotential on each isobaric/Exner level because inverting

$\nabla^2\Phi$ with homogeneous boundary condition results in Φ'. By adding the perturbation geopotential to the domain-averaged JRA geopotential on each Exner level, we obtain the basic state geopotential $\bar{\Phi}$. A Gaussian filter has been applied to smooth the third- and fourth-order derivatives of $\bar{\Phi}$ and $\bar{\Psi}$.

4.3.3 Results

4.3.3.1 Sensitivity by Each Variable

An investigation into the original adjoint output from the WRFPLUS model will set up the stage for us better understand the physical meaning of the sensitivity to PV. The adjoint model follows the procedure described in Chapter 2 section 2.8.

Figure 4.4 shows the adjoint sensitivities to temperature and to winds at 800 hPa as a representation of the lower-level sensitivity. Circular areas of warm temperature sensitivity and cyclonic sensitivity to winds that overlap the storm center at each time steps are both indicators of conducive conditions for storm intensification. This aligns with the fact that hurricanes develop under warm temperature anomaly in the their eyes. During the earlier time step (e.g. F00, F06), positive temperature sensitivity maxima are located northeast of the storm center, while some negative sensitivity to temperature is preferred to the southwest of the center. These features might be associated with the scattered convection either in the rainband or in the convective bursts. Note sensitivity to the wind is also not uniformly cyclonic about the storm center in these convective areas, which might reflect a wind-temperature balance of adjoint variables on a small scale. Other

notable features across all time steps are the preference for southeasterly wind around the subtropical high pressure on the Atlantic and the preference for southwesterly west of coastal Central America.

Although the moist sensitivity variable is not included in the study of sensitivity to PV, it is important to examine the distribution of moisture in tropical cyclone development. Shown in Fig. 4.5, the sensitivity to water vapor mixing ratio (moisture) exhibits a consistent preference for more moisture near the storm center at all time steps. At F00 and F06, the sensitivity to moisture maximum aligns to the south of the maximum relative humidity (magenta contour), indicating the requirement for axisymmetric moistening about the storm center. Introducing slight dry air in the surrounding environment at an outer radius seems to help the storm develop. It is unclear whether this ring of dry sensitivity is created by unbalance between temperature and moisture sensitivity at F18 and F12 during the adjoint spin-up time. At F00, small-scale positive and negative sensitivities to moisture north of the storm address the contribution of small-scall scale convection, similar to what is indicated by the temperature sensitivity (Figs. 4.4a,b). As a reminder, these moisture sensitivity patterns are primarily controlled by the WRF nonlinear trajectory, which invokes a Heaviside function during the phase change of water that commonly occurs in a convective system.

The 500 hPa WRF trajectory shows that the subtropical high-pressure northeast of Hurricane Ian and a broad trough dominating the CONUS, indicated by high PV values (Fig. 4.6), are two primary midlatitude systems influencing Ian's intensification. A small PV

anomaly is observed at the US-Mexico border at F00, which becomes less organized at F18. Sensitivities to winds and temperature suggest the broad trough over CONUS has no impact on the TC intensity (not shown). The distribution of the sensitivity to the temperature at 500 hPa resembles that at 800 hPa (Fig. 4.4), concentrating near the storm center near the final time step and spreading out close to the initial time. Away from the TC center, the zebra-striped positive and negative sensitivities to the temperature, along with shifts in the direction of sensitivity to wind at F00 and F06, again highlight the significance of regional convection in supporting TC intensification. Broadly speaking, the sensitivity to winds is more cyclonic and inwardly organized at F18. There is also a secondary cyclonic feature present in the Gulf, with its southern branch contrasting the easterly wind in southern Mexico. This feature over Mexico persists at F12 but becomes less organized by F06 and F00 (Figs. 4.6c,d). When comparing with the 500 hPa background wind at F00 (Figs. 4.6a), we notice the cyclonic sensitivity to winds reverses the anticyclonic wind direction present in the background state. The wind sensitivity east of the TC is more outwardly organized from F12 to F00, differing from the cyclonically inward sensitivity at 800 hPa (Figs. 4.5a,b,c).

The tropical cyclone enters the outflow level at about 250 hPa, where a broad anticyclonic outward flow is observed in the WRF simulation (Figs. 4.7a,b). The shortwave trough northwest of Hurricane Ian slowly develops from F00 to F18 and helps the outflow's connection to the subtropical jet. This passage from the outflow to the subtropical jet accelerates the air evacuation in the hurricane's eyewall, creating stronger upward

vertical motion. The PV streamer northeast of Ian becomes more meridionally organized as negative PV builds up between the PV streamer and the hurricane.

Comparing the 500 hPa and 800 hPa sensitivity that highlights cyclonic sensitivity to wind near the TC center, the dominant feature at 250 hPa is cyclonic sensitivity to wind over Mexico (Figs. 4.7c,d,e,f). This feature is stretched along a west-northwesterly oriented axis from F18 to F00, smoothly connecting with the anticyclonic sensitivity to winds at the outflow level. The southeasterly branch of this feature seems to counteract the background cyclonic wind associated with the shortwave trough (Figs. 4.7a,b). However, this also suggests that deepening the shortwave trough at 250 hPa could potentially intensify the storm. Batches of sensitivities to wind and to temperature northeast of the storm are again speculated to be associated with the convection. The presence of deep convection in this region helps pump more negative PV to the lower stratosphere and upper troposphere.

4.3.3.2 Sensitivity to Ertel PV

Figure 4.8 depicts the distribution of 850 hPa sensitivity to QGPV (first column), to geostrophic imbalance (second column), and to Ertel PV (third column) at F00, F06, F12, F18 of the simulation. $\hat{q}_g$ and $\hat{a}$ are inverted over the whole domain, while $\hat{q}_E$ is inverted only in the domain shown in the figure. $\hat{q}_g$ is circular around the storm center indicated by 850 hPa Ertel PV contour at F18 and F12 (Figs. 4.8j,g), suggesting that an increase in QGPV at 850 surrounding the storm center will intensify the hurricane

12 or 6 hours later. Characterized by a deep positive PV tower in the troposphere, the tropical cyclone's intensity certainly benefits from having more positive PV perturbation near the storm center. At F06 and F00, the largest sensitivity to QGPV started to spiral outwards, forming a "flipped comma" shape around the storm center.

At F18, the sensitivity to geostrophic imbalance, $\hat{a}$, is predominantly negative near the storm center, with a strip of positive value to its east (Fig. 4.8k). As the adjoint model continues to integrate backward, the area of $\hat{a} < 0$ expands outward, accompanied by $\hat{a} > 0$ radially outward. From what we discussed in Chapter 3, the *vertical* gradient of $\hat{a}$ recovers most of the temperature sensitivity (e.g. Fig. 3.2). One possible cause for the *horizontal* $\hat{a}$ dipole pattern could be its collocation with temperature sensitivity (e.g. Fig. 4.5d and Fig. 4.11c). More importantly, notice the positive $\hat{q}_g$ area overlaps where $\hat{a} < 0$ at all time steps (Fig. 4.8 column 1 and column 2). Both $\hat{q}_g$ and $\hat{a}$ have spatial scales possibly larger than the Rossby radius of deformation, which is comparably smaller than the synoptic scale in TCs due to high relative vorticity. In Chapter 3, we discussed that $\hat{a} < 0$ is surrounded by a cyclonic sensitivity to winds (e.g. Fig. 3.3). Since the horizontal scale of the negative $\hat{a}$ is large enough, we speculate that instead of $\hat{\theta}$, it should be $\hat{\mathbf{v}}$ that adjusts to the existence of $\hat{a}$. The additional sensitivity to cyclonic wind, marked by the broad negative $\hat{a}$ pattern, suggests that the sensitivity to winds in the TC boundary layer is super-geostrophic. Although supergradient winds are often observed in the TC boundary layer (e.g. Kepert and Wang 2001; Montgomery and Smith 2017; Fei et al. 2021), they usually occur near the radius of maximum wind ($40 \sim 60$ km from the TC center), much smaller than the radius of $\hat{q}_g > 0$ pattern.

Next, we will examine the sensitivity to Ertel PV[4]. Unlike the broad positivity of $\hat{q}_g$, positive $\hat{q}_E$ is concentrated to the storm center at F18 (Fig. 4.8l), surrounded by a ring of negative sensitivity to Ertel PV. $\hat{q}_E$ spreads outward like $\hat{a}$ as the adjoint integrate backward. Contrary to $\hat{q}_g$, at F12 and F06, $\hat{q}_E$ locates northeast of the storm center. At F00, positive $\hat{q}_E$ and $\hat{q}_g$ maximum strips locate at the same location, spiral anticyclonic from east of the storm into the storm center like a "flipped comma". The random distribution of $\hat{q}_E$ at F00 near Cuba and Jamaica is similar to that of $\hat{a}$. This could be an indication of having more convection if we compare the pattern with the sensitivity to mixing ratio, $\hat{q}_{vapor}$ (Fig. 4.5c). Based on what we discussed in Chapter 3, $\hat{a}$ is associated with sensitivity to temperature that is related to diabatic heating release. $\hat{q}_{vapor}$ also co-locates with sensitivities to Ertel PV and to QGPV south of the storm center, aligning with the previous studies that recorded the relevance between moisture and PV (e.g., Vich et al. 2012; Doyle et al. 2012; Doyle et al. 2014).

The distribution of 500 hPa sensitivity to QGPV (Fig. 4.8 column 1) is similar to that at 850 hPa, displaying a circular pattern that aligns with the TC center indicated by the 500 hPa Ertel PV contour. The negative $\hat{q}_g$ southwest of the storm center crossing Honduras and Nicaragua is more prominent in the mid-troposphere than in the boundary layer. Sensitivity to anticyclonic wind associated with $\hat{q}_g < 0$ adds more northwesterly wind sensitivity along the east coast of Honduras, effectively addressing the 500 hPa sensitivity to wind pattern in Fig. 4.6.

[4]The distribution of sensitivity to Ertel PV should be viewed with caution. The author manually tuned many procedures during the SOR inversion and the sensitivity to Ertel PV might not converge before the SOR is subjectively terminated.

In contrast to the broad negativity surrounding the storm center at 850 hPa, the sensitivity to geostrophic imbalance at the 500 hPa level appears more scattered across all four timesteps (Fig. 4.8 column 2). A possible explanation is that, at 500 hPa, the adjoint sensitivities to wind and temperature are generally in "geostrophic balance" since $\hat{a}$ has a relatively small scale and is more scattered. While the broad 850 hPa $\hat{a}$ negativity suggests that geostrophic balance is not applicable to the relationship between $\hat{\theta}$ and $\hat{\mathbf{v}}$ in the boundary layer of a mature TC.

The radial $\hat{q}_E$ dipole expands outward as the model integrates backward. At F00, the negative $\hat{q}_E$ shares the same location with $\hat{q}_g$ (Fig. 4.8a) over Honduras and Nicaragua. Contrary to the 850 hPa $\hat{q}_E$ that wraps around the storm (Fig. 4.8c), the 500 hPa $\hat{q}_E$ exhibits a more linear pattern with a maximum located southwest of the storm at an outer radius. At 850 hPa, it is easy to imagine that positive $\hat{q}_E$ is cyclonically advected by the winds from the nonlinear trajectory and gradually wraps around the TC center from F00 to F18 (Fig. 4.8 column 3). At 500 hPa, positive $\hat{q}_E$ contracts towards the center radially rather than cyclonically. This behavior is intriguing because the background 500 hPa flow is largely rotational instead of radially inward like in the boundary layer. This might serve as a reminder that the adjoint sensitivity is merely an inflection of the state variable adjoint gradient at each timestep and no calculation has been shown that the $\hat{q}_E$ is a conserved variable, either on isentropic or isobaric surfaces.

At 250 hPa, where the TC outflow is located, the background Ertel PV is either close to zero or negative (e.g. Fig. 4.7a,b). This layer is typically associated with negative

PV and low inertial stability. Research by Wang et al. (2020) points out the balance constraint is not applicable at the storm outflow level. Through an idealized simulation, Rappin et al. (2011) illustrated that having a TC-jet couplet helps the tropical cyclone outflow expand into the region of weak inertial stability on the anticyclonic shear side of the jet stream, therefore, minimizing the energy required to evacuate the air mass and to complete the Carnot cycle.

The minus 0.3 PVU contour at 250 hPa in Fig. 4.10 could suggest the region of deep convection in the trajectory. The 250 hPa sensitivity to QGPV is generally negative south of the TC center at the final time (Fig. 4.10j). The $\hat{q}_g$ minimum rotates cyclonically around the TC center from F18 to F06 and ultimately propagates to the east of Cuba at F00. Since the outflow of a TC is characterized by an anticyclonic flow and so is the sensitivity to winds (e.g. Figs. 4.7c,d,e,f), one can expect $\hat{q}_g < 0$ as it is also associated with anticyclonic wind sensitivity (e.g. Fig. 2.1). Following the schematic of sensitivity to PV, where $\hat{q}_g > 0$ ($\hat{q}_g < 0$) corresponds to $\hat{\theta} > 0$ above (below), and $\hat{\theta} < 0$ below (above), it becomes evident that having $\hat{q}_g < 0$ at upper levels and $\hat{q}_g > 0$ at mid-troposphere points to have warm temperature sensitivity in between, consistent with the typical TC warm core structure.

Areas with negative PV values often coincide with low inertial stability (e.g., Mecikalski and Tripoli 1998; Rowe and Hitchman 2016). This implies that interpreting $\hat{q}_g < 0$ goes beyond just anticyclonic wind sensitivity; it also indicates a preference for lower instability, facilitating storm intensification. The preference for having positive $\hat{q}_g$ to the

southwest of the storm is not necessarily associated with the TC itself within this limited domain and shall be explained later in section 4.3.3.4 with Fig. 4.15.

Consistent with 850 hPa and 500 hPa, sensitivity to geostrophic imbalance is again scattered northeast of the TC, especially at F06 and F12 (Figs. 4.10b,e). At F18, the sensitivity to Ertel PV is broadly negative to the south of the TC at F18 (Fig. 4.10l). Just like $\hat{q}_g$, $\hat{q}_E$ resolve some positive sensitivity over Honduras at F00. At the same time, the spatial distribution of $\hat{q}_E$ closely resembles $\hat{a}$, indicating that most features not captured by geostrophic balance can be resolved by applying nonlinear balance. Unfortunately, the dissertation does not include the schematic for sensitivity to Ertel PV, particularly regarding its implications on temperature sensitivity, such as whether it has the potential to represent diabatic heating patterns similar to $\hat{a}$.

At all the shown levels, the sensitivity to Ertel Potential Vorticity displays a more intricate structure compared to the sensitivity to QGPV in the context of tropical cyclones, while capturing major features in the sensitivity to geostrophic imbalance. Moreover, when integrated backward from F24 to F00, the maximum magnitude of $\hat{q}_g$ at 850 hPa and 500 hPa diminishes over time, while the maximum of $\hat{q}_E$ increases.

Overall, the fact that the structure of $\hat{q}_E$ combines essential features of both $\hat{q}_g$ and $\hat{a}$ suggests that $\hat{q}_E$ is able to resolve some features covered in nonlinear balance but not included under the geostrophic balance. This addresses the limitations of using sensitivity to QGPV and the QG balance constraint in tropical cyclones.

The $\hat{q}_g$ patterns at different levels suggest that having more positive PV near the storm center at lower- and mid-levels, along with more negative PV at the outflow level contributes to TC's rapid intensification within 24 hours. As for $\hat{a}$ and $\hat{q}_E$ close to F00, they exhibit scattered distributions to the northeast of Hurricane Ian throughout the troposphere from 850 hPa to 250 hPa. These distributions resemble the low-level sensitivity to moisture field (e.g. Fig.4.5) and indicate the importance of mesoscale deep convections in the periphery of the tropical cyclone to the rapid intensification.

4.3.3.3 Sensitivity to Nonlinear-Balanced State

Following Equation (4.28), we recovered the sensitivity to the nonlinear-balanced wind ($\hat{\mathbf{v}}_E$) and temperature ($\hat{\theta}_E$) from the sensitivity to Ertel PV, $\hat{q}_E$. It should be noted that $\hat{\mathbf{v}}_E$ and $\hat{\theta}_E$ are only qualitative stems from the inaccuracies in the basic state variables like $\bar{\Phi}_{\pi\pi}$ required in Equation (4.28). On the other hand, sensitivity to geostrophically balanced and unbalanced wind and temperature (e.g. $\hat{u}_g$ and $\hat{u}_i$) are quantitative and can be directly compared with the result from WRF-adjoint output.

Figures 4.11, 4.12, 4.13 compare the sensitivity to wind and temperature from WRF-adjoint (panel a) and those recovered from $\hat{q}_E$ (panel b; follows (4.28)), from $\hat{a}$ (panel c; follows (3.7a)), and from $\hat{q}_g$ (panel d; follows (2.19)) valid at 1200 UTC 26 September 2022 (F18). Presenting results at F18 is enough to illustrate the feasibility of recovering wind and temperature sensitivity fields from $\hat{q}_E$. Additionally, patterns close to the final timestep offer simpler interpretations before complexities emerge.

At 850 hPa, warm temperature sensitivity and cyclonic wind sensitivity favor the development of the storm. Both geostrophically balanced ($\hat{\theta}_g$; Fig. 4.11d) and unbalanced temperatures ($\hat{\theta}_i$; Fig. 4.11c) are consistent with the WRF-adjoint output but on a smaller magnitude. Geostrophically balanced wind sensitivity ($\hat{\mathbf{v}}_g$; Fig. 4.11d) closely resembles the wind sensitivity field from WRF-adjoint output. Although the sensitivity to nonlinear balanced temperature ($\hat{\theta}_E$; Fig. 4.11b) is negative at the lower level, it is able to recover the cyclonic sensitivity to wind patterns. When computing $\hat{q}_g$, the sensitivity to temperature near the surface is employed as the Neumann boundary condition. However, when applying the same boundary condition to $\hat{q}_E$, it leads to a drastic change in $\hat{q}_E$ and quick failure in SOR convergence.

At 500 hPa, $\hat{\mathbf{v}}_g$ and $\hat{\theta}_g$ (Fig. 4.12d) accurately replicate the primary features of $\hat{\mathbf{v}}$ and $\hat{\theta}$ (Fig. 4.12a) from the WRF-adjoint output. $\hat{\mathbf{v}}_i$ is negligible at all three levels, while $\hat{\theta}_i$ identifies the $\hat{\theta}$ maximum northwest of the storm center (Fig. 4.12c). The presence of a gravity wave pattern in $\hat{\theta}_i$ 6 hours into the backward integration suggests that the geostrophically balanced adjoint forcing is not able to fully achieve the "adjoint thermal wind balance". $\hat{\mathbf{v}}_E$ (Fig. 4.12b) is cyclonic to the west of the TC center at a closer radius, transitioning to anticyclonic behavior at an outer radius. As for $\hat{\theta}_E$, it captures the anticyclonically inward spiraling characteristic of positive $\hat{\theta}$ near the storm center like the other two temperature sensitivities. At the same time, the positive $\hat{\theta}_E$ is accompanied by a strip of $\hat{\theta}_E < 0$ immediately outwards.

At 250 hPa, sensitivities are of smaller magnitudes than at lower levels. Specifically, $\hat{\theta}_g$

(Fig. 4.13b) associated with $\hat{q}_g$ and $\hat{\mathbf{v}}_i$ (Fig. 4.13c) associated with $\hat{a}$ are almost negligible. $\hat{\mathbf{v}}_g$ recovers the anticyclonic $\hat{\mathbf{v}}$ (Fig. 4.13a) and successfully removes its divergent component. $\hat{\theta}_i$ (Fig. 4.13d) recovers $\hat{\theta}$ but at a smaller magnitude and retains the gravity wave pattern in temperature sensitivity. Although $\hat{\mathbf{v}}_E$ does not match $\hat{\mathbf{v}}$, $\hat{\theta}_E$ shows a warm temperature at the TC's outflow level and a temperature sensitivity dipole over Guatemala, recovering some features in $\hat{\theta}$. Additionally, unlike $\hat{\theta}_i$, $\hat{\theta}_E$ does not retain the gravity wave pattern in $\hat{\theta}$, again proving $\hat{q}_E$'s ability to encompass the structure of both sensitivity to winds like $\hat{q}_g$ and sensitivity to temperature like $\hat{a}$.

Analyzing the cross-section of Hurricane Ian at F18, the sensitivity to temperature from the WRF-adjoint output (Fig. 4.14a) is overall positive from the surface to 500 hPa, captured by a triangle shape. Both $\hat{a}$ and $\hat{q}_g$ (Figs. 4.14c and d) resolve warm temperature sensitivity at the surface or lower-to-mid troposphere. Although $\hat{q}_E$ (Fig. 4.14b) itself is positive around the PV core (Fig. 4.14a) similar to $\hat{q}_g$, $\hat{\theta}_E$ turns negative beneath the maximum of $\hat{q}_E$. Applying surface level $\hat{\theta}$ as the Neumann bottom boundary condition might solve this temperature sensitivity mismatch, but it could also lead to SOR convergence failure at the current stage of research. Note that it is difficult to show cross-section comparisons at other time steps due to their distinct horizontal structures.

4.3.3.4 Optimal Perturbation

Next, perturbation experiments are conducted to scrutinize the validity of the sensitivities discussed above, following the optimal perturbation method described in Chapter 3

section 3.5. Unfortunately, perturbation experiments that are intended to increase the storm by adding optimal perturbation all result in *weakening* the storm. Therefore, for the optimal perturbation experiments, we seek to increase the perturbation column dry air mass, μ, within 1004 hPa sea level pressure (SLP) contour by an average of 1 hPa at the final time. The optimal perturbation experiments should be analyzed with caution for another reason: the boundary layer perturbation added is extremely large, risking the potential of violating the small perturbation assumption necessary for the validity of the tangent and adjoint models (e.g., Brown and Hakim 2015).

To create optimal perturbation informed by nonlinear balanced sensitivities to wind and to temperature, $\hat{q}_E$ needs to be computed over the full domain to recover $\hat{\mathbf{v}}_E$ and $\hat{\theta}_E$. Figure 4.15 depicts the distribution of $\hat{q}_g$, $\hat{a}$, $\hat{q}_E$ at lower-, mid-, and upper-troposphere at 1800 UTC 25 September 2022 (F00). In the lower- and mid-troposphere, sensitivities are concentrated near the storm center as described in section 4.3.3.2. At 250 hPa, the most pronounced sensitivity to PV locates over Central America (e.g. 4.15g,l), possibly suggesting that modifying the upper-level shortwave (Fig. 4.7a) could impact on Hurricane Ian's development. The $\hat{q}_E$ dipole strips make it unclear whether a positive or negative Ertel PV is preferred in the region. Remember that cyclonic (anticyclonic) wind sensitivity surrounds positive (negative), therefore, a meridionally oriented $\hat{q}_E$ dipole with a configuration of negative values to its west and positive values to its east shall be associated with a northerly wind sensitivity. This interpretation is consistent with the northerly wind sensitivity from the WRF-adjoint output (Fig. 4.7c). Similarly, the horizontally oriented dipole over coastal Mexico would suggest sensitivity to easterly wind, which is

consistent with the WRF-adjoint $\hat{\mathbf{v}}$ at the same location. Figures 4.16g and 4.16l show the connection between cyclonic wind sensitivity, recovered from either $\hat{q}_g$ or $\hat{q}_E$, and the upper-level shortwave over Mexico (e.g. Fig. 4.7a).

The baseline unperturbed experiment is referred to as "ctrl." The optimal perturbation experiment informed by the adjoint sensitivity from the WRF adjoint output (initial perturbation proportional to Fig. 4.4a, Fig. 4.6c, and Fig. 4.7c) is labeled as "WRF-adj". "qgbal" labels the experiment informed by QG balanced sensitivity fields at F00 (initial perturbation proportional to Fig. 4.16 column 1), "imbal" labels the experiment informed by the unbalanced sensitivity fields at F00 (initial perturbation proportional to Fig. 4.16 column 2), and "nlbal" labels the experiment informed by the nonlinear balanced sensitivity fields at F00 (initial perturbation proportional to Fig. 4.16 column 3). All perturbed experiments are carried out from 1800 UTC 25 September 2022 to 1800 UTC 26 September 2022, the same as the unperturbed control experiment.

The evolution of Hurricane Ian's minimum SLP for each experiment is shown in Fig. 4.18. With a prescribed 1 hPa column dry air increase averaged inside the 1004 hPa contour at the final time (e.g. green area in Fig. 4.3), both "qgbal" and "nlbal" are able to achieve a weaker storm at the final time with a 3 hPa rise in the minimum SLP, while "WRF-adj" and "imbal" deepen the storm center pressure by 1 hPa. Figure 4.18 illustrates the SLP difference between the perturbed experiments and the control experiment, $SLP_{pert} - SLP_{ctrl}$, where the subscript "pert" can be "WRF-adj", "qgbal", "imbal", or "nlbal". The SLP difference dipoles (e.g. zoom-in plots) are generally caused

by the location shift of Hurricane Ian's eye. "WRF-adj" (Fig. 4.18a), "qgbal" (Fig. 4.18b), and "nlbal" (Fig. 4.18d) experiments all retard the northwest moving progression of TC, while the "imbal" (Fig. 4.18c) experiment shifts the TC center location slightly to the west.

Apply the same linearity measurement method used in Chapter 3 where the change in response function $\Delta R \approx \delta R = \langle \partial R/\partial \mathbf{x}_\tau, \mathbf{x}'_\tau \rangle$ at each timestep $\tau = 0$ ... 24 is calculated. Here, the perturbation $\mathbf{x}'_\tau$ is the deviation in variables $\mathbf{x} = (u, v, \theta)$ of the perturbed experiment from the control experiment, $\mathbf{x}' = \mathbf{x}_{pert} - \mathbf{x}_{ctrl}$. The normalized δR with respect to the prescribed energy ΔR_0 is shown in Fig. 4.19. In a linear model, such as the tangent linear model, $\delta R/\Delta R_0$ should equal 1 at all time steps. We notice that only "WRF-adj" starts from unity. This is because sensitivities used to create perturbations in other experiments differ, but only "WRF-adj" sensitivity is used to calculate δR. In both "WRF-adj" and "imbal" perturbations, δR quickly loses more than 60% of its initial value at the first timestep. This suggests a loss in linearity and rapid dissipation of perturbation energy due to the spin-up/adjustment process. Conversely, both "qgbal" and "nlbal" experiments retain most of their perturbation energy input. The observation that QG balanced perturbation undergoes less adjustment than the nonlinear balanced one could suggest that either the model adjusts to the QG balance, or the recovery of the nonlinear balanced perturbation from sensitivity to Ertel PV is not accurate enough. All four experiments share a similar trend of slow decrease in linearity ($\delta R/\Delta R_0$) until F19, where both balanced perturbations start to increase.

Comparing the perturbation energy evolution of four perturbed experiments in Fig. 4.20, we find "WRF-adj" inserts the least amount of energy at the initial time. "Imbal" inserts the largest amount of energy near the boundary layer top at 900 hPa, probably due to the supergradient wind sensitivity that is not resolved by the geostrophic balance. "WRF-adj", "qgbal", and "nlbal" distribute most of their energy near the surface, gradually decreasing to a minor amount near 600 hPa. In the first few hours, most perturbation energy is concentrated near the surface; around F09, upper-level energy near 150 hPa starts growing for "qgbal", "imbal", and "nlbal", with "WRF-adj" picking up upper-level development three hours later. At the final time, all experiments show three energy peaks at the surface, in the boundary layer, and near the upper-troposphere-lower-stratosphere (UTLS) around 150 hPa (e.g. tropopause indicated by θ_e contour in Fig. 4.14).

Despite distinct distributions of sensitivity to Ertel PV and QGPV shown in Fig. 4.8, Fig. 4.9, and Fig. 4.10, the fact that the balanced perturbation informed by QG- and nonlinear-balanced sensitivities to wind and to temperature are able to have a similar impact on the storm development suggests two points. Firstly, $\hat{q}_E$ is relatively accurately inverted and the method to recover $\hat{\mathbf{v}}_E$ and $\hat{\theta}_E$ are qualitatively correct. Secondly, $\hat{q}_E$ leverages the advantages of both $\hat{q}_g$ and $\hat{a}$.

4.3.3.5 Approximation of Sensitivity to PV with PV Perturbation

Like in Chapter 2 section 2.5.4, we wish to assess the validity of approximating the sensitivity to PV with the PV perturbation by comparing two different PV perturbations.

The first one is the PV difference between the optimally perturbed experiment and the control experiment, both experiments run for 24 hours. The calculation of the second kind of PV perturbation requires no additional model integration. Optimal perturbations informed by the balanced adjoint field are introduced to the control experiment at each time step and PV measured in the unperturbed state is subtracted from the PV measured in the perturbed state.

Figures 4.21a,d,g,j show 500 hPa QGPV difference between the perturbed "WRF-adj" experiment from section 4.3.3.4 and the control experiment. The initial QGPV perturbation introduced to the model state is at the outer radius of the storm. Over the next 6 hours, the perturbation quickly grows from 0.1 s^{-1} to 8 s^{-1}, forming a dipole near the TC center – indicating the shift in storm center location. Sensitivity to QGPV is reversed to better align with the optimal perturbation that seeks to reduce storm pressure. Figures 4.21b,e,h,k suggest that less positive QGPV supports storm weakening. Since $\hat{q}_g$ is solved through a Poisson-like equation, the spatial pattern for $-\hat{q}_g$ is much broader than the perturbation.

To make a fair comparison between the spatial structures of QGPV perturbation and sensitivity to QGPV, geostrophically balanced optimal perturbations, $u'_{g,t}$, $v'_{g,t}$, $\theta'_{g,t}$, informed by the geostrophically balanced adjoint sensitivities, $\hat{u}_{g,t}$, $\hat{v}_{g,t}$, $\hat{\theta}_{g,t}$ at each time step $t = 0, 6, 12, 18$ are introduced to the control simulation at their corresponding time step (Figs. 4.21c,f,i,l). Column 3 suggests the QGPV perturbation introduced at the instantaneous time step has a finer structure than the sensitivity field in column 2, differing

from the QGPV perturbation in column 1 except at F00. Although the initial optimal perturbations (Fig. 4.21a) are not in QG balance, its unbalanced component does not seem to contribute to the perturbation QGPV. This might be why Fig. 4.21a and Fig. 4.21c share the same pattern and provide numerical support for the energy norm sensitivity to QGPV derivation method shown in Chapter 2 section 2.2.4, which utilizes the common Lagrange multiplier across variables.

Figure 4.22 replicates Figure 4.21 but with the Ertel PV. The reversed sensitivity to Ertel PV, $-\hat{q}_E$ has a finer spatial structure than $-\hat{q}_g$ but does not show the northwest-southeast "WRF-adj - ctrl" Ertel PV perturbation dipole (e.g., Figs. 4.22b,e,h,k). Nonlinear-balanced optimal perturbations, $u'_{E,t}$, $v'_{E,t}$, $\theta'_{E,t}$, informed by the nonlinear-balanced adjoint sensitivities, $\hat{u}_{E,t}$, $\hat{v}_{E,t}$, $\hat{\theta}_{E,t}$ are added to the control simulation at each time step. Compare the QGPV perturbation added by the QG-balanced state variable perturbation (e.g. Figs. 4.21c,f,i,l) and the Ertel PV perturbation added by the nonlinear-balanced state variable perturbation (e.g. Figs. 4.22c,f,i,l), their spatial distribution are strikingly similar, inferring that QGPV could represent Ertel PV in TCs to some extent. More interestingly, contouring $-\hat{q}_E$ on these instantaneous Ertel PV perturbations shows remarkable overlap between the two features. Maybe we *can approximate* the sensitivity to PV with the PV perturbation, with the condition that the perturbation must be added at the individual time (e.g., Fig. 4.22 column 3) rather than taking the difference between two complete model runs (e.g., Fig. 4.22 column 1).

4.4 Conclusion

The formulation for three-dimensional adjoint sensitivity to Ertel's potential vorticity under the nonlinear balance constraint is derived in this chapter, along with the nonlinear-balanced sensitivity to winds and to potential temperature. Using the case of WRF-simulated Hurricane Ian (2022), we calculate the sensitivity of Ian's minimum sea level pressure to Ertel PV with the successive over-relaxation technique. In short, sensitivity to Ertel PV is able to capture the structure of both sensitivities to winds like sensitivity to QGPV, and sensitivity to temperature like sensitivity to geostrophic imbalance.

Comparing the sensitivity to Ertel PV and QGPV qualitatively, it is evident that sensitivity to Ertel PV, $\hat{q}_E$, exhibits a more detailed spatial distribution than sensitivity to Ertel PV, $\hat{q}_g$ (e.g. Figs. 4.8, 4.9, 4.10). The patterns in $\hat{q}_E$ near the initial time exhibit small and sparse features resembling $\hat{a}$ (e.g. F00, F06 in Figs. 4.8, 4.9, 4.10), indicating $\hat{q}_E$'s ability to resolve certain nonlinear balance-covered features that are not included under geostrophic balance. These features are speculated to be associated with small-scale convection in TC's ambient region due to their collocation with the moisture sensitivity field (e.g., Doyle et al. 2014; Doyle et al. 2011; Demirdjian et al. 2020). They can also be linked to convective vertical "hot towers" that contribute to TC development found in recent studies (e.g., Hendricks et al. 2004; Montgomery et al. 2006).

Despite the distinct structure difference between $\hat{q}_E$ and $\hat{q}_g$ close to the initial time (F00), optimal perturbations informed by QG balanced sensitivities recovered from $\hat{q}_g$ and by

nonlinear-balanced sensitivities recovered from $\hat{q}_E$ have similar impacts on Hurricane Ian in terms of how much the storm has weakened (Fig. 4.18), vertical perturbation energy distribution (Fig. 4.20), and the linearity retention (Fig. 4.19).

The similarity between QG-balanced and nonlinear-balanced sensitivity states is reflected in the QGPV and EPV perturbations added to the system at individual timestep (Figs. 4.21, 4.22). The overlapping of instantaneous QGPV/EPV perturbation and $\hat{q}_E$ provides a piece of strong evidence that $\hat{q}_E$ is a better representation of the actual PV sensitivity than $\hat{q}_g$, although the boundary condition is not considered in $\hat{q}_E$ inversion and the choice of the basic state is not precise enough.

Differentiating the contributions of TC outflow and boundary layer processes through sensitivity to winds or PV magnitudes isn't straightforward due to the model's inherent characteristics.

Finding the contribution of nonlinear imbalance in TC development can shed light on understanding processes like supergradient wind in the boundary layer process (e.g., Kepert and Wang 2001; Montgomery and Smith 2017; Fei et al. 2021) and the outflow layer, where nonlinear balance is violated (e.g., Cohen et al. 2017; Wang et al. 2020). At the same time, we should note that the sensitivity to PV calculated from the model output does not necessarily follow the "adjoint PV dynamics" in models that use PV as a diagnostic variable, such as the QG channel model (e.g., Kim and Beare 2011). The sensitivity to PV merely rearranges the sensitivity to diagnostic variables from the model output into a more interpretable form to the dynamical processes behind the system development.

Neither $\hat{q}_g$ nor $\hat{q}_E$ shows PV sensitivity robust enough at the outflow layer when compared with the boundary layer sensitivity. If the preference for having inertial instability or low PV at TC's outflow layer is not recognized by the model's adjoint, assessing the sensitivity to PV only provides qualitative knowledge of PV preference at UTLS. From previous cases with either μ or mid-level circulation as a response function, the WRF adjoint model always produces larger wind and temperature sensitivities near the surface, with sensitivity magnitude decreasing with height. Thus it is impossible to determine the relative importance and contribution of TC outflow and TC boundary layer process by looking at the magnitude of sensitivity to winds or to PV at these levels. One way to compare their relative contribution is by comparing how much the storm will intensify when optimal perturbation carries the same amount of kinetic and thermal energy to each level is added to the initial condition (Barrett et al. 2016; Brooke-Zibton 2022). One can also choose the circulation at the outflow level as the response function, anticipating the sensitivity will decrease from the upper to the lower level. Another method would be having a model that can produce an idealized hurricane and uses Ertel PV or QGPV as the diagnostic variable (e.g., Kim and Beare 2011; Xu 1994). Those being said, the sensitivity to PV remains valuable for TC track predictability since TC's track is often steered by mid-latitude features in the mid-troposphere, where the model-generated adjoint sensitivities have a broader horizontal presence.

Operator	Coefficient	Coef Scale
∇^2	$\nabla^2 \frac{\partial^2 \Phi}{\partial^2 \pi}$	10^{-11}
∇^4	$\frac{\partial^2 \Phi}{\partial^2 \pi}$	10^{-2}
$\partial^2_{x\pi}$	$\nabla^2 \frac{\partial^2 \bar{\Psi}}{\partial x \pi} + \frac{f}{x}\frac{\partial \bar{\Psi}_{x\pi}}{\partial x} + \frac{f}{y}\frac{\partial \bar{\Psi}_{x\pi}}{\partial y} + f\nabla^2 \frac{\partial^2 \Psi}{\partial x \pi}$ $+2\frac{\partial^2 \bar{\Psi}}{\partial x^2}\frac{\partial^2 \bar{\Psi}_{x\pi}}{\partial y^2} + 2\frac{\partial^2 \bar{\Psi}}{\partial y^2}\frac{\partial^2 \bar{\Psi}_{x\pi}}{\partial y^2} - 4\frac{\partial^2 \bar{\Psi}}{\partial xy}\frac{\partial^2 \bar{\Psi}_{x\pi}}{\partial xy}$	10^{-15}
$\partial^2_{y\pi}$	$\nabla^2 \frac{\partial^2 \bar{\Psi}}{\partial y \pi} + \frac{f}{x}\frac{\partial \bar{\Psi}_{y\pi}}{\partial y} + \frac{f}{y}\frac{\partial \bar{\Psi}_{y\pi}}{\partial y} + f\nabla^2 \frac{\partial^2 \bar{\Psi}}{\partial y \pi}$ $+2\frac{\partial^2 \bar{\Psi}}{\partial x^2}\frac{\partial^2 \bar{\Psi}_{y\pi}}{\partial y^2} + 2\frac{\partial^2 \bar{\Psi}}{\partial y^2}\frac{\partial^2 \bar{\Psi}_{y\pi}}{\partial y^2} - 4\frac{\partial^2 \bar{\Psi}}{\partial xy}\frac{\partial^2 \bar{\Psi}_{y\pi}}{\partial xy}$	10^{-15}
$\nabla^2 \partial^2_{x\pi}$	$\frac{\partial^2 \bar{\Phi}}{\partial x \pi} + f\frac{\partial^2 \bar{\Psi}}{\partial x \pi}$	10^{-5}
$\nabla^2 \partial^2_{y\pi}$	$\frac{\partial^2 \bar{\Phi}}{\partial y \pi} + f\frac{\partial^2 \bar{\Psi}}{\partial y \pi}$	10^{-5}
∂^2_{π}	$-f_x\bar{\zeta}_x - f_y\bar{\zeta}_y - f\nabla^2\bar{\zeta} - 2\frac{\partial^2 \bar{\Psi}}{\partial x^2}\frac{\partial^2 \zeta}{\partial x^2}$ $-2\frac{\partial^2 \bar{\Psi}}{\partial y^2}\frac{\partial^2 \bar{\zeta}}{\partial x^2} + 4\frac{\partial^2 \bar{\Psi}}{\partial xy}\frac{\partial^2 \bar{\zeta}}{\partial xy}$	10^{-17}
$\partial^3_{x\pi^2}$	$-f_x\bar{\zeta}$	0
$\partial^3_{y\pi^2}$	$-f_y\bar{\zeta}$	10^{-15}
$\nabla^2 \partial^2_{\pi^2}$	$-f\bar{\zeta}$	10^{-8}
$\partial^3_{x^2\pi}$	$f_x\frac{\partial^2 \bar{\Psi}}{\partial x \pi}$	0
$\partial^3_{y^2\pi}$	$f_y\frac{\partial^2 \bar{\Psi}}{\partial y \pi}$	10^{-12}
$\partial^3_{xy\pi}$	$f_x\frac{\partial^2 \bar{\Psi}}{\partial x \pi} + f_y\frac{\partial^2 \bar{\Psi}}{\partial y \pi}$	10^{-12}
$\partial^4_{x^2\pi^2}$	$-2\frac{\partial^2 \bar{\Psi}}{\partial y^2}\bar{\zeta}$	10^{-8}
$\partial^4_{y^2\pi^2}$	$-2\frac{\partial^2 \bar{\Psi}}{\partial x^2}\bar{\zeta}$	10^{-8}
$\partial^4_{x^3\pi}$	$2\frac{\partial^2 \bar{\Psi}}{\partial y^2}\frac{\partial^2 \bar{\Phi}}{\partial x \pi}$	10^{-5}
$\partial^4_{y^3\pi}$	$2\frac{\partial^2 \bar{\Psi}}{\partial x^2}\frac{\partial^2 \bar{\Phi}}{\partial y \pi}$	10^{-5}
$\partial^4_{xy^2\pi}$	$2\frac{\partial^2 \bar{\Psi}}{\partial x^2}\frac{\partial^2 \bar{\Phi}}{\partial x \pi} - 4\frac{\partial^2 \bar{\Psi}}{\partial xy}\frac{\partial^2 \bar{\Phi}}{\partial y \pi}$	10^{-5}
$\partial^4_{x^2y\pi}$	$2\frac{\partial^2 \bar{\Psi}}{\partial y^2}\frac{\partial^2 \bar{\Phi}}{\partial y \pi} - 4\frac{\partial^2 \bar{\Psi}}{\partial xy}\frac{\partial^2 \bar{\Phi}}{\partial x \pi}$	10^{-5}
$\partial^4_{xy\pi^2}$	$4\frac{\partial^2 \bar{\Psi}}{\partial xy}\bar{\zeta}$	10^{-8}

TABLE 4.1: List of different operators, coefficients, and the magnitude of the coefficients involved in the sensitivity to Ertel PV calculation.

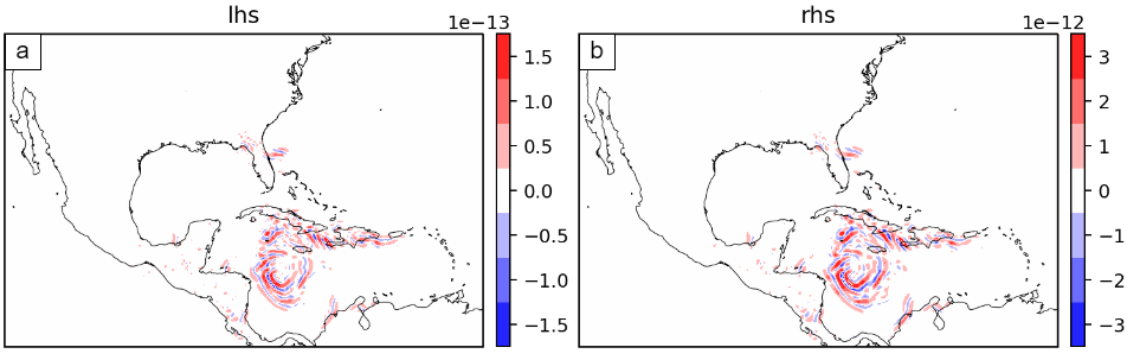

FIGURE 4.1: a) LHS of (4.20) if φ_P operates on 250 hPa sensitivity to QGPV ($\varphi_P \hat{q}_g$) for the case of Hurricane Ian valid at 1800 UTC 26 September 2022. b) RHS of (4.20) at 250 hPa and the same valid time, equivalent to $\varphi_P \hat{q}_E$.

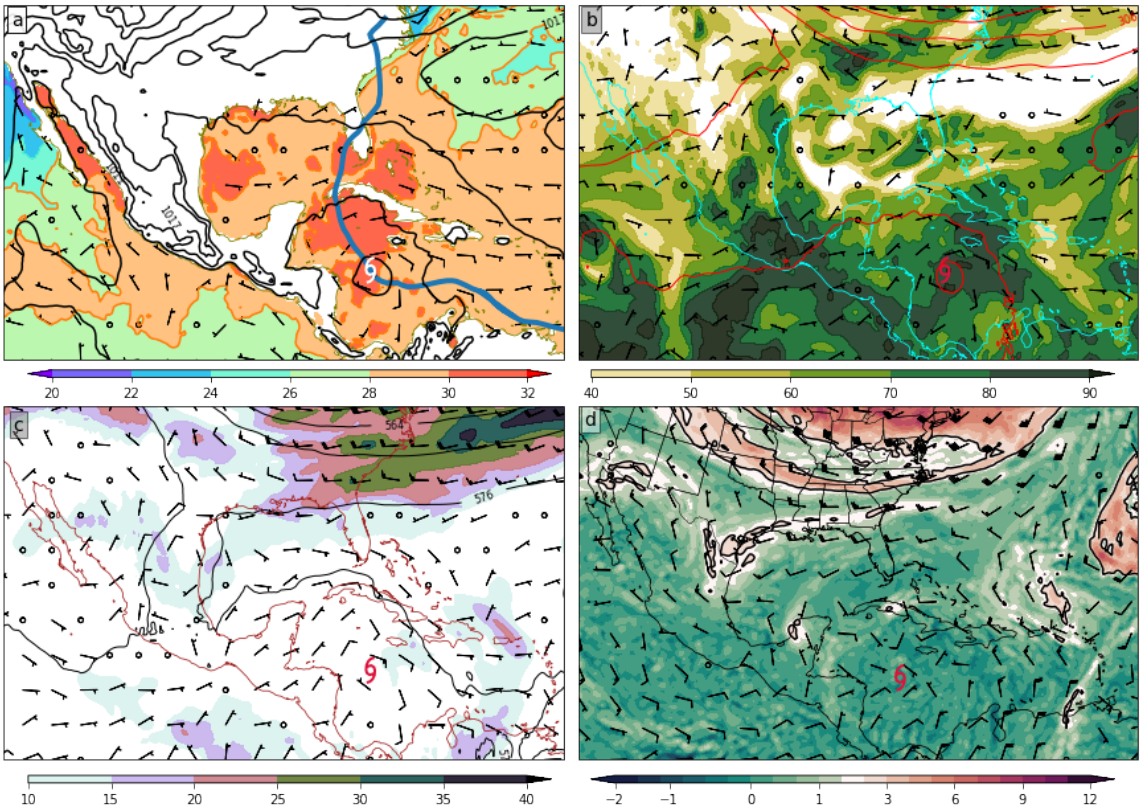

FIGURE 4.2: Synoptic set-up of Hurricane Ian in ERA5 reanalysis valid at 1800 UTC 25 September 2022. a) Sea surface temperature (shaded with unit K), mean sea level pressure (contour; interval 5 hPa), 10-m wind barbs, and thick blue curve depicts the best track from IBTrARCs; b) 850 - 700 hPa average relative humidity (shaded in percentage value), 700 geopotential height (contour; interval 3 dam), and 700 hPa wind barbs; c) 850 - 200 hPa vertical wind shear (shaded with unit m/s), 500 hPa geopotential height (black contour; interval 6 dam) and wind barbs d) 200 hPa Ertel PV (shaded with PV unit) from the WRF model at the initial time, and 200 hPa wind barbs from ERA 5 reanalysis. The hurricane symbol indicates Hurricane Ian's location valid at 1800 UTC 25 September 2022

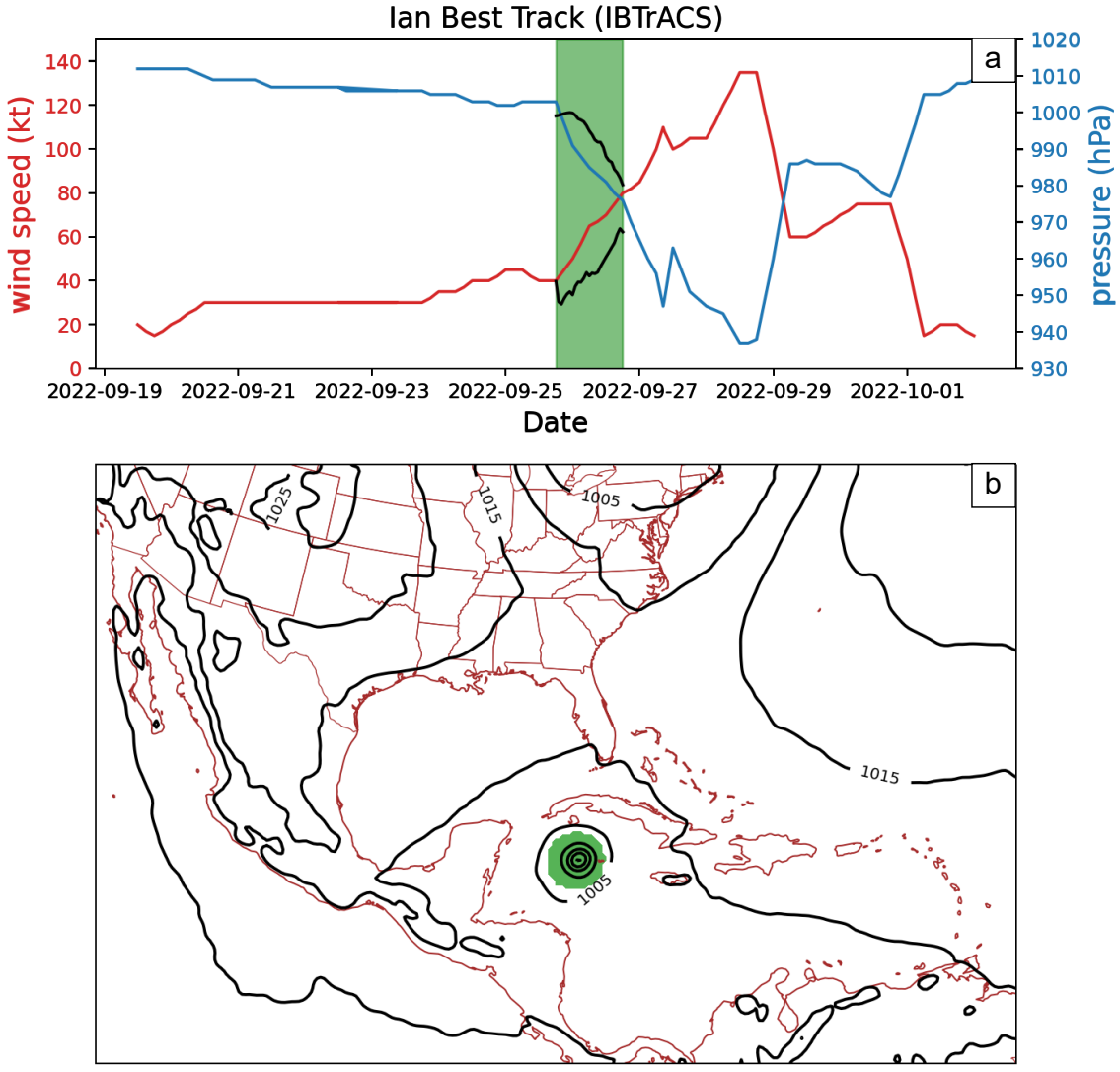

FIGURE 4.3: a) Hurricane Ian's Best Track maximum wind speed (red) and minimal pressure (blue). Maximum wind speed and minimal pressure from WRF simulation are in black lines. b) Sea level pressure from the WRF model at 1800 UTC 26 September 2022 (F24) and the response function area for ($R = -\mu'$) indicated by the green patch

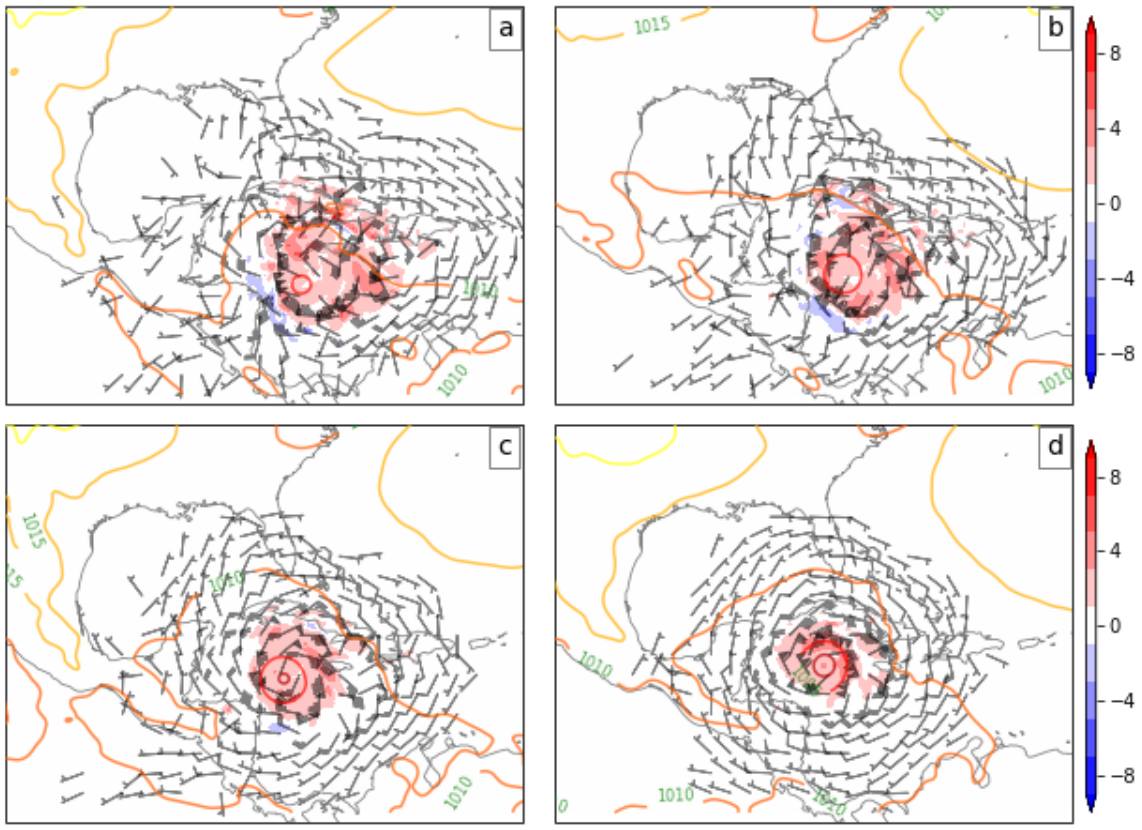

FIGURE 4.4: Qualitative 800 hPa sensitivity to horizontal wind in barbs, sensitivity to temperature (shaded with unit Pa/K), and sea level pressure (contour; interval 5 hPa) valid at a) 1800 UTC 25 September 2022 (F00); b) 0000 UTC 26 September 2022 (F06); c) 0600 UTC 26 September 2022 (F12); d) 1200 UTC 26 September 2022 (F18)

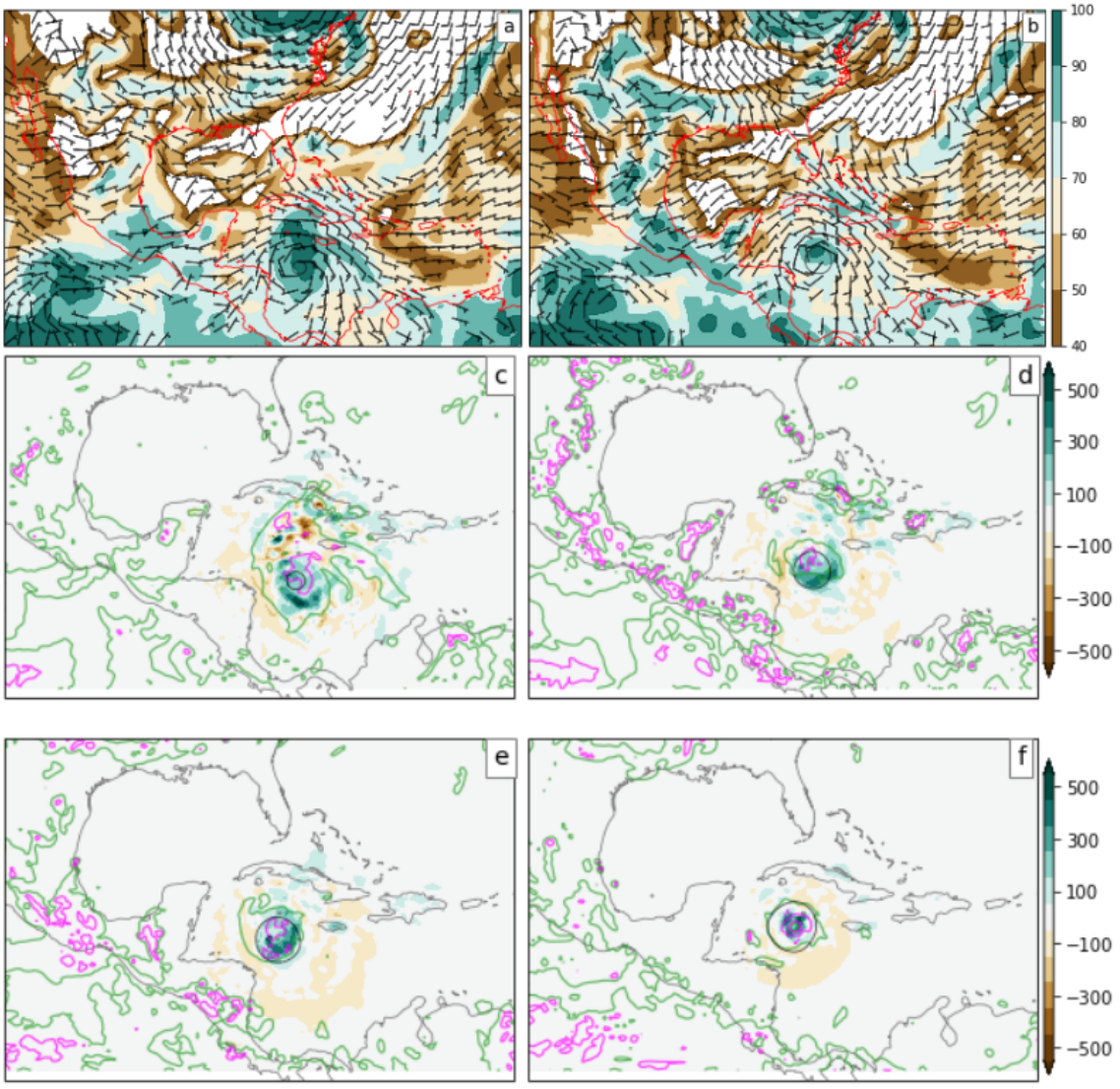

FIGURE 4.5: 800 hPa relative humidity (shaded with value in percentage) and wind (barbs) from WRF trajectory valid at a) 1800 UTC 25 September 2022 (F00); b) 1200 UTC 26 September 2022 (F18). 800 hPa relative humidity contour (80% in green, 95% in magenta) and sensitivity to water vapor mixing ratio (shaded with unit $Pa/(kg/kg)$) valid at c) 1800 UTC 25 September 2022 (F00); d) 0000 UTC 26 September 2022 (F06); e) 0600 UTC 26 September 2022 (F12); f) 1200 UTC 26 September 2022 (F18)

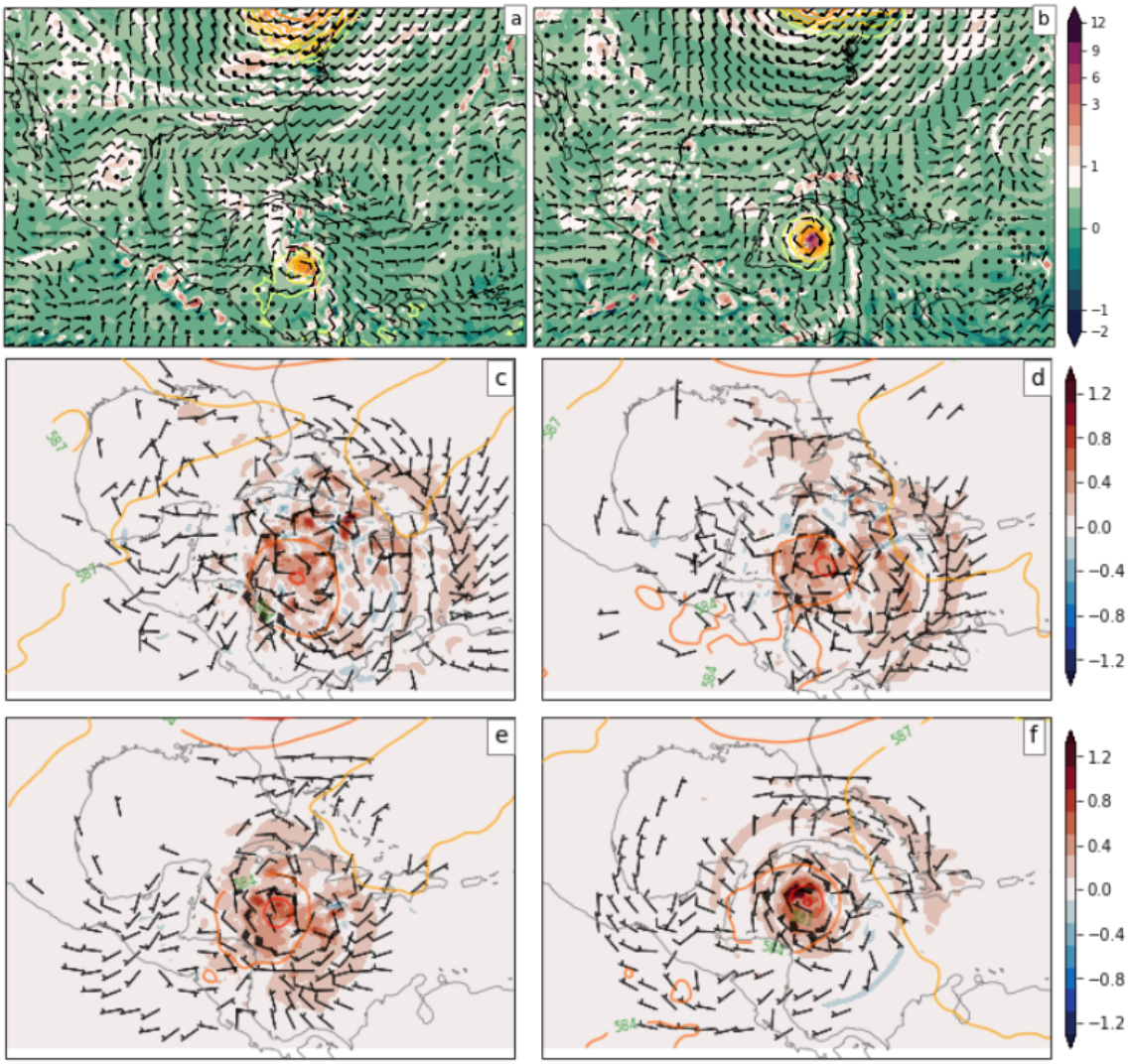

FIGURE 4.6: 500 hPa wind field (barbs) and Ertel PV (shaded with PVU) from WRF trajectory valid at a) 1800 UTC 25 September 2022 (F00); b) 1200 UTC 26 September 2022 (F18). 500 hPa sensitivity to the wind (barbs), sensitivity to temperature (shaded with unit Pa/K), and 500 hPa geopotential height (contour, interval 3 dam) valid at c) 1800 UTC 25 September 2022 (F00); d) 0000 UTC 26 September 2022 (F06); e) 0600 UTC 26 September 2022 (F12); f) 1200 UTC 26 September 2022 (F18)

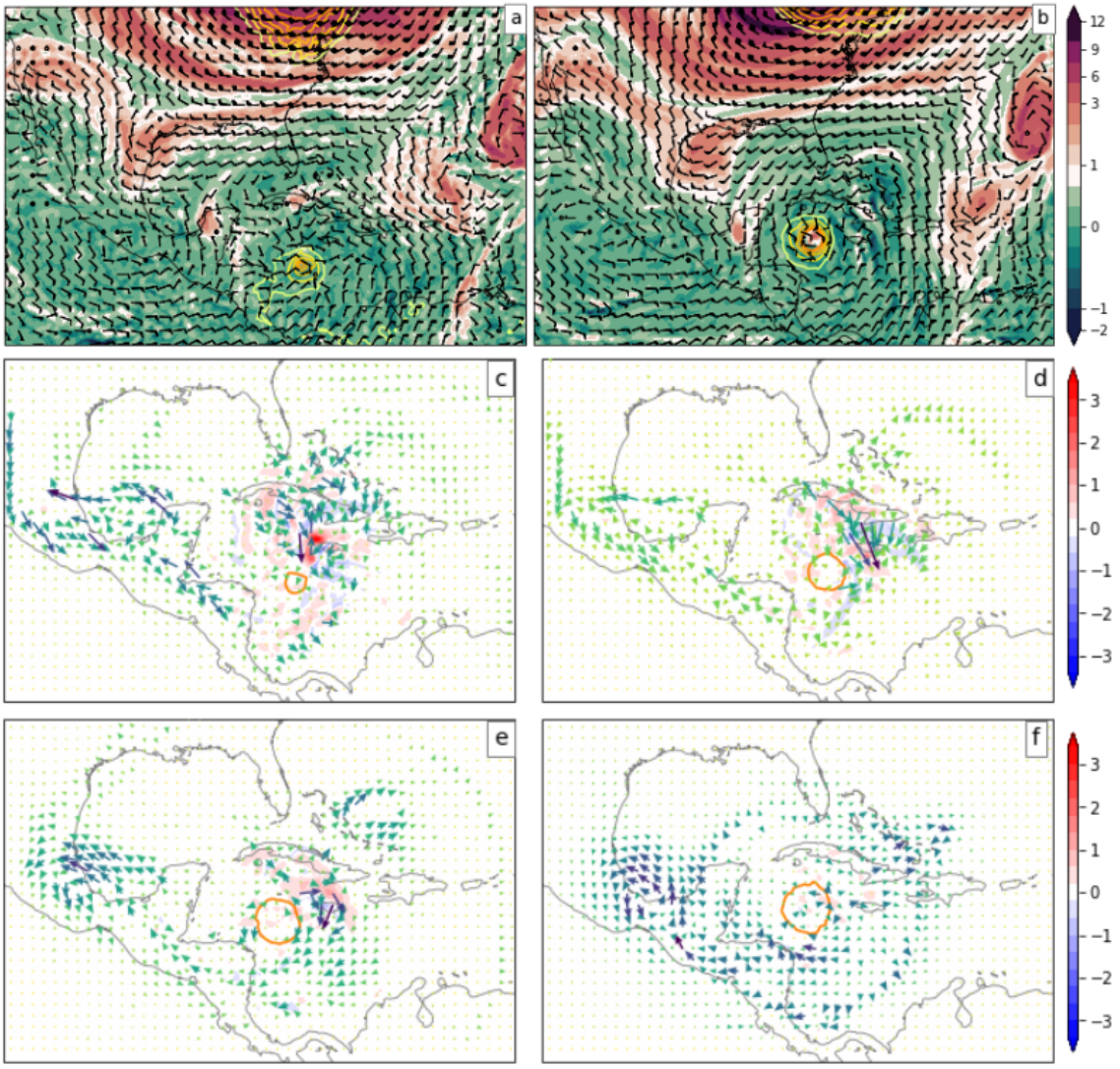

FIGURE 4.7: 250 wind field (barbs), jet (contour, interval 10 $m \cdot s^{-1}$), Ertel PV (shaded with PVU) and 1004 hPa sea level pressure contour from WRF trajectory valid at a) 1800 UTC 25 September 2022 (F00); b) 1200 UTC 26 September 2022 (F18). 250 hPa sensitivity to the wind (quiver, darker color for larger sensitivity), sensitivity to temperature (shaded with unit Pa/K), and 1005 hPa sea level pressure contour valid at c) 1800 UTC 25 September 2022 (F00); d) 0000 UTC 26 September 2022 (F06); e) 0600 UTC 26 September 2022 (F12); f) 1200 UTC 26 September 2022 (F18)

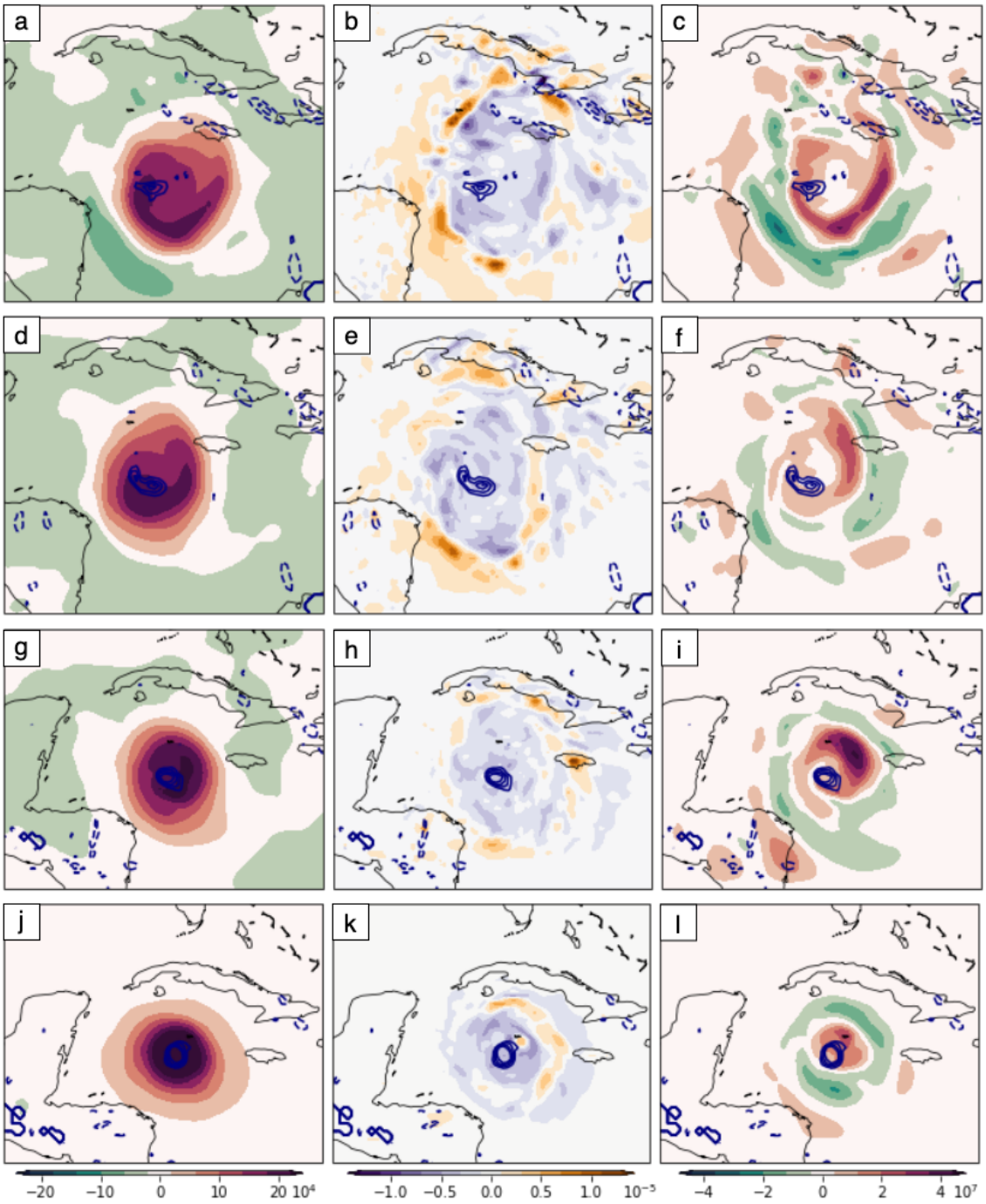

FIGURE 4.8: 850 hPa Sensitivity to QGPV (shaded; a,d,g,j), sensitivity to geostrophic imbalance (shaded; b,e,h,k), and sensitivity to Ertel PV (shaded; c,f,i,l) inverted in a small domain near the storm center. Trajectory 850 hPa Ertel PV (blue contours with 1 PVU interval) valid at 1800 UTC 25 September 2022 (F00; a,b,c), 0000 UTC 26 September 2022 (F06; d,e,f), 0600 UTC 26 September 2022 (F12; g,h,i), and 1200 UTC 26 September 2022 (F18; j,k,l) show Hurricane Ian's location.

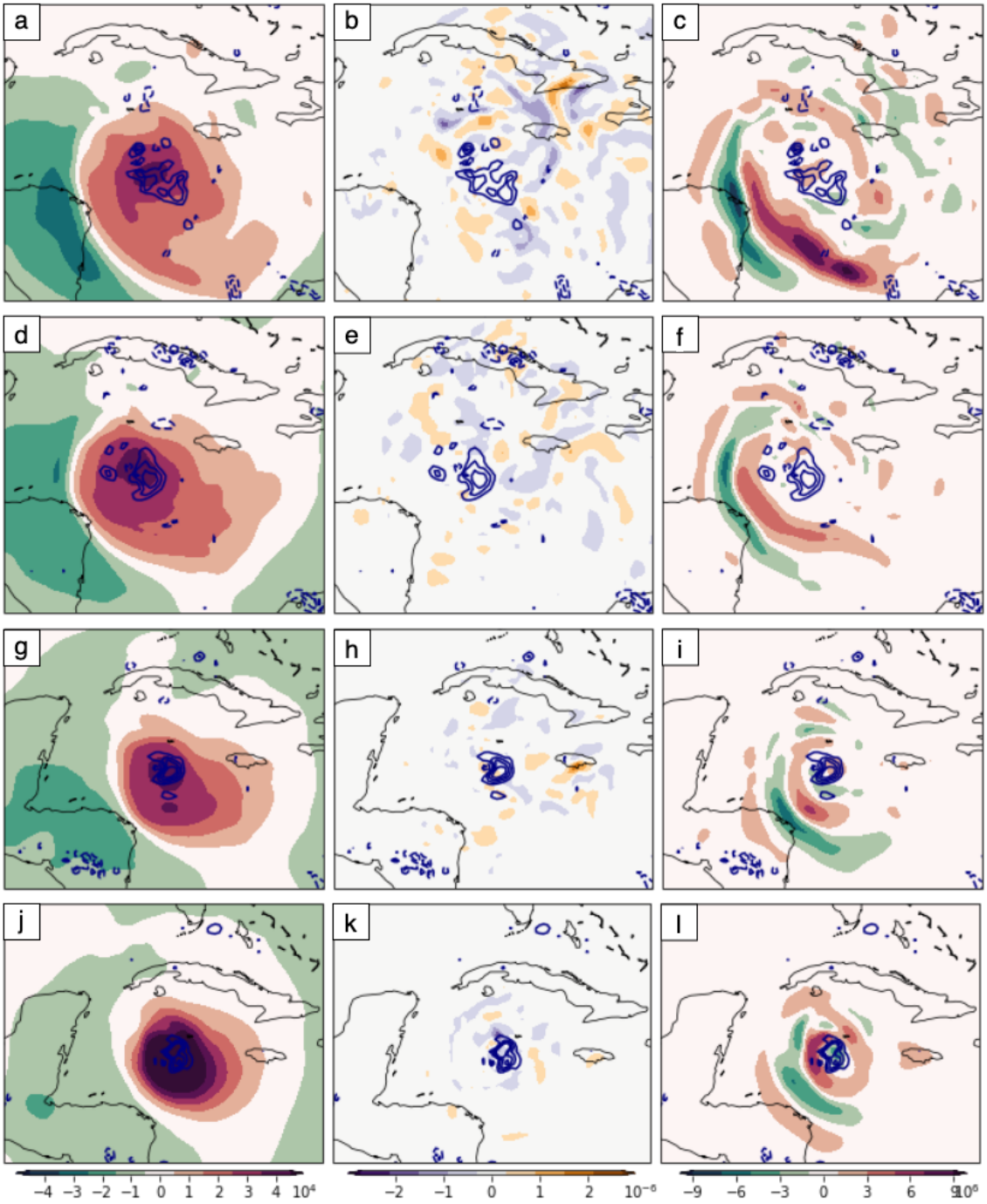

FIGURE 4.9: Same as Fig. 4.8 but for sensitivity to QGPV, sensitivity to geostrophic imbalance, sensitivity to Ertel PV, and trajectory Ertel PV near storm center at 500 hPa

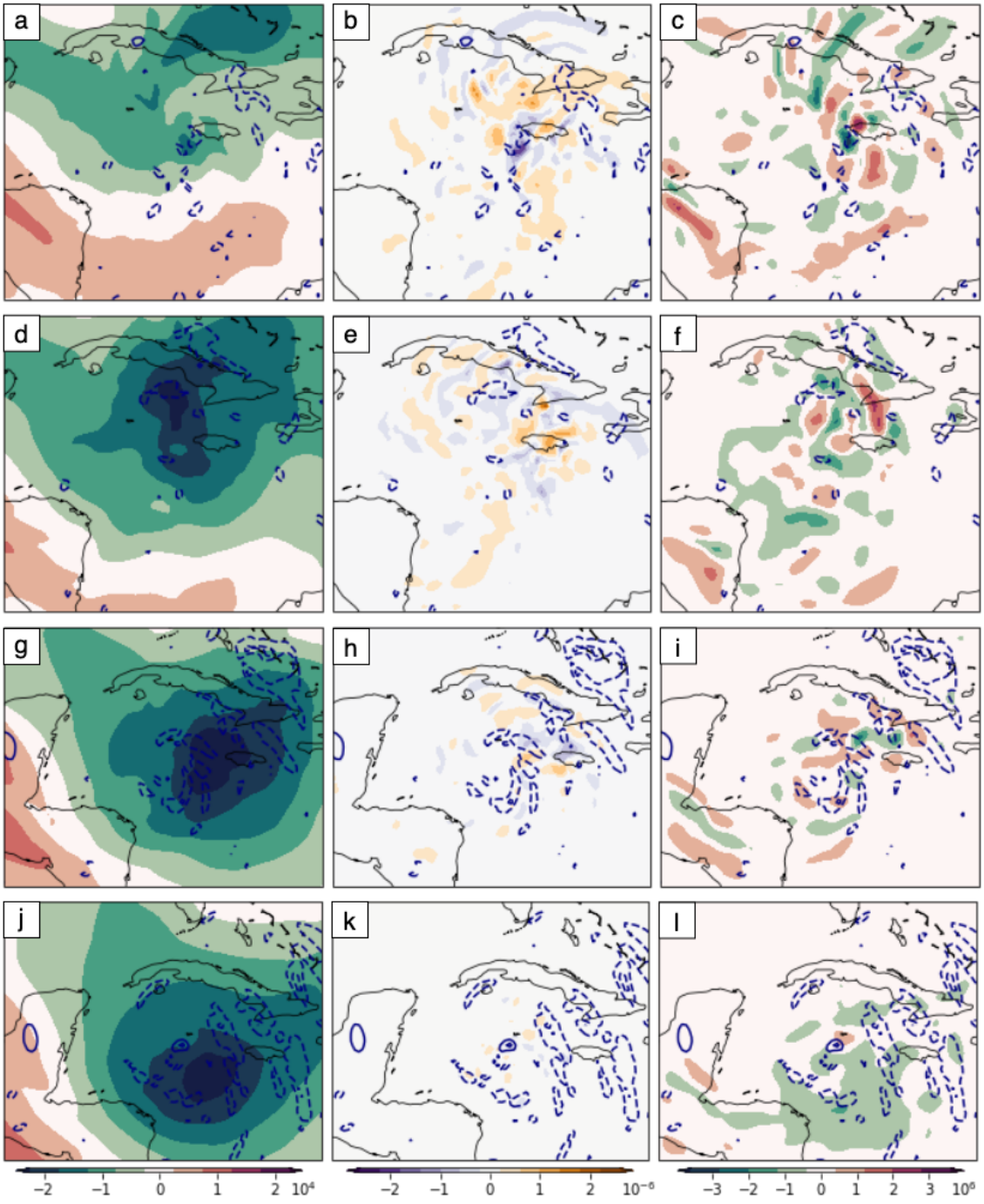

FIGURE 4.10: Same as Fig. 4.8 but for sensitivity to QGPV, to Imbalance, and to Ertel PV near storm center at 250 hPa. -0.3 PVU contour of 250 hPa Ertel PV depicted by the blue dashed line

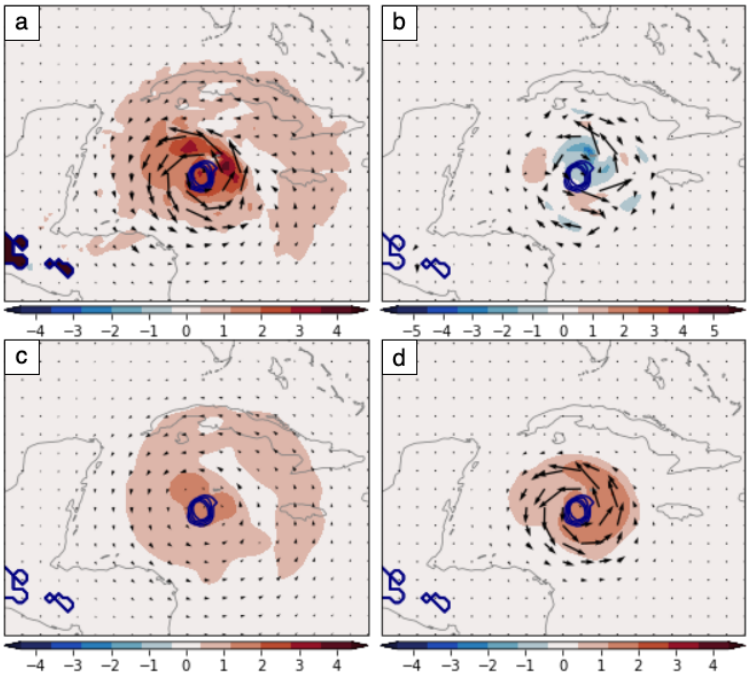

FIGURE 4.11: 850 hPa sensitivity to winds (vector) and sensitivity to temperature (shaded, scaled differently in each panel) valid at 1200 UTC 26 September 2022 (F18) a) from WRF-adjoint output; b) recovered from sensitivity to Ertel PV; c) recovered from sensitivity to geostrophic imbalance; and d) recovered from sensitivity to QGPV.

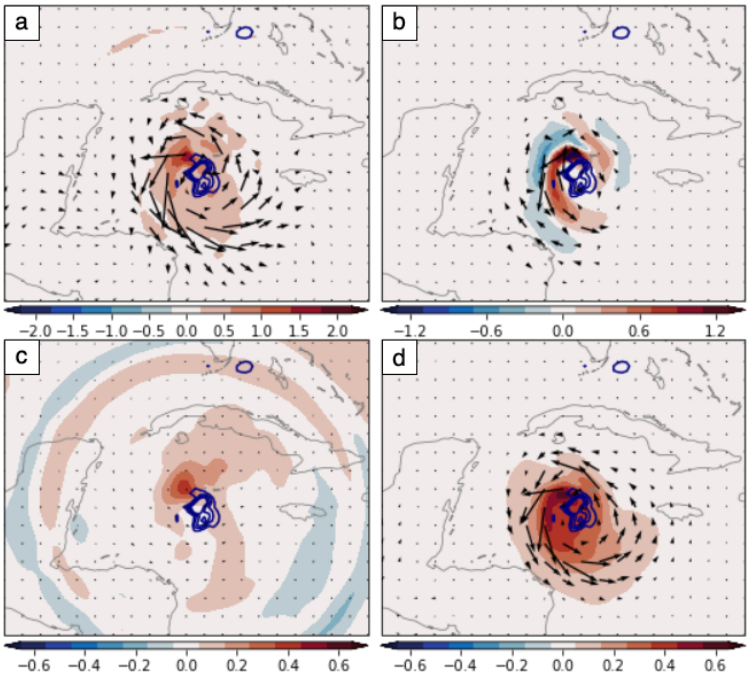

FIGURE 4.12: Same as Fig. 4.11 but at 500 hPa.

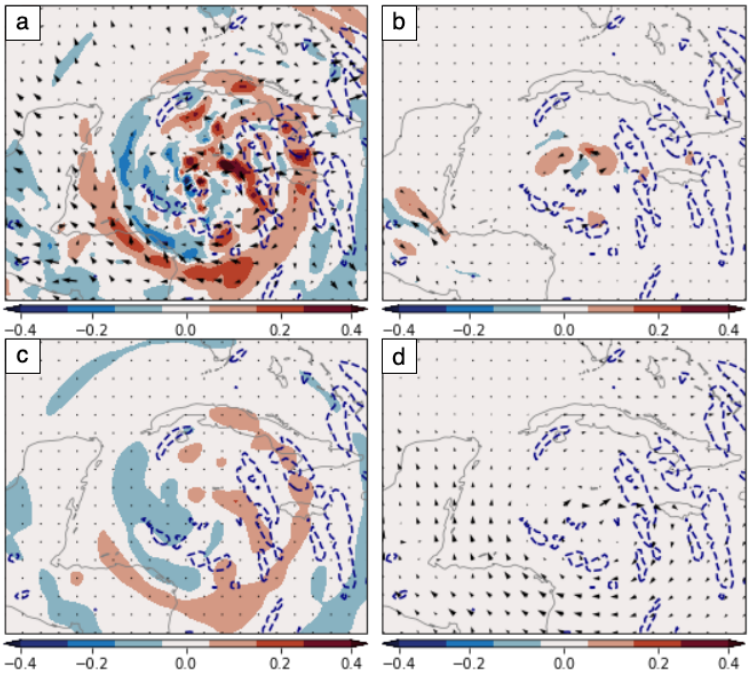

FIGURE 4.13: Same as Fig. 4.11 but at 250 hPa.

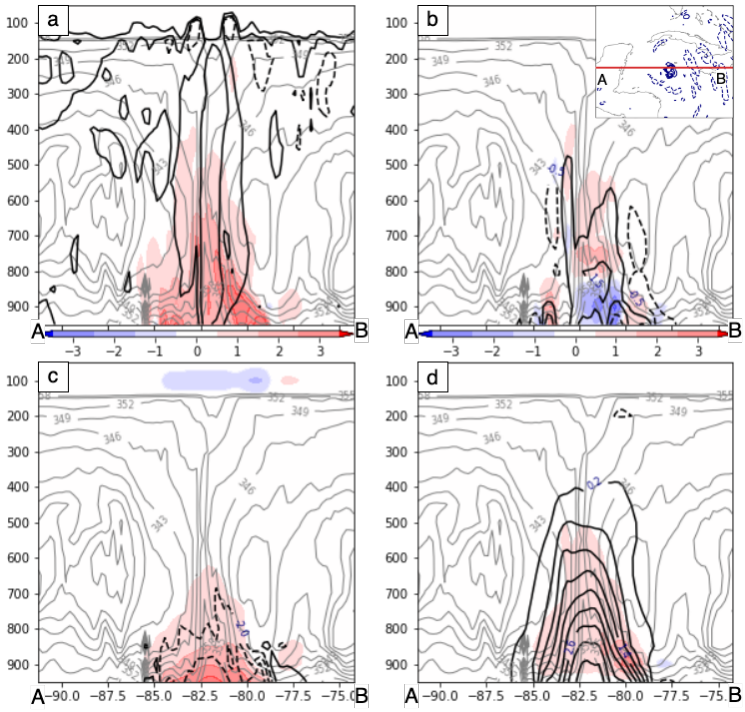

FIGURE 4.14: F18 cross-section of sensitivity to the temperature and trajectory equivalent potential temperature (gray contour with 3 K interval). a) $\hat{\theta}$ from WRF-adjoint with trajectory PV (-0.3, 0.5, and 2 PVU contour), b) $\hat{\theta}_E$ (shaded) with $\hat{q}_E$ contour (solid positive, dashed negative; 10^7 Pa/PVU interval), c) $\hat{\theta}_i$ (shaded) with $\hat{a}$ contour (solid positive, dashed negative; 4×10^{-6} $Pa \cdot s \cdot m^{-2}$ interval), and d) $\hat{\theta}_g$ (shaded) and $\hat{q}_g$ contour (solid positive, dashed negative; 4^4 $Pa \cdot s$ interval). The cross-section taken is shown at the upper right of panel b, with 500 hPa positive PV contours and a 250 hPa negative PV contour.

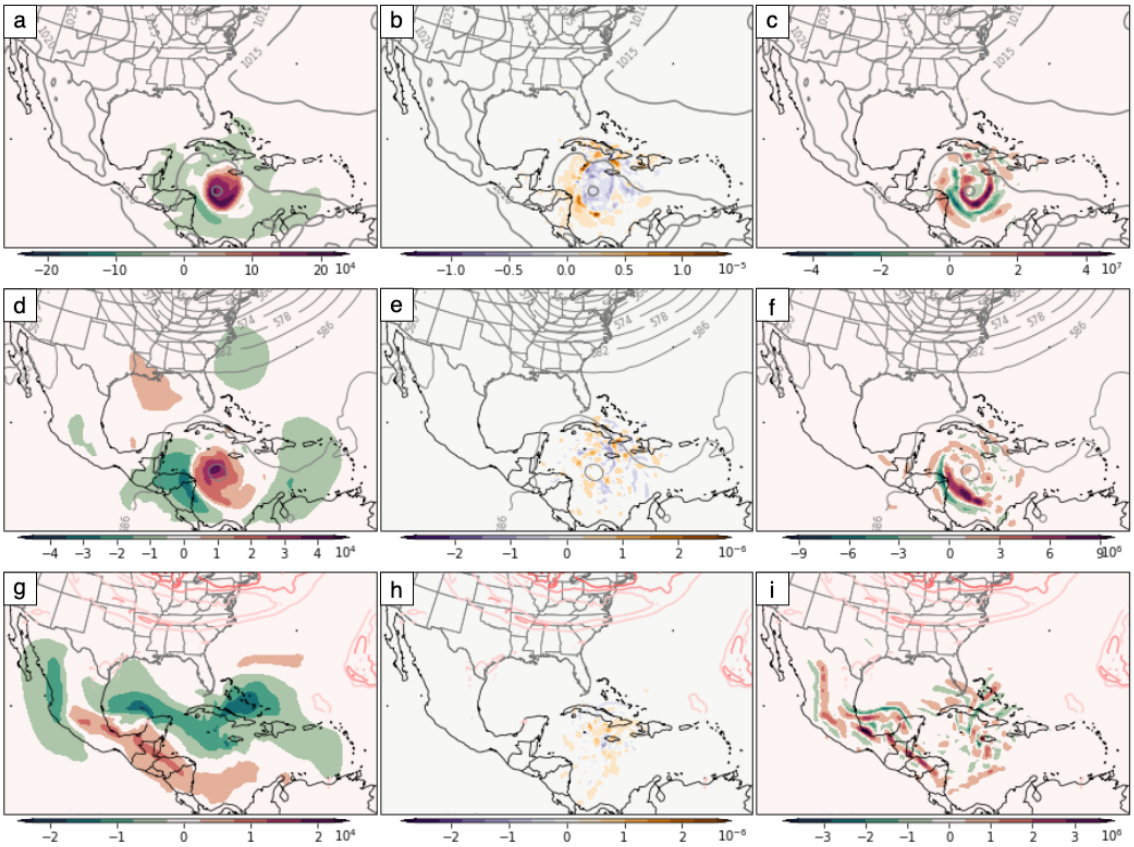

FIGURE 4.15: Same as Fig. 4.8 but only valid at 1800 UTC 25 September 2022 (F00). In addition to $\hat{q}_g$, $\hat{a}$, and $\hat{q}_E$, panels a,b,c show 850 hPa with sea level pressure (contour; 5 hPa interval). Panels d,e,f show 500 hPa with geopotential height (contour; 4 dam interval). Panels g,h,i show 850 hPa with Ertel PV contour (1 PVU interval).

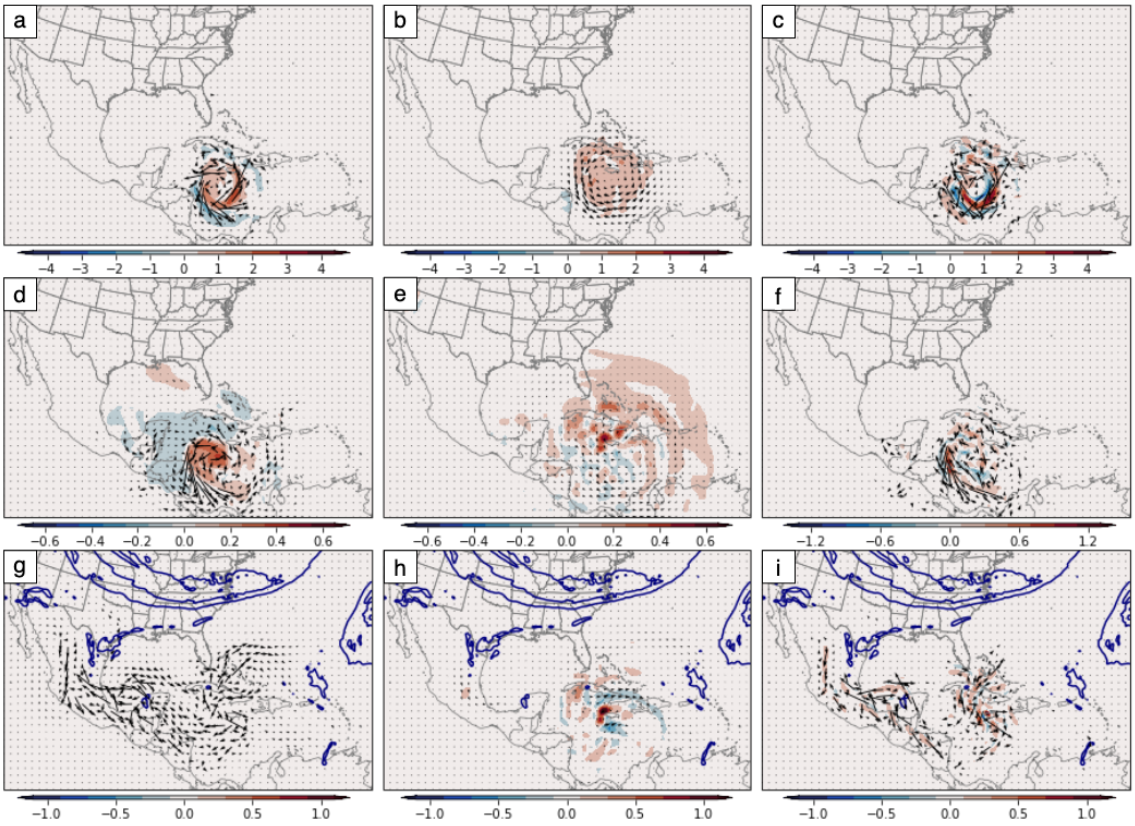

FIGURE 4.16: Column 1 shows $\hat{\mathbf{v}}_g$ (barbs) and $\hat{\theta}_g$ (shaded with unit Pa/K) recovered from $\hat{q}_g$, column 2 shows $\hat{\mathbf{v}}_i$ (barbs) and $\hat{\theta}_i$ (shaded with unit Pa/K) recovered from $\hat{a}$, column 3 shows $\hat{\mathbf{v}}_E$ (barbs) and $\hat{\theta}_E$ (shaded with unit Pa/K) recovered from $\hat{q}_E$, all valid at 1800 UTC 25 September 2022 (F00). Row 1 shows the above variables at 850 hPa, row 2 is 500 hPa and row 3 is 250 hPa with 2 PVU contour.

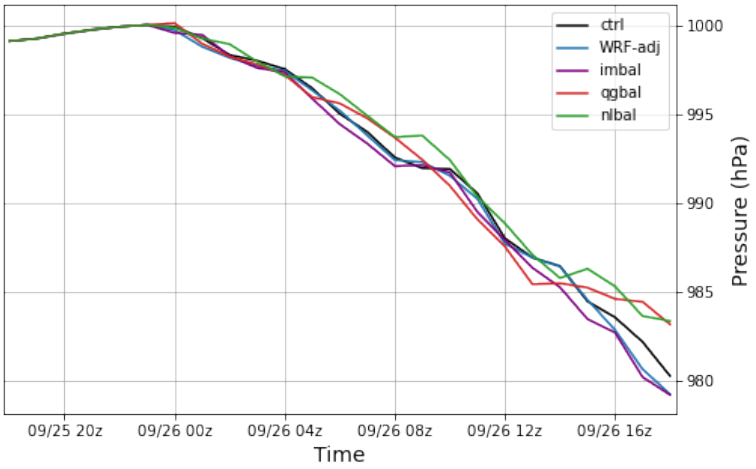

FIGURE 4.17: Minimum SLP of Hurricane Ian from exp "ctrl" (black), exp "WRF-adj" (blue), exp "qgbal" (red), exp "imbal" (purple), and exp "nlbal" (green)

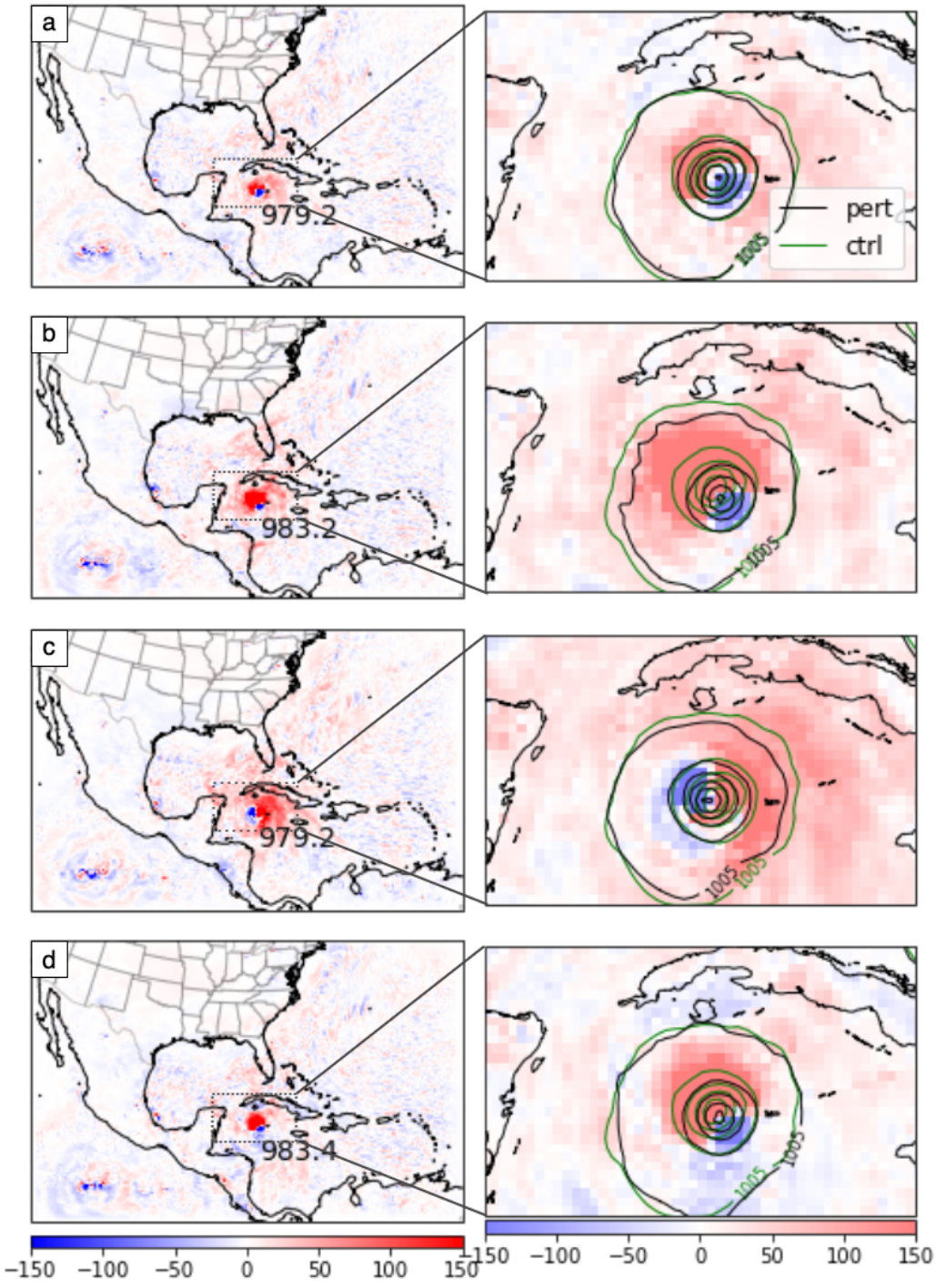

FIGURE 4.18: Column 1 shows the difference in SLP (shaded with the unit in Pa) between the perturbed experiments a) "WRF-adj", b) "qgbal", c) "imbal", d) "nlbal" and the unperturbed experiment "ctrl" in color shading, red if "pert" > "ctrl", blue if "pert" < "ctrl". Column 2 zooms in the TC center with SLP contour from "ctrl" (green; 5 hPa interval) and each perturbed experiment (black; 5 hPa interval).

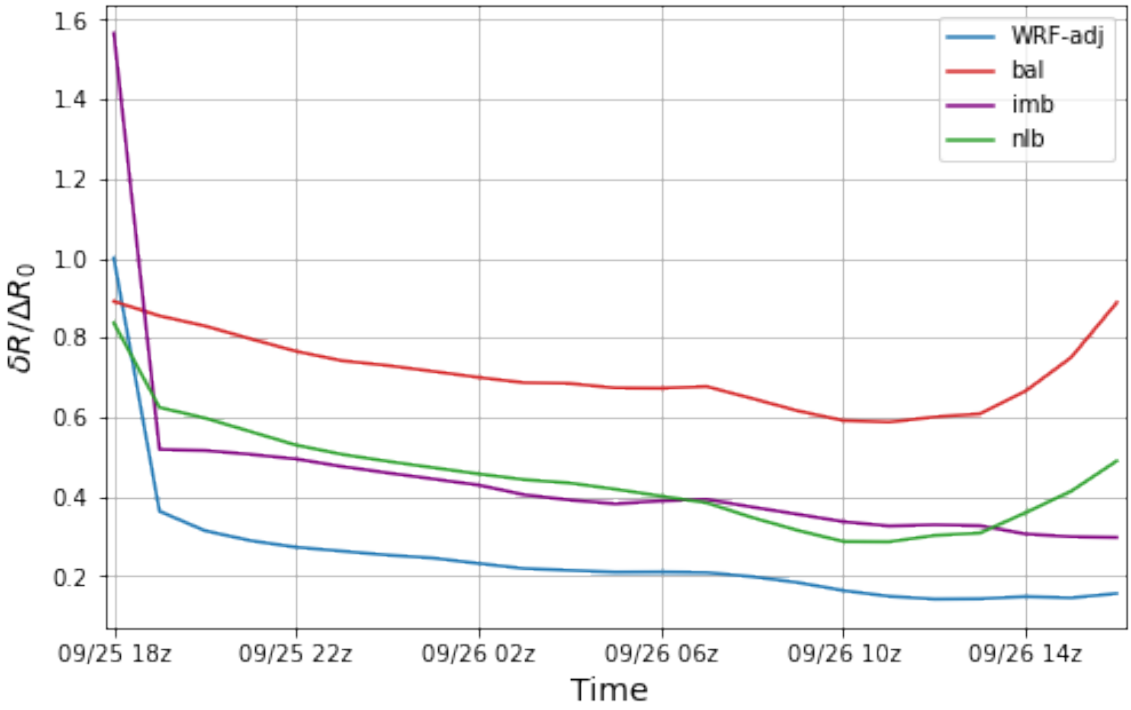

FIGURE 4.19: Time evolution of the change in response function ($\delta R = \langle \partial R/\partial \mathbf{x}, \mathbf{x}' \rangle$) normalized by the prescribed perturbation energy, ΔR_0, for optimal perturbations informed by WRF-adjoint sensitivity (blue; "WRF-adj"-"ctrl"), geostrophically balanced adjoint sensitivity (red; "qgbal"-"ctrl"), unbalanced adjoint sensitivity (purple; "imbal"-"ctrl"), and nonlinear balanced adjoint sensitivity (green; "nlbal"-"ctrl")

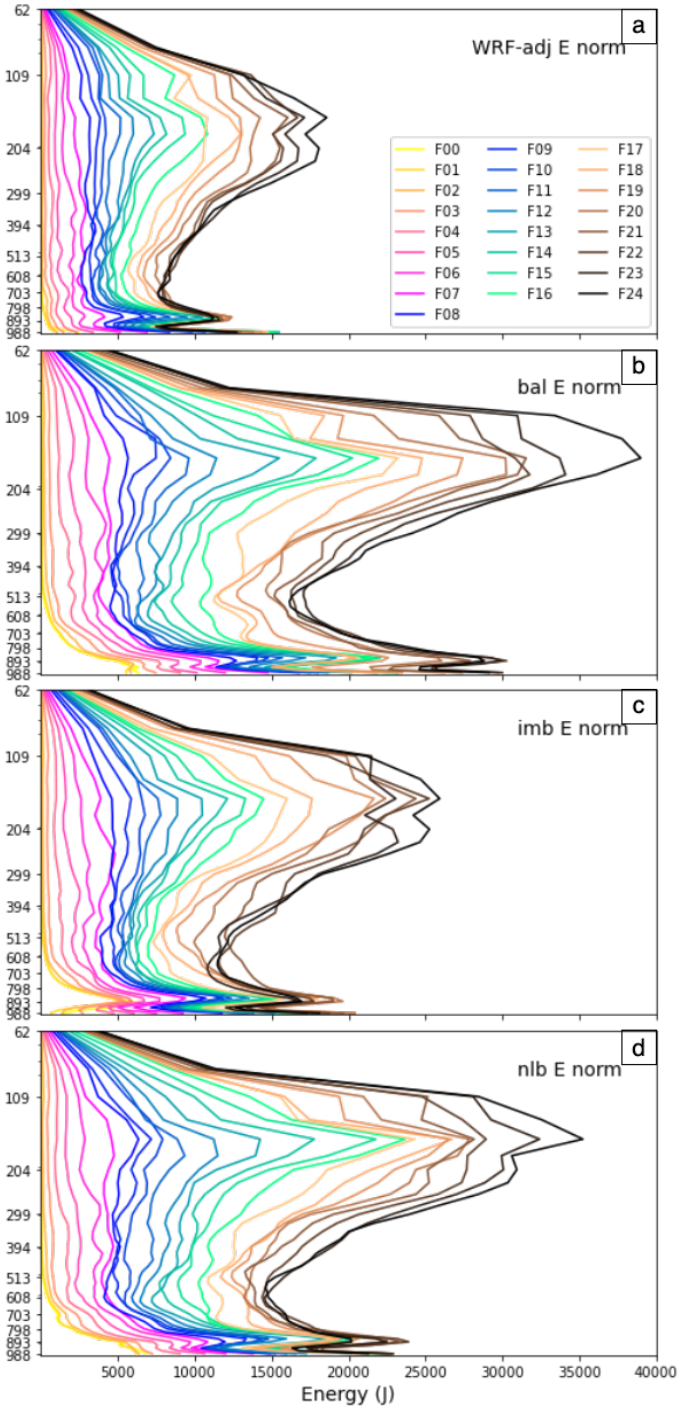

FIGURE 4.20: Perturbation energy norm $\frac{1}{2}\left(u'^2 + v'^2 + \frac{c_p}{T_{ref}}T'^2\right)$ summed over each model level for optimal perturbation informed by a) WRF-adjoint sensitivity, b) geostrophically balanced adjoint sensitivity, c) unbalanced adjoint sensitivity and d) nonlinear balanced adjoint sensitivity at each time steps from forecast hour F00 to F24 (color legends for each time step listed in panel a).

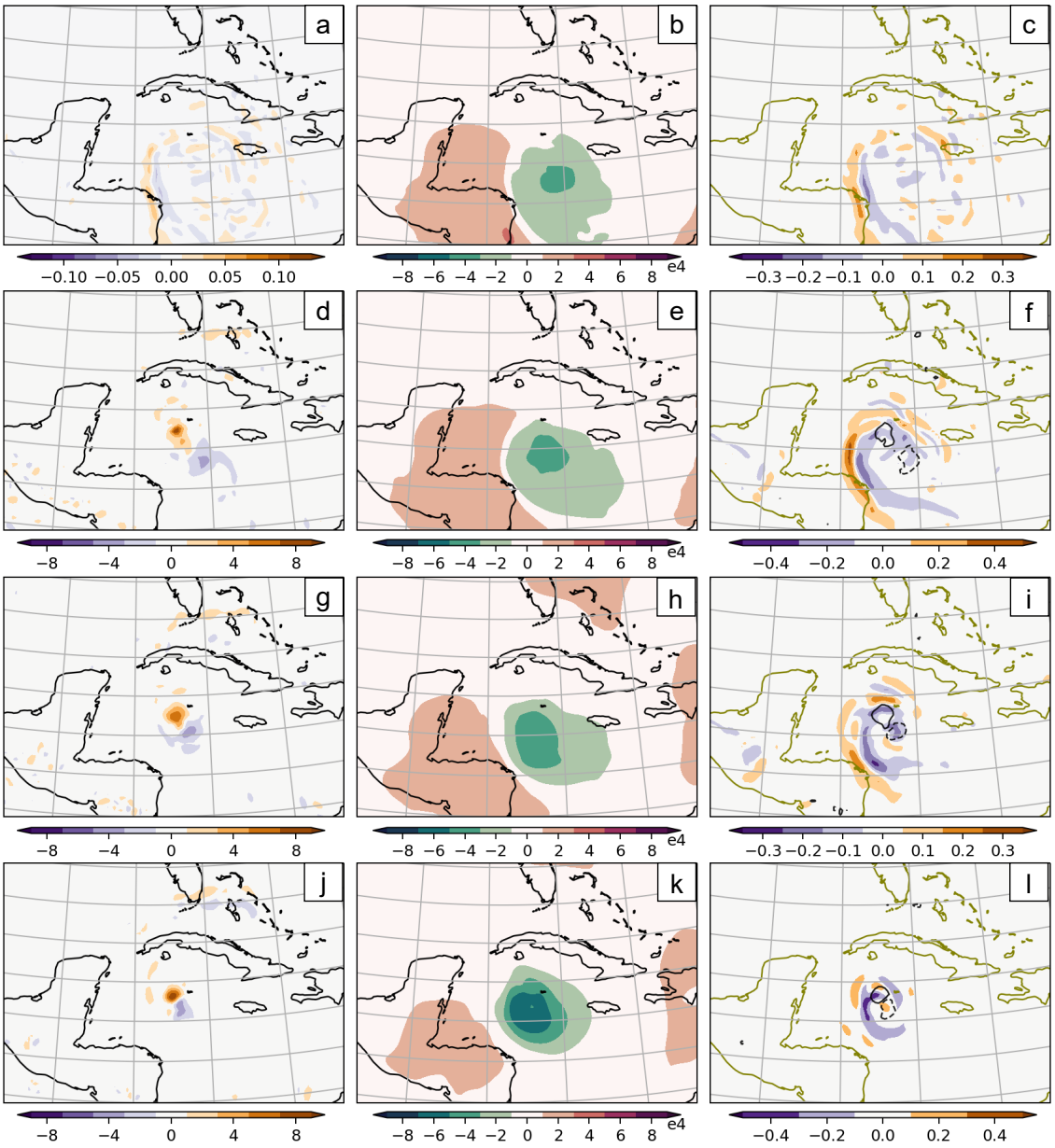

FIGURE 4.21: 500 hPa QGPV difference from "WRF-adj"-"ctrl" (shaded with unit s^{-1}, column 1). 500 hPa minus sensitivity to QGPV, $-\hat{q}_g$, (shaded with unit $Pa \cdot s$, column 2). 500 hPa Perturbation QGPV (shaded with unit s^{-1}) when geostrophically balanced perturbations, $u'_{g,t}$, $v'_{g,t}$, $\theta'_{g,t}$ are introduced at each time step $t = 0, 6, 12, 18$, (column 3) with perturbation QGPV from column 1 contoured (1 s^{-1} in solid contour; -1 s^{-1} in dashed contour). Time step F00, F06, F12, F18 are shown in rows in ascending order. "WRF-adj"-"ctrl" QGPV perturbation is not contoured in panel c for figure clarity

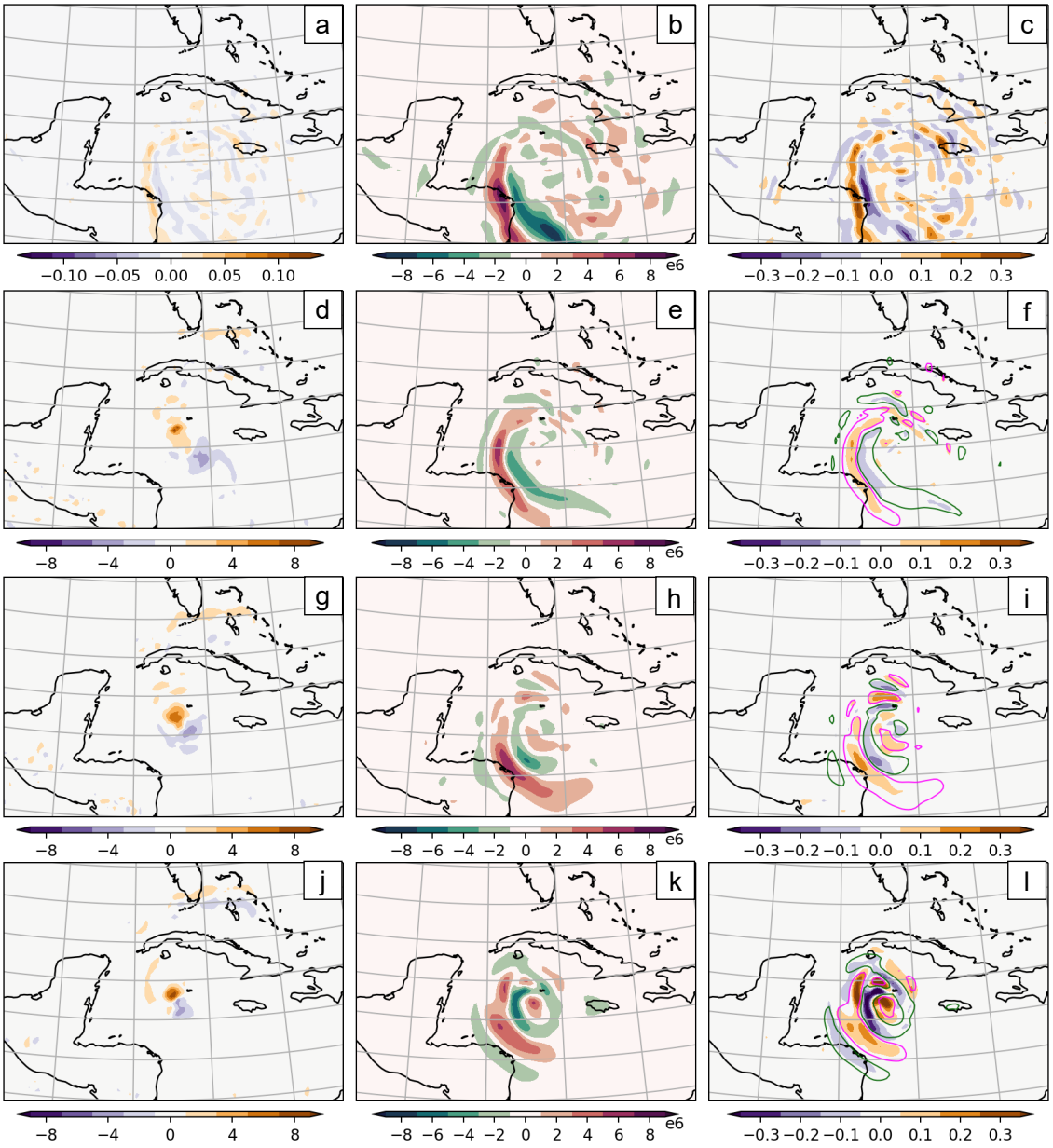

FIGURE 4.22: 500 hPa Ertel PV difference from "WRF-adj"-"ctrl" (shaded with unit PVU, column 1). Minus sensitivity to Ertel PV, $-\hat{q}_E$, at 500 hPa (shaded with unit Pa/PVU, column 2). 500 hPa Perturbation Erel PV (shaded) when nonlinear-balanced perturbations, $u'_{E,t}$, $v'_{E,t}$, $\theta'_{E,t}$ are introduced at each time step $t = 0, 6, 12, 18$, (column 3) with $-\hat{q}_E$ (1×10^6 Pa/PVU in magenta contour; -1×10^6 Pa/PVU in green contour). Time step F00, F06, F12, F18 are shown in rows in ascending order. $-\hat{q}_E$ is not contoured in panel c for figure clarity

Chapter 5

Conclusions and Future Directions

5.1 Conclusions

Known for its conservation property and invertibility, potential vorticity is an indispensable variable extensively used for diagnosing and understanding synoptic meteorology's dynamic processes (e.g., Hoskins et al. 1985; Morgan and Nielsen-Gammon 1998). Utilizing the adjoint of NWP models, the adjoint sensitivity study is a method to identify the dynamical aspect of synoptic weather systems and mostly focuses on the interpretation of individual adjoint sensitivity gradients. So far, few studies have transplanted the "PV thinking" and adjusted it to better suit the adjoint framework.

Although Philippe Arbogast laid down a comprehensive framework for adjoint sensitivity to PV as early as 1998, studies on PV adjoint sensitivity have mainly been studied with

the perturbation sensitivity method in the following decades (e.g., Fehlmann and Davies 1997; Ancell and Mass 2006; Vukićević and Raeder 1995; Doyle et al. 2014; Kim and Beare 2011), except for Romero et al. (2005). Kleist and Morgan (2005) established a technique to compute sensitivities to divergence and to vorticity using the adjoint of the MM5 model. Additionally, Morgan (2018) derived sensitivity to shallow water PV and stated that in the absence of extra forcing, only the balanced composition of adjoint sensitivities to wind and to height is retained after sufficient integration time.

Motivated by the attempt to enhance the interpretability of adjoint sensitivity fields in WRF's adjoint model by eliminating high-frequency wave patterns in adjoint integrations, we derived the adjoint sensitivity to QGPV, $\hat{q}_g$, by reckoning that the optimal perturbation of a variable is proportional to the adjoint sensitivity of this variable scaled by the Lagrange multiplier. During this process, we found the weighting for the pseudo-energy norm corresponds to the QGPV inversion operator. Further, we recovered sensitivities to winds and to the potential temperature that are under geostrophic balance. Analyzing the recovered wind and temperature sensitivities, we illustrated that a positive sensitivity to PV is surrounded by cyclonic sensitivity to winds, with warm temperature sensitivity above and cold temperature sensitivity below. The general formulation of sensitivity to PV derivation (Arbogast, 1998) yields the same expression for $\hat{q}_g$ and reinforces the close relationship between balance constraint and PV under the adjoint framework.

With the case of the March 2020 Atlantic Storm, we first demonstrated that the high-frequency wave in the WRF adjoint integration can be largely alleviated when a balanced

adjoint forcing is used. In addition, evidences such as the alignment of 500 hPa $\hat{q}_g$ maximum with the background trough (Fig. 2.4b), and the upshear tilting of $\hat{q}_g$ against the background thermal wind that leads to PV superposition, suggested $\hat{q}_g$ serves as a valuable diagnostic tool of being a combination of $\hat{\mathbf{v}}$ and $\hat{\theta}$ in adjoint sensitivity studies.

In the context of Arbogast (1998)'s derivation of sensitivity to PV, although the adjoint sensitivity to imbalance is provided as a by-product, the concept of geostrophic imbalance is barely addressed. We attempted to illustrate the notion of geostrophic imbalance (e.g. Fig. 3.1 and Fig. 3.2) and compared the difference between its associated unbalanced wind and the ageostrophic wind. Then the sensitivity to geostrophic imbalance, $\hat{a}$, is derived and illustrated with the schematic (Fig. 3.3). In the conceptual model of $\hat{a}$, we treated sensitivities to certain variables as small perturbations and introduced the idea of geostrophic adjustment and adiabatic response under the adjoint framework. In order to recover the sensitivity to unbalanced winds and unbalanced temperature, we discovered a general connection between $\hat{\mathbf{v}}$ and $\hat{\Psi}$, as well as the one between $\hat{\theta}$ and $\hat{\Phi}$. In addition, the geostrophic imbalance is speculated to be linked to the local time tendency of the velocity potential, from which diagnostic sensitivity to vertical velocity (ω) was derived.

The practical usage of sensitivity to imbalance is demonstrated through a case study of a November 1998 Winter Storm. Like $\hat{q}_g$, $\hat{a}$ combines $\hat{\mathbf{v}}$ and $\hat{\theta}$. However, in contrast to $\hat{q}_g$, $\hat{a}$ itself does not provide too much dynamical insight into the system development; rather, its time tendency partially reveals the secondary vertical circulation in the adjoint analysis. In a comparison between balanced and unbalanced wind and temperature sensitivities

(e.g. Fig. 3.14), we found the total wind sensitivity is dominated by the balanced wind, while the total temperature sensitivity is dominated by the unbalanced temperature. This behavior can be possibly attributed to the adjustment within the Rossby radius of deformation under their respective horizontal scale. A cross-examination between the accumulated precipitation and the unbalanced sensitivity to temperature suggests a potential link between the unbalanced sensitivity to temperature, $\hat{\theta}_i$, and $\hat{a}$ to diabatic heating, which is not captured by the geostrophic balance.

To extend the application of sensitivity to PV to the tropical region where QG assumption is less valid, the adjoint sensitivity to Ertel PV, $\hat{q}_E$, is derived following Arbogast (1998) and is solved with the successive over-relaxation method. A scale analysis is conducted to ensure the correctness of $\hat{q}_E$'s magnitude.

Using the case of Hurricane Ian, we compared sensitivity to Ertel PV, QGPV, and to geostrophic imbalance. Although $\hat{q}_E$ and $\hat{q}_g$ share a similar spatial distribution, positive $\hat{q}_E$ is not centered near the eyewall like $\hat{q}_g$ at lower- and mid-troposphere (e.g. Fig. 4.8). Compared with $\hat{q}_g$, $\hat{q}_E$ adeptly captures finer-scale details present in $\hat{a}$, especially at later stages of the adjoint integration. The nonlinear balanced wind and temperature sensitivities, $\hat{\mathbf{v}}_E$ and $\hat{\theta}_E$ qualitatively recovered from $\hat{q}_E$, resembles $\hat{\mathbf{v}}_g$ and $\hat{\theta}_i$, which dominate the wind and temperature sensitivity fields.

Optimal perturbations experiments informed by $\hat{q}_g$ and by $\hat{q}_E$ are similar in terms of how much they lead Hurricane Ian to weaken, their vertical perturbation energy distributions, and the amount of linearity retained in both experiments. This suggests that $\hat{q}_E$ is

successfully computed, despite numerous shortfalls in its calculation, such as issues in SOR convergence, the choice of basic states, and boundary conditions omitted in the sensitivity to Ertel PV operators, which should all be included in the future work.

Finally, we addressed the validity of approximating the sensitivity to PV by the PV perturbation that has been used in most of the previous studies to explore the sensitivity of PV to storm development (e.g., Fehlmann and Davies 1997; Ancell and Mass 2006; Vukićević and Raeder 1995; Doyle et al. 2014). Both sensitivities to QGPV and to Ertel PV are examined against the perturbation PV. It is observed that the optimal PV perturbation is similar to the sensitivity to PV at the initial time and diverges apart as the integration continues (e.g. Fig. 4.21). However, when the optimal perturbations are added to the model at individual timestep, the perturbation Ertel PV overlaps the sensitivity to Ertel PV (e.g. Fig. 4.22). Although the approximation shall still be made with caution, this examination presents a more reliable and easier way to assess the adjoint sensitivity to PV.

5.2 Future Directions

5.2.1 Sensitivity to Ertel PV Improvements

.

A few improvements shall be made in the future in sensitivity to Ertel PV calculation. First of all, boundary points should be added to the Ertel PV operators. Currently,

only interior points are included in the calculation and updated in the SOR iterations. Secondly, similar to the sensitivity to QGPV calculation, the surface sensitivity to temperature should be employed as the bottom boundary condition. This modification can likely turn the cold temperature sensitivity beneath the $\hat{q}_E$ maximum into a warm temperature sensitivity, aligning with TC's warm core nature. Finally, the choice of the basic state should be improved. It would be ideal to obtain the streamfunction and geopotential fields from the WRF model forward trajectory instead of using the JRA reanalysis. A simulation domain with no evident topographical feature can alleviate the SOR convergence failure due to the erroneous lower-level basic state. The possibility of solving sensitivity to Ertel PV using the minimization technique still needs to be explored. At the same time, sensitivity to nonlinear imbalance can be calculated with easy modification to the sensitivity to Ertel PV code.

5.2.2 Sensitivity to Balanced Moisture

Doyle et al. (2014), Doyle et al. (2011), and Demirdjian et al. 2020 have demonstrated the importance of moist processes in both tropical and mid-latitude systems using adjoint sensitivity analysis. They found that sensitivities to water vapor and to vorticity are co-located. In Chapter 3, we established a potential linkage between the diabatic process from latent heat release and the sensitivity to geostrophic imbalance. This is particularly relevant in tropical regions where the environment is largely under homogeneous temperature distribution and the moisture gradient control the region of convective events and

vertical motion (e.g., Sobel et al. 2001; Wolding et al. 2016). These convections are sometimes precursors to tropical cyclogenesis. Therefore constructing a balanced sensitivity to the moisture field is essential to extend the application of adjoint sensitivity analysis for studying tropical cyclone genesis and phenomena like the Madden-Julian Oscillation. This balance constraint can be the weak temperature gradient (WTG) balance which suggests the balanced state between column-integrated moisture and vertical motion.

Many previous studies have substituted the potential temperature with the moist potential temperature to calculate the moist potential vorticity and separate out the moisture/diabatic contribution to PV (e.g., Cao and Cho 1995; Schubert et al. 2001; McTaggart-Cowan et al. 2003). Smith and Stechmann (2017) argued that this moist PV is not conserved and introduced a moisture variable, M, with units of mixing ratio. They combined PV and moisture under the geostrophic balance and formulated a *PV-and-M* inversion that describes the balance among wind, temperature, and moisture. This approach opens a pathway to formulate a balanced adjoint forcing that includes the sensitivity to water vapor, even to liquid precipitation. An alternative, quicker approach is to scrutinize the relationship between sensitivity to temperature and to moisture variables in the WRF adjoint model. In WRFPLUS's limited options of microphysics scheme, such as the Kessler scheme (Kessler, 1995) and the large-scale condensation scheme, sensitivity to temperature and moisture variables are interconnected through the continuity equations for precipitation.

5.2.3 Background Error Covariance

Four-dimensional variational data assimilation (4D-Var) integrates the sensitivity of the forecast error to perturbation of the model state along the nonlinear model trajectory backward in time using the adjoint model. The 4D-Var procedure finds the analysis $\mathbf{x}_0$ by minimizing the cost function:

$$J(\mathbf{x}_0) = \frac{1}{2}(\mathbf{x}_0 - \mathbf{x}_0^b)^T \mathbf{B}^{-1}(\mathbf{x}_0 - \mathbf{x}_0^b) + \frac{1}{2}\sum_{i=0}^{N}(H(\mathbf{x}_i) - y_i^o)^T \mathbf{R}_i^{-1}(H(\mathbf{x}_i) - y_i^o)$$

where $\mathbf{x}_i^b$ represents the previous forecast (background), y_i^o denotes observations taken at time i. The first term measures the background cost at the analysis time and the second term evaluates the observation cost throughout the assimilation window. The background covariance matrix $\mathbf{B}$ spreads out the innovation in space and updates other variables to impose balance (e.g., Bannister 2008; Chen et al. 2013). The balance embedded in $\mathbf{B}$ is usually statistically generated and is often geostrophic and hydrostatic.

In both Gridpoint Statistical Interpolation (GSI) system and WRFDA, user-generated background error covariances are allowed and users can tune between the climatological $\mathbf{B}$ (geostrophic) and the ensemble $\mathbf{B}$ (flow dependent). The limited number of ensemble members restricts the accuracy of the matrix $\mathbf{B}$, which is why climatological $\mathbf{B}$ is often blended in. However, this geostrophic balance in climatological $\mathbf{B}$ can be problematic, as it might throw out useful unbalanced observations in the minimization process.

Shown in Chapter 3, **the geostrophically unbalanced part is extremely important in explaining the temperature sensitivity when secondary circulation is involved**. Derber and Bouttier (1999) showed that calibrating the background error covariance matrix away from the geostrophic balance in tropical and upper-troposphere results in a better analysis in early European Centre for Medium-Range Weather Forecasts' 3D- and 4D-Var assimilation. Thus research on the importance of the deviation from the geostrophic balance in the background error covariance **B** could improve the data assimilation quality in extreme events with high unpredictability.

5.2.4 Sensitivity Diagnoses from Neural Network

Toms et al. (2020) and Barnes et al. (2020) first employed an explainable artificial neural network to investigate the sensitivity of sea surface temperature 60, 120, and 180 days before the onset of El Niño or La Niña event. They used techniques like backward propagation and layerwise relevance propagation, akin to chain rule and adjoint model backward propagation. In addition, neural networks overcame the linearity constraint in the adjoint model. Wang et al. (2022) used a non-local neural net to improve midlatitude frontal system predictions in their machine-learning climate model. The algorithm also unveiled learned physical laws like divergence using layerwise relevance propagation. Leveraging pre-trained machine learning weather models, evaluating input predictor weighting, and comparing results with adjoint sensitivity might uncover mechanisms underlying cyclone development.

Bibliography

Aberson, S. D., 2003: Targeted observations to improve operational tropical cyclone track forecast guidance. *Monthly Weather Review*, **131**, 1613 – 1628, doi:https://doi.org/10.1175//2550.1.

Allen, J. S., 1991: Balance equations based on momentum equations with global invariants of potential enstrophy and energy. *Journal of Physical Oceanography*, **21**, 265 – 276, doi:https://doi.org/10.1175/1520-0485(1991)021¡0265:BEBOME¿2.0.CO;2.

Ancell, B. C. and C. F. Mass, 2006: Structure, growth rates, and tangent linear accuracy of adjoint sensitivities with respect to horizontal and vertical resolution. *Monthly Weather Review*, **134**, 2971 – 2988, doi:https://doi.org/10.1175/MWR3227.1.

Anderson, J., T. Hoar, K. Raeder, H. Liu, N. Collins, R. Torn, and A. Avellano, 2009: The data assimilation research testbed: A community facility. *Bulletin of the American Meteorological Society*, **90**, 1283 – 1296, doi:https://doi.org/10.1175/2009BAMS2618.1.

Arbogast, P., 1998: Sensitivity to potential vorticity. *Quarterly Journal of the Royal Meteorological Society*, **124**, 1605–1615, doi:https://doi.org/10.1002/qj.49712454912.

Arbogast, P., K. Maynard, and F. Crepin, 2008: Ertel potential vorticity inversion using a digital filter initialization method. *Quarterly Journal of the Royal Meteorological Society*, **134**, 1287–1296, doi:https://doi.org/10.1002/qj.283.

Argence, S., D. Lambert, E. Richard, J. Pierre Chaboureau, J. Philippe Arbogast, and K. Maynard, 2009: Improving the numerical prediction of a cyclone in the mediterranean by local potential vorticity modifications. *Quarterly Journal of the Royal Meteorological Society*, **135**, 865–879, doi:https://doi.org/10.1002/qj.422.

Bannister, R. N., 2008: A review of forecast error covariance statistics in atmospheric variational data assimilation. i: Characteristics and measurements of forecast error covariances. *Quarterly Journal of the Royal Meteorological Society*, **134**, 1951–1970, doi:https://doi.org/10.1002/qj.339.

Barnes, E. A., B. Toms, J. W. Hurrell, I. Ebert-Uphoff, C. Anderson, and D. Anderson, 2020: Indicator patterns of forced change learned by an artificial neural network. *Journal of Advances in Modeling Earth Systems*, **12**, e2020MS002195, doi:https://doi.org/10.1029/2020MS002195.

Barrett, B. S., E. R. Sanabia, S. C. Reynolds, J. K. Stapleton, and A. L. Borrego, 2016: Evolution of the upper tropospheric outflow in hurricanes iselle and julio (2014) in the navy global environmental model (navgem) analyses and in satellite and dropsonde observations. *Journal of Geophysical Research: Atmospheres*, **121**, 13,273–13,286, doi:https://doi.org/10.1002/2016JD025656.

Brooke-Zibton, Z. A., 2022: *Adjoint Sensitivity Studies of Tropical Cyclone Intensity Measures*. Ph.D. thesis, University of Wisconsin-Madison.

URL `http://digital.library.wisc.edu/1793/83308`

Brown, B. R. and G. J. Hakim, 2015: Sensitivity of intensifying atlantic hurricanes to vortex structure. *Quarterly Journal of the Royal Meteorological Society*, **141**, 2538–2551, doi:https://doi.org/10.1002/qj.2540.

Cao, Z. and H.-R. Cho, 1995: Generation of moist potential vorticity in extratropical cyclones. *Journal of Atmospheric Sciences*, **52**, 3263 – 3282, doi:https://doi.org/10.1175/1520-0469(1995)052¡3263:GOMPVI¿2.0.CO;2.

Charney, J., 1955: The use of the primitive equations of motion in numerical prediction. *Tellus*, **7**, 22–26, doi:https://doi.org/10.1111/j.2153-3490.1955.tb01138.x.

Charney, J. G., R. Fjörtoft, and J. Von Neumann, 1950: Numerical integration of the barotropic vorticity equation. *Tellus*, **2**, 237–254, doi:https://doi.org/10.1111/j.2153-3490.1950.tb00336.x.

Charney, J. G. and M. E. Stern, 1962: On the stability of internal baroclinic jets in a rotating atmosphere. *Journal of Atmospheric Sciences*, **19**, 159 – 172, doi:https://doi.org/10.1175/1520-0469(1962)019¡0159:OTSOIB¿2.0.CO;2.

Chen, Y., S. R. H. Rizvi, X.-Y. Huang, J. Min, and X. Zhang, 2013: Balance characteristics of multivariate background error covariances and their impact on analyses and

forecasts in tropical and arctic regions. *Meteorology and Atmospheric Physics*, **121**, 79–98, doi:10.1007/s00703-013-0251-y.

Cohen, Y., N. Harnik, E. Heifetz, D. S. Nolan, D. Tao, and F. Zhang, 2017: On the violation of gradient wind balance at the top of tropical cyclones. *Geophysical Research Letters*, **44**, 8017–8026, doi:https://doi.org/10.1002/2017GL074552.

Cunningham, P. and D. Keyser, 2004: Dynamics of jet streaks in a stratified quasi-geostrophic atmosphere: Steady-state representations. *Quarterly Journal of the Royal Meteorological Society*, **130**, 1579–1609, doi:https://doi.org/10.1256/qj.03.35.

Daley, R., 1978: Variational non-linear normal mode initialization. *Tellus*, **30**, 201–218, doi:https://doi.org/10.1111/j.2153-3490.1978.tb00836.x.

Davis, C. A. and K. A. Emanuel, 1991: Potential vorticity diagnostics of cyclogenesis. *Monthly Weather Review*, **119**, 1929 – 1953, doi:https://doi.org/10.1175/1520-0493(1991)119¡1929:PVDOC¿2.0.CO;2.

Davis, C. A., E. D. Grell, and M. A. Shapiro, 1996: The balanced dynamical nature of a rapidly intensifying oceanic cyclone. *Monthly Weather Review*, **124**, 3 – 26, doi:https://doi.org/10.1175/1520-0493(1996)124¡0003:TBDNOA¿2.0.CO;2.

Demirdjian, R., J. D. Doyle, C. A. Reynolds, J. R. Norris, A. C. Michaelis, and F. M. Ralph, 2020: A case study of the physical processes associated with the atmospheric river initial-condition sensitivity from an adjoint model. *Journal of the Atmospheric Sciences*, **77**, 691 – 709, doi:https://doi.org/10.1175/JAS-D-19-0155.1.

Derber, J. and F. Bouttier, 1999: A reformulation of the background error covariance in the ecmwf global data assimilation system. *Tellus A: Dynamic Meteorology and Oceanography*, **51**, 195–221, doi:10.3402/tellusa.v51i2.12316.

Dickinson, R. P. and R. J. Gelinas, 1976: Sensitivity analysis of ordinary differential equation systems—a direct method. *Journal of Computational Physics*, **21**, 123–143, doi:https://doi.org/10.1016/0021-9991(76)90007-3.

Dimet, F.-X. L. and O. Talagrand, 1986: Variational algorithms for analysis and assimilation of meteorological observations: theoretical aspects. *Tellus A*, **38A**, 97–110, doi:https://doi.org/10.1111/j.1600-0870.1986.tb00459.x.

Doyle, J., C. Amerault, and C. Reynolds, 2011: Diagnosing tropical cyclone sensitivity. *Computing in Science & Engineering*, **13**, 31–39, doi:10.1109/MCSE.2010.146.

Doyle, J. D., C. Amerault, C. A. Reynolds, and P. A. Reinecke, 2014: Initial condition sensitivity and predictability of a severe extratropical cyclone using a moist adjoint. *Monthly Weather Review*, **142**, 320 – 342, doi:https://doi.org/10.1175/MWR-D-13-00201.1.

Doyle, J. D., C. A. Reynolds, and C. Amerault, 2019: Adjoint sensitivity analysis of high-impact extratropical cyclones. *Monthly Weather Review*, **147**, 4511 – 4532, doi:https://doi.org/10.1175/MWR-D-19-0055.1.

Doyle, J. D., C. A. Reynolds, C. Amerault, and J. Moskaitis, 2012: Adjoint sensitivity and predictability of tropical cyclogenesis. *Journal of the Atmospheric Sciences*, **69**, 3535 – 3557, doi:https://doi.org/10.1175/JAS-D-12-0110.1.

Ehrendorfer, M., R. M. Errico, and K. D. Raeder, 1999: Singular-vector perturbation growth in a primitive equation model with moist physics. *Journal of the Atmospheric Sciences*, **56**, 1627 – 1648, doi:https://doi.org/10.1175/1520-0469(1999)056¡1627:SVPGIA¿2.0.CO;2.

Eliassen, A., 1962: On the vertical circulation in frontal zones. *Geofys. publ*, **24**, 147–160.

Errico, R. M., 1997: What is an adjoint model? *Bulletin of the American Meteorological Society*, **78**, 2577 – 2592, doi:https://doi.org/10.1175/1520-0477(1997)078¡2577:WIAAM¿2.0.CO;2.

Errico, R. M. and K. D. Raeder, 1999: An examination of the accuracy of the linearization of a mesoscale model with moist physics. *Quarterly Journal of the Royal Meteorological Society*, **125**, 169–195, doi:https://doi.org/10.1002/qj.49712555310.

Ertel, H., 1942: Ein neuer hydrodynamischer wirbelsatz. *Meteorologische Zeitschrift*, **59**, 277–281.

Fehlmann, R. and H. C. Davies, 1997: Misforecasts of synoptic systems: Diagnosis via pv retrodiction. *Monthly Weather Review*, **125**, 2247 – 2264, doi:https://doi.org/10.1175/1520-0493(1997)125¡2247:MOSSDV¿2.0.CO;2.

Fei, R., Y. Wang, and Y. Li, 2021: Contribution of vertical advection to supergradient wind in tropical cyclone boundary layer: A numerical study. *Journal of the Atmospheric Sciences*, **78**, 1057 – 1073, doi:https://doi.org/10.1175/JAS-D-20-0075.1.

Godinez, H. C. and D. N. Daescu, 2009: A second order adjoint method to targeted observations. *Computational Science – ICCS 2009*, G. Allen, J. Nabrzyski, E. Seidel, G. D. van Albada, J. Dongarra, and P. M. A. Sloot, eds., Springer Berlin Heidelberg, Berlin, Heidelberg, 322–331.

Goldstein, A. M., 2018: *A Methodology for Modulating the Intensification Rates of Forecast Mid-latitude Cyclones with Implications for Predictability*. Ph.D. thesis, University of Wisconsin-Madison.

Hakim, G. J. and R. D. Torn, 2008: Ensemble synoptic analysis. *Synoptic—Dynamic Meteorology and Weather Analysis and Forecasting: A Tribute to Fred Sanders*, L. F. Bosart and H. B. Bluestein, eds., American Meteorological Society, Boston, MA, 147–161.

Hall, M. C. G. and D. G. Cacuci, 1983: Physical interpretation of the adjoint functions for sensitivity analysis of atmospheric models. *Journal of Atmospheric Sciences*, **40**, 2537 – 2546, doi:https://doi.org/10.1175/1520-0469(1983)040¡2537:PIOTAF¿2.0.CO;2.

Henderson, J. M., G. M. Lackmann, and J. R. Gyakum, 1999: An analysis of hurricane opal's forecast track errors using quasigeostrophic potential vorticity inversion. *Monthly Weather Review*, **127**, 292 – 307, doi:https://doi.org/10.1175/1520-0493(1999)127¡0292:AAOHOS¿2.0.CO;2.

Hendricks, E. A., M. T. Montgomery, and C. A. Davis, 2004: The role of "vortical" hot towers in the formation of tropical cyclone diana (1984). *Journal of the Atmospheric Sciences*, **61**, 1209 – 1232, doi:https://doi.org/10.1175/1520-0469(2004)061¡1209:TROVHT¿2.0.CO;2.

Hersbach, H., B. Bell, P. Berrisford, S. Hirahara, A. Horányi, J. Muñoz-Sabater, J. Nicolas, C. Peubey, R. Radu, D. Schepers, A. Simmons, C. Soci, S. Abdalla, X. Abellan, G. Balsamo, P. Bechtold, G. Biavati, J. Bidlot, M. Bonavita, G. De Chiara, P. Dahlgren, D. Dee, M. Diamantakis, R. Dragani, J. Flemming, R. Forbes, M. Fuentes, A. Geer, L. Haimberger, S. Healy, R. J. Hogan, E. Hólm, M. Janisková, S. Keeley, P. Laloyaux, P. Lopez, C. Lupu, G. Radnoti, P. de Rosnay, I. Rozum, F. Vamborg, S. Villaume, and J.-N. Thépaut, 2020: The era5 global reanalysis. *Quarterly Journal of the Royal Meteorological Society*, **146**, 1999–2049, doi:https://doi.org/10.1002/qj.3803.

Holliday, C. R. and A. H. Thompson, 1979: Climatological characteristics of rapidly intensifying typhoons. *Monthly Weather Review*, **107**, 1022 – 1034, doi:https://doi.org/10.1175/1520-0493(1979)107¡1022:CCORIT¿2.0.CO;2.

Holton, J. and G. Hakim, 2019: *An Introduction to Dynamic Meteorology*. International Geophysics, Elsevier Science.

Hoover, B. T., 2015: Identifying a barotropic growth mechanism in east pacific tropical cyclogenesis using adjoint-derived sensitivity gradients. *Journal of the Atmospheric Sciences*, **72**, 1215 – 1234, doi:https://doi.org/10.1175/JAS-D-14-0053.1.

Hoover, B. T. and M. C. Morgan, 2011: Dynamical sensitivity analysis of tropical cyclone steering using an adjoint model. *Monthly Weather Review*, **139**, 2761 – 2775, doi:https://doi.org/10.1175/MWR-D-10-05084.1.

Hoskins, B. J., M. E. McIntyre, and A. W. Robertson, 1985: On the use and significance of isentropic potential vorticity maps. *Quarterly Journal of the Royal Meteorological Society*, **111**, 877–946, doi:https://doi.org/10.1002/qj.49711147002.

Hu, M., G. Ge, C. Zhou, D. Stark, H. Shao, K. Newman, J. Beck, and X. Zhang, 2018: *Grid-point Statistical Interpolation (GSI) User's Guide Version 3.7*. Developmental Testbed Center.
URL `https://dtcenter.org/community-code/gridpoint-statistical-interpolation-gsi/documentation`

Jung, B.-J., H. M. Kim, Y.-H. Kim, E.-H. Jeon, and K.-H. Kim, 2010: Observation system experiments for typhoon jangmi (200815) observed during t-parc. *Asia-Pacific J Atmos Sci*, **46**, 305–316, doi:10.1007/s13143-010-1007-y.

Kaplan, J. and M. DeMaria, 2003: Large-scale characteristics of rapidly intensifying tropical cyclones in the north atlantic basin. *Weather and Forecasting*, **18**, 1093 – 1108, doi:https://doi.org/10.1175/1520-0434(2003)018¡1093:LCORIT¿2.0.CO;2.

Kaplan, M. L., R. K. Vellore, J. M. Lewis, and M. Young, 2011: The role of unbalanced mesoscale circulations in dust storms. *Journal of Geophysical Research: Atmospheres*, **116**, doi:https://doi.org/10.1029/2011JD016218.

Kepert, J. and Y. Wang, 2001: The dynamics of boundary layer jets within the tropical cyclone core. part ii: Nonlinear enhancement. *Journal of the Atmospheric Sciences*, **58**, 2485 – 2501, doi:https://doi.org/10.1175/1520-0469(2001)058¡2485:TDOBLJ¿2.0.CO;2.

Kessler, E., 1995: On the continuity and distribution of water substance in atmospheric circulations. *Atmospheric Research*, **38**, 109–145, doi:https://doi.org/10.1016/0169-8095(94)00090-Z.

Keyser, D. and M. A. Shapiro, 1986: A review of the structure and dynamics of upper-level frontal zones. *Monthly Weather Review*, **114**, 452 – 499, doi:https://doi.org/10.1175/1520-0493(1986)114¡0452:AROTSA¿2.0.CO;2.

Kieu, C. Q. and D.-L. Zhang, 2010: A piecewise potential vorticity inversion algorithm and its application to hurricane inner-core anomalies. *Journal of the Atmospheric Sciences*, **67**, 2616 – 2631, doi:https://doi.org/10.1175/2010JAS3421.1.

Kim, H. M. and R. J. Beare, 2011: Characteristics of adjoint sensitivity to potential vorticity. *Meteorology and Atmospheric Physics*, **111**, 91–102, doi:https://doi.org/10.1007/s00703-010-0119-3.

Kleist, D. T. and M. C. Morgan, 2005: Interpretation of the structure and evolution of adjoint-derived forecast sensitivity gradients. *Monthly Weather Review*, **133**, 466 – 484, doi:https://doi.org/10.1175/MWR-2865.1.

Kobayashi, S., Y. OTA, Y. HARADA, A. EBITA, M. MORIYA, H. ONODA, K. ONOGI, H. KAMAHORI, C. KOBAYASHI, H. ENDO, K. MIYAOKA, and K. TAKAHASHI, 2015: The jra-55 reanalysis: General specifications and basic characteristics. *Journal of the Meteorological Society of Japan. Ser. II*, **93**, 5–48, doi:10.2151/jmsj.2015-001.

Komaromi, W. A. and J. D. Doyle, 2017: Tropical cyclone outflow and warm core structure as revealed by hs3 dropsonde data. *Monthly Weather Review*, **145**, 1339 – 1359, doi:https://doi.org/10.1175/MWR-D-16-0172.1.

Ladwig, W., 2017: wrf-python. Technical report, Boulder, Colorado: UCAR/NCAR.

Langland, R. H., R. L. Elsberry, and R. M. Errico, 1995: Evaluation of physical processes in an idealized extratropical cyclone using adjoint sensitivity. *Quarterly Journal of the Royal Meteorological Society*, **121**, 1349–1386, doi:https://doi.org/10.1002/qj.49712152608.

Lewis, J. M. and J. C. Derber, 1985: The use of adjoint equations to solve a variational adjustment problem with advective constraints. *Tellus A*, **37A**, 309–322, doi:https://doi.org/10.1111/j.1600-0870.1985.tb00430.x.

Lorenz, E. N., 1963: Deterministic nonperiodic flow. *Journal of Atmospheric Sciences*, **20**, 130 – 141, doi:https://doi.org/10.1175/1520-0469(1963)020¡0130:DNF¿2.0.CO;2.

Machenhauer, B., 1977: On the dynamics of gravity oscillations in a shallow water model, with applications to normal mode initialization. *Beitr. Phys. Atmos*, **50**.

Martin, J. E., 1999: Quasigeostrophic forcing of ascent in the occluded sector of cyclones and the trowal airstream. *Monthly Weather Review*, **127**, 70 – 88, doi:https://doi.org/10.1175/1520-0493(1999)127¡0070:QFOAIT¿2.0.CO;2.

McTaggart-Cowan, R., J. R. Gyakum, and M. K. Yau, 2003: Moist component potential vorticity. *Journal of the Atmospheric Sciences*, **60**, 166 – 177, doi:https://doi.org/10.1175/1520-0469(2003)060¡0166:MCPV¿2.0.CO;2.

— 2004: The impact of tropical remnants on extratropical cyclogenesis: Case study of hurricanes danielle and earl (1998). *Monthly Weather Review*, **132**, 1933 – 1951.

Mecikalski, J. R. and G. J. Tripoli, 1998: Inertial available kinetic energy and the dynamics of tropical plume formation. *Monthly Weather Review*, **126**, 2200 – 2216, doi:https://doi.org/10.1175/1520-0493(1998)126¡2200:IAKEAT¿2.0.CO;2.

Molinari, J., S. Skubis, D. Vollaro, F. Alsheimer, and H. E. Willoughby, 1998: Potential vorticity analysis of tropical cyclone intensification. *Journal of the Atmospheric Sciences*, **55**, 2632 – 2644, doi:https://doi.org/10.1175/1520-0469(1998)055¡2632:PVAOTC¿2.0.CO;2.

Montgomery, M. T., M. E. Nicholls, T. A. Cram, and A. B. Saunders, 2006: A vortical hot tower route to tropical cyclogenesis. *Journal of the Atmospheric Sciences*, **63**, 355 – 386, doi:https://doi.org/10.1175/JAS3604.1.

Montgomery, M. T. and R. K. Smith, 2017: Recent developments in the fluid dynamics of tropical cyclones. *Annual Review of Fluid Mechanics*, **49**, 541–574, doi:10.1146/annurev-fluid-010816-060022.

Morgan, M. C., 2018: On the dynamics of adjustment in the f-plane shallow water adjoint system. *Journal of the Atmospheric Sciences*, **75**, 1571 – 1585, doi:https://doi.org/10.1175/JAS-D-17-0100.1.

Morgan, M. C. and J. W. Nielsen-Gammon, 1998: Using tropopause maps to diagnose midlatitude weather systems. *Monthly Weather Review*, **126**, 2555 – 2579, doi:https://doi.org/10.1175/1520-0493(1998)126¡2555:UTMTDM¿2.0.CO;2.

National Centers for Environmental Prediction, National Weather Service, NOAA, U.S. Department of Commerce, 2015: Ncep gdas/fnl 0.25 degree global tropospheric analyses and forecast grids.

Nolan, D. S. and B. F. Farrell, 1999: Generalized stability analyses of asymmetric disturbances in one- and two-celled vortices maintained by radial inflow. *Journal of the Atmospheric Sciences*, **56**, 1282 – 1307, doi:https://doi.org/10.1175/1520-0469(1999)056¡1282:GSAOAD¿2.0.CO;2.

Orr, W. M., 1907: The stability or instability of the steady motions of a perfect liquid and of a viscous liquid. part ii: A viscous liquid. *Proceedings of the Royal Irish Academy. Section A: Mathematical and Physical Sciences*, **27**, 69–138.

Park, S. K. and K. K. Droegemeier, 1997: Validity of the tangent linear approximation in a moist convective cloud model. *Monthly Weather Review*, **125**, 3320 – 3340, doi:https://doi.org/10.1175/1520-0493(1997)125¡3320:VOTTLA¿2.0.CO;2.

Posselt, D. J., 2001: *The role of latent heating in the formation of a warm-occluded thermal structure in an intense continental cyclone*. Master's thesis, University of Wisconsin-Madison.

Pu, Z.-X., E. Kalnay, J. Sela, and I. Szunyogh, 1997: Sensitivity of forecast errors to initial conditions with a quasi-inverse linear method. *Monthly Weather Review*, **125**, 2479 – 2503, doi:https://doi.org/10.1175/1520-0493(1997)125¡2479:SOFETI¿2.0.CO;2.

Rabier, F. and P. Courtier, 1992: Four-dimensional assimilation in the presence of baroclinic instability. *Quarterly Journal of the Royal Meteorological Society*, **118**, 649–672, doi:https://doi.org/10.1002/qj.49711850604.

Rappin, E. D., M. C. Morgan, and G. J. Tripoli, 2011: The impact of outflow environment on tropical cyclone intensification and structure. *Journal of the Atmospheric Sciences*, **68**, 177 – 194, doi:https://doi.org/10.1175/2009JAS2970.1.

Rappin, E. D., D. S. Nolan, and S. J. Majumdar, 2013: A highly configurable vortex initialization method for tropical cyclones. *Monthly Weather Review*, **141**, 3556 – 3575, doi:https://doi.org/10.1175/MWR-D-12-00266.1.

Raymond, D. J., 1992: Nonlinear balance and potential-vorticity thinking at large rossby number. *Quarterly Journal of the Royal Meteorological Society*, **118**, 987–1015.

Reynolds, C. A., J. D. Doyle, and X. Hong, 2016: Examining tropical cyclone–kelvin wave interactions using adjoint diagnostics. *Monthly Weather Review*, **144**, 4421 – 4439, doi:https://doi.org/10.1175/MWR-D-16-0174.1.

Reynolds, C. A., J. D. Doyle, F. M. Ralph, and R. Demirdjian, 2019: Adjoint sensitivity of north pacific atmospheric river forecasts. *Monthly Weather Review*, **147**, 1871 – 1897, doi:https://doi.org/10.1175/MWR-D-18-0347.1.

Reynolds, C. A., R. Gelaro, and J. D. Doyle, 2001: Relationship between singular vectors and transient features in the background flow. *Quarterly Journal of the Royal Meteorological Society*, **127**, 1731–1760, doi:https://doi.org/10.1002/qj.49712757514.

Romero, R., A. Martín, V. Homar, S. Alonso, and C. Ramis, 2005: Predictability of prototype flash flood events in the western mediterranean under uncertainties of the precursor upper-level disturbance: the hydroptimet case studies. *Natural Hazards and Earth System Sciences*, **5**, 505–525, doi:10.5194/nhess-5-505-2005.

Rowe, S. M. and M. H. Hitchman, 2016: On the relationship between inertial instability, poleward momentum surges, and jet intensifications near midlatitude cyclones. *Journal of the Atmospheric Sciences*, **73**, 2299 – 2315, doi:https://doi.org/10.1175/JAS-D-15-0183.1.

Schubert, W. H., S. A. Hausman, M. Garcia, K. V. Ooyama, and H.-C. Kuo, 2001: Potential vorticity in a moist atmosphere. *Journal of the Atmospheric Sciences*, **58**, 3148 – 3157, doi:https://doi.org/10.1175/1520-0469(2001)058¡3148:PVIAMA¿2.0.CO;2.

Skamarock, C., B. Klemp, J. Dudhia, O. Gill, Z. Liu, J. Berner, W. Wang, G. Powers, G. Duda, D. M. Barker, and X. Huang, 2019: A description of the advanced research wrf model version 4. Technical report, University Corporation for Atmospheric Research.

Skamarock, W. C. and J. B. Klemp, 2008: A time-split nonhydrostatic atmospheric model for weather research and forecasting applications. *Journal of Computational Physics*, **227**, 3465–3485, doi:https://doi.org/10.1016/j.jcp.2007.01.037, predicting weather, climate and extreme events.

Skamarock, W. C., J. B. Klemp, J. Dudhia, D. O. Gill, D. Barker, M. G. Duda, X. yu Huang, W. Wang, and J. G. Powers, 2008: A description of the advanced research wrf version 3 (no. ncar/tn-475+str). Technical report, University Corporation for Atmospheric Research.

Smith, L. M. and S. N. Stechmann, 2017: Precipitating quasigeostrophic equations and potential vorticity inversion with phase changes. *Journal of the Atmospheric Sciences*, **74**, 3285 – 3303, doi:https://doi.org/10.1175/JAS-D-17-0023.1.

Smith, R. K., M. T. Montgomery, and H. Bui, 2018: Axisymmetric balance dynamics of tropical cyclone intensification and its breakdown revisited. *Journal of the Atmospheric Sciences*, **75**, 3169 – 3189, doi:https://doi.org/10.1175/JAS-D-17-0179.1.

Snyder, C. and A. Joly, 1998: Development of perturbations within growing baroclinic waves. *Quarterly Journal of the Royal Meteorological Society*, **124**, 1961–1983, doi:https://doi.org/10.1002/qj.49712455009.

Sobel, A. H., J. Nilsson, and L. M. Polvani, 2001: The weak temperature gradient approximation and balanced tropical moisture waves. *Journal of the Atmospheric Sciences*, **58**, 3650 – 3665, doi:https://doi.org/10.1175/1520-0469(2001)058¡3650:TWTGAA¿2.0.CO;2.

Stoelinga, M. T., 1996: A potential vorticity-based study of the role of diabatic heating and friction in a numerically simulated baroclinic cyclone. *Monthly Weather Review*, **124**, 849 – 874, doi:https://doi.org/10.1175/1520-0493(1996)124¡0849:APVBSO¿2.0.CO;2.

Sundqvist, H. and G. Veronis, 1970: A simple finite-difference grid with non-constant intervals. *Tellus*, **22**, 26–31, doi:10.3402/tellusa.v22i1.10155.

Sutcliffe, R. C. and A. G. Forsdyke, 1950: The theory and use of upper air thickness patterns in forecasting. *Quarterly Journal of the Royal Meteorological Society*, **76**, 189–217, doi:https://doi.org/10.1002/qj.49707632809.

Thacker, W. C. and R. B. Long, 1988: Fitting dynamics to data. *Journal of Geophysical Research: Oceans*, **93**, 1227–1240, doi:https://doi.org/10.1029/JC093iC02p01227.

Thompson, C. F. and D. M. Schultz, 2021: The release of inertial instability near an idealized zonal jet. *Geophysical Research Letters*, **48**, e2021GL092649, doi:https://doi.org/10.1029/2021GL092649.

Toms, B. A., E. A. Barnes, and I. Ebert-Uphoff, 2020: Physically interpretable neural networks for the geosciences: Applications to earth system variability. *Journal of Advances in Modeling Earth Systems*, **12**, e2019MS002002, doi:https://doi.org/10.1029/2019MS002002.

Torn, R. D. and G. J. Hakim, 2008: Ensemble-based sensitivity analysis. *Monthly Weather Review*, **136**, 663 – 677, doi:https://doi.org/10.1175/2007MWR2132.1.

Vich, M.-D.-M., R. Romero, E. Richard, P. Arbogast, and K. Maynard, 2012: Perturbing the potential vorticity field in mesoscale forecasts of two mediterranean heavy precipitation events. *Tellus A: Dynamic Meteorology and Oceanography*, doi:10.3402/tellusa.v64i0.17224.

Vukićević, T. and K. Raeder, 1995: Use of an adjoint model for finding triggers for alpine lee cyclogenesis. *Monthly Weather Review*, **123**, 800 – 816, doi:https://doi.org/10.1175/1520-0493(1995)123¡0800:UOAAMF¿2.0.CO;2.

Wang, P., J. Yuval, and P. A. O'Gorman, 2022: Non-local parameterization of atmospheric subgrid processes with neural networks. *Journal of Advances in Modeling Earth Systems*, **14**, e2022MS002984, doi:https://doi.org/10.1029/2022MS002984.

Wang, S., R. K. Smith, and M. T. Montgomery, 2020: Upper-tropospheric inflow layers in tropical cyclones. *Quarterly Journal of the Royal Meteorological Society*, **146**, 3466–3487, doi:https://doi.org/10.1002/qj.3856.

Wang, X. and D.-L. Zhang, 2003: Potential vorticity diagnosis of a simulated hurricane. part i: Formulation and quasi-balanced flow. *Journal of the Atmospheric Sciences*, **60**, 1593 – 1607, doi:https://doi.org/10.1175/2999.1.

Wolding, B. O., E. D. Maloney, and M. Branson, 2016: Vertically resolved weak temperature gradient analysis of the madden-julian oscillation in sp-cesm. *Journal of Advances in Modeling Earth Systems*, **8**, 1586–1619, doi:https://doi.org/10.1002/2016MS000724.

Wu, C.-C., 1993: *Understanding hurricane movement from a potential vorticity perspective: a numerical model and an observational study*. Ph.D. thesis, Massachusetts Institute of Technology.

Wu, C.-C., J.-H. Chen, P.-H. Lin, and K.-H. Chou, 2007: Targeted observations of tropical cyclone movement based on the adjoint-derived sensitivity steering vector. *Journal of the Atmospheric Sciences*, **64**, 2611 – 2626, doi:https://doi.org/10.1175/JAS3974.1.

Wu, C.-C. and K. A. Emanuel, 1995: Potential vorticity diagnostics of hurricane movement. part 1: A case study of hurricane bob (1991). *Monthly Weather Review*, **123**, 69 – 92, doi:https://doi.org/10.1175/1520-0493(1995)123¡0069:PVDOHM¿2.0.CO;2.

Xu, M., D. J. Stensrud, J.-W. Bao, and T. T. Warner, 2001: Applications of the adjoint technique to short-range ensemble forecasting of mesoscale convective systems. *Monthly Weather Review*, **129**, 1395 – 1418, doi:https://doi.org/10.1175/1520-0493(2001)129¡1395:AOTATT¿2.0.CO;2.

Xu, Q., 1994: Semibalance model—connection between geostrophic-type and balanced-type intermediate models. *Journal of Atmospheric Sciences*, **51**, 953 – 970, doi:https://doi.org/10.1175/1520-0469(1994)051¡0953:SMBGTA¿2.0.CO;2.

Xu, Q., J. Gao, and W. Gu, 1998: Generalized adjoint for physical processes with parameterized discontinuities. part v: Coarse-grain adjoint and problems in gradient check. *Journal of the Atmospheric Sciences*, **55**, 2130 – 2135, doi:https://doi.org/10.1175/1520-0469(1998)055¡2130:GAFPPW¿2.0.CO;2.

Zhang, F., 2004: Generation of mesoscale gravity waves in upper-tropospheric jet–front systems. *Journal of the Atmospheric Sciences*, **61**, 440 – 457, doi:https://doi.org/10.1175/1520-0469(2004)061¡0440:GOMGWI¿2.0.CO;2.

Zhang, F., K. Steven E., D. Christopher A., and K. Michael L., 2000: A survey of unbalanced flow diagnostics and their application. *Advances in Atmospheric Sciences*, **17**, 165–183, doi:10.1007/s00376-000-0001-1.

Zhang, X., X.-Y. Huang, and N. Pan, 2013: Development of the upgraded tangent linear and adjoint of the weather research and forecasting (wrf) model. *Journal of Atmospheric and Oceanic Technology*, **30**, 1180 – 1188, doi:https://doi.org/10.1175/JTECH-D-12-00213.1.

Ziemiański, M. Z. and A. J. Thorpe, 2003: Nonlinear balanced models for stratified fluids conserving ertel–rossby pv. *Quarterly Journal of the Royal Meteorological Society*, **129**, 139–156, doi:https://doi.org/10.1256/qj.02.58.